

Summer 8-2011

Self-Repairable Polymeric Networks: Synthesis and Network Design

Biswajit Ghosh

University of Southern Mississippi

Follow this and additional works at: <https://aquila.usm.edu/dissertations>



Part of the [Polymer Chemistry Commons](#)

Recommended Citation

Ghosh, Biswajit, "Self-Repairable Polymeric Networks: Synthesis and Network Design" (2011). *Dissertations*. 480.
<https://aquila.usm.edu/dissertations/480>

This Dissertation is brought to you for free and open access by The Aquila Digital Community. It has been accepted for inclusion in Dissertations by an authorized administrator of The Aquila Digital Community. For more information, please contact Joshua.Cromwell@usm.edu.

The University of Southern Mississippi

SELF-REPAIRABLE POLYMERIC NETWORKS:
SYNTHESIS AND NETWORK DESIGN

by

Biswajit Ghosh

Abstract of a Dissertation
Submitted to the Graduate School
of The University of Southern Mississippi
in Partial Fulfillment of the Requirements
for the Degree of Doctor of Philosophy

August 2011

ABSTRACT

SELF-REPAIRABLE POLYMERIC NETWORKS:
SYNTHESIS AND NETWORK DESIGN

by Biswajit Ghosh

August 2011

This dissertation describes the design, synthesis and development of a new class of polymeric networks that exhibit self-repairing properties under UV exposure. It consists of two parts: (a) modification and synthesis of oxetane (OXE), and oxolane (OXO) substituted chitosan (CHI) macromonomer, and (b) design, and synthesis of self-repairing polyurethane (PUR) networks consisting of modified chitosan. Unmodified CHI consisting of acetamide ($-\text{NHCOCH}_3$), primary hydroxyl ($-\text{OH}$), and amine ($-\text{NH}_2$) functional groups were reacted with OXE or OXO compounds under basic conditions in order to substitute the 1° $-\text{OH}$ groups, and at the same time, convert $-\text{NHCOCH}_3$ functionalities into $-\text{NH}_2$ groups, while maintaining their un-reacted form to generate OXE/OXO-substituted CHI macromonomer. These substituted CHI macromonomers were incorporated within the PUR backbone by reacting with trifunctional isocyanate in the presence of polyethylene glycol (PEG) and dibutyl tin dilaurate catalyst (DBTDL). Utilizing spectroscopic analysis combined with optical microscopy, these studies showed that the kinetics of self-repair depends on the stoichiometry of the individual entities as well as the time required for self-repairing to occur decrease with increasing OXE quantity within the network. Internal reflection infrared imaging (IRIRI) of OXE/OXO-CHI-PUR networks as well as Raman and Fourier transform IR (FT-IR) studies of OXE/OXO-CHI macromonomers revealed that cationic OXE/OXO ring opening, free

radical polyurea (PUA)-to-PUR conversion, along with chair-to-boat conformational changes of CHI backbone are responsible for repairing the damaged network. The network remodeling process, investigated by utilizing micro-thermal analyzer (μ TA), revealed that mechanical damage generates small fragments or oligomers within the scratch, therefore glass transition temperature (T_g) decreases, and under UV exposure cross-linking reactions propagate from the bottom of the scratch to the top resulting in an increase of T_g within the scratch and subsequently repair.

COPYRIGHT BY
BISWAJIT GHOSH

2011

The University of Southern Mississippi

SELF-REPAIRABLE POLYMERIC NETWORKS:

SYNTHESIS AND NETWORK DESIGN

by

Biswajit Ghosh

A Dissertation

Submitted to the Graduate School
of The University of Southern Mississippi
in Partial Fulfillment of the Requirements
for the Degree of Doctor of Philosophy

Approved:

Marek W. Urban

Director

Sergei I. Nazarenko

Jeffrey S. Wiggins

Sarah E. Morgan

William L. Jarrett

Ras B. Pandey

Susan A. Siltanen

Dean of the Graduate School

August 2011

ACKNOWLEDGMENTS

First and foremost, I want to thank my advisor Dr. Marek W. Urban. It has been an honor to be a Ph.D. student in his research group. He has taught me, both consciously and unconsciously, how to work in a smart way and to always look at the big picture. I appreciate all his contribution of time, ideas, and funding to make my Ph.D. experience productive and stimulating. The joy and enthusiasm he has for his research was contagious and motivational for me, even during tough times in the Ph.D. pursuit. I am also thankful for the excellent example he has provided as a successful polymer scientist and professor in the School of Polymer Science and High Performance Materials.

I would like to thank Dr. William L. Jarrett for his advice and suggestions in NMR measurements and analysis. I acknowledge my graduate committee members, Dr. Jeffrey S. Wiggins, Dr. Sergei I. Nazarenko, Dr. Sarah E. Morgan, and Dr. Ras B. Pandey, for their advice and support.

The members of the Urban Research Group have contributed immensely to my personal and professional time at USM. The group has been a source of friendship as well as good advice and collaboration. I am grateful to all my colleagues of URG for being my surrogate family during the many years I stayed here and for their continued moral support thereafter.

Lastly, I would like to thank my parents, Sukdev Ghosh and Protima Ghosh, who raised me with a love of science and supported me in all my pursuits. They have lost a lot due to my research abroad. Without their love, encouragement, and understanding, it would have been impossible for me to finish this work. I would also like to give a special thanks to the person who was always with me during my research.

TABLE OF CONTENTS

ABSTRACT.....	ii
ACKNOWLEDGMENTS.....	iv
LIST OF ILLUSTRATIONS.....	vii
LIST OF TABLES.....	xii
INTRODUCTION.....	xiii
CHAPTER	
I. DAMAGES AND REPAIR IN BIOLOGICAL AS WELL AS POLYMERIC SYSTEMS.....	1
Introduction	
Damage and Repair Mechanisms in Polymers	
Dimensions of Damages and Repairs	
Angstrom Level Repairs	
Nanometer Level Repairs	
Micrometer Level Repairs	
Milimeter Level Repairs	
Conclusion	
References	
II. SYNTHESIS OF OXETANE-SUBSTITUTED CHITOSAN MACROMONOMERS.....	37
Introduction	
Experimental	
Results and Discussion	
Conclusion	
References	
III. SELF-REPAIRING OXETANE-SUBSTITUED CHITOSAN CHITOSAN-POLYURETHANE NETWORKS.....	47
Introduction	
Experimental	
Results and Discussion	
Conclusion	
References	

IV. CHEMO-MECHANICAL REPAIRS INSIDE A SCRATCH OF OXETANE-SUBSTITUTED CHITOSAN-POLYURETHANE (OXE-CHI-PUR) NETWORKS.....	58
Introduction	
Experimental	
Results and Discussion	
Conclusion	
References	
V. THE INFLUENCE OF RING STRENGTH ON THE SELF-REPAIRING OF CHITOSAN-SUBSTITUTED POLYURETHANE NETWORKS.....	92
Introduction	
Experimental	
Results and Discussion	
Conclusion	
References	
VI. CONCLUDING REMARKS.....	121
APPENDIXES.....	124

LIST OF ILLUSTRATIONS

Figure

1.1.A. Selected examples of damage and repair mechanism occurring in mammals as a function of time.....	17
1.1.B. Selected examples of damages and repair mechanism occurring in plants as a function of time.....	18
1.2 Schematic diagram illustrating an ideal self-healing polymeric network.....	19
1.3. Schematic diagram of examples of damages and repairs in synthetic materials.....	20
1.4. Ester exchange reaction in polycarbonate leading to healing.....	21
1.5. Schematic representation of covalent bond formation between scission chain ends in the presence of Cu catalyst leading to healing in polypropylene ether.....	22
1.6. [2+2] cycloaddition reactions of cinnamoyl groups leading to healing.....	23
1.7. Schematic representation of Diels-Alder mechanism (A), specific mechanism of multi-furan and multi-maleimide containing backbone within crosslink polymer system for reversible self-repair (B), and optical images of self-repairing polymer network (C).....	24
1.8. Synthetic steps involved in creating self-healing polyurethanes containing oxetane and chitosan (A), and optical images of OXE-CHI-PUR network healed under UV exposure (B).....	25
1.9. Proposed molecular healing mechanism of ureaisopyrimidone (UPy) network via H-bonding.....	26
1.10. Schematic representation of reversible network formed by a mixture of fatty diacid and triacid condensed with diethylene triamine followed by reaction with urea to produce a mixture of oligomers equipped with complementary hydrogen bonding.....	27
1.11. Schematic representation of a self-healing supramolecular polymer network (A) containing coordinated Terpyridine-Ru pincer complex (B), and aqueous micelle (C) formation by copolymerization with monomers.....	28
1.12. Optical images of self-repairing MMA/nBA/HDFMA films containing 14 w/w% of γ -Fe ₂ O ₃ nanoparticles in the presence of oscillating magnetic field.....	29
1.13. Schematic representation of dynamic equilibrium between a monomer species and organometallic polymer leading to healing (A) and SEM images of the	

damaged polymeric film before (B) and after (C) exposure to 200 °C, respectively.....	30
1.14. Schematic representation of self-repairing in polymer composites containing encapsulated hollow-fibers (A), micro-particles (B), by ring-opening metathesis reaction of DCPD (C).....	31
1.15. Schematic diagram of self-healing in the context of time and dimensions.....	32
2.1. Synthetic route of OXE-CHI macromonomer synthesis.....	42
2.2. ATR-FT-IR spectra of (A) CHI and (B) OXE-CHI products.....	43
2.3. Raman spectra of (A) CHI and (B) OXE-CHI products.....	44
2.4. Solid state ^{13}C -NMR spectra of (A) CHI and (B) OXE-CHI products.....	45
3.1. Synthetic steps involved in the formation of OXE-CHI. 1, Reactions of OXE with CHI, leading to the formation of OXE-CHI precursor; 2, Reactions of OXE-CHI with HDI and PEG, leading to formations of remendable OXE-CHI-PUR network.....	53
3.2. IRIR (upper) and optical (lower) images of OXE-CHI-PUR networks recorded as a UV exposure time. A1, 0min; A2, 15 min; A3, 30 min.....	54
3.3. Optical images of mechanically damaged films: PUR (A1, A2, and A3 are images after exposure for 0, 15 and 30 min to UV radiation; HDI/PEG/CHI = 1:1.5:0); CHI-PUR (B1, B2, and B3 are images after exposure for 0, 15 and 30 min to UV radiation; HDI/PEG/CHI = 1:1.4:0.57x10 ⁻⁴); OXE-CHI-PUR (C1, C2, and C3 are images after exposure for 0, 15 and 30 min to UV radiation; HDI/PEG/OXE-CHI = 1:1.4:0.57x10 ⁻⁴); OXE-CHI-PUR (D1, D2 and D3 are images after exposure for 0, 15 and 30 min to UV radiation; HDI/PEG/OXE-CHI = 1:1.33:1.17x10 ⁻⁴).	55
4.1. A) Synthesis of OXE-CHI-PUR networks, B) Molar ratios of network components and reactive groups of the reagents, and C) Optical images of damaged and repaired networks.....	78
4.2. Optical images represent OXE-CHI-PUR networks (HDI:PEG:OXE- CHI:DBTDL=1.0:1.33:1.17x10 ⁻⁴ :2x10 ⁻⁵) containing 1:1 (A1-A3), 1:4 (B1-B2), and 1:10 (C1-C3) molar OXE-CHI recorded as a UV exposure time. Optical images of PUR networks (D1-D3) recorded as a UV exposure time 0, 30, 60 min. Optical images of OXE-CHI-PUR networks (HDI:PEG:OXE- CHI:DBTDL=1.0:1.33:1.17x10 ⁻⁴ :1x10 ⁻²) containing 1:1 molar OXE-CHI recorded as a UV exposure time 0, 30, 60 min (E1-E3).....	79

4.3. IRIR images (A) and ATR-FTIR spectra (B) of OXE-CHI-PUR (HDI:PEG:OXE-CHI=1.0:1.33:1.17x10 ⁻⁴) networks containing a) 2x10 ⁻⁵ , b) 4x10 ⁻⁵ , c) 1x10 ⁻⁴ , d) 1x10 ⁻³ and e) 1x10 ⁻² mole DBTDL	80
4.4. Optical images of OXE-CHI-PUR networks (HDI:PEG:OXE-CHI:DBTDL =1.0:1.33:1.17x10 ⁻⁴ :2x10 ⁻⁵) exposed to UV light without acidic environments (A1-A3), at pH=6.8 (B1-B3), 6 (C1-C3), 5 (D1-D3), 4 (E1-E3), 3(F1-F3) and list of DBTDL, AA, and total proton concentration within the crack at various pH.....	81
4.5. IRIRI images of OXE-CHI-PUR networks (HDI:PEG:OXE-CHI:DBTDL =1.0:1.33:1.17x10 ⁻⁴ :2x10 ⁻⁵) containing 1:1 molar OXE-CHI at pH=3 recorded as a UV exposure time 0, 10, and 20 min, respectively. (A1-A3) images were obtained by tuning into the 1520 cm ⁻¹ band; (A1'-A3', A1''-A3'') IR spectra recorded from mechanically damaged and undamaged areas.....	82
4.6. IRIRI images of OXE-CHI-PUR networks (HDI:PEG:OXE-CHI:DBTDL =1.0:1.33:1.17x10 ⁻⁴ :2x10 ⁻⁵) containing 1:1 molar OXE-CHI at pH=6.8 recorded as a UV exposure time 0, 10, and 20 min, respectively. (A1-A3) images were obtained by tuning into the 1520 cm ⁻¹ band; (A1'-A3', A1''-A3'') IR spectra recorded from mechanically damaged and undamaged areas.....	83
4.7. Schematic diagram of reaction products and band assignments obtained from UV exposure of OXE-CHI.....	84
4.8. Optical images of OXE-CHI-PUR networks (HDI:PEG:OXE-CHI:DBTDL =1.0:1.33:1.17x10 ⁻⁴ :2x10 ⁻⁵) containing OXE-CHI of 1:1 (A1-A3), 1:4 (B1-B3), and 1:10 (C1-C3) molar ratios, respectively along with 1 % HALS in each network exposed to UV.....	85
4.9. IRIRI images of OXE-CHI-PUR networks (HDI:PEG:OXE-CHI:DBTDL =1.0:1.33:1.17x10 ⁻⁴ :2x10 ⁻⁵) containing 1:1 molar OXE-CHI and 1% HALS recorded as a UV exposure time 0, 30, and 120 min, respectively. (A1-A3) images were obtained by tuning into the 1542 cm ⁻¹ band; (A1'-A3', A1''-A3'', A1'''-A3''') IR spectra recorded from mechanically damaged and undamaged areas.....	86
4.10. Proposed self-healing mechanism of OXE-CHI-PUR network under UV exposure.....	87
4.11. Repair of PUR network in the presence of external OXE-CHI in A) AA, and B) DMSO+DBTDL.....	88
4.12. Atomic force microscopy (AFM) images of undamaged (A1), damaged (A2), UV-exposed (A2 ¹ ,A2 ²) and repaired (A3) OXE-CHI-PUR network (HDI:PEG:OXE-CHI:DBTDL =1.0:1.33:1.17x10 ⁻⁴ :2x10 ⁻⁵), and plot of height vs width profile of undamaged (A1'), damaged (A2'), UV exposed (A2 ¹ ') and repaired (A3') networks, and d(Δl)/dT vs temperature (A1''-A3'') for the same. AFM images of	

undamaged (B1), damaged (B2), and UV-exposed (B3,B3 ²) PUR network and plot of height vs width profile of undamaged (B1'), damaged (B2'), and UV-exposed (B3') networks, and $d(\Delta l)/dT$ vs temperature (B1''-B3'') for the same.....	89
5.1. Optical images represent OXO-CHI-PUR networks (HDI:PEG:OXO-CHI:DBTDL=1.0:1.33:1.17x10 ⁻⁴ :2x10 ⁻⁵) containing 1:1 (A1-A3), 1:4 (B1-B2), and 1:10 (C1-C3) molar OXO-CHI recorded as a function of UV exposure time. Optical images represent OXO-CHI-PUR networks (HDI:PEG:OXO-CHI:DBTDL=1.0:1.33:1.17x10 ⁻⁴ :1x10 ⁻⁴) containing 1:1 molar OXO-CHI recorded as a function of UV exposure time.....	107
5.2. Atomic force microscopy (AFM) images of undamaged (A1), damaged and UV exposed (A2), and repaired (A3) OXO-CHI-PUR network (HDI:PEG:OXO-CHI:DBTDL =1.0:1.33:1.17x10 ⁻⁴ :2x10 ⁻⁵) containing OXO-CHI of 1:1 molar ratios, and plot of height vs width profile of undamaged (A1'), damaged and UV exposed (A2'), and repaired (A3') networks, and $d(\Delta l)/dT$ vs temperature (A1''-A3'') for the same.....	108
6.3. IRIRI images of OXO-CHI-PUR networks (HDI:PEG:OXO-CHI:DBTDL =1.0:1.33:1.17x10 ⁻⁴ :2x10 ⁻⁵) containing 1:1 molar OXO-CHI recorded as a UV exposure time 0, 30, and 60 min, respectively. (A1-A3) images were obtained by tuning into the 1545 cm ⁻¹ band; (A1'-A3', A1''-A3'', A1'''-A3''') IR spectra recorded from mechanically damaged and undamaged areas.....	109
5.4. IRIRI images of OXO-CHI-PUR networks (HDI:PEG:OXO-CHI:DBTDL =1.0:1.33:1.17x10 ⁻⁴ :2x10 ⁻⁵) containing 1:4 molar OXO-CHI recorded as a UV exposure time 0, 60, and 90 min, respectively. (A1-A3) images were obtained by tuning into the 1545 cm ⁻¹ band; (A1'-A3', A1''-A3'', A1'''-A3''') IR spectra recorded from mechanically damaged and undamaged areas.....	110
5.5. IRIRI images of OXO-CHI-PUR networks (HDI:PEG:OXO-CHI:DBTDL =1.0:1.33:1.17x10 ⁻⁴ :2x10 ⁻⁵) containing 1:10 molar OXO-CHI recorded as a UV exposure time 0, 90, and 120 min, respectively. (A1-A3) images were obtained by tuning into the 1545 cm ⁻¹ band; (A1'-A3', A1''-A3'', A1'''-A3''') IR spectra recorded from mechanically damaged and undamaged areas.....	111
5.6. IRIR images (A) and ATR-FTIR spectra (B) of OXO-CHI-PUR (HDI:PEG:OXO-CHI=1.0:1.33:1.17x10 ⁻⁴) networks containing a) 2x10 ⁻⁵ , b) 4x10 ⁻⁵ , c) 1x10 ⁻⁴ , d) 1x10 ⁻³ and e) 1x10 ⁻² mole DBTDL.....	112
5.7. Optical images of OXO-CHI-PUR networks (HDI:PEG:OXO-CHI:DBTDL =1.0:1.33:1.17x10 ⁻⁴ :2x10 ⁻⁵) exposed to UV light at pH=3 (A1-A3), 4 (B1-B3), 5 (C1-C3), 6 (D1-D3).....	113

5.8. IRIRI images of OXO-CHI-PUR networks (HDI:PEG:OXO-CHI:DBTDL =1.0:1.33:1.17x10 ⁻⁴ :2x10 ⁻⁵) containing 1:1 molar OXO-CHI at pH=3 recorded as a UV exposure time 0, 30, and 60 min, respectively. (A1-A3) images were obtained by tuning into the 1520 cm ⁻¹ band; (A1'-A3', A1''-A3'') IR spectra recorded from mechanically damaged and undamaged areas.....	114
5.9. IRIRI images of OXO-CHI-PUR networks (HDI:PEG:OXO-CHI:DBTDL =1.0:1.33:1.17x10 ⁻⁴ :2x10 ⁻⁵) containing 1:1 molar OXO-CHI at pH=6 recorded as a UV exposure time 0, 30, and 60 min, respectively. (A1-A3) images were obtained by tuning into the 1520 cm ⁻¹ band; (A1'-A3', A1''-A3'') IR spectra recorded from mechanically damaged and undamaged areas.....	115
5.10. Optical images of OXO-CHI-PUR networks (HDI:PEG:OXO-CHI:DBTDL =1.0:1.33:1.17x10 ⁻⁴ :2x10 ⁻⁵) containing OXO-CHI of 1:1 (A1-A3), 1:4 (B1-B3), and 1:10 (C1-C3) molar ratios, respectively along with 1 % w/w HALS in each network exposed to UV.....	116
5.11. IRIRI images of OXO-CHI-PUR networks (HDI:PEG:OXO-CHI:DBTDL =1.0:1.33:1.17x10 ⁻⁴ :2x10 ⁻⁵) containing 1:1 molar OXO-CHI and 1 % w/w HALS recorded as a UV exposure time 0, 120, and 300 min, respectively. (A1-A3) images were obtained by tuning into the 1542 cm ⁻¹ band; (A1'-A3', A1''-A3'', A1'''-A3''') IR spectra recorded from mechanically damaged and undamaged areas.....	117
5.12. IRIRI images of OXO-CHI-PUR networks (HDI:PEG:OXO-CHI:DBTDL =1.0:1.33:1.17x10 ⁻⁴ :2x10 ⁻⁵) containing 1:4 molar OXO-CHI and 1 % w/w HALS recorded as a UV exposure time 0, 240, and 360 min, respectively. (A1-A3) images were obtained by tuning into the 1542 cm ⁻¹ band; (A1'-A3', A1''-A3'', A1'''-A3''') IR spectra recorded from mechanically damaged and undamaged areas.....	118
5.13. Proposed self-healing mechanism of OXO-CHI-PUR network under UV exposure.....	119

LIST OF TABLES

Table

A.1. Damage width as a function of UV exposure time for different OXE-CHI-PUR compositions.....	133
B.1. Vibrational bands observed in Raman measurements for 1:1, 1:2, 1:4, 1:6, and 1:10 OXE-CHI molar ratios. Arrows $\uparrow\downarrow$ indicate band increase or decrease for a given OXE-CHI ratio.....	154
B.2. Vibrational bands observed in IR measurements 1:1, 1:2, 1:4, 1:6, and 1:10 OXE-CHI molar ratios Arrows $\uparrow\downarrow$ indicate band increase or decrease for a given OXE-CHI ratio.....	154
C.1. Vibrational bands observed in IR measurements 1:1, 1:4, and 1:10 OXO-CHI molar ratios Arrows $\uparrow\downarrow$ indicate band increase or decrease for a given OXO-CHI ratio.....	171
C.2. Vibrational bands observed in Raman measurements 1:1, 1:4, and 1:10 OXO-CHI molar ratios Arrows $\uparrow\downarrow$ indicate band increase or decrease for a given OXO-CHI ratio.....	171

INTRODUCTION

This dissertation is concerned with the design and synthesis of self-repairing polymer networks by utilizing bio-inspired materials. The goal is to advance limited synthetic, spectroscopic, and thermo-mechanical knowledge pertaining to molecular and macroscopic level processes governing distribution of molecular entities within the network and their role in self-repairing processes. While the major portion of these studies will highlight the synthesis, modification and optimization of the substitution of chitosan-based biomaterials followed by their incorporation within polyurethane (PUR) networks, molecular level spectroscopic as well as microscopic approaches to characterize chemical structures of the macromonomers and network formations will be of particular focus.

Chapter I outlines recent advances in self-repairing polymers which are related to autonomous healing processes mastered by the nature. Damages and repairs ranging from Å to mm levels are discussed in terms of chemical reactions and diffusion in time scales. While length scales of damages and repairs is one feature, other anticipated features are that the declining dimensions reduce the time for healing. Larger dimensions require longer transport and laborious diffusion paths. To mimic these complex and not well understood at molecular level processes the development of materials capable of self-repairing by internal or external stimuli, multi-level chemical reactions and transport requirements is a challenge. Furthermore, to understand superimposed chemical-physical interactions of individual processes at various scale lengths that will lead to autonomous repair is another aspect of self-healing. Although recent attempts and advances to create self-repairable polymeric systems reflect some of these steadily growing trends, the

sequence of orchestrated and overlapping signaling, detection and repairing events are yet to be explored.

Chapter II illustrates the synthesis of oxetane-substituted chitosan (OXE-CHI) macromonomer as a function of reactant stoichiometry in order to determine their effects on self-repairing kinetics of polymeric networks. In these studies, the incorporation of OXE will be investigated and detailed analysis is performed in order to determine structure-property relationships. Using NMR, ATR, Raman spectroscopy, these studies showed that OXE is incorporated in C6 position of glycosine units of CHI.

Chapter III discusses polyurethanes which have many properties that qualify them as high performance polymeric materials, but they still suffer from mechanical damage. In this section, the development of polyurethane networks that exhibit self-repairing characteristics upon exposure to ultraviolet light is discussed. The network consists of an oxetane-substituted chitosan precursor incorporated into a two-component polyurethane. Upon mechanical damage of the network, four-member oxetane rings open to create two reactive ends. When exposed to UV light, the chitosan chain scission occurs which form crosslinks with the reactive oxetane ends, thus repairing the network. These materials are capable of repairing themselves in less than an hour and can be used in many coatings applications ranging from transportation to packaging or fashion and biomedical industries.

Chapter IV elucidates the origin of molecular and macroscopic processes of oxetane-substituted chitosan-polyurethane (OXE-CHI-PUR) crosslinked network that occur inside mechanically produced scratch which is self-repaired by UV exposure. Chemical reactions of each component of the network, OXE, CHI, PUR, and dibutyl tin

dilaurate (DBTDL) inside the crack of OXE-CHI-PUR networks are analyzed using localized chemical imaging combined with thermal expansion measurements and atomic force microscopy. These studies show that the presence of acidic environments (pH=6.8) induce cationic OXE ring opening which parallels polyurea-to-polyurethane (PUA-to-PUR) conversions via the free radical process, leading to -C-O-C- bond formation associated with chair-to-boat conformational changes of glycosine units of CHI moieties. Upon mechanical damage of OXE-CHI-PUR network the glass transition temperature (T_g) diminishes inside the crack, but upon UV-initiated repair increases to its original values. The network remodeling during UV-induced repair reactions is initiated at the lowest location of the scratch which exhibits the highest surface energy and the growth continues to the top to form a scar. These studies show for the first time that minute localized chemical changes influence network rearrangements during UV-initiated repair process.

Chapter V illustrates that oxolane-substituted polyurethane (OXO-CHI-PUR) networks exhibit self-repairing behavior upon mechanical damage, followed by exposure to UV light. As a result of mechanical damage, the glass transition temperature (T_g) is lowered in a damaged area resulting from smaller fragments or oligomers. Upon repair, the T_g increases due to frontal growth of the cross-linking reactions from the bottom of the scratch resulting in self-repairing of the network. Spectroscopic studies revealed that mild acidic conditions facilitate self-repairing of OXO-CHI-PUR networks which involve free radically catalyzed polyurea-to-polyurethane conversion, formation of new linear -C-O-C- bond via ring opening of OXO, as well as chair-to-boat conformational changes of glycosine units of the CHI backbone.

CHAPTER I

DAMAGES AND REPAIRS IN BIOLOGICAL AS WELL AS POLYMERIC SYSTEMS

Introduction

Damages occurring in biological systems typically trigger multi-level chemico-physical responses leading to autonomous repairs. Depending upon the size and the degree of damages in a given biological system, repair mechanisms will vary. As an example, Figure 1.1. A, illustrates a collage of damage types and corresponding repair mechanisms in the context of their dimensions and biological environments. Ranging from Angstrom (\AA) level bond cleavage in DNA to millimeter (mm) size bone fractures, each damage and repair mechanisms exhibit their own attributes. For example, endogenous and exogenous sources of DNA damages lead to structural alterations that may result in destructions with potentially dire cellular consequences. These damages, if interfere with the “normal” DNA-template processes of transcription and replication, may cause a permanent mutation of genomes and defect formations.¹ Nucleobases are the most commonly occurring damages accounting for thousands of damage bases per human every day, but fortunately majority of lesions are repaired by bases or nucleotide excision. On the nanometer scale, in the case of skeletal muscle fibers myogenic precursors are activated at the site of an injured fiber, leading to myoblasts proliferation which repair damaged tissues by differentiating into multinucleated myocytes.² Satellite and myelomonocytic cells also contribute to the repair processes in which dysferlin acts as a Ca^{+2} sensor of the muscle membrane damages, triggering vesicle fusion and directing Ca^{+2} ions along the membrane to seal the lesion by sending messages to neutrophils for

repair.^{3,4} At micron and millimeter scales, skin injury wounds penetrate into the dermis layer of skin, upon which the red blood cells transfer as a result of rupture of blood vessels. At the same time, platelets and inflammatory cells or cytokines arrive to the site of the injury and signal the event. These signals obtained by a specific receptor activate fibroblasts and other connective tissue cells to deposit collagen, resulting in the new tissue at the injury site and wound healing.⁵ In contrast, the bone fracture repairs follow a different path, involving reactions of inorganic tissues comprised of a cascade of molecular events. When a fracture occurs, repairs are initiated by immediate inflammatory responses that lead to the recruitment of mesenchymal stem cells, followed by subsequent differentiation into chondocytes that produce bone forming cartilage and osteoblasts. Cartilage matrix formation is initiated by the resorption of mineralized cartilage, a transition from mineralized cartilage to bone occurs, and the primary bone formation is followed by remodeling, in which the initial bony callus is reshaped by secondary bone formation and resorption to restore anatomical structures capable of supporting mechanical loads.^{3,4}

Unlike in mammals, plant damage is primarily due to attacks of predators as well as destructive environmental factors. Figure 1.1.B schematically illustrates the levels of damage in plants. Again, considering the size, the damage may occur from an angstrom scale in DNA⁶ to centimeter levels for bark rupture. Due to similarities in the basic leaf,^{7,8} fruit,^{9,10} root,¹¹ stem, and bark¹² structural features, micron level damage in plants typically involves cell as well as tissue damage. In contrast to mammals, DNA damage in plants is repaired by photoreactivation.⁶ Cell and tissue damage repairs are achieved by intercellular fusion or expansion as well as cell wall thickening with lignification or

suberization. On the micron scale damages, release of extrudate in fruits protects them from further dehydration upon the damages and the repair mechanism is initiated by sclerified parenchyma cells development, followed by periderm formation beneath the wound in presence of suberin and lignin.^{9,10} Similarly, damages in leaves can be signaled by concentration changes of jasmonic and salicylic acids, nitric oxide, or ethylene, depending upon the type of the plant, followed by the deposition of suberin and lignin resulting in periderm formation which repairs the damage site.^{7,8} For larger dimensional damage in millimeter to centimeter range similar mechanisms appear to be responsible for self-healing, although the molecular level processes are far from being understood.

Although damage and autonomous repairs in mammals and plants occur over a broad spectrum of chemical and morphological environments, one common feature of these processes regardless of their size is that they are macroscopically manifested by highly orchestrated events initiated by signaling molecules. In mammals these are typically categorized into (1) pro-inflammatory cytokines, (2) transforming growth factor (TGF- β) superfamily members, and (3) angiogenic factors. Each of these groups of cytokines and morphogens exhibit overlapping processes such as hemostasis, inflammation, proliferation, remodeling, and orchestrated interactions which are essential for successful repairs.⁵ Similarly, structurally different plant macromolecules such as oligopeptides or oligosaccharides released from damaged cell walls, or molecules inducing hormonal changes such as abscisic or jasmonic or ascorbic acids, ethylene, and nitric oxide signal the damage, followed by sequences of chemical events.⁷⁻¹¹

Damage and Repair Mechanisms in Polymers

An ideal self-repairing material will continually sense and respond to damage over its lifetime, and restore or possibly enhance the original structural features without adversely affecting other properties. Figure 1.2 depicts a schematic diagram of a potentially ideal self-repairable network which consists of functional crosslinked macromolecular chains containing sensing and reactive components. Here sensor groups are anticipated to remain dormant until activated by the damage, reactive, repairable groups are silent until triggered by the sensing groups. This one dimensional repair will occur usually in one spatially confined environment, and as we recall, the interplay of many cascading events is necessary for repairs in biological systems. Although simplified, Figure 1.2 also illustrates that damage occurs when two main events happen: a bond cleavage (path A) and a chain slippage (path B). When the bond cleavage (path A) takes place, sensing groups will trigger the formation of reactive bond forming species, which may include formation of free radicals or other reactive groups, such as $-\text{COOH}$, $-\text{NH}_2$, $-\text{OH}$, $-\text{SH}$, $-\text{C}=\text{O}$, and $-\text{C}=\text{C}$. On the chemical bond level, self-healing processes can be considered as chemical, and or physical adhesion without an adhesive, in which covalent, H-bonding, electrostatic and/or ionic interactions, as well as Van der Waals forces may individually or collectively contribute to the repair. Thus in designing polymeric self-repairing reactive networks directional bonding is essential.

When the chain slippage occurs at the interface or surface of the damage site (path B), loose chain ends form which may or may not exhibit reforming efficiency, depending upon the Gibbs free energy (ΔG) of the system. If $\Delta G < 0$, recombination conditions primarily driven by entropic contributions are favored, but self-repair via diffusion may

not be favored if enthalpic components of the ΔG dominates the process. If slippage of polymer chains occurs during the damage, diffusion at nano or higher scales, which relates adhesion to inter-penetrating processes at two interfaces are the major driving forces. To achieve the repair state, temperature and pressure changes, concentration levels or internal stress gradients, along with other stimuli (electromagnetic radiation, chemical potential) may be necessary. To reach an equilibrium state which minimizes the Gibbs free energy, diffusion rates are in the order of 10^{-5} m/min should be anticipated, and may vary from system to system. For liquids they are approximately 10^{-3} m/min.¹³ Thus, when liquid is dispersed in a solid matrix, the kinetics of repair will favor the process. Since diffusion rates in solids are also reflected in the free volume of a polymer network, and the free volume depends upon the glass transition temperature (T_g), below T_g , polymer chains will exhibit limited mobility as well as diminished transport properties. Above T_g , Fickian diffusion is significantly enhanced,^{14,15} which in the context of the self-repairing processes, will enhance mobility and self-diffusion, primarily driven by entanglement coupling and reptation.¹⁶ In non-crosslinked and crosslinked polymers the presence of trapped entanglements affects the elastic modulus during irradiation or chain scission due to diffusion caused by entanglement slippage, which will be significant above the T_g .¹⁷ Similarly, the reptation model in polymeric network solutions attributes topological constraints imposed by the surrounding polymer chains on entanglements to move along tube-like paths that follow their own contour and result in inter-diffusion.¹⁶ Although the T_g of the network and its free volume typically represent bulk properties, it should be realized that damage formation increases the T_g at the surface created by the damage. Since the mobility of loose ends further away from the

surface is higher as compared to their anchoring points, the very top surface entities will have lower T_g . Spectroscopic studies confirmed that T_g varies with the distance from the surface and the thickness of polymer films.^{18,19}

By analogy to biological damage and repair mechanisms, Figure 1.3 depicts damage and repairs occurring in materials from angstrom to nano-, micro-, to millimeter scales, where covalent and H-bonding is primarily attributed at the angstrom level repairs, whereas metal-ligand and ionic interactions require longer nano-scale ranges. Similarly, at a micron scale level controlled diffusion and relaxation processes may occur, whereas larger mm repairs may require insertions of the secondary phases. As damage at different length scales occur, healing mechanisms responding to these structural disruptions occur in a synchronous manner. While several studies conducted on each of the individual repairing processes are depicted in Figure 1.3, the fundamental difference between repairs in synthetic and biological materials is the ability of biological systems to superimpose individual events, thus resulting in orchestrated repairs across larger length scales. While there are many opportunities and challenges to further advance materials chemistry of autonomous repairs, studies conducted during the first decade have resulted in significant progress in this field. The remaining sections of this chapter will outline the damage and repair mechanisms in polymeric materials at the scale lengths that parallel biological systems depicted in Figure 1.1, A and B.

Dimensions of Damages and Repairs

The damages and repairs along with chemical and physical processes associated with them shown in Figure 1.3 exhibit similarities to biological systems, but as pointed

out above the main differences are orchestrated, superimposed events of biological processes that occur at different scales. That is not to say that the damages and repairs at nm or higher scales do not involve angstrom level covalent and H-bonding. On the contrary, at the microscopic level the overlap of various length scales is essential for repairs to occur. The main problem is their measurements; namely what molecular events are associated with a millimeter repair. Thus, there are many opportunities for exploring these uncharted waters with regard to synthetic materials involving covalent or H-bonding, ionic and metal-ligand coordination, diffusion and relaxation or combinations thereof.

Angstrom Level Repairs

Covalent Bonding

As stated above, an ideal self-healing network should contain reactive species that are activated upon damage. The most commonly occurring reactive species in polymer networks are free radicals. Their affinity for reacting with other species is high in solutions, but lower in solid polymer networks. In spite of relatively longer lifetimes of free radicals in polymer networks, in order for two cleaved reactive end chains to react, both ends must diffuse toward each other and react before other competing processes that may intercept these reactions. Since the most common termination process is oxidation of free radicals, one approach to prevent undesirable reactions is to create suitable environments. For example, polycarbonate (PC) synthesis capable of self-repair by the ester exchange method is accomplished using a steam pressure at 120 °C.^{20,21} This is illustrated in Figure 1.4, which shows reactions of the first carbonate group upon cleavage by hydrolysis giving rise to higher concentration levels of the end-capped

phenoxy functionalities. Addition of a base (e.g., NaHCO_3) forces additional ester reactions, thus facilitating substitution reactions between phenoxide and phenyl-carbonyl chain ends, followed by recombination with CO_2 resulting in reformation of the PC to self-heal the network.

The chain-end recombination was also utilized in poly(phenylene-ether)s (PPE) with the repairing agent generated by oxygen. As shown in Figure 1.5, if a PPE backbone is damaged by heat, light, or external mechanical forces, free radicals are produced as a result of chain scission. However, their stabilization by a hydrogen donor and the presence of Cu (II) secures reactions with each end of the scission chains to form a complex, thus preventing further oxidation. When two end chains are recombined eliminating two protons from both ends, Cu (II) is reduced to Cu (I), and then reformed using molecular O_2 as an oxidizing agent to create Cu (II).^{22,23,24} Although very promising, these approaches at this point exhibit limited applicability for self-healing composites because the recovery of the cleaved bonds requires elevated temperatures. Alternatively, higher concentration levels of effective catalysts should be utilized to activate the recombination of degraded oligomers under ambient conditions, which may adversely affect polymer matrix properties. To overcome these issues, the presence of photoactive species such as cinnamate monomer (1,1,1-tris- [cinnamoyloxymethyl]ethane [TCE]) may alleviate high temperature requirements.²⁵ As shown in Figure 1.6, crack formation results in the C-C bond cleavage of cyclobutane rings between TCE monomers resulting in formation of original cinnamoyl groups and the crack-healing occurs due to reversion of cyclobutane crosslinks of TCE via [2+2] photocycloaddition upon UV (> 280 nm) exposure.²⁶⁻²⁹

Furan-maleimide, dicyclopentadiene, and anthracene based polymers exhibit thermal reversibility.³⁰⁻³² The concept of reversible cross-linking via Diels-Alder (DA) reaction was utilized in epoxy, acrylate and polyamide systems, where retro-DA reaction at higher temperature result in disconnection between diene and dienophile resulting crack propagation, whereas lower temperature reconstruct the covalent bonds to repair the crack. As illustrated in Figure 1.7, lower temperature results in adduct (exo or endo) formation between furan (diene) and maleimide (dienophile) entities which break apart at 120 °C.³³⁻³⁶ The main problems with these materials are the use of relatively expensive and robust methylene chloride solvent as well as longer time requirements for healing. Although a solvent free route for the synthesis of the next generations of crosslinked networks was reported, the response time frame is still long which may adversely affects network crosslinking density building.^{34, 35}

One of the most abundantly available natural polysaccharides chitin can be readily modified by acetylation reactions to form chitosan (CHI).³⁷ In our lab CHI was modified with the four member oxetane (OXE), followed by crosslinking with tri-functional hexamethylene di-isocyanate (HDI) in the presence of polyethylene glycol to form heterogeneous crosslinked PUR networks. Upon mechanical damage of the network, self-repairing occurs upon exposure to UV radiation. The reactions promoting to network formation are shown in Figure 1.8, the choice of these components was driven by their ability to serve specific functions. PUR in combination with polyurea (PUA) generated as a result of reaction between isocyanate and amine-functionalized OXE-CHI provides desirable integrity and localized network heterogeneity, whereas OXE-CHI itself facilitates cleavage of a constrained 4-member ring (OXE) to form free radicals

along with UV sensitivity (CHI) for self-repair. PUR network repairs occur only when OXE-CHI moieties are incorporated which upon UV exposure results in the ring opening of OXE along with the PUA-PUR conversion. The main advantage of these systems is that the OXE-CHI macromolecule can be added to existing thermoset polymers, ensuring easy processability and desirable self-healing characteristics.³⁸

Hydrogen Bonding

Although hydrogen bonds between neutral organic molecules are not among the strongest non-covalent interactions, due to their directionality and affinity they play a significant role in supramolecular chemistry.³⁹ As shown in Figure 1.9, the four H-bonds in a functional unit of ureaisopyrimidone (Upy) resulted in enhanced association strengths between those units and polysiloxane, polyethers, and polyesters.⁴⁰⁻⁴²

Supramolecular polymers based on bifunctional ureidopyrimidinone derivatives behave like conventional polymers, but exhibit strong temperature dependence on their mechanical properties. As anticipated, at room temperature supramolecular polymers exhibit polymer-like viscoelastic behavior in the bulk and in solutions, but at elevated temperatures liquid-like properties are observed.^{43,44} An obvious advantage is the ability to controlling rheological behavior as a function of temperature which can be accompanied by combining supramolecular monomers with traditional polymers. When fatty diacids and triacids from renewable resources were utilized in two-step synthetic route, a self-healing network was obtained. As shown in Figure 1.10, the first step involves condensation of acid groups with an excess of diethylene triamine, followed by reactions with urea. This material is capable of self-repair by bringing two cut ends together at room temperature without external heating by forming hydrogen bonds

between the --C=O groups of amide with amine-functionalized ends. These examples show how complexity and chemical tuning may lead to self-healing polymers similar to those in biological systems.⁴⁵

Nanometer Level Repairs

Metal-Ligand Coordination

Similar to H-bonding, metal-ligand supramolecular interactions can be used to design supramolecular polymers.^{46,47} Due to their optical and photophysical properties, metal complexes offer many advantages with their reversibility tuneable via different metal ion and ligand substitutes. As shown in Figure 1.11, A, metal-ligand supramolecules can be disassembled using an excess amount of water-soluble ligands. Under these conditions, temperature changes and hydroxyl ethylenediamine triacetic acid (HEDTA) facilitate the reactions to switch back and forth, thus serving as molecular weight or crosslink density controller. Figure 1.11, B, shows an example of terpyridine-based ligand pincer complexes which were introduced into a polymer matrix by copolymerization with the ethylene oxide and ethylene-co-butylene monomers.⁴⁸ The permanent structural component is the polymer network (PEB and PEO in Figure 1.11,C), whereas the reversible self-healing component is the metal–ligand coordination complex between a pincer complex and a polymer side-chain pyridine ligand.

Ionic Interactions

Ionic interactions including ionomers utilized in polymeric materials, and selected polymers have exhibited self-healing attributes, including poly(ethylene-co-methacrylic acid) and polyethylene-*g*-poly(hexyl methacrylate).⁴⁹ Instead of external heat or an alternative stimulus to promote polymer diffusion in a damaged area, repairs occur under

ambient and elevated temperatures upon projectile puncture testing.^{50,51} A ballistic puncture in LDPE does not show healing, whereas the puncture in EMMA film heals the puncture leaving a scar on the surface. The proposed healing mechanism is a two stage process in which upon projectile impact, ionomeric network is disrupted, and heat generated by the friction during the damage is transferred to the polymer surroundings, generating localized melt state. Elastic responses of the locally molten polymer facilitated by a puncture are known as puncture reversal. During the second stage, the molten polymer surfaces fuse together via interdiffusion resulting from ionic interactions between ionic clusters, which seal the puncture. This is followed by rearrangement of the clustered regions and long-term relaxation processes which continue until ambient temperatures are reached.

Micrometer Level Repairs

Diffusion

Diffusion is primarily responsible for self-healing of non-reactive systems, or in polymer networks where the damage results in a chain slippage (Figure 1.2, path B). In poly(methyl methacrylate) (PMMA) induced crack healing was achieved by heating it above the T_g under light pressure.⁵² A recovery of the fracture stresses was suggested to be proportional to $t^{1/4}$, where t is the heating time. While craze healing occurs at temperatures above and below the T_g , crack healing happens only at or above the T_g .⁵³⁻⁵⁶ In order to reduce the effective T_g of PMMA organic solvents were used as plasticizing agents that facilitated healing.^{57,58}

In another approach, small grain thermoplastic epoxy particle adhesives were embedded within glass-epoxy composite matrixes, which melted upon heating and

therefore repaired damage sites.⁵⁹ However, the voids left after the melting of adhesives adversely affected the integrity of the epoxy polymer matrix. In addition, the higher temperatures required to melt the embedded epoxy particles caused damage to the surfaces of the polymer. The same concept was utilized by blending thermoplastic poly(bisphenol-A-co-epichlorohydrin) with epoxy resin at 80 °C to dissolve it into the thermoset. During damage formation, thermoplastic polymer in the vicinity of the crack may flow to the newly created crack regions, thereby healing the crack.^{59,60}

Interfacial diffusion plays a significant role in heterogeneous networks where self-healing is expected to occur. Typically, diffusion is enhanced in a molten state, which enhances diffusion and possibly repairs networks. When γ -Fe₂O₃ nanoparticles were incorporated into emulsion polymerization of p-methyl methacrylate/ n-butylacrylate/ heptadecafluorodecyl methacrylate (p-MMA/nBA/HDFMA) matrix, and allowed coalesces, such films exhibit self-repairing when oscillating magnetic field is used.⁶¹ The first step in this development was to prepare polymeric films with uniformly dispersed γ -Fe₂O₃ nanoparticles. This was accomplished by the in-situ synthesis of (p-MMA/nBA/HDFMA) colloidal particles in the presence of γ -Fe₂O₃, followed by their coalescence. As shown in Figure 1.12, A-B, polymeric films were cut into two pieces and when the broken pieces were physically placed in contact with each other. Upon application of an oscillating magnetic field (OMF), the γ -Fe₂O₃ nanoparticles increase the nanoparticle-polymer interface temperature, thus generating localized melt flow which permanently repair physically separated polymer (Figure 1.12, C-D). As shown in Figure 1.12, A'-D', the self-repairing process can be repeated many times. This approach

may find many useful applications in composites, where damage is not easily detectable, and repairs are necessary to maintain mechanical integrity of a composite.

Organometallic conductive polymers comprising of N-heterocyclic carbenes (NHCs) used to control corrosion in coatings also exhibits self-healing and conductive properties. As illustrated in Figure 1.13, A, conductive and stimuli responsive attributes were achieved synthetically by utilizing NHCs and transition metals which exhibit conductivity in the order of 10^{-3} Scm^{-1} .⁶² When the damaged material is heated to 200 °C without solvent vapor, or to 150 °C in the presence of DMSO vapor, the damage disappears due to the dynamic equilibrium between metal and the polymer, resulting in flow into microcracks. This is shown in Figure 1.13, B-C.⁶²

Relaxations and Shape Memories

Mechanical deformations of synthetic materials can also be repaired by stress relaxation processes. Shape memory polymers (SMPs) are a group of responsive materials that have the ability to return from a temporary deformed shape to their original permanent form induced by an external stimulus, such as temperature, electrical or magnetic field,⁶³ solvent⁶⁴ or light.⁶⁵ Similar to diffusion controlled self-healing, the T_g plays a significant role. At temperatures above the T_g , polymer chains display increased mobility, enabling the bulk material to flow and therefore behave as viscous liquid with irreversible mechanical responses. At temperatures below the T_g , mobility is restricted, and polymer chains behave like a glassy, elastic solid with reversible mechanical responses. Translating macroscopic responses to micro- and molecular deformations is challenging, and the mobility of polymer chains in the presence of external stimuli depends on the proximity of the T_g and the degree of cross-linking as well as

entanglements present in the network.⁶⁶ These competing processes within polymeric networks result in chain deformation as a response to external stresses and chain contractions as an entropic response result in mass flow.⁶⁷ One example is the light activated shape memory polymers (LASMP) which utilize one wavelength of light(ν_1) for photo-crosslinking while a second wavelength(ν_2) of light cleaves the photo-crosslinked bonds, allowing the material to reversibly switch between an elastomer and a rigid polymer by changing the effective T_g .⁶⁵

Millimeter Level Repairs

Multi-Phase Systems

The concept of self-healing thermosetting polymers as well as fiber-reinforced thermosets was adopted from civil engineering, where cementation composites were healed by releasing of chemicals within the crack which to cure in the presence of air.^{68,69} This concept inspired material scientists to develop polymer matrices containing vessels (fibers or microcapsules) filled with repair chemicals. For example, as shown in Figure 1.14, A, to construct polymer composites epoxy-amine or epoxy-vinyl ester, hollow fibers were embedded which contain repairing chemicals. When damage occurs, and when the crack propagates through the polymer matrix and breaks the fibers, release of repair chemicals, such as low viscosity adhesives, two-component resins, or monomers such as dicyclopentadiene (DCPD) or 5- ethylidene-2-norbornene (ENB) which fill up the void. In the presence catalysts, cessation of the crack occurs via crosslinking reactions or ring opening metathesis polymerization (ROMP). Another method utilized encapsulated micro-particles filled with crosslinking agents. As shown in Figure 1.14, B, when the crack propagates and breaks the particle, crosslinking agents are released to

heal the matrix. Again, the presence of catalysts in the matrix accelerates the process by ROMP reaction shown in Figure 1.14, C. The concept is limited by the mechanical integrity of the matrix, size and diameter dependency of encapsulated vessels, challenges in manufacturing and dispersion, as well as kinetics of deactivation of the catalysts.⁷⁰⁻⁷²

Conclusion

This chapter attempted to outline recent advances in repair of polymeric networks. The main challenge is understanding and subsequently developing orchestrated events capable of autonomous repairs where there is superposition of chemical and physical events. Figure 1.15 depicts the overlapping events going from molecular to macroscopic levels of self-repairs, involving an interplay between the environment (network) and repairing species. The snapshot of an ideal network shown in Figure 1.2 illustrates that the presence of signaling and repairing species built into the network, longer dimensional scale repairs will be possible if signaling and repairs occur as sequential events. There are many unexplored areas that will require and only systematic sophisticated steps to develop self-repairing networks, but also analytical tools capable of measuring these events.

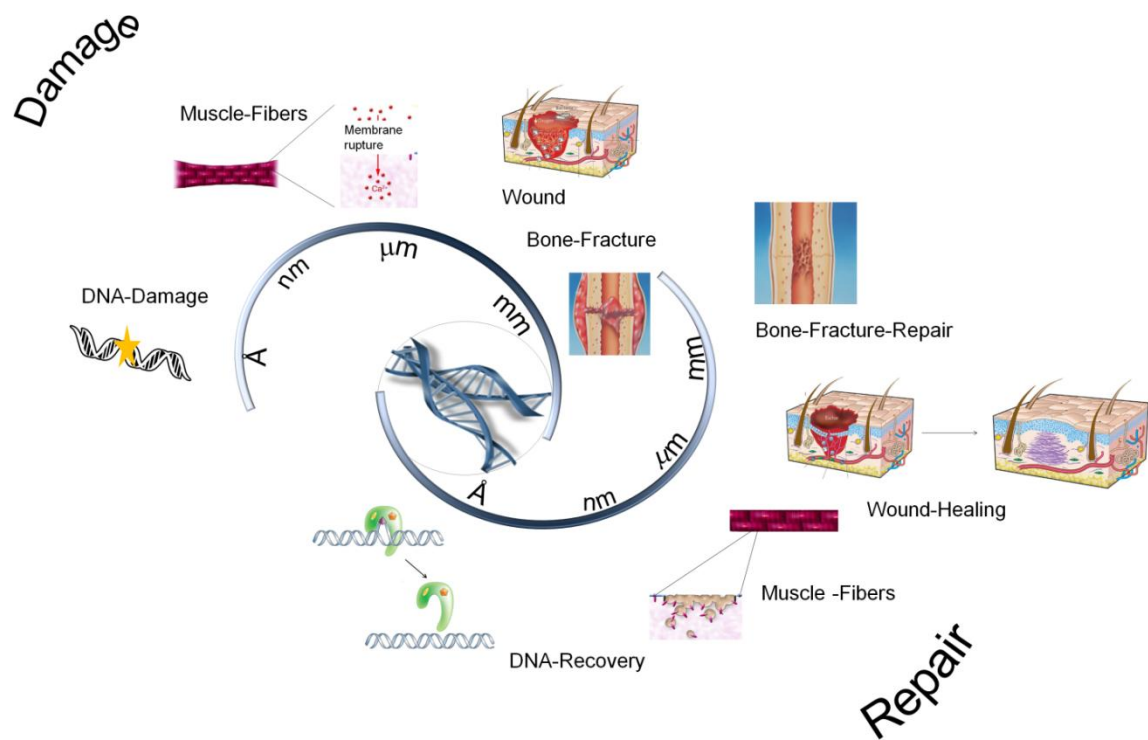


Figure 1.1.A. Selected examples of damage types and repair mechanisms occurring in mammals as a function of time.

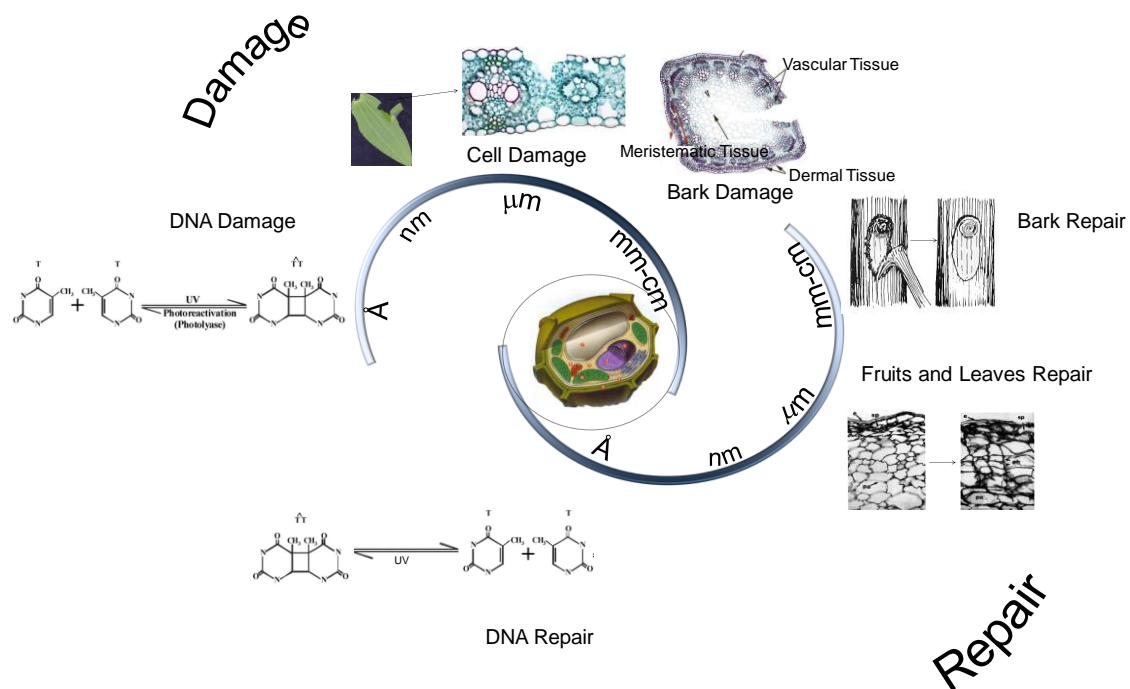


Figure 1.1.B. Selected examples of damage and repair mechanisms occurring in plants as function of time.

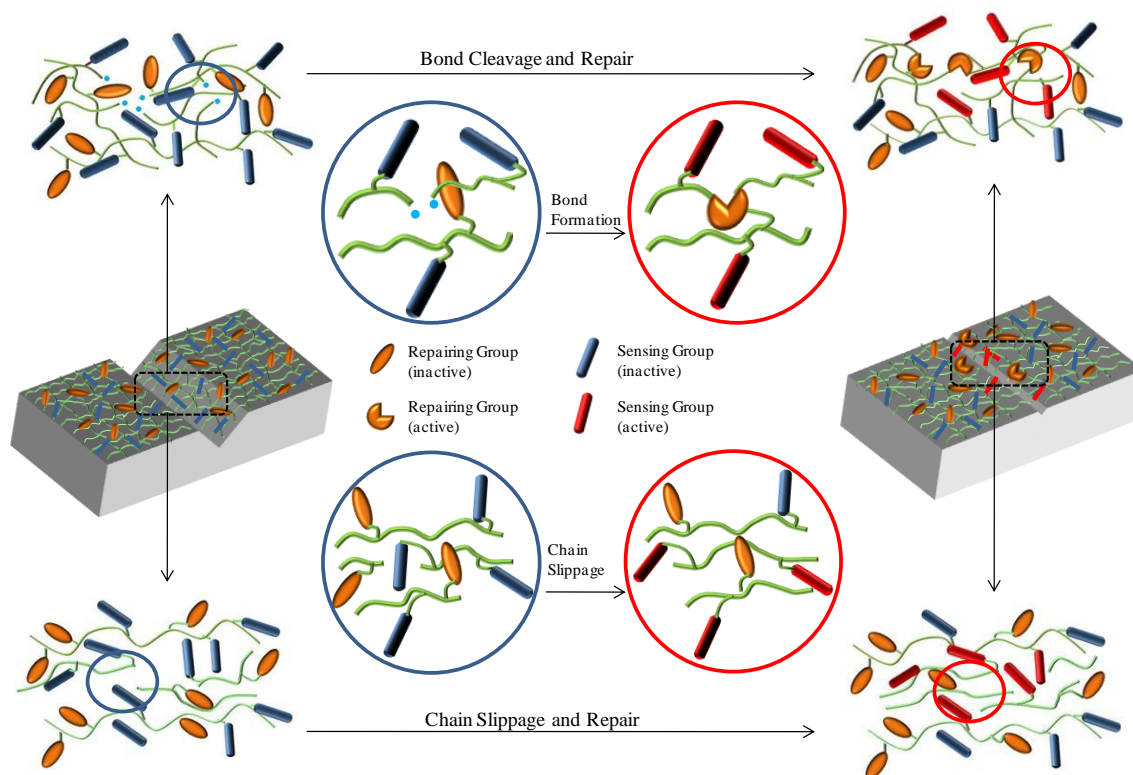


Figure 1.2. Schematic diagram illustrating an ideal self-healing polymeric network.

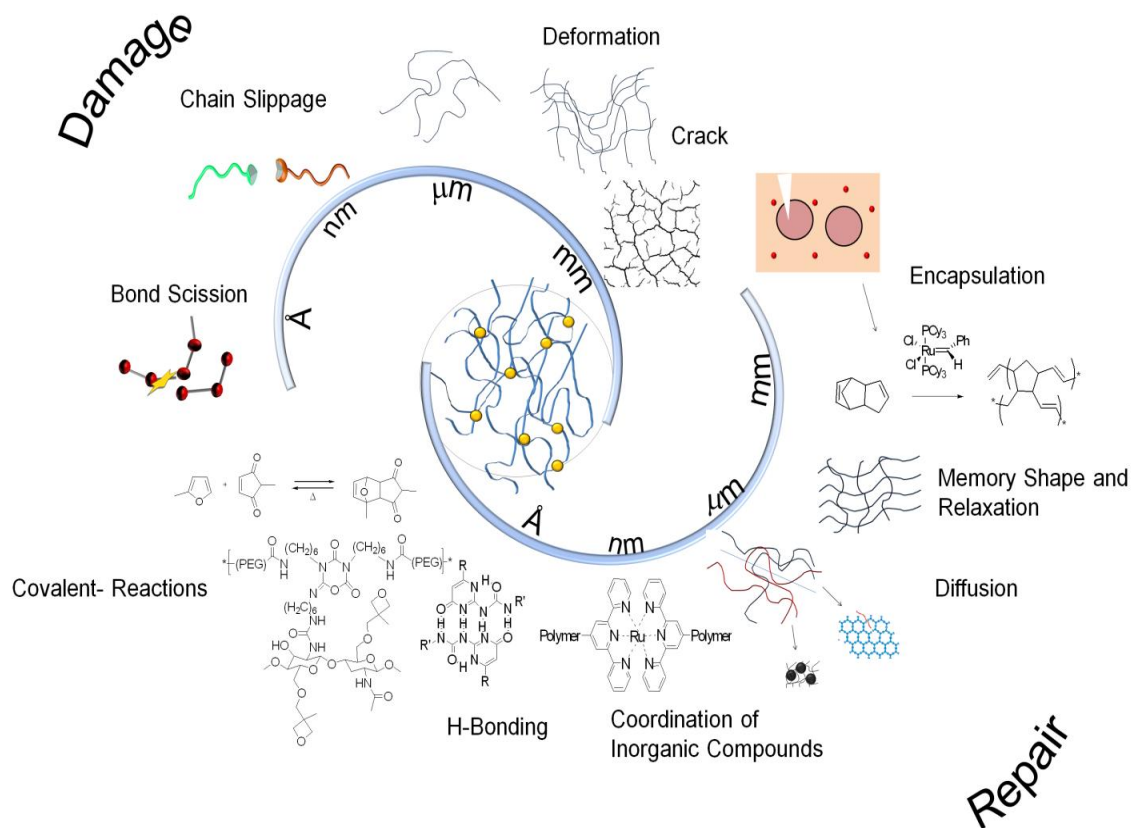


Figure 1.3. Schematic diagram of examples of damages and repairs in synthetic materials.

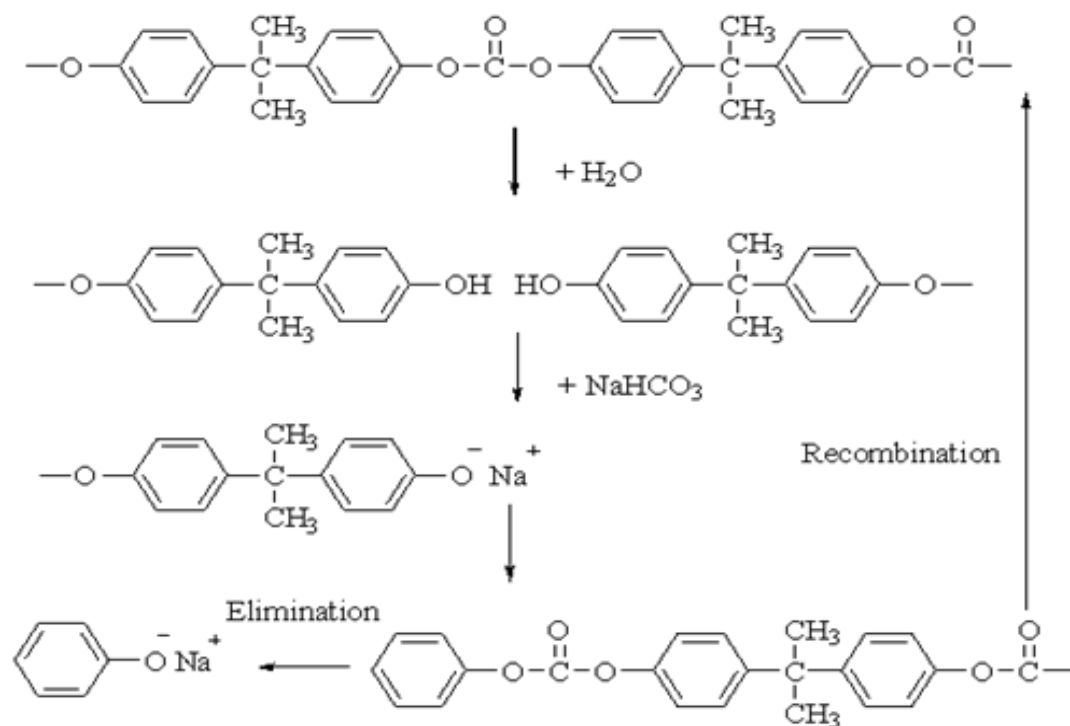


Figure 1.4. Ester exchange reaction in polycarbonate leading to healing.

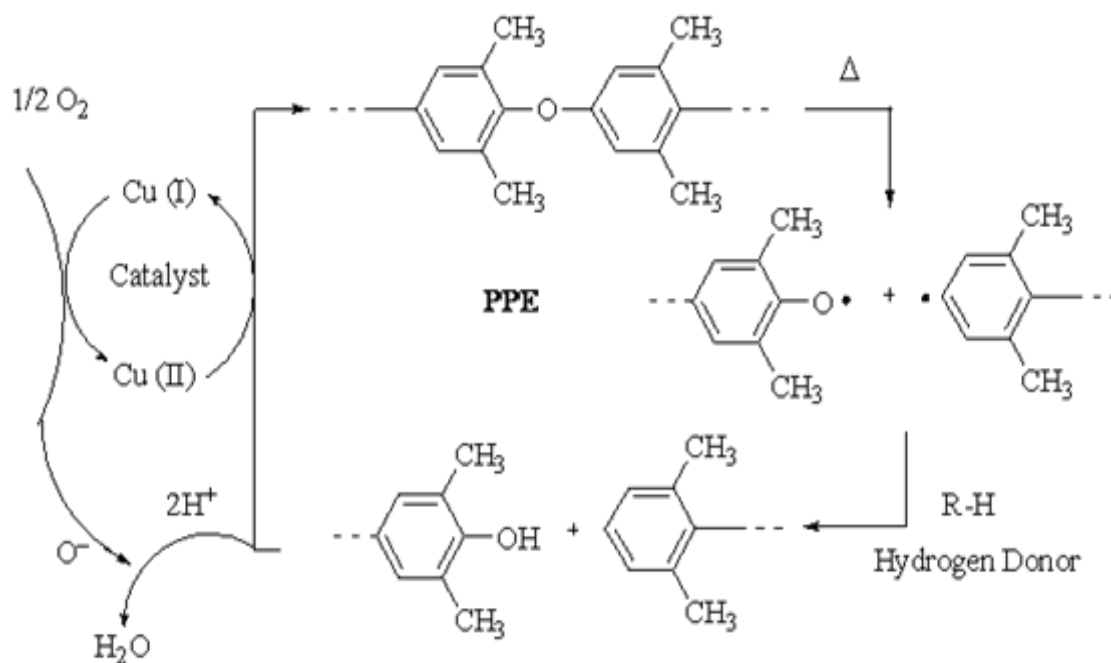


Figure 1.5. Schematic representation of covalent bond formation between scission chain ends in the presence of Cu catalyst leading to healing in polypropylene ethers.

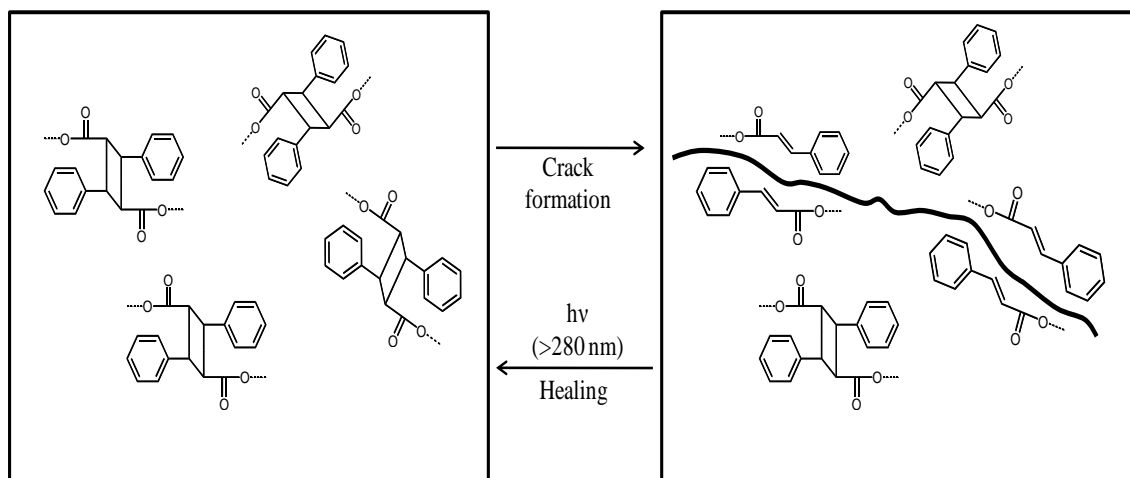


Figure 1.6. [2+2] cycloaddition reactions of cinnamoyl groups leading to healing.

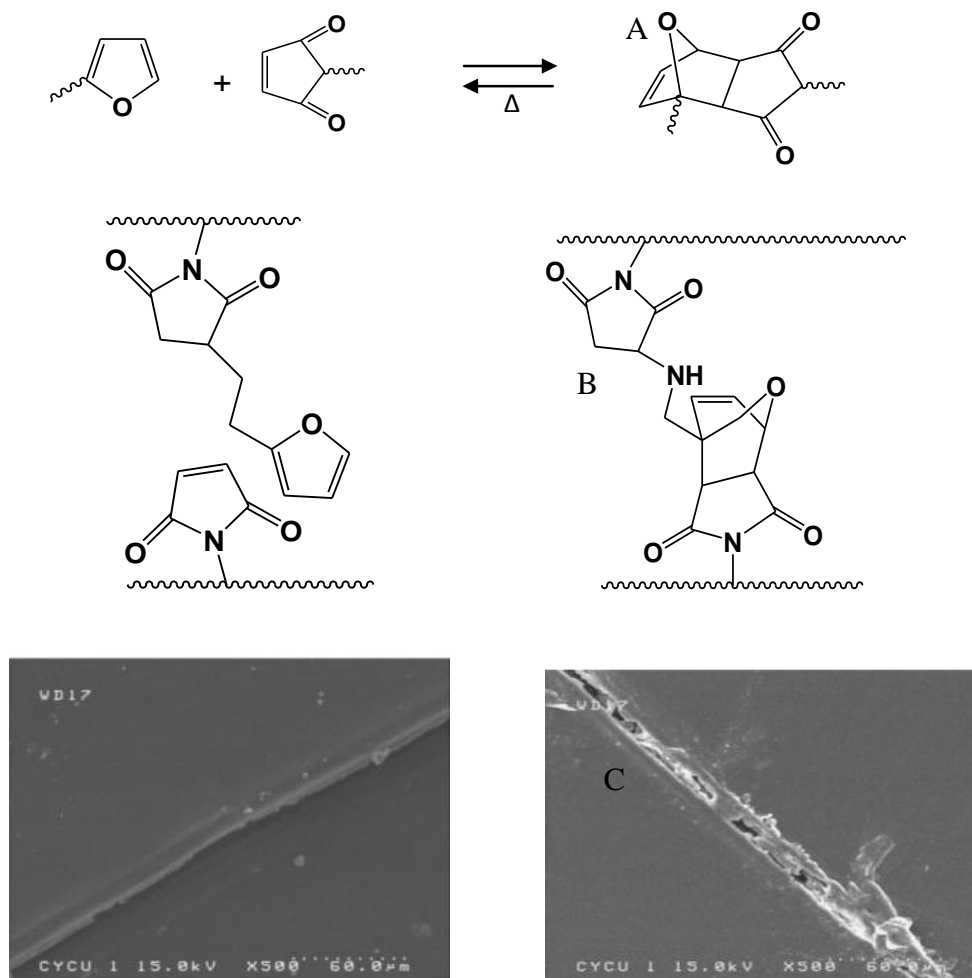
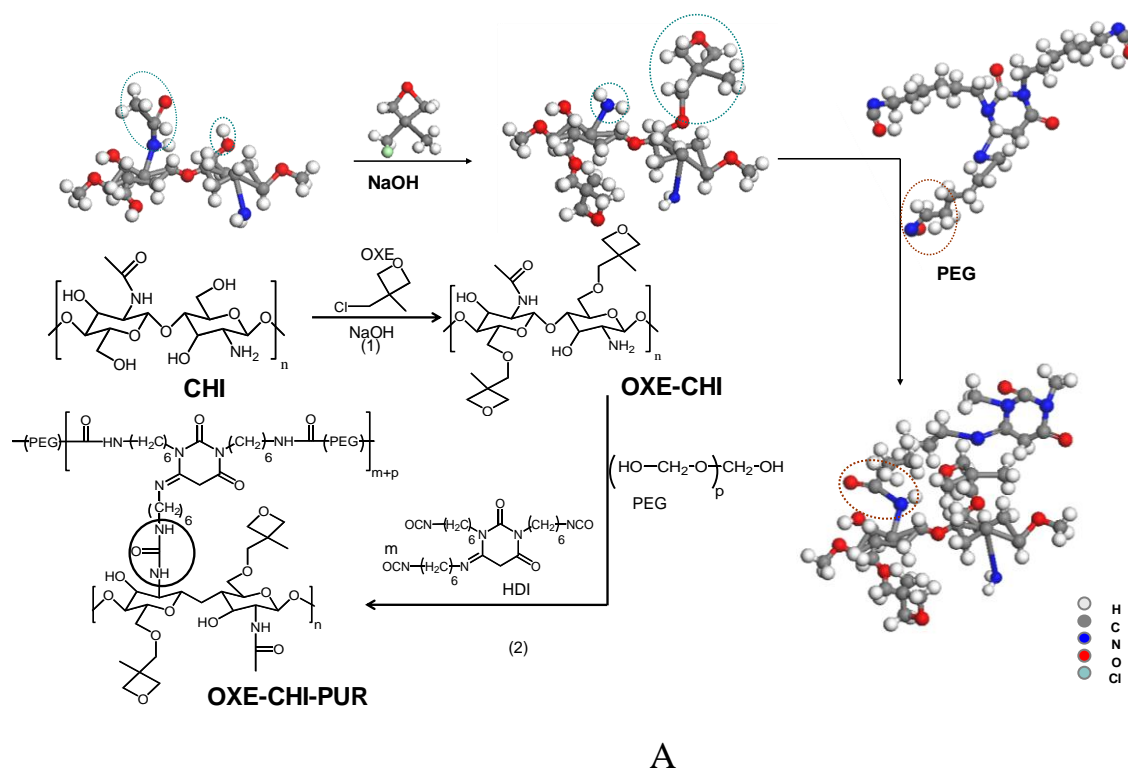


Figure 1.7. Schematic representation of Diels-Alder mechanism (A), specific mechanism of multi-furan and multi-maleimide containing backbone within crosslink polymer system for reversible self-repair (B), and optical images of self-repairing polymer network (C).



UV Exposure time

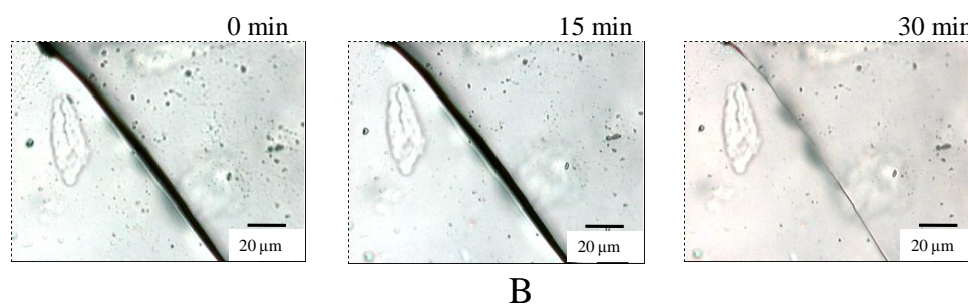


Figure 1.8. Synthetic steps involved in creating self-healing polyurethanes containing oxetane and chitosan (A), and optical images of OXE-CHI-PUR network healed under UV exposure (B).

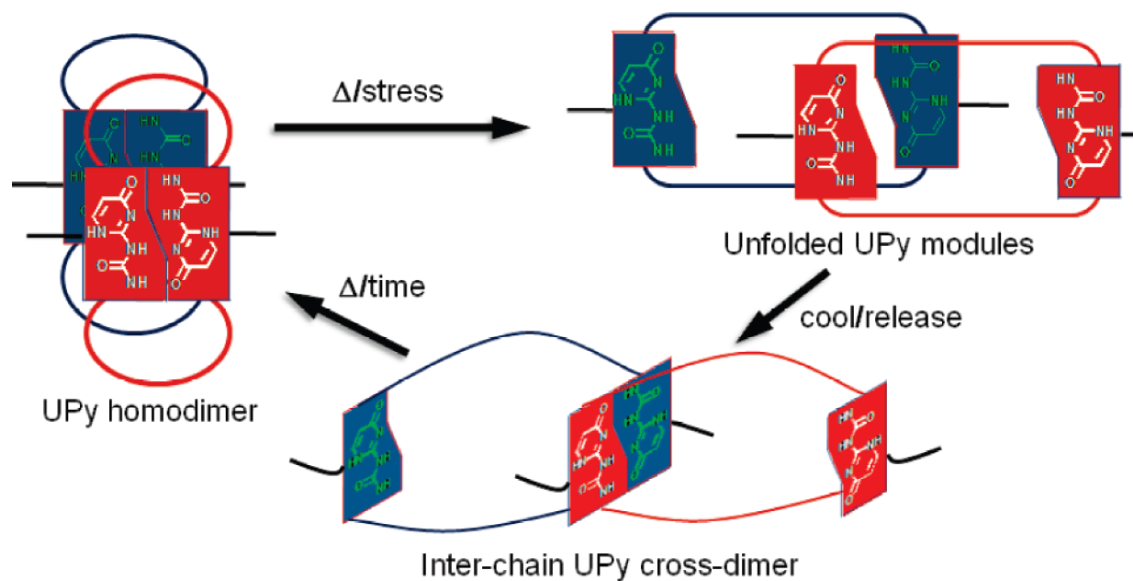


Figure 1.9. Proposed molecular healing mechanism of ureaisopyrimidone (UPy) network via H-bonding.

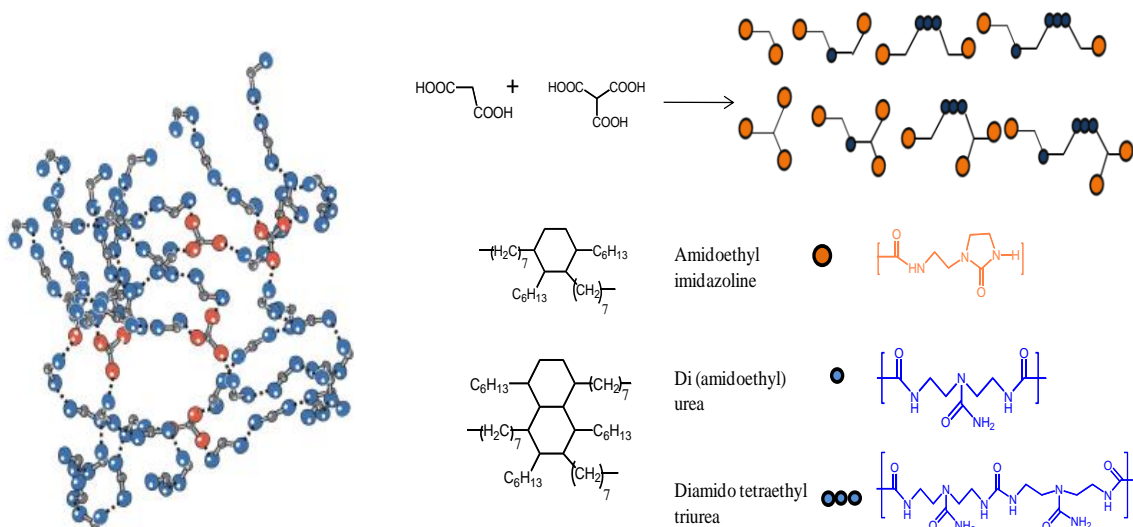


Figure 1.10. Schematic representation of reversible network formed by a mixture of fatty diacid and triacid condensed with diethylene triamine followed by reaction with urea to produce a mixture of oligomers capable of complementary hydrogen bonding.

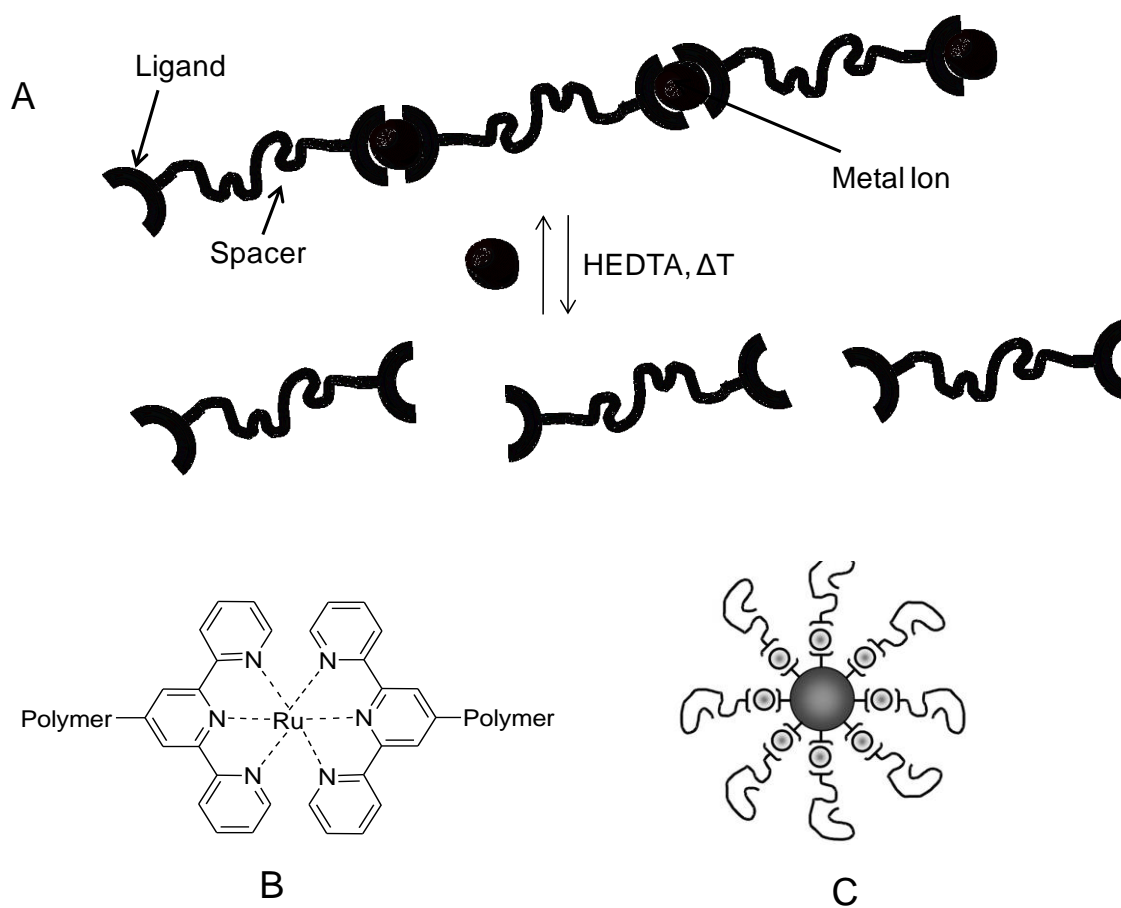


Figure 1.11. Schematic representation of a self-healing supramolecular polymer network (A) containing coordinated Terpyridine-Ru pincer complex (B), and aqueous micelle (C) formation by copolymerization with monomers.

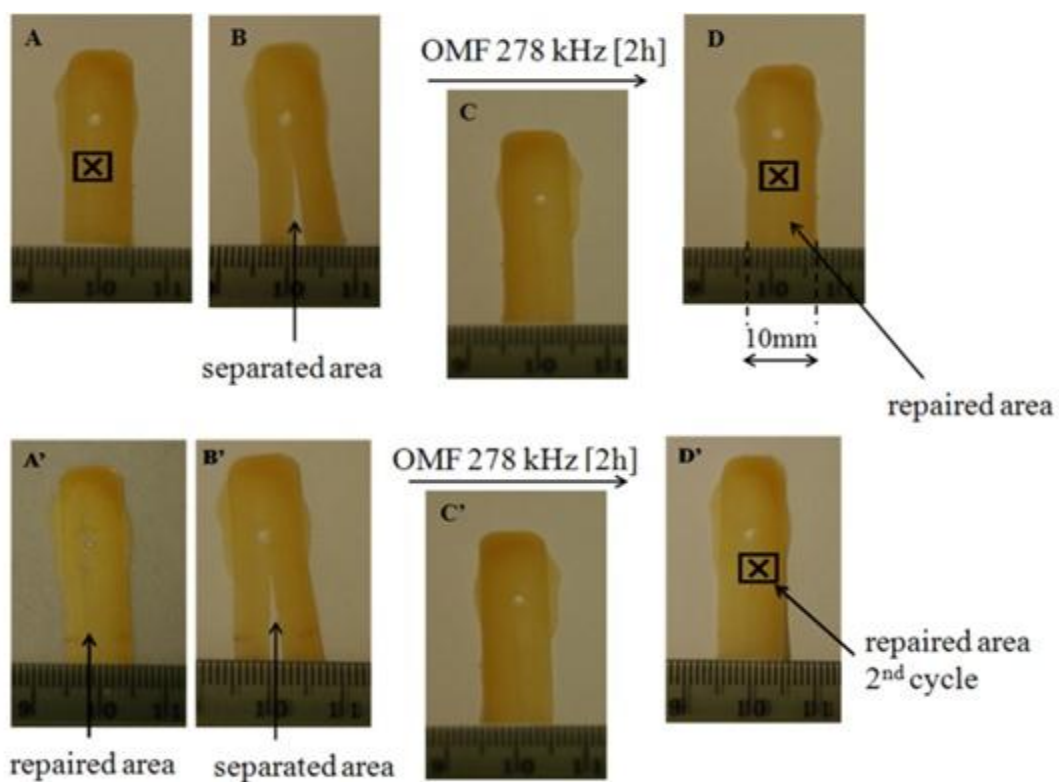
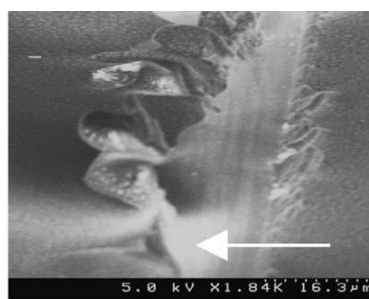
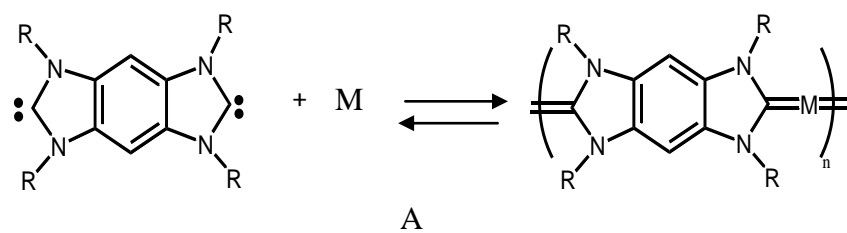
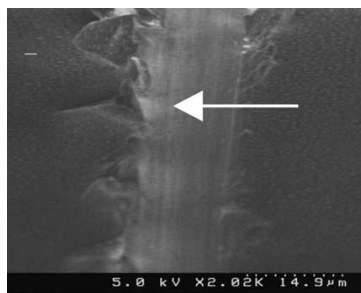


Figure 1.12. Optical images of self-repairing MMA/nBA/HDFMA films containing 14 w/w% of $\gamma\text{-Fe}_2\text{O}_3$ nanoparticles in the presence of oscillating magnetic field.



B



C

Figure 1.13. Schematic representation of dynamic equilibrium between a monomer species and organometallic polymer leading to healing (A) and SEM images of the damaged polymeric film before (B) and after (C) exposure to 200 °C, respectively.

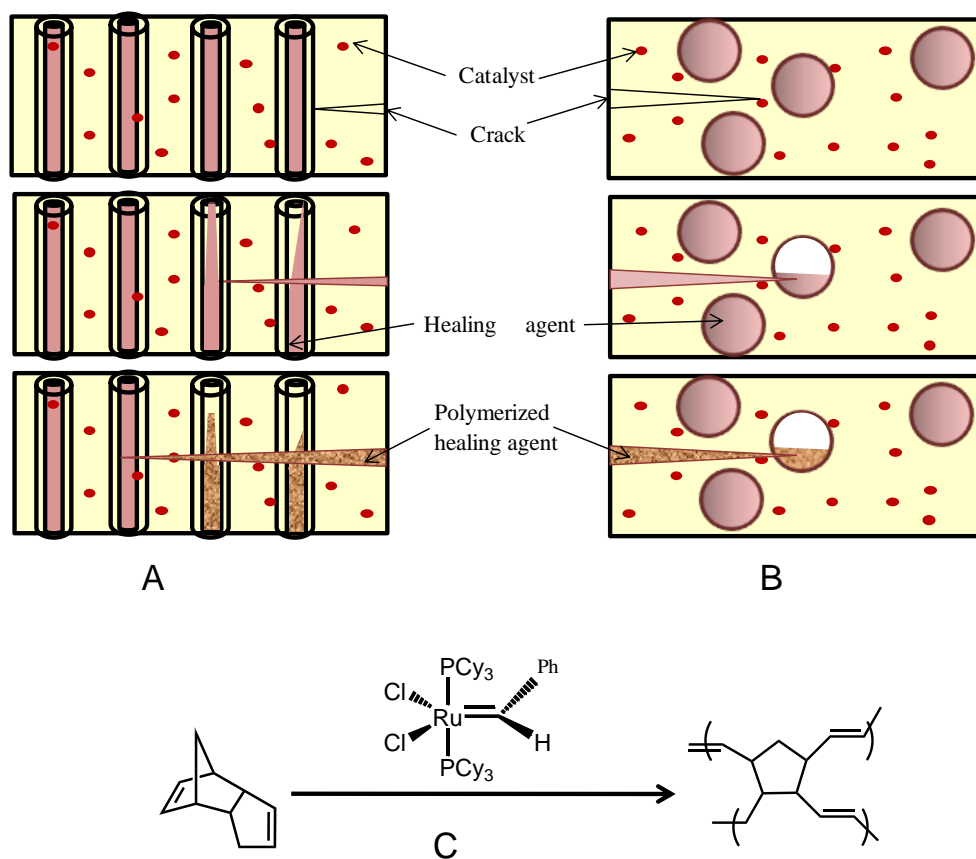


Figure 1.14. Schematic representation of self-repairing in polymer composites containing encapsulated hollow-fibers (A), micro-particles (B), by ring-opening metathesis reaction of DCPD (C).

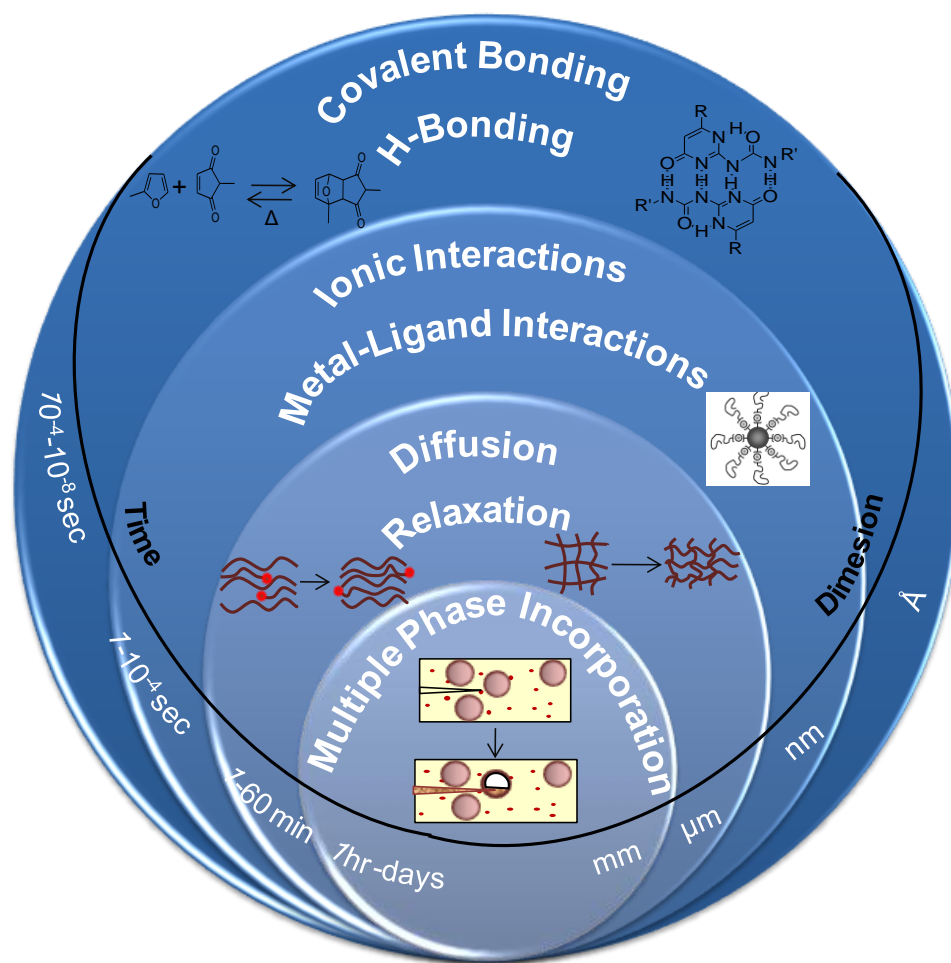


Figure 1.15. Schematic diagram of self-healing in the context of time and dimensions.

References

1. Lindahl, T. *Nature* **1993**, 362, 709.
2. Taylor, D. J. *Mater. Sci.*, **2007**, 42, 8911.
3. Long, M. A.; Stephane, Y.; Crobel, Y.; Rossi, F.M.V. *Semin Cell Dev Bio* **2005**, 16, 632.
4. Han, R.; Campbell, K. P. *Curr. Opin Cell Biol.*, **2007**, 19, 409.
5. Diegelmann, R. F.; Evans, C. M. *Front. Biosci.* **2004**, 9, 283.
6. Sinha, P. R.; Hader, P. D. *Photochem. Photobiol. Sci.*, **2002**, 1, 225.
7. Paris, R.; Lamattina, L.; Casalongue, C. A. *Plant Physio. Biochem.* **2007**, 45, 80.
8. Leon, J.; Rojo, E.; Sanchez-Serrano, J. J. *J. Exp. Bot.* **2001**, 52, 1.
9. Walter, M. W.; Schadel-Randall, B.; Schadel, E. M. *J. Amer. Soc. Hort. Sci.* **1990**, 115, 444.
10. Artschwager, E. *J. Agr. Res.* **1927**, 35, 995.
11. Ibrahim, L.; Spackman, V. M. T.; Cobb, A. H. *Ann. Bot.* **2001**, 88, 313.
12. Biggs, A. R. *Phytopathology*, **1985**, 75, 1191.
13. Cussler E. L. Diffusion, mass transfer in fluids systems, 2nd. Ed. Cambridge University Press, **1997**.
14. Grinsted R. A.; Clark L.; Koemnig J. L. *Macromolecules* **1992**, 25, 1235.
15. Qin W.; Shen Y. ; Fei L. *J. Polym. Sci.* **1993**, 11, 358.
16. De Gennes, P. G. *J. Chem. Phys.* **1971**, 55, 572.
17. Ngai, K. L.; Plazek, D. J. *Macromolecules* **1990**, 23, 4282.
18. Priestley, R. D.; Ellison, C. J.; Broadbelt, L. J.; Torkelson, J. M. *Science* **2005**, 309, 456.
19. O'Connell, P. A.; McKenna, G. B. *Science* **2005**, 307, 1760.
20. Jang, B. N.; Wilkie, C. A. *Thermochim. Acta* **2005**, 426, 73.

21. Takeda, K.; Unno, H.; Zhang, M. *J. Appl. Polym. Sci.* **2004**, 93, 920.
22. Hay A.S., *Adv. Polym. Sci.* **1967**, 4, 496.
23. White D.M.; Klopfer H.J. *J. Polym. Sci.: Part A-* **1970**, 1, 1427.
24. Yang H.; Hay A.S. *J. Polym. Sci.: Part A: Polym. Chem.* **1993**, 31, 261.
25. Chung, C. M.; Roh, Y. S.; Cho, S. Y.; Kim, J. G. *Chem. Mater.* **2004**, 16, 3982.
26. Paczkowski, J. In *Polymeric Materials Encyclopedia*; Salamone, J. C., Ed.; CRC Press: Boca Raton, FL, **1996**, 5142.
27. Ramamurthy, V.; Venkatesan, K. *Chem. Rev.* **1987**, 87, 433.
28. Egerton, P. L.; Hyde, E. M.; Trigg, J.; Payne, A.; Beynon, P.; Mijovic, M. V.; Reiser, A. *J. Am. Chem. Soc.* **1981**, 103, 3859.
29. Hasegawa, M.; Katsumata, T.; Ito, Y.; Saigo, K.; Iitaka, Y. *Macromolecules* **1988**, 21, 3134.
30. Craven J. M. US Pat 3 435 003, 1969.
31. Chen, X.; Wudl, F.; Mal, A. K.; Shen, H.; Nutt, S. R. *Macromolecules*, **2003**, 36, 1802.
32. Liu, Y. L.; Hseih, C. Y. *J. Poly. Sci. Part A* **2006**, 44, 905.
33. Stevens M.; Jenkins A.; *J. Polym. Sci* **1979**, 17, 3675.
34. Liu, Y. L.; Hseih, C. Y.; Chen, Y. W. *Polymer*, **2006**, 47, 2581.
35. Liu, Y. L.; Hseih, C. Y.; Chen, Y. W. *Macromolecular Chem. Phys.* **2007**, 208, 224.
36. Liu, Y. L.; Hseih, C. Y. *J. Polym. Sci. part A* **2005**, 44, 905.
37. Burrows, F.; Louime, C.; Abazinge, M.; Onokpise, O. *Am-euras. J. Agric & Environ. Sci.*, **2007**, 2, 103.
38. Ghosh, B.; Urban, M. W. *Science*, **2009**, 323, 1458.

39. Fredericks, J. R.; Hamilton, A. D. *Comprehensive Supramolecular Chemistry*, Chapter 16, Lehn, J.-M. Pergamon, New York, 1996.
40. Beijer, F. H.; Kooijman, H.; Spek, A. L.; Sijbesma, R. P.; Mejer, E. W. *Angew. Chem. Int. Ed. Engl.* **1998**, 37, 75.
41. Sijbesma, R. P.; Beijer, F. H.; Brunsveld, L.; Fomer, B. J. B. ; Hirschberg, J. H. K. ; Lange R. F. M.; Lowe J. K. L.; Mejer E. W. *Science* **1997**, 278, 1601.
42. Soentjes, S. H. M.; Sijgesma, R. P.; van Genderson, M. H. P.; Mejer , E. W. *J. Am. Chem. Soc.* **2000**, 122, 7487.
43. Bosman, A. W.; Sijbesma, R. P.; Meijer, E. W. *Mater. Today* **2004**, 7, 34.
44. Feldmann, K. E.; Mathew, J. k.; De Greef, T.K. A.; Mijer,E. W.; Kramer, E. J.; Hawker, C. J. *Macromolecules*, **2008**, 41, 4694.
45. Cordier, P.; Tournilhac, F.; Soulié-Ziakovic, C. ; Leibler, L. *Nature* **2008**, 451, 977.
46. Schubert, U. S.; Eschbaumer ,C.; Hien, O.; Andres, P. R.; Schubert U. S. *Tetrahedron Lett.* **2001**, 42, 4705.
47. Kersey F. R.; Loveless D. M.; Craig S. L. *J R Soc Interface.* **2007**, 4, 373.
48. Gohy, J-F.; Lohmeijer, B. G.G.; Schubert, U. S. *Macromol. Rapid Commun.* **2002**, 23, 555.
49. Valery R. Ionomers as Self Healing Polymers in Self-Healing Materials: An Alternative Approach to 20 Centuries of Materials Science, van der Zwaag, S. Ed.; Springer: New York, **2007**, 95.
50. Kalista, S.; Ward, T. *J. R.Soc Interface* **2007**, 4, 405.
51. Kalista, S. J.; Ward, T.C.; Oyetunji, Z. *Mech. Adv. Mater. Struct.* **2007**, 14, 391.
52. de Gennes, P.-G. *Hebd. Seances Acad. Sci., Ser. B* **1980**, 291, 219.
53. Prager, S.; Tirrell, M. *J. Chem. Phys.* **1981**, 75, 5194.
54. Wool, R.P.; O'Connor, K. M.; *J Appl Phys* **1981**, 52, 5953.
55. Jud, K.; Kausch, H.; Williams, J. G. *J. Mater. Sci.* **1981**, 16, 204.
56. Kim, Y.H.; Wool, R.P. *Macromolecules* **1983**, 16, 1115.

57. Wang, P.P.; Lee, S.; Harmon, J.P. *J Polym Sci, Part B: Polym Phys* **1994**, 32, 1217.
58. Lin, C.B.; Lee, S.; Liu K.S. *Polym Eng. Sci* **1990**, 30,1399.
59. Zako, M.; Takano, N. *J. Intel. Mat. Sys. Str.* **1999**, 10, 836.
60. Bleay, S. M.; Loader, C. B.; Hawyes, V. J.; Humberstone, L.; Curtis, P. A. *Composites A*, **2001**, 32, 1767.
61. Corten, C. C.; Urban M. W. *Adv. Mater.* **2009**, 21, 5011.
62. Williams, A.; Boydston, J. ; Bielawski, W. *J. R. Soc. Interface*, **2007**, 4, 359.
63. Mohr, R.; Kratz,.K.; Weigel, T.; Luca-Gabor, M.; Moneke, M.; Lendlein, A. *Proc. Natl. Acad. Sci. U.S.A.*, **2006**, 103, 3540.
64. Leng, J.; Haibao, L. V.; Liu, Y.; Du, S. *Appl. Phys. Lett.* **2008**, 92, 206105.
65. Lendlein, A. *Nature* 2009, **434**, 872.
66. Porter, R. S.; Johnson, J. F. *Chem. Rev.* **1966**, 66, 1.
67. Outwater, J. O.; Gerry, D. J. *J. Adhesion*, **1969**, 1, 290.
68. Dry, C. *Composite Structures* **1996**, 35, 263.
69. Li, C. V.; Lim, Y. M.; Chan, Y. –W. *Composites Part B*, **1998**, 29B, 819.
70. Trask, R. S.; Williams, G. J.; Bond, I. P. *J. R. Soc. Interface*, **2007**, 4, 363.
71. Motuku, M.; Vaidya, U. K.; Janowski, G. M. *Smart Mater. Struct.* **1999**, 8, 623.
72. Kessler, M. R.; White, S. R. *Composites: Part A*, **2001**, 32, 683.

CHAPTER II

SYNTHESIS OF OXETANE-SUBSTITUTED CHITOSAN MACROMONOMERS

Introduction

Chitin is one of the most abundant natural polymers, and is second only to cellulose in annual production.¹ Chitosan, the N-deacetylated derivative of chitin is a copolymer consisting of 2-acetamido-2-deoxy- β -D-glucopyranose and 2-amido-2-deoxy- β -D-glucopyranose. The main reason for its wide use is due to its appealing intrinsic properties such as biodegradability, biocompatibility, film-forming ability, bioadhesivity, poly-functionality, hydrophilicity and adsorption properties.¹⁻³

Three crystalline forms are known for chitin: α -, β - and γ -chitins. The most abundant and easily accessible form is α -chitin.^{4,5} Chitosan is also crystalline and shows polymorphism depending on its physical state, although depending on the basis of its origin of and its treatment during extraction from raw resources, the residual crystallinity may vary considerably. Maximum crystallinity for chitin and chitosan is achieved when chitin is 0% deacetylated and chitosan is fully deacetylated (100%). Generally, commercial chitosans are semi-crystalline polymers whose the degree of crystallinity is a function of the degree of deacetylation.

Chitosan has three types of reactive functional groups, an amino group ($-\text{NH}_2$) as well as both secondary and primary hydroxyl groups ($-\text{OH}$) at the C-2, C-3 and C-6 positions, respectively. Its advantage over other polysaccharides is that its chemical structure allows straight forward modifications, especially, at the C-2 and C-6 positions.⁶⁻⁹ These functional groups can be used for direct substitution reactions and chemical modifications, yielding numerous useful materials for different types of applications. In

order to maintain amino functionalities while incorporating hydroxyl groups at C-6 positions with OXE groups and maintain their ring structure need special synthetic route. In these studies, we reported the synthetic route utilized to create oxetane-substituted chitosan (OXE-CHI) and characterize the attachment of OXE in the backbone of CHI by various spectroscopic techniques.

Experimental

Chitosan (CHI) (degree of deacetylation 75-85%), isopropyl alcohol, methanol, sodium hydroxide beads, acetone, were purchased from Sigma Aldrich Co., 3-(Chloromethyl)-3-methyloxetane from TCI America. Low molecular weight CHI ($M_n \sim 5 \times 10^5$ g/mol) (2 g) was added into a 150 g 1(N) NaOH solution in a three-neck flask and stirred for 24 hrs at -5°C , followed by refrigeration at -18°C for 48 hrs. The solution was thawed and mixed with pre-cooled isopropyl alcohol and stirred for 1hr. To the mixture 0.06 mole of pre-cooled 3-chloro-3-methyl oxetane was added, the temperature increased to 80°C , and the solution stirred for 12 hr. The product was filtered and washed several times with methanol until the wash was neutral pH, followed by drying at 60°C for 12 h. The resulting product was identified as oxetane-substituted chitosan (OXE-CHI) using NMR, Raman and IR spectroscopy

Solid-state ^{13}C NMR measurements were performed on a Varian ^{UNIT}YINOV A 400 spectrometer using a standard Chemagnetics 7.5 mm PENCIL-style probe. Samples were loaded into zirconia rotor sleeves, sealed with Teflon caps, and spun at a rate of 4.5 kHz. The standard cross-polarization magic angle spinning (CP/MAS) technique was used with a high-power proton decoupling implemented during data acquisition. The

acquisition parameters were as follows: the ^1H 90° pulse width was 4.0 μs , the cross-polarization contact time was 1 ms and the dead time delay between scans was 3 sec.

FT-Raman spectra were acquired using an IFS 55/FRA 106 FT-IR/Raman spectrometer (Bruker Instruments, Inc.). A diode pumped Nd:YAG laser as the excitation source, was used to provide a maximum power of 500 mW at the sampling area. WIRE 2.0 (Bruker Instruments, Inc.), and GRAM were used to analyze spectra.

Microscopic micro attenuated total reflectance Fourier transform infrared (μATR FT-IR) were obtained using a Bio-Rad FTS-6000 FTIR single-beam spectrometer at 4 cm^{-1} resolution. A 2 mm Ge crystal, with a 45° face angle maintains at all times with a constant contact pressure between crystal and the film specimens were used. All spectra were corrected for spectral distortions and optical effects using the Urban-Huang algorithm.¹⁰ Chitosan powders were analyzed by diffuse reflectance Fourier transfer infrared (DRIFT) spectroscopy. In a typical experiment 100 scans were collected and ratioed to 100 reference scans collected using an empty attenuated total reflectance (ATR) cell. As similar procedure was used for DRIFT spectroscopy except the number of spectra was 500.

Results and Discussion

The first step in this investigation was the synthesis of OXE-CHI. The reaction of 1° -OH groups of CHI was reacted with chloromethyl oxetane (OXE-Cl) is shown in Figure 2.1.¹¹ The attachment of an OXE ring to the C_6 position of the CHI molecule was confirmed by IR, Raman and ^{13}C -NMR spectroscopy (Figures 2.2, 2.3, and 2.4, respectively). Figure 2.2, Traces A and B, illustrate ATR-FT-IR spectra of CHI and

OXE-CHI, respectively. The bands at 1665 cm^{-1} (-C=O of -NH-CO-CH_3) decrease accompanied by increase band intensities at 1580 cm^{-1} (-NH_2 , amide I) due to the conversion of acetamide into amide groups (Step 1). Comparison of the band intensities between CHI (Trace A) and OXE-CHI (Trace B) shows the broadening of the 1070 cm^{-1} band as a result of the overlap of symmetric -C-O-C- stretching vibrations of OXE ring at 1040 cm^{-1} with the -C-O-C- stretching modes of CHI. The symmetric -C-O-C- stretching band at 985 cm^{-1} also increases with respect to the 1070 cm^{-1} band.¹¹⁻¹³

Further, confirmation of OXE ring incorporation into the CHI backbone is illustrated in the Raman spectra shown in Figure 2.3. Trace A shows the reference spectrum of CHI. Trace B shows an increase of the symmetric $\text{-CH}_2\text{-}$ stretching band of $\text{-OCH}_2\text{-}$ of chitosan at 2885 cm^{-1} due to symmetric and asymmetric stretching of -CH_3 group of OXE. The presence of the quaternary (-CC_4) carbon in the OXE ring and breathing of the ring (forbidden in IR) contributes to the enhanced intensity of the band shown in Trace B. The appearance of new bands at 1420 and 1255 cm^{-1} also shows $\text{-CH}_2\text{-}$ scissoring and -CH_2 breathing modes of OXE ring, respectively.

Solid-state ^{13}C NMR spectra are shown in Figure 2.4, Trace A shows the ^{13}C NMR spectrum of CHI and the characteristics resonances due to carbonyl carbon (a) of acetamide group in pyranose ring and carbon (b) attributed to the methyl of acetamide group at 175 and 22.5 ppm are detected, respectively. These resonances are not detected in Trace B due to the conversion of acetamide into primary amine groups and give rise to a new resonances at 23.7 and 40.5 ppm which correspond to carbon atom (d) of the dangling -CH_3 group and -CC_4 (e) of OXE ring. In Trace A, the resonance at 33.5 ppm

corresponds to carbon (c) of the pyranose ring which shifts to 49.8 ppm (Trace B) due to OXE substitution.¹³⁻¹⁵

Conclusion

In conclusion, OXE-CHI macromonomers were effectively synthesized via a simple non-acidic route in order to maintain the un-opened OXE ring structure as well as -NH_2 functionalities within the macromonomers. The main advantage of this system is that all procedures were performed in aqueous medium which reduces the solvent cost as well as impurities and the end product is not hydrophilic, ensuring pure OXE-CHI product. The chemical structure of OXE-CHI macromonomers were characterized by solid state ^{13}C NMR, ATR FT-IR and Raman spectroscopy.

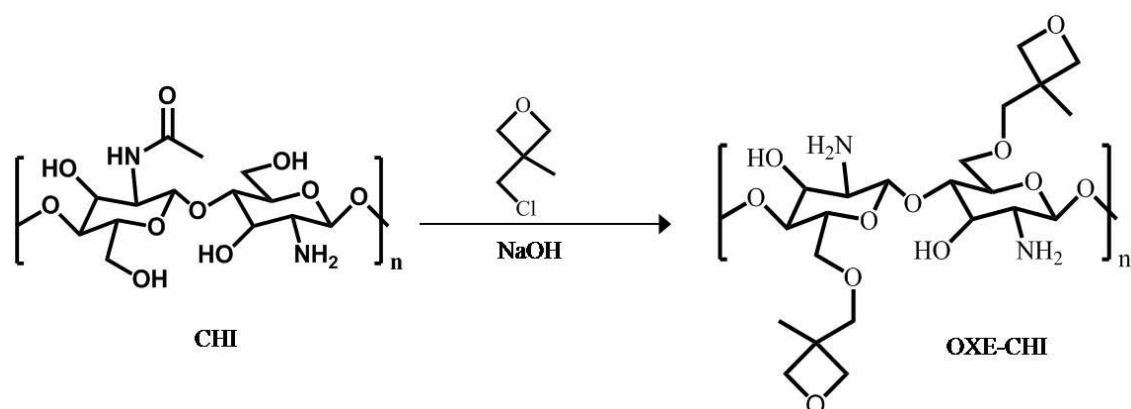


Figure 2.1. Synthetic route of OXE-CHI macromonomer synthesis.

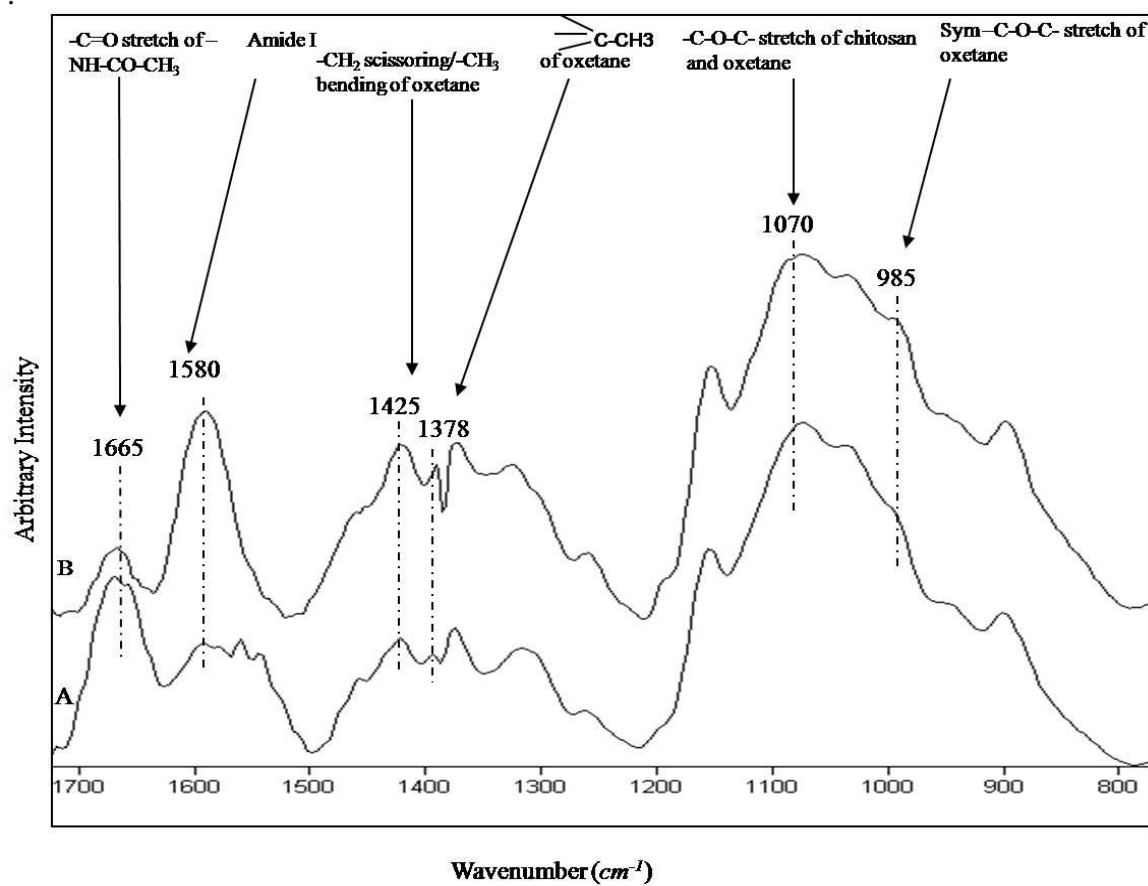


Figure 2.2. ATR-FT-IR spectra of (A) CHI and (B) OXE-CHI products.

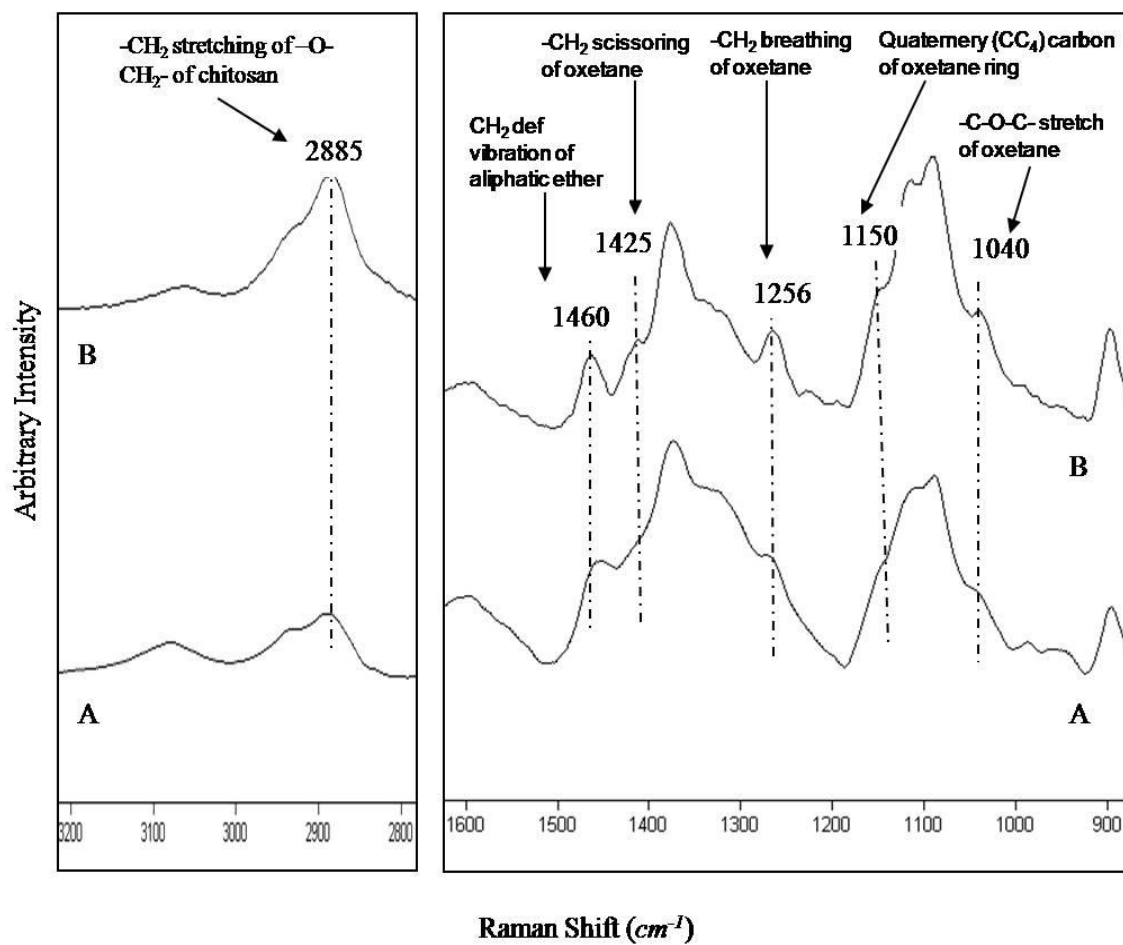


Figure 2.3. Raman spectra of (A) CHI and (B) OXE-CHI products.

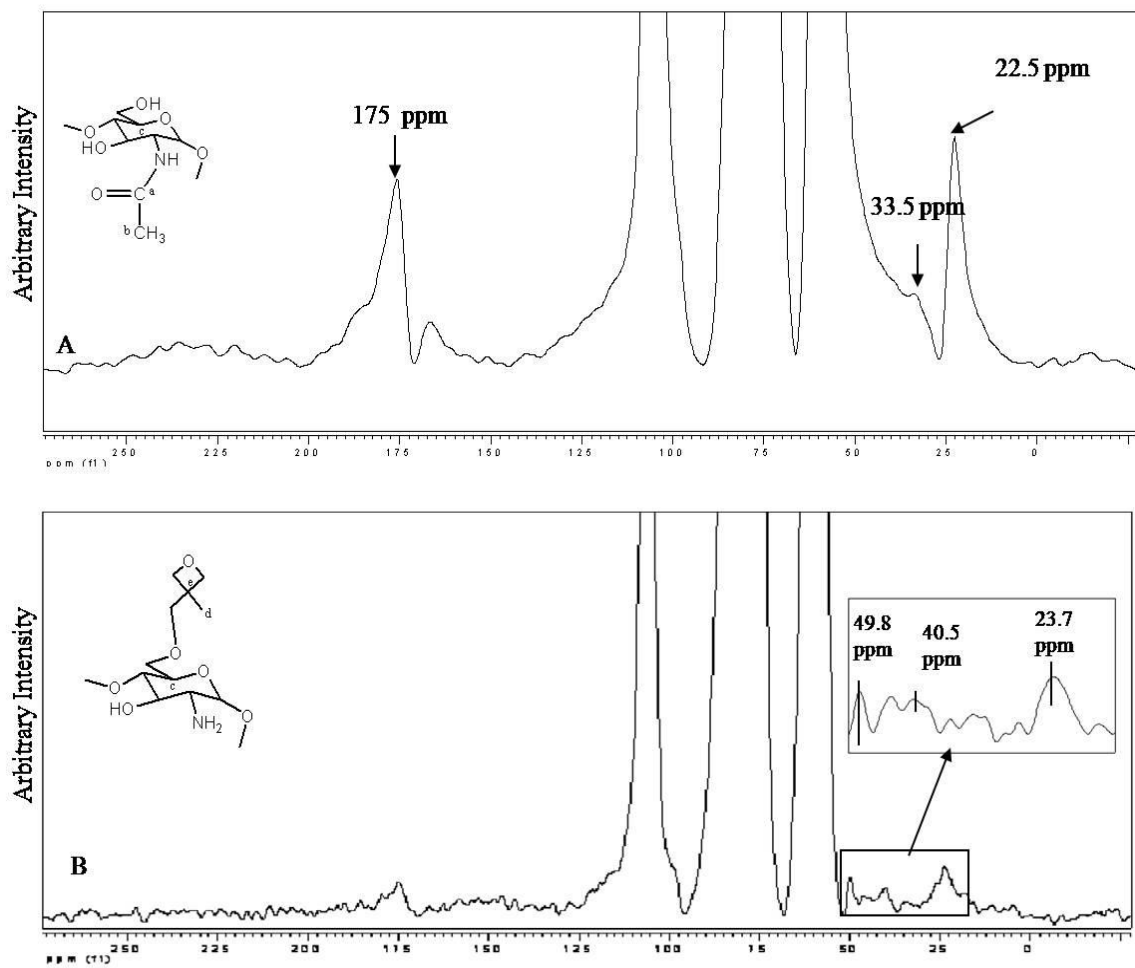


Figure 2.4. Solid state ^{13}C -NMR spectra of (A) CHI and (B) OXE-CHI products.

References

1. Senel, S.; McClure, S. *J. Adv. Drug. Deliver. Rev.* **2004**, 56, 1467.
2. Thacharodi, D.; Panduranga, R. K. *J. Chem. Tech. Biotechnol.* **1993**, 58, 177.
3. Hirano, S.; Hirochi, K.; Hayashi, K.; Mikami, T.; Tachibana, H. *Cosmetic Pharm. Appl. Polym.* **1991**, 95.
4. Braun, J.; Le, C. P.; Le G. F. *Biotechnol. Bioeng.* **1989**, 33, 242.
5. Onsoyen, E.; Skaugrud, O. *J. Chem. Tech. Biotechnol.* **1990**, 49, 395.
6. Marguerite, R.; Pham, L. D.; Claude, G. *Int. J. Biol. Macromol.* **1992**, 14, 122.
7. Muzzarelli, R. A. A.; Tanfani, F.; Emanuelli, M.; Mariotti, S. *Carbohydr. Res.* **1982**, 107, 199.
8. Zhishen, J.; Dongfen, S.; Weiliang, X. *Carbohydr. Res.* **2001**, 333, 1.
9. Sony, Y.; Onishi, H.; Nagai, T. *Chem. Pharm. Bull.* **1992**, 40, 2822.
10. Urban, M. W. *Attenuated Total Reflectance Spectroscopy of Polymers; Theory and Applications*, American Chemical Society and Oxford University Press, Washington, DC, 1996.
11. Y. Wan, K. A. M. Creber, B. Peppley, V. T. Bui, *J. Polym. Sci., Part B: Polym. Phys.* **2004**, 42, 1379.
12. Vuen, D. L.; Colthup, N. B.; Fateley, W. G.; Grasselli, J. G. *The Handbook of Infrared and Raman Characteristic Frequencies of Organic Molecules*, Academic Press, California, 1991.
13. Pretsch E. B. P.; Affolter, C. *Structure Determination of Organic Compounds*. 3rd ed.; Springer: 2000.
14. Socrates, G. *Infrared and Raman Characteristic Group Frequencies: Tables and Charts*, 3rd ed.; John Wiley and Sons Ltd., New York, 2001.
15. Nosal, W.H.; Thompson, D.W.; Yan, L. S.; Sarkar, A.; Subramanian, Woollam, J. A.; *Colloids Surf., B* **2005**, 43, 131.

CHAPTER III

SELF-REPAIRING OXETANE-SUBSTITUTED CHITOSAN-POLYURETHANE NETWORKS

Introduction

When a hard or sharp object hits vehicle, it is likely that it will leave a scratch, and for this reason the automotive industry looks for coatings with high scratch resistance. Due to their hardness and elasticity polyurethanes exhibit good scratch resistance, but can still suffer from mechanical damage. An ideal automotive coating would mend itself while a vehicle is driven. To heal mechanical damages in plants, suberin, tannins, phenols, or nitric oxide are activated to prevent further lesions,¹⁻³ whereas in a human skin outer flow of blood cells are arrested by the crosslink network of fibrin, giving rise to wound-healing.^{4,5} Concentration gradients or stratification in living organisms inspired the development of spatially heterogeneous remendable polymers,^{6,7} composites containing micro-encapsulated spheres,⁸⁻¹¹ en-capsulated fibers,¹²⁻¹⁴ reversible cross-linking,^{15,16} and microvascular networks.¹⁷ One example are epoxy matrices containing a glass hollow fiber filled with a monomer and an initiator with the 'bleeding' ability to heal polymer networks during crack formation.¹² Similar phenomenon was utilized in another approach, where a micro-encapsulated dicyclopentadiene monomer was introduced in a catalyst embedded polymer matrix, which healed the crack by the ring opening of the monomer.⁸⁻¹¹ Reversibility of Diels-Alder reactions resulted in another attractive approach to thermally repair damaged areas which utilized maleimide-furan adducts.^{15,16} Mimicking of microvascular structures,¹⁷ water-responsive expandable gels,⁷ and formation of supramolecular assemblies¹⁸ are other avenues of remendability.

Experimental

Polyethylene glycol (PEG) ($M_w = 300$), dimethyl sulfoxide (DMSO), dibutyltin dilaurate (DBTL) were purchased from Sigma Aldrich Co., whereas 3-(Chloromethyl)-3-methyloxetane and tri-functional homopolymer of hexamethylene diisocyanate (HDI) (Desmodur XP 2410) were obtained from TCI America and Bayer Materials Science.

OXE-CHI product was dispersed in DMSO by sonicating at 25 °C for 12 h followed by continuous stirring at 80 °C for 48 h. OXE-CHI-PUR films were prepared by reacting tri-functional HDI with dispersed OXE-CHI and polyethylene glycol (PEG) using overhead agitation at 500 rpm with a small four-blade polytetrafluoroethylene (PTFE) impeller in a 50 ml three-neck reaction flask at 25 °C for 10 min under N_2 atmosphere. A series of PUR networks were prepared by adjusting stoichiometric ratios of NCO, OH, and NH_2 reactive groups. The following molar ratios of HDI/PEG/CHI and HDI/PEG/OXE-CHI (where HDI/PEG forms PUR) were utilized: HDI/PEG/CHI = 1:1.5:0 and 1:1.4:0.57 $\times 10^{-4}$; HDI/PEG/OXE-CHI = 1:1.4:0.57 $\times 10^{-4}$ and 1:1.33:1.17 $\times 10^{-4}$, respectively, while maintaining 38% (w/w) solids. Such mixtures yields films with an approximate film thickness of 300 μm ($\pm 4 \mu m$) on PTFE substrates at 30 °C under 15% relative humidity (RH) for 12 hrs and in a vacuum oven at 80 °C for 48 hrs. The films were mechanically scratched with a razor blade to obtain a desired width and depth of the scratch. Exposure to UV radiation was conducted using a 120W fluorescent UV lamp of 302 nm wavelength.

Microscopic micro attenuated total reflectance Fourier transform infrared (μ ATR FT-IR) were obtained using a Bio-Rad FTS-6000 FTIR single-beam spectrometer at 4 cm^{-1} resolution. A 2 mm Ge crystal, with a 45° face angle maintains at all times with a

constant contact pressure between crystal and the film specimens were used. All spectra were corrected for spectral distortions and optical effects using the Urban-Huang algorithm.¹⁰ Chitosan powders were analyzed by diffuse reflectance Fourier transfer infrared (DRIFT) spectroscopy. In a typical experiment 100 scans were collected and ratioed to 100 reference scans collected using an empty attenuated total reflectance (ATR) cell. As similar procedure was used for DRIFT spectroscopy except the number of spectra was 500.

Internal reflection infrared (IRIR) images were obtained using a Bio-Rad FTS 7000 Stingray system equipped with internal reflection IR imaging (IRIRI) providing 1 micron spatial resolution. This system consists of a Bio-Rad FTS 7000 spectrometer, a Varian 600 UMA microscope, an Image IR focal plane array (FPA) image detector, and IRIRI. The IR images were collected using the following spectral acquisition parameters: under sampling ratio 2, rapid-scan speed 5 Hz, number of images per step 64, and spectral resolution 4 cm⁻¹. In a typical experiment, spectral data set acquisition time was 1min. Image processing was performed using ENVI software (The Environment for Visualizing Images, Research Systems, Inc.) version 3.5.

Solid-state ¹³C NMR measurements were performed on a Varian ^{UNIT}YINOV 400 spectrometer using a standard Chemagnetics 7.5 mm PENCIL-style probe. Samples were loaded into zirconia rotor sleeves, sealed with Teflon caps, and spun at a rate of 4.5 kHz. The standard cross-polarization magic angle spinning (CP/MAS) technique was used with a high-power proton decoupling implemented during data acquisition. The acquisition parameters were as follows: the ¹H 90° pulse width was 4.0 μs, the cross-polarization contact time was 1 ms and the dead time delay between scans was 3 sec.

Results and Discussion

This study departs from previous approaches and reports the development of heterogeneous polyurethane (PUR) networks based on oxetane-substituted derivative of chitosan (OXE-CHI) which upon reactions with hexamethylene diisocyanate (HDI) and polyethylene glycol (PEG),¹⁹ form heterogeneous OXE-CHI-PUR networks. The choice of these components was driven by their ability to serve specific functions, where PUR networks provide desirable heterogeneity through polyurethane and polyurea components, and OXE-CHI provides the cleavage of a constrained 4-membered ring (OXE) and UV sensitivity through CHI, the latter being a product of deacetylation of chitin which is the structural element of exoskeletons of crustaceans (crabs, shrimp, etc.) occurring in abundance in nature. Figure 3.1²⁰ illustrates a two-step reaction sequence leading to the OXE-CHI-PUR formation. The first step in this investigation was the synthesis of OXE-CHI, where the primary alcohol of CHI was reacted with chloromethyl of OXE.²¹ An OXE ring was reacted to the C₆ position of the chitosan molecule, confirmed by IR, Raman and ¹³C-NMR spectroscopy (Figure 2.2, 2.3, and 2.4, respectively). The second step illustrates the reactions leading to the incorporation of OXE-CHI into tri-functional HDI in the presence of PEG (1:1.4 and 1:1.33 molar ratios), confirmed by ¹³C-NMR and IR spectroscopy (Figure A.1 and Figure A.2, respectively).

Networks were allowed to crosslink under ambient conditions to form solid films, which were mechanically damaged. Figure 3.2, A1 illustrates the repair process of OXE-CHI-PUR films. When the damaged area is exposed to 120 W fluorescent UV lamp of 302 nm wavelength of light for 15 (Trace A2) and 30 (Trace A3) mins, the damaged area vanishes. A series of controlled experiments were conducted on specimens prepared with

different stoichiometric amounts of OXE-CHI with respect to the PUR content (Table A.1). Optical images shown in Figure 3.3, A-D, illustrate the results of the experiments conducted under the same UV exposure conditions (0, 15, and 30 min) conducted on the specimens listed in Table A.1.

These experiments illustrate that the presence of OXE-CHI precursor is the key factor responsible for the remendability of the network (Figure 3.2, 3.3). Neither PUR nor CHI-PUR alone (Table A.1, Series A and B) are able to repair the mechanical damage, whereas covalently bonded OXE-CHI (Table A.1, Series C and D) facilitates the self-healing process. Table A.1 also shows the damage width as a function of UV exposure evaluations conducted on the specimens shown in Figure 3.3. Note that the rate of repair for networks containing half the OXE-CHI precursor concentration is also reduced.

While a cut is a local event at micrometer or smaller scales, the actual cleavage is a molecular level event. To determine the mechanism of repair and to follow molecular events in the damaged area, we utilized localized micro-Attenuated Total Reflectance (ATR) FT-IR spectroscopy²² and internal reflection IR imaging (IRIRI).²³ In summary, as shown in Figures A.3, A.4 and A.5, the loss of urea and ether linkages to CHI (circled in Figure 2.1) and the extended exposure of OXE to UV light due to the large surface areas resulting from mechanical damage are responsible for repairing. It is well-known that degradation of polymers resulting from artificial UV exposure cannot be directly correlated with the degradation by the Sun. The repair process, however, utilizes UV light to recombine free radicals to form crosslinks. In the 280-400 nm range, a fluorescent UV lamp generates approximately 0.3 W/m^2 per nm power density, whereas the Sun gives

0.25 W/m² per nm. Thus, the time frame for the repair in the Sun light will be similar.

Since crosslinking reactions are not moisture sensitive, dry or humid climate conditions will not affect the repair process. Although the above networks exhibit the ability to self-repair upon exposure to UV light, if repaired areas are damaged again, due to the thermosetting nature of the reactions the ability for further repair may be limited.

Conclusion

We have developed a new generation of thermosetting polymers of considerable technical and commercial importance. The use of UV light for repairing mechanical damages offers a low temperature approach to healing, critical in a number of applications and does require the placement of micro-capsules or microvascular networks.

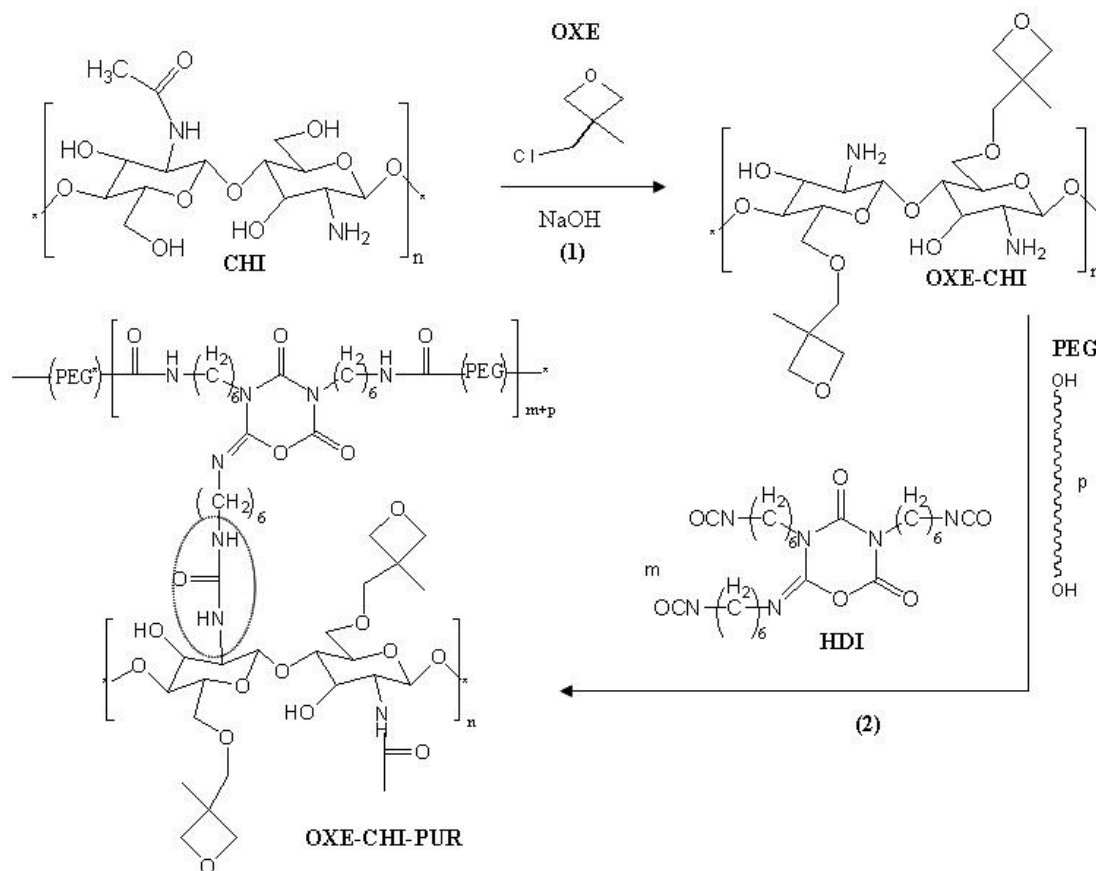


Figure 3.1. Synthetic steps involved in the formation of OXE-CHI. (1) Reactions of OXE with CHI, leading to the formation of OXE-CHI precursor; (2) Reactions of OXE-CHI with HDI and PEG, leading to formations of remendable OXE-CHI-PUR network.

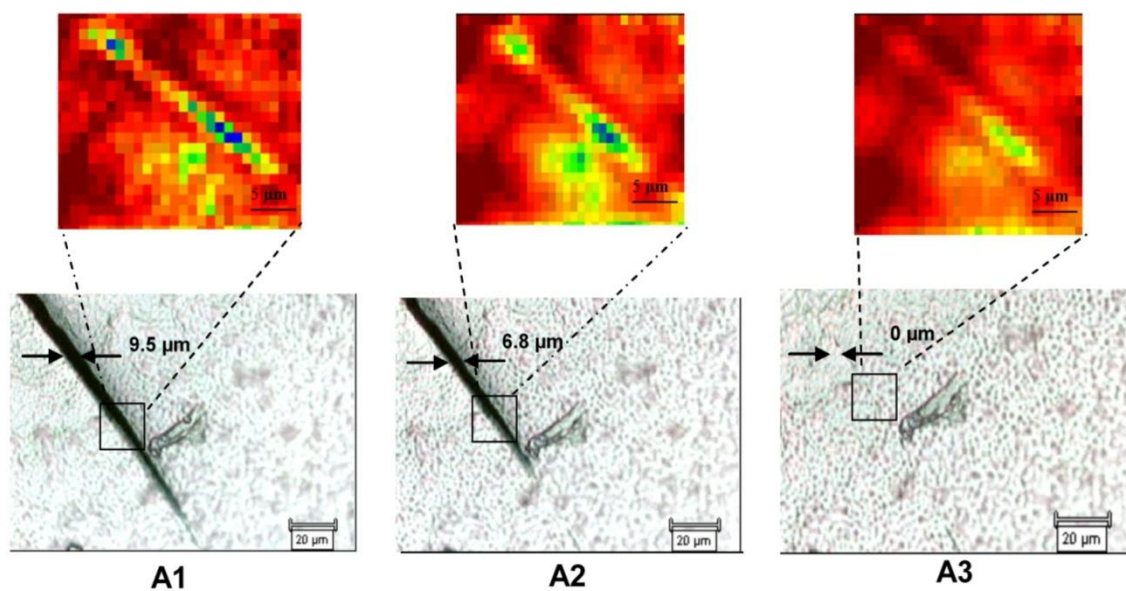


Figure 3.2. IRIR (upper) and optical (lower) images of OXE-CHI-PUR networks recorded as a UV exposure time. A1, 0min; A2, 15 min; A3, 30 min.

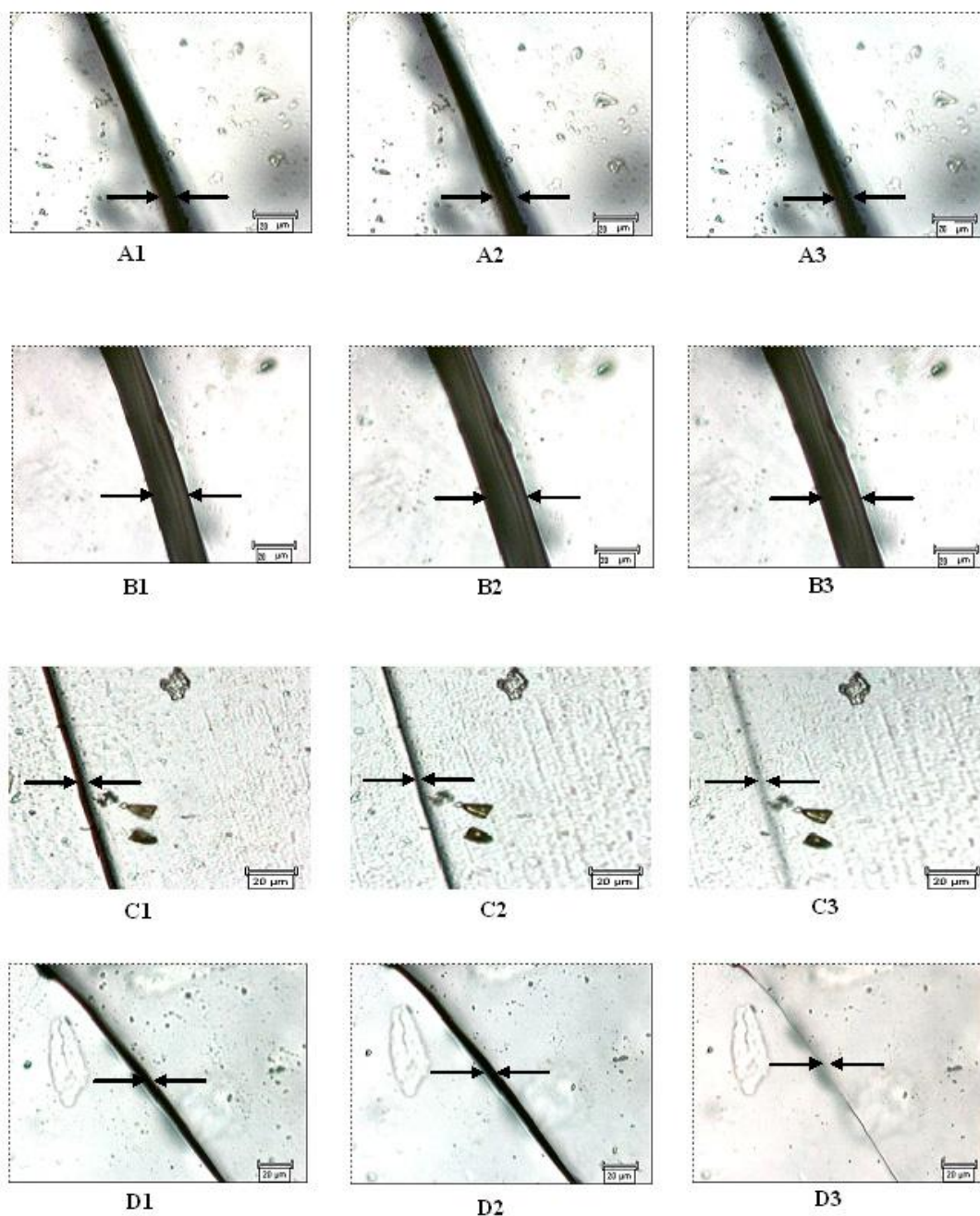


Figure 3.3. Optical images of mechanically damaged films: PUR (A1, A2, and A3 are images after exposure for 0, 15 and 30 min to UV radiation; HDI/PEG/CHI = 1:1.5:0); CHI-PUR (B1, B2, and B3 are images after exposure for 0, 15 and 30 min to UV radiation; HDI/PEG/CHI = 1:1.4:0.57 $\times 10^{-4}$); OXE-CHI-PUR (C1, C2, and C3 are images after exposure for 0, 15 and 30 min to UV radiation; HDI/PEG/OXE-CHI = 1:1.4:0.57 $\times 10^{-4}$); OXE-CHI-PUR (D1, D2 and D3 are images after exposure for 0, 15 and 30 min to UV radiation; HDI/PEG/OXE-CHI = 1:1.33:1.17 $\times 10^{-4}$).

References

1. J. Leon, E. Rojo, J. J. Sanchez-Serrano, *J.Exp. Bot.* **2001**, 52, 1.
2. R. F. Diegelmann, M. C. Evans, *Front. Biosci.* **2004**, 9, 285.
3. R. Paris, L. Lamattina, C. A. Casalongue, *Plant Physiol. Biochem.* **2007**, 45, 81.
4. G. Henry, W. Li, W. Garner, D. T. Woodley, *The Lancet* **2003**, 361, 574.
5. K. G. Mann, K. Brummel-Ziedins, T. Orefo, S. Butenas, *Blood Cells Mol. Dis* **2006**, 36, 108.
6. P. Sonntag, P. Hoerner, A. Cheymol, G. Argy, G. Riess, G. Reiter, *Nature Materials* **2004**, 3, 311.
7. K. Nagaya, S. Ikai, M. Chiba, X. Chao, *JSME Int. J., Series C.* **2006**, 49, 379.
8. S. R. White *et al.*, *Nature* 2001, 409, 794.
9. E. N. Brown, M.R. Kessler, N. R. Sottos, S.R. White, *J. Microencapsul.* **2003**, 20, 719.
10. E. N. Brown, S.R. White, N. R. Sottos, *J. Mater. Sci.* **2004**, 39, 1703.
11. M. R. Kessler, N. R. Sottos, S. R. White, *Composites: Part A.* **2003**, 34, 743.
12. J. W. C. Pang, I. P. Bond, *Compos. Sc. and Tech.* **2005**, 65, 1791.
13. J. W. C. Pang, I. P. Bond, *Composites: Part A.* **2004**, 36A, 183.
14. S. R. Trask, H. R. Williams, I. P. Bond, *Bioinsp. Biomim* **2007**, 2, 1.
15. X. Chen *et al.* *Science* **2002**, 295, 16998.
16. R. Gheneim, C. Perez-Berumen, A. Gandini, *Macromolecules* **2002**, 35, 7246.
17. S. K. Toohey, N. R. Sottos, J. A. Lewis, J. S. Moore, S. R. White, *Nature Mat.* **2007**, 6, 581.
18. P. Cordier, F. Tournilhac, C. Soulie-Ziakovic, L. Leibler, *Nature Lett.* **2008**, 451, 977.
19. D. B. Otts, M. W. Urban, *Polymer* **2005**, 46, 2699.
20. Appendix A.

21. Y. Wan, K. A. M. Creber, B. Peppley, V. T. Bui, *J. Polym. Sci., Part B: Polym. Phys.* **2004**, 42, 1379.
22. M.W. Urban, *Attenuated Total Reflectance Spectroscopy of Polymers; Theory and Applications* (American Chemical Society and Oxford University Press, Washington, DC, 1996).
23. D. Otts, P. Zhang, M.W. Urban, *Langmuir* **2002**, 18, 6473.

CHAPTER IV

CHEMO-MECHANICAL REPAIRS INSIDE A SCRATCH OF OXETANE-SUBSTITUTED CHITOSAN-POLYURETHANE (OXE-CHI-PUR) NETWORKS

Introduction

Recently, we have established that combining polyurethane (PUR) and oxetane-substituted chitosan (OXE-CHI) into one crosslinked network generates polymeric materials capable of self-repair.¹ The choice of these components was dictated by their ability to serve specific functions. While isocyanate-polyol crosslinking reactions result in PUR and or polyurea (PUA) formation which provides desirable mechanical integrity and localized network heterogeneity, incorporation of the OXE-CHI macromonomer into the PUR network as a crosslinker furnishes constrained 4-member rings (OXE) and UV sensitivity (CHI) necessary for self-repair. These studies showed that the presence of covalently attached 4-member ring (OXE) with relatively low ring opening activation energy (19.3 kcal/mol) is required for recombining mechanically damaged network upon UV exposure,² with the dormant oxonium ion essential for a long induction period necessary to trigger network remodeling reactions.³⁻⁵ In view of these considerations and the complexity of NCO-OH catalyzed reactions under specific stoichiometric conditions, it was cleared that further investigation into the role of each network component was necessary along with the molecular processes responsible for macroscopic network remodeling during UV-initiated repair.

Figure 4.1-A precisely illustrates defined the network consisting of PEG crosslinked with tri-functional HDI and OXE-CHI macromonomer, with the

HDI:PEG:OXE-CHI stoichiometry adjusted to obtain NCO:OH:NH₂ reactive group ratios of 6.0:5.3:0.7 (Figure 4.1,B). When all components are crosslinked, the OXE-CHI-PUR network depicted in Figure 4.1-A is formed which upon mechanical damage a visible scratch is formed. However, upon UV exposure, self-repair occurs, such as that shown in Figure 4.1-C. It should be noted that this process occurs only when relatively minute quantities of OXE-CHI macromonomer replace HDI crosslinker during cross-linking reactions, and its excessive amounts will lead to phase separation and a loss of network mechanical properties. Although the presence of OXE-CHI is essential for self-repair to occur,¹ during the course of these experiments it becomes apparent that the minute stoichiometry and acidity changes within the damage area significantly influence network macroscopic responses initiated by UV light. These studies will attempt to correlate molecular processes within the damaged site with physical network remodeling during and after repair in effort to elucidate the origin of molecular and macroscopic events during network repair.

Experimental

OXE-CHI Macromonomer Synthesis and OXE-CHI-PUR Network Formation

Chitosan (CHI) (degree of deacetylation 75-85%), isopropyl alcohol, methanol, polyethylene glycol (PEG) (M_w=300), sodium hydroxide beads, acetone, dimethyl sulfoxide (DMSO), dibutyltin dilaurate (DBTDL) were purchased from Sigma Aldrich Co., 3-(Chloromethyl)-3-methyloxetane and tri-functional homopolymer of hexamethylene diisocyanate (HDI) (Desmodur XP 2410) obtained from TCI America and Bayer Material Science, respectively. Hindered amine light stabilizer (HALS) TINUVIN

P was supplied by Ciba Chemicals. Two grams of low molecular weight CHI ($M_n \sim 5 \times 10^5$ g/mol) was added into a 150 g 1(N) NaOH solution in a three-neck flask and stirred for 24 h at -5°C , followed by refrigeration at -18°C for 48 h. The solution was thawed and mixed with pre-cooled isopropyl alcohol and stirred for 1 h. Pre-cooled 3-chloro-3-methyl oxetane was added to the mixture, the temperature increased to 80°C and the solution stirred for 12 h. The product was filtered and washed several times with methanol until the effluent exhibit neutral pH. This was followed by drying at 60°C for 12 h, and the product was characterized by ATR and Raman spectroscopy. A series of OXE-CHI were synthesized with the following molar ratios 1:1, 1:2, 1:4, 1:6, and 1:10. To polymerize OXE-CHI, 1:1 molar OXE-CHI was dispersed in DMSO (in presence of 2×10^{-5} moles DBTDL) and acetic acid (pH=6.8) solutions, followed by UV exposure for 20 min. Polymerized OXE-CHI was isolated by washing with methanol.

The OXE-CHI-PUR networks were prepared by dispersing OXE-CHI macromonomer into DMSO by sonicating the solution at 25°C for 12 h, followed by continuous stirring at 80°C for 48 h. The OXE-CHI-PUR films were prepared by reacting tri-functional HDI with dispersed OXE-CHI and polyethylene glycol (PEG) using overhead agitation at 500 rpm with a small four-blade polytetrafluoroethylene (PTFE) impeller in a 50 ml three-neck reaction flask at 25°C for 10 min under N_2 atmosphere. A series of PUR networks were prepared by adjusting stoichiometric ratios of NCO, OH, and NH_2 reactive groups. The following molar ratio of HDI/PEG/OXE-CHI (where HDI/PEG forms PUR) was utilized: HDI:PEG:OXE-CHI=1:1.33:1.17 $\times 10^{-4}$, while maintaining 38% (w/w) solids. Three different molar ratios of OXE-CHI were

introduced within the PUR networks to prepare model systems and the same synthetic procedure was performed at each stoichiometry using 1 wt % of TINUVIN P HALS.

Approximately 300 μm (± 4 μm) thick films were formed on PTFE substrates at 30 °C and 15% relative humidity (RH) for 12 h and in a vacuum oven at 80 °C for 48 h. The films were mechanically scratched with a razor blade to obtain approximate scratch dimension of 30 μm (± 5) width and 20 μm (± 2) depth. Exposure to UV radiation was conducted using a 120 W fluorescent UV lamp (from Spectraline) of 302 nm wavelength of light. In each experiment specimen was placed 10 (± 1) cm from the lamp.

Following the same route, a series of OXE-CHI-PUR networks were synthesized containing 2×10^{-5} , 4×10^{-5} , 1×10^{-4} , 1×10^{-3} 1×10^{-2} molar DBTDL. For the purpose of these studies, acetic acid solutions with pH=3, 4, 5, 6, and 6.8 were prepared. OXE-CHI-PUR networks were mechanically damaged, and different pH solutions were injected into the crack using a 5 mL syringe followed by UV exposure. To determine $[\text{H}^+]$ concentrations of the acidic acid solutions, the following formula was applied: $\text{pH} = \text{pK}_a + \log [\text{A}^-]/[\text{HA}]$ with $\text{K}_a = [\text{H}^+][\text{A}^-]/[\text{HA}]$; and $\text{pK}_a = 4.75$ at 25 °C for acetic acid. Similarly, OXE-CHI-PUR networks containing 1% HALS were synthesized by first dissolving HALS (TINUVIN P) within DMSO, followed by addition of OXE-CHI macromonomer and HDI. All spectroscopic and imaging analysis associated with these and controlled experiments are detailed in the Supporting Documents.

Variable-angle dynamic light scattering (DLS) measurements were conducted using an incident light at 633 nm from a Spectra Physics Model 127 HeNe laser operating at 40 mW. The angular dependence of the autocorrelation functions was measured using

a Brookhaven Instruments BI-200SM goniometer with an avalanche photodiode detector and a Turbo Corr correlator. The angular dependence of the inverse excess scattering intensity (I_{ex}) was determined via Zimm/Berry analysis by plotting I_{ex}^{-1} versus the square of the scalar magnitude of the scattering vector (q^2), with the molecular weight of the polymer equal to the increase value of the Y intercept.

Spectroscopic and Thermo-Mechanical Measurements

Optical images were collected from an IFS 55/FRA 106 FT-IR/Raman spectrometer (Bruker Instruments, Inc.). Microscopic micro attenuated total reflectance Fourier transform infrared (μ ATR FT-IR) were obtained using a Bio-Rad FTS-6000 FTIR single-beam spectrometer at 4 cm^{-1} resolution. A 2 mm Ge crystal, with a 45° face angle was used with constant contact pressure maintained between crystal and the film specimens was used. All spectra were corrected for spectral distortions and optical effects using the Urban-Huang algorithm.⁶ Chitosan powders were analyzed using the diffuse reflectance Fourier transfer infrared (DRIFT) method. Each film spectrum represented 100 co-added scans ratioed to 100 reference scans collected using an empty attenuated total reflectance (ATR) cell. The same procedure was used for DRIFT spectra except the number of scans was 500.

Internal reflection infrared (IRIR) images were obtained using a Bio-Rad FTS 7000 Stingray system equipped with internal reflection IR imaging capable of 1 micron spatial resolution. This system consists of a Bio-Rad FTS 7000 spectrometer, a Varian 600 UMA microscope, an image IR focal plane array (FPA) image detector, and internal reflection IR imaging crystal. The IR images were collected using the following spectral

acquisition parameters: under sampling ratio 2, rapid-scan speed 5 Hz, number of images per step 64, and spectral resolution 4 cm^{-1} . Spectral data set acquisition time was normally 1 min. Image processing was done using ENVI software (The Environment for Visualizing Images, Research Systems, Inc.) version 3.5.

FT-Raman spectra were measured using an IFS 55/FRA 106 FT-IR/Raman spectrometer (Bruker Instruments, Inc.). The excitation source was a diode pumped Nd:YAG laser having a maximum power of 500 mW over the sampling area. WIRE 2.0 (Bruker Instruments, Inc.), and GRAM were used to analyze spectra.

Differential scanning calorimetry (DSC) measurement was carried out on a TA instruments DSC Q100 under a N_2 atmosphere. The specimen was equilibrated at $-50\text{ }^\circ\text{C}$ for 3 min, followed by heating at $10\text{ }^\circ\text{C}/\text{min}$ to $275\text{ }^\circ\text{C}$, and cooling down at $10\text{ }^\circ\text{C}/\text{min}$ to $-50\text{ }^\circ\text{C}$. The same cycle was repeated several times, and the resulting data analyzed using TA Universal Analysis software.

Localized thermo-mechanical analysis was conducted using a microthermal analyzer model (μTA) 2990 (TA Instruments) equipped with a $5\text{ }\mu\text{m}$ Wollaston thermal tip calibrated with biphenyl (melting point= $69\text{ }^\circ\text{C}$), anisic acid (melting point= $183\text{ }^\circ\text{C}$), and polyethylene terephthalate (melting point= $245\text{ }^\circ\text{C}$). In a typical experiment, the displacement of the thermo-couple tip was monitored as the tip temperature was increased from 30 to $120\text{ }^\circ\text{C}$ at a heating rate of $10\text{ }^\circ\text{C}/\text{s}$ with an accuracy of $(\pm)1\text{ }^\circ\text{C}$. The tip displacements $d(\Delta l/T)$ at a given temperature (T) yield information concerning the thermal network expansion changes as a function of temperature and were obtained by

taking the first derivative of the displacement values (Δl vs temperature), and were normalized the results with respect to their initial values.

Results and Discussion

The first step in these studies was to determine the influence of OXE-CHI stoichiometry on kinetics of the self-repair process of the OXE-CHI-PUR network upon UV exposure. For that reason we prepared OXE-CHI-PUR networks with HDI:PEG:OXE-CHI=1.0:1.33:1.17 $\times 10^{-4}$ stoichiometries in which the OXE-CHI content was varied. Such networks were subjected to a mechanical scratch, followed by UV exposure. Figure 4.2, A1-A3, B1-B3, and C1-C3 illustrate the optical images of self-repair as a function of UV exposure time for 1:1, 1:4 to 1:10 OXE-CHI stoichiometries, respectively. As seen, when the OXE-CHI ratio decreases, the repair process of OXE-CHI-PUR is slower, and ranges from 20 to 60 min. As was shown in previous studies,¹ the network repair does not occur at elevated temperatures. For reference purposes, Figure 4.2, D1-D3 illustrate the results of UV exposure of the PUR network without OXE-CHI macromonomer and does not exhibit self-healing attributes.

Since DBTDL is utilized as a catalyst, it is of interest to observe the influence of DBTDL on OXE ring opening reactions in OXE-CHI-PUR networks (HDI:PEG:OXE-CHI=1.0:1.33:1.17 $\times 10^{-4}$) that exhibit self-repair attributes illustrated in Figure 4.2, A1-A3. For that reason we incorporated 2 $\times 10^{-5}$, 4 $\times 10^{-5}$, 1 $\times 10^{-4}$, 1 $\times 10^{-3}$ and 1 $\times 10^{-2}$ moles of DBTDL into OXE-CHI-PUR (OXE-CHI=1:1) and followed the UV initiated self-repair process. As shown in Figure 4.2, A1-A3, when 2 $\times 10^{-5}$ moles of DBTDL are used, OXE-CHI-PUR network exhibits self-repair behavior, but to our surprise any excess of DBTDL above 4 $\times 10^{-5}$ moles inhibits this process. This is illustrated in the optical images

shown in Figure 4.2, E1-E3 for 4×10^{-5} DBTDL molar content. Based on these data, it is quite apparent that the self-repair process is affected not only by the stoichiometry of individual components, but also their acidity. These observations prompted us to identify molecular processes occurring inside the scratch.

Using IRIR imaging⁷ we analyzed spectroscopic changes inside the scratch of OXE-CHI-PUR network as a function of DBTDL concentration by tuning to the 1562 cm^{-1} band due to -NH-CO-NH- stretching vibrations of PUA. Figure 4.3-A illustrates a spatial distribution of the 1562 cm^{-1} band for OXE-CHI-PUR containing 2×10^{-5} , 4×10^{-5} , 1×10^{-4} , 1×10^{-3} , and 1×10^{-2} moles of DBTDL, and Traces a-e of Figure 4.3-B are the FT-IR spectra collected from circled areas in the images a-e of Figure 4.3-A of OXE-CHI-PUR. Analysis of these data show that when the DBTDL concentration increases, the band at 1562 cm^{-1} due to PUA decreases and, at the same time, the 1542 cm^{-1} band due to PUR increases. Concurrently, the band at 985 cm^{-1} due to -C-O-C- stretching vibrations of OXE is detected only for 2×10^{-5} DBTDL mole content (Trace a), and diminishes to minimum at higher molar concentrations (Traces b-e). These results combined with the results of macroscopic data shown in Figure 4.2, A1-A3 and E1-E3, indicate that OXE-CHI-PUR network self-repair process (Figure 4.2, A1-A3) occurs when DBTDL and OXE-CHI are present at a relatively narrow (HDI:PEG:OXE-CHI:DBTDL=1.0:1.33:1.17 $\times 10^{-4}$:2.0 $\times 10^{-5}$) stoichiometric window. It should be noted that the functions of DBTDL and OXE-CHI are substantially different: DBTDL catalyses HDI and PEG crosslinking reactions, whereas OXE-CHI acts as an additional crosslinker during network formation and thus replaces a small fraction of HDI bonding sites. Because the synthesis of PUR in the presence of DBTDL involves cationic

intermediates,⁸ excess of DBTDL in the OXE-CHI-PUR network promotes premature OXE ring opening (Traces b-e, Figure 4.3-B), and thus inhibits the self-repair process. In contrast, when the DBTDL stoichiometry is such that it catalyzes crosslinking reactions only, the OXE rings remain in their dormant state as oxonium ions.³ It is well known that solutions of the OXE monomer can retain the presence of oxonium ions for as long as 100 hrs in the presence of catalysts,⁴ and its stability is expected to be significantly greater in the solid state, where the mobility is drastically diminished, thus making DBTDL inactive after being regenerated during crosslinking. In summary, during the first step of crosslinking, Sn of DBTDL coordinates with -OH and -NH₂ groups of PEG and OXE-CHI, respectively. This is followed by the addition of tri-functional HDI to form an intermediate, where Sn of DBTDL coordinates with N and C of -NCO as well as -OH and -NH₂ groups, respectively. The final step involves covalent bond formation between -NCO(C), PEG(O) and OXE-CHI(N), via protonation of the C=O of -NCO, which regenerates DBTDL and creates the OXE-CHI-PUR network.⁸ To test this hypothesis we conducted controlled experiments in which the OXE-CHI macromonomer was reacted with DBTDL in DMSO. These results showed that indeed OXE ring opens cationically in the presence of DBDTL, with spectra shown in Figure B.1 of the Supporting Documents provides spectroscopic evidence that the OXE -C-O-C- linkages cleave, whereas the -C-O-C- linkages between CHI-OXE and CHI-CHI remain unchanged.

These results show that DBTDL not only catalyze HDI and PEG reactions but also contribute to OXE ring protonation. To further examine the role of protic environments we conducted a series of experiments in which acidic acid (AA)

solution[†] was introduced into a mechanically generated scratched OXE-CHI-PUR (HDI:PEG:OXE-CHI=1.0:1.33:1.17x10⁻⁴) network. Figure 4.4, A1-A3, B1-B3, C1-C3, D1-D3, E1-E3, F1-F3 show the optical images of the damaged OXE-CHI-PUR films in which the scratches (with the exception of A1-A3) were filled with AA solutions having pH=6.8 (B1-B3), 6 (C1-C3), 5 (D1-D3), 4 (E1-E3), and 3 (F1-F3). Figure 4.4 also provides corresponding values of molar concentration levels of DBTDL and AA as well as pH changes for each condition. As seen, when AA is not added, self-repair occurs (Figure 4.4, A1-A3), and the addition of 1.56x10⁻⁷ moles of [H⁺], which corresponds to pH=6.8, still shows repair (Figure 4.4, B1-B3). However, when the pH decreases to 6, which represents an increase of the [H⁺] ions by 0.98x10⁻⁶ above DBTDL initial molar concentration levels, the repair process is stopped, as manifested by unchanging width of the scratch. Furthermore, when the pH values further decrease to 5, 4, and 3, the scratch actually expands. This is shown in Figure 4.4, D1-D3 through F1-F3, respectively.

To determine molecular processes occurring and the role of [H⁺] ions responsible for expansion (pH=3-6) and self-healing (pH=6.8) of OXE-CHI-PUR networks, changes inside the scratch due to UV exposure were monitored spectroscopically. Since OXE-CHI-PUR network also contains PUA linkages, and exposure to acidic environments may often lead to the formation of carbamic acid,⁹ we tuned to the 1520 cm⁻¹ band of the –C=O stretching vibrations of carbamic acid and monitored its intensity as a function of UV exposure. Images A1, A2, and A3 of Figure 4.5 illustrate the distribution of OXE-

[†][Although onium salts could be used to catalyze OXE ring opening, their use is limited due to salt formation in the damaged area and the possibility of undesirable side reactions with water. Ideally, lauric acid [CH₃(CH₂)₁₀CO₂H] with a pKa=5.02 should be used, but it is insoluble in water;⁹ the use of organic solvents could result in adverse network swelling. Therefore, we utilized acetic acid [CH₃CO₂H], pKa=4.75.]

CHI species in the areas labeled A'/A'', B'/B'', and C'/C'' (un-damaged/damaged area) for the pH=3 solution, spectroscopic changes are shown in Figure 4.5, A1'-A3', A1''-A3'' in the 1500-1600, and 1600-1750 cm^{-1} regions. When the scratch is exposed to UV for 10 minutes, the bands at 1566, 1535, and 1520 cm^{-1} corresponding to $-\text{NH}_2^+\text{CO}_2^-$ increase significantly.^{10,11} Also, the band at 1650 cm^{-1} characteristic of $-\text{NH}_2^+$ vibrations due to protonation of PUA increases. These observations indicate that, under acidic conditions, PUA linkages of the OXE-CHI-PUR network are converted to carbamic acid, resulting in the expansion of the scratch due to the loss of CO_2 .¹⁰⁻¹³ This process continues as the network is exposed further, which is manifested by the increased bands at 1650, 1566, 1535, and 1520 cm^{-1} in Figure 4.5, A1''-A3'' due to carbamic acid formation. In contrast, for the same scratch contains AA at pH=6.8, the IR images illustrated in Figure 4.6, A1-A3 recorded from areas A' (undamaged) and A'' (damaged) show no 1520 cm^{-1} band, indicating that carbamic acid is not generated. Instead, the 1542 cm^{-1} band increases, signifying PUR formation. The same observations were detected in Figure 4.3-A for OXE-CHI-PUR networks. Since the 1650 cm^{-1} band remains unchanged, no protonation of PUR nor PUA linkages is detected, and self-healing occurs when $[\text{H}^+]$ concentrations are at $\sim 1.56 \times 10^{-7}$ (pH=6.8), and initiated by cationic OXE ring opening.^{3-5,14-17}

Although the presence of acidic environments facilitates OXE ring opening, it is also of interest to examine its sensitivity to UV exposure. Therefore we conducted a series of model experiments whereby the OXE-CHI macromonomer was synthesized in the following OXE: CHI molar ratios: 1:1, 1:2, 1:4, 1:6, and 1:10, and spectroscopically monitored chemical changes before and after UV exposure. The Raman and FT-IR

spectra recorded before and after each exposure are shown in Figures B.2-B.6 and B.7-B.11 of Supporting Documents, respectively, analysis of the intensity changes of the vibrational bands sensitive to UV exposure allowed us to identify reactions resulting from UV exposure which are summarized in Figure 4.7: (a) OXE ring opening, manifested by the decrease of the -C-O-C- vibrations at 1043 cm^{-1} , OXE-ring breathing mode at 985 cm^{-1} as well as the CH bending modes at 1425 cm^{-1} ; (b) and (c) chain scission of the -C-O-C- segments shown by the decrease of the -C-O-C- vibrations at 1043 cm^{-1} and the increase of the 890 cm^{-1} band due to O-C-O formation; (d) the chair-to-boat conformational changes of pyranose units of CHI manifested by the decrease of the 778 cm^{-1} band;^{11,13,18,19} (e) -O-NH formation shown by the decrease of the 970 cm^{-1} band; (f) NH_2 oxidation, leading to the formation of NO_2 manifested by the decrease of amide I band at 1580 cm^{-1} band, and (g) the formation of hydrazine reflected by the appearance of the band at 1117 cm^{-1} .^{1,11,13} Because the OXE-CHI macromonomer serves as a crosslinker during PEG and HDI reactions with all NH_2 functionalities consumed during the network formation, only the reactions depicted in Figure 4.7, a-d are relevant in the OXE-CHI-PUR self-repair process. Combining the results of acidic and UV exposure experiments, it appears mild acidic conditions combined with UV exposure facilitate cationic OXE ring opening as well as free radical cleavage of -C-O-C- linkages. Chair-to-boat conformational changes of glycosine units are accompanied by the formation of dormant oxonium cations which trigger ring opening reactions.^{3-5,20,21} Also, as has been shown in the previous studies,¹ and spectroscopically confirmed by the intensity changes of the 1562 and 1542 cm^{-1} bands of PUA and PUR, (Figure 4.3-B), PUA is converted to

PUR upon UV exposure, manifested by free radical cleavage of the C-N bonds of –CO-NH-CO- linkages.

Although spectroscopic analysis indicates the cleavage of specific bonds, it does not show if cationic OXE ring opening and free radically induced reactions are occurring simultaneously. To determine if both processes occur simultaneously, we introduced 1 wt% hindered amine light stabilizers (HALS) to serve as free radical scavengers.²²

Figure 4.8, A1-A3, B1-B3, and C1-C3, illustrates the progression of OXE-CHI-PUR network repair upon UV exposure containing 1:1, 1:4, and 1:10 OXE-CHI molar ratios and 1 wt% HALS, respectively. Incorporation of HALS retards the kinetics of the repair process from 20, 30, and 60 minutes (Figure 4.2, A1-A3, B1-B3, and C1-C3) for OXE-CHI-PUR containing OXE-CHI of 1:1, 1:4, 1:10 molar ratios, respectively, to 120, 240, and 300 minutes (Figure 4.8, A1-A3, B1-B3, C1-C3).

Similar to the previous experiments, to examine which covalent bonds are affected by the presence of HALS, IRIR imaging was employed. Figure 4.9, A1, A2, and A3, shows the IR images of OXE-CHI-PUR (OXE-CHI=1:1) recorded after UV exposure for 0, 30 and 120 min, respectively. The corresponding spectra recorded from undamaged (A') and damaged (A'') areas are shown in Figure 4.9, A1'-A3', A1''-A3'', and A1'''-A3''' and illustrate the increase of the –C-O-C- 1108 cm⁻¹ band due to the stretching vibrations of linear aliphatic ethers along with the decrease of the 985 cm⁻¹ band due to –C-O-C- stretching vibrations of OXE rings. As shown in Figure 4.9, A2', A2'', and A2''', upon exposure to UV for 30 minutes, intensities of the 1562, 1378, and 985 cm⁻¹ bands decrease significantly. Simultaneously, the intensity of the 1542, 1530, and 1348 cm⁻¹ bands, characteristic of PUR N-H deformation of PUR, and –CH₂- wagging and C-

N stretching of linear alkyls, increase. These observations signify OXE ring opening and the conversion of PUA-to-PUR in the damaged area, which continues upon further exposure for 120 min. As shown in Figure 4.9, A3', A3'', and A3''', the intensity of the 1108 cm^{-1} band increases whereas the 1562 cm^{-1} band further diminishes and the 985 cm^{-1} vibrations disappear in the damaged area. However, the 985 cm^{-1} band does not diminish in the undamaged area, but a slight decrease of this band is observed after 240 and 300 min of UV exposure (Figure B.12-A3''-A', and B.13-A3''-A'). Since OXE ring remains closed even after extensive exposure times of OXE-CHI-PUR network, these data indicate that the presence of PUA and PUR linkages hinders OXE ring opening in the OXE-CHI-PUR networks during UV exposure in the absence of external mechanical damage. As we recall, the presence of -C-O-C- linkages of CHI and linear ether bonds accelerate the ring opening (B.2-B.11), thus supporting the hypothesis that was also observed in epoxy monomers in the presence of ester linkages.^{3,16} IRIR imaging experiment conducted on OXE-CHI-PUR networks containing 1:4 and 1:10 OXE-CHI molar ratios and HALS are shown in Figures B.12 and B.13 also show the disappearance of the 985 cm^{-1} band as well as the decrease of the 1562 cm^{-1} band upon UV exposure.

In summary, spectroscopic analysis of molecular events inside the scratch of OXE-CHI-PUR network along with the results of the model OXE-CHI studies (Figure B.2-B.11) indicate that four labile linkages circled in Figure 4.10-a are primarily responsible for UV-induced self-repairing: 1) -NHCONH- PUA linkage, 2) -C-O-C- between CHI-CHI, 3) -C-O-C- between CHI-OXE, and 4) -C-O-C- of OXE ring, which undergo bond cleavages when the OXE-CHI-PUR network is mechanically damaged and exposed to UV radiation. These processes generate reactive free radicals (b1, b2, and b3) and

carbocation (b4) during self-repairing process, where OXE ring opening reaction (b4) propagate cationically,^{3-5,18,19} but –NHCONH– (PUA) and –C–O–C– bond cleavage generate free radicals (b2).^{1,11,12} On the other hand, close packing and/or network shrinkage upon UV exposure due to chair-to-boat conformational changes (Figure 4.7-d) of the glycosine units of CHI parallels DBTDL catalyzed OXE ring opening reactions as well as PUA-to-PUR conversion lead to self-repair of the network consisting of the reformed urethane and ether linkages (c) without peroxide formation.

While chemical and optical imaging analysis allowed us to follow molecular and visual events associated with a mechanical damage and UV-induced repair by monitoring chain cleavage and bonds formation, the next question is how these processes are responsible for physical network remodeling during repair. Mechanical damage and subsequent repair will not only alter molecular weight in the damaged and repaired areas, but will also lead to macroscopic mass transport during the repair. As the first step, let us recall that the presence of OXE-CHI macromonomer facilitates UV induced repair, which is initiated by cationic OXE ring opening under mild acidic (pH=6.8) conditions. Postponing temporarily analysis of network physical remodeling, we conducted control experiments in which we determined molecular weight changes of OXE-CHI macromonomer dispersed in DMSO containing DBTDL and AA at pH=6.8 before and after UV exposure (20 min). The results of dynamic light scattering (DLS) showed that the initial 5×10^5 OXE-CHI molecular weight increases to 6.8×10^5 and 6.5×10^5 , respectively, suggesting that inter or/and intra-molecular crosslinking between –C–O–C– linkages resulting from OXE ring opening occur.

Keeping in mind that OXE-CHI molecular weight increases upon UV exposure, let us examine if UV induced repair occurs in PUR network alone by injection of OXE-CHI macromonomer in AA solution at pH=6.8 as well as in DMSO containing 2×10^{-5} moles of DBTDL into a mechanically generated crack. Figure 4.11, A and B illustrate a sequence of optical images of PUR network recorded as a function of UV exposure time for OXE-CHI in AA and DMSO solutions, respectively. As seen, the repair occurs under both conditions, thus indicating that the same process can be reproduced by inducing mild acidic conditions inside scratch area which are necessary for self-repairing.

Let us going back to the main theme and examine the localized thermal expansion of OXE-CHI-PUR network as a function of temperature before and after mechanical damage, and after self-repair initiated by UV exposure. Figure 4.12, A1, A2, A2¹ and A3 illustrate topographical AFM images of OXE-CHI-PUR network (HDI:PEG:OXE-CHI=1.0:1.33: 1.17×10^{-4}) before (A1) and after mechanical damage (A2) and after UV exposure (A2¹, A2², A3). As seen, the formation of a groove along with the expected “side banks” resulting from mechanical damage are observed (Image A2) from which IRIR images were collected, and the shape of the damaged area resulting from materials piling follows previous observations.²³ Upon UV exposure, a frontal flow which resembles frontal polymerization occurs from the bottom of the scratch (A2¹, A2²). The heights of the surface topological features plotted as a function of the displacement perpendicular to the damaged area are illustrated in Figure 4.12, A1', A2', A2¹' and A3'. As shown in Figure 4.12, A1', the undamaged surface of the network does not show height differences, but the network scratch formation leads to (Figure 4.12, A2') mass flow involving physical irreversible damage superimposed on the slight of plastic

deformation of the bulk no longer capable of restoring the original form.²⁴ However, upon UV exposure, the heights of the side banks decrease, and the frontal growth within the damage appears (A2^{1'}), followed by scratch closure (A3') occurs. If these observations are indicative of self-repair process initiated at the bottom of the scratch followed by the mass transport of cleaved shorter segments or oligomers from the side banks, it is anticipated that thermo-mechanical properties inside the scratch will be affected.

In an effort to identify thermo-mechanical responses of OXE-CHI-PUR network in the damaged areas from which IRIR images were collected (Figures 4.3-A,a), thermal OXE-CHI-PUR expansion was measured as a function of temperature. The open (a) and closed (b) circles in Figure 4.12, A1-A3 show the data collection points. Open circles (line a) represent mechanical damage and UV induced repair areas, and closed circles (line b) serve as controls. The premise behind these experiments is to determine network thermal expansion changes in mechanically damaged and repaired areas as a function of temperature and relate these values to the glass transition temperature (T_g) as well as spectroscopic analysis discussed above. It is well known from the Fox-Flory relationship ($[T_g = T_{g\infty} - C/\overline{M_N}]$, the T_g is the glass transition temperature of the polymer with a given molecular weight M_N , $T_{g\infty}$ is the limiting glass transition temperature and C is a constant), that when molecular weight decreases, the T_g decreases.²⁵ As a result of the scratch formation, two surfaces are created, and the T_g values inside the surface of the scratch are expected to be lower due to chain cleavage or slippage.²⁶ As we recall the results of spectroscopic analysis, the main events are OXE ring opening, breaking of PUA linkages and $-C-O-C-$ bonds between CHI-OXE and CHI-CHI (Figure 4.10, b1-b4).

These events are expected to be different below and above the T_g and alter the thermal expansion coefficient which reflects network expansibility. As shown in Supporting Documents (B.14), the thermal expansion raw data exhibits two regions: the glassy state below and the rubbery state above the T_g , and the transition region, and to determine the thermal expansion changes $d(\Delta l)$ of the network as a function of temperature, Figure 4.12, A1'', A2'', and A3'' normalized $d(\Delta l)/dT$ values for undamaged, damaged, and self-repair areas were plotted as a function of temperature, respectively. As seen in Figure 4.12-A1'', the rate of $d(\Delta l)/dT$ changes with T , and the maximum value is detected at 61 °C, which corresponds to the T_g values obtained by DSC (Figure B.15). However, in the damaged area (open circles, Figure 4.12, A2-a), not only the $d(\Delta l)/dT$ maximum is lowered to 56 °C, but the width of the $d(\Delta l)/dT$ values also increase, indicating the lower T_g values inside the scratch. These observations suggest lower and broader molecular weight distribution which result from the bond cleavage, as determined spectroscopically and was summarized in Figure 4.9, b1-b4. Also, as shown in Figure 4.12, A2'', a new weaker transition is detected at 102 °C. As we recall the analysis of the spectroscopic data shown in Figure 4.3, the formation of PUA results from mechanical damage and this transition likely corresponds to the T_g of PUA, which was reported in the same range for modified diphenylmethane diisocyanate (MDI)-diamine PUA systems.^{27,28} However, upon UV exposure, this transition diminishes due to PUA-to-PUR conversion which was again confirmed spectroscopically¹ and the $d(\Delta l)/T$ maximum is shifted to 62 °C, thus indicating enhanced crosslink density resulting from self-repair. For reference purposes, Figure 4.12, B1-B3 illustrate undamaged (B1), damaged (B2), and UV exposed (B3¹,B3) PUR network (Figure 4.2, D1-D3). As shown,

no self-healing is detected. Similarly, the corresponding AFM height images of PUR network are shown in Figure 4.12, B1'-B3' and illustrate that UV exposure does not change the shape of neither the side banks nor the groove. As shown in Figure 4.12, B1''-B3'', the T_g at the undamaged (B1'') area (61 °C) decreases to 59 °C in the damaged (B2'') area and does not change upon UV exposure (B3''), which is indicative of minimal or no crosslinking reactions in the damaged area under UV exposure.

Conclusion

These studies show that a precise control of crosslinked OXE-CHI-PUR networks is necessary for OXE-CHI-PUR networks to exhibit self-repairing properties under UV exposure to occur. Using chemical imaging along with thermo-mechanical analysis inside the scratch of OXE-CHI-PUR network, these studies show that the repair mechanism is initiated by cationic OXE ring opening, followed by free radical PUA-to-PUR conversion combined with chair-to-boat conformational changes of the glycosine units of the CHI backbone. As a result of mechanical damage, formation of lower molecular weight fragments or oligomers results in the lower T_g values inside the scratch. However, upon UV irradiation, CHI chair-to-boat conformational changes trigger the intra and inter molecular crosslinking reactions resulting in -C-O-C- linkages which are initiated at the high surface energy areas inside the scratch, and propagate to the top accompanied by the mass transport from side banks of the damaged area. This process resembles frontal polymerization which is also driven by surface tension flow.²¹ As a result of UV-induced network remodeling, the T_g increases in the repaired area. These studies also show that the increased OXE-content within the OXE-CHI-PUR network decreases the time for self-repairing, whereas the presence of HALS retards self-repair.

In summary, these studies show for the first time the correlation between molecular processes and mass conservation as well as the role of each of the OXE-CHI-PUR network components on orchestrated self-repairing process.

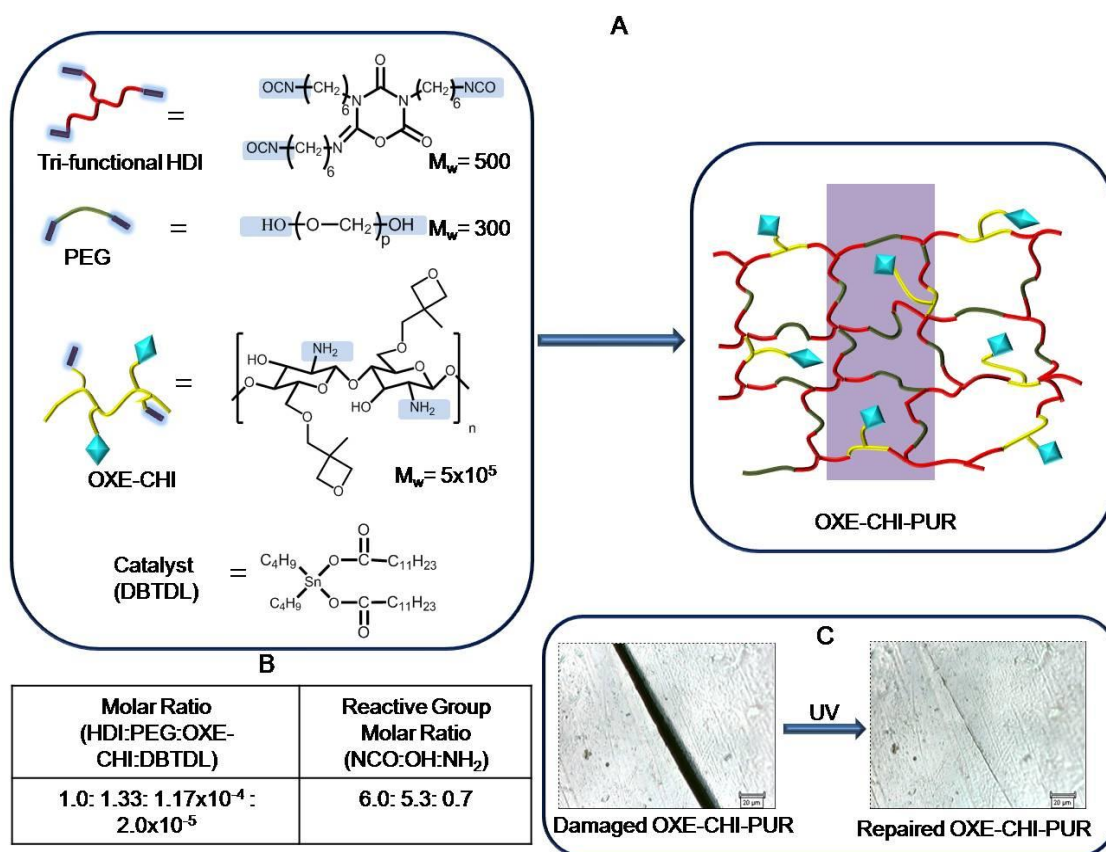


Figure 4.1. A) Synthesis of OXE-CHI-PUR networks, B) Molar ratios of network components and reactive groups of the reagents, and C) Optical images of damaged and repaired networks.

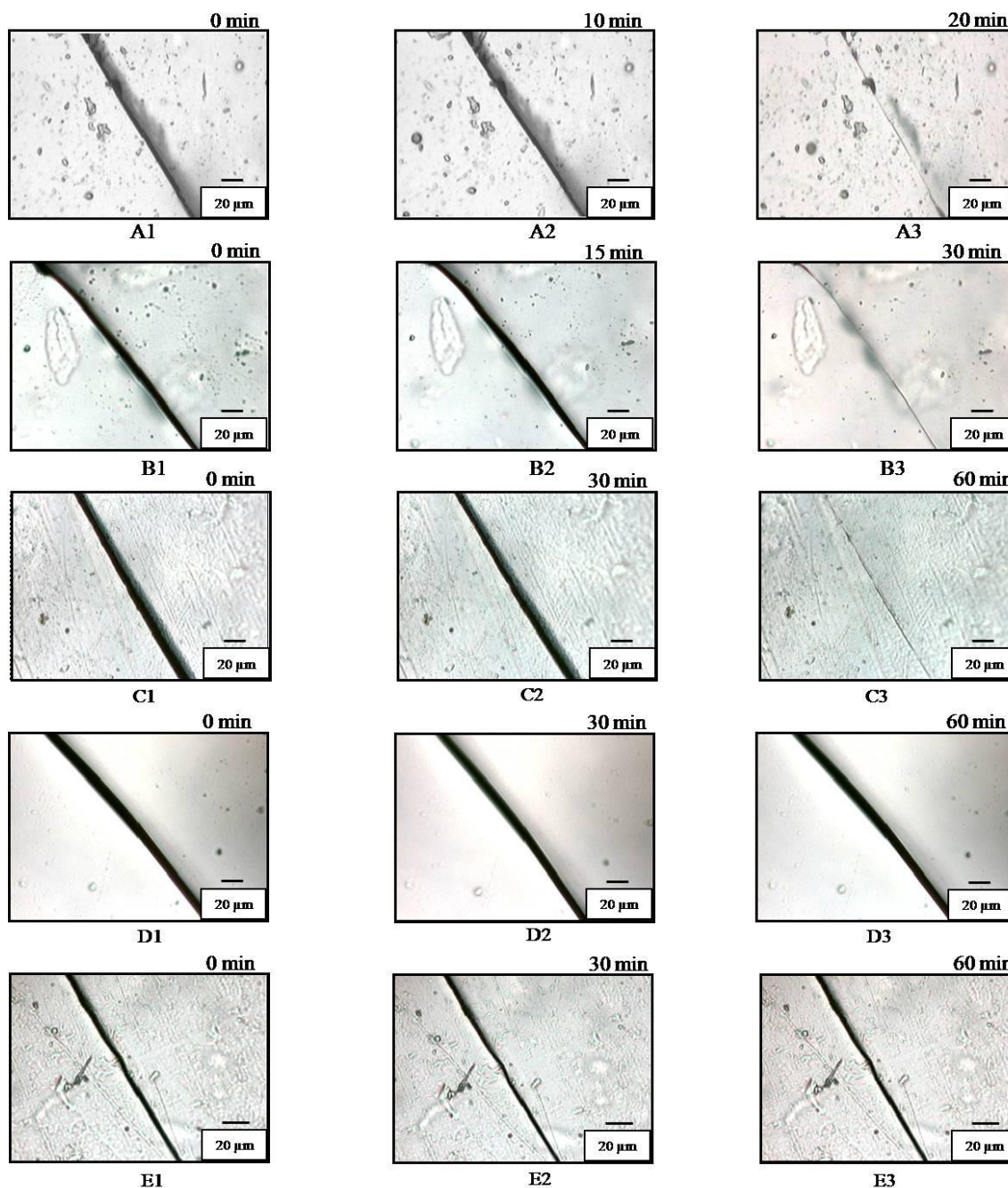
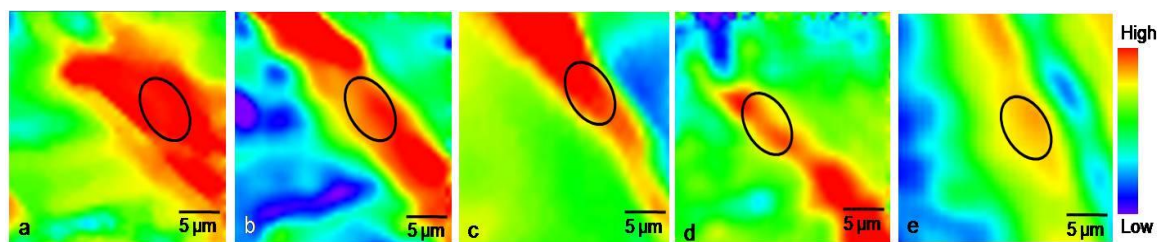
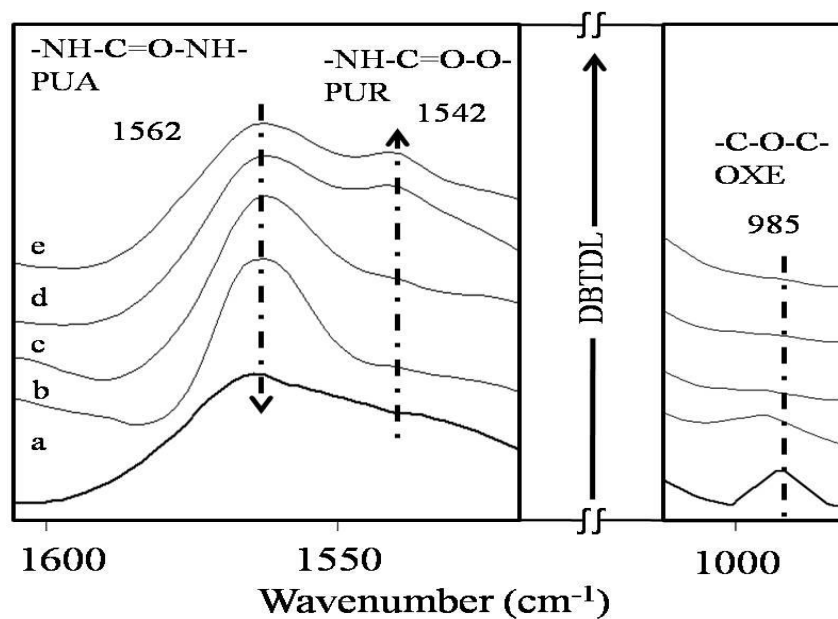


Figure 4.2. Optical images represent OXE-CHI-PUR networks (HDI:PEG:OXE-CHI:DBTDL=1.0:1.33:1.17 $\times 10^{-4}$:2 $\times 10^{-5}$) containing 1:1 (A1-A3), 1:4 (B1-B2), and 1:10 (C1-C3) molar OXE-CHI recorded as a UV exposure time. Optical images of PUR networks (D1-D3) recorded as a UV exposure time 0, 30, 60 min. Optical images of OXE-CHI-PUR networks (HDI:PEG:OXE-CHI:DBTDL=1.0:1.33:1.17 $\times 10^{-4}$:1 $\times 10^{-2}$) containing 1:1 molar OXE-CHI recorded as a UV exposure time 0, 30, 60 min (E1-E3).



A



B

Figure 4.3. IRIR images (A) and ATR-FTIR spectra (B) of OXE-CHI-PUR (HDI:PEG:OXE-CHI=1.0:1.33:1.17 $\times 10^{-4}$) networks containing a) 2×10^{-5} , b) 4×10^{-5} , c) 1×10^{-4} , d) 1×10^{-3} and e) 1×10^{-2} mole DBTDL.

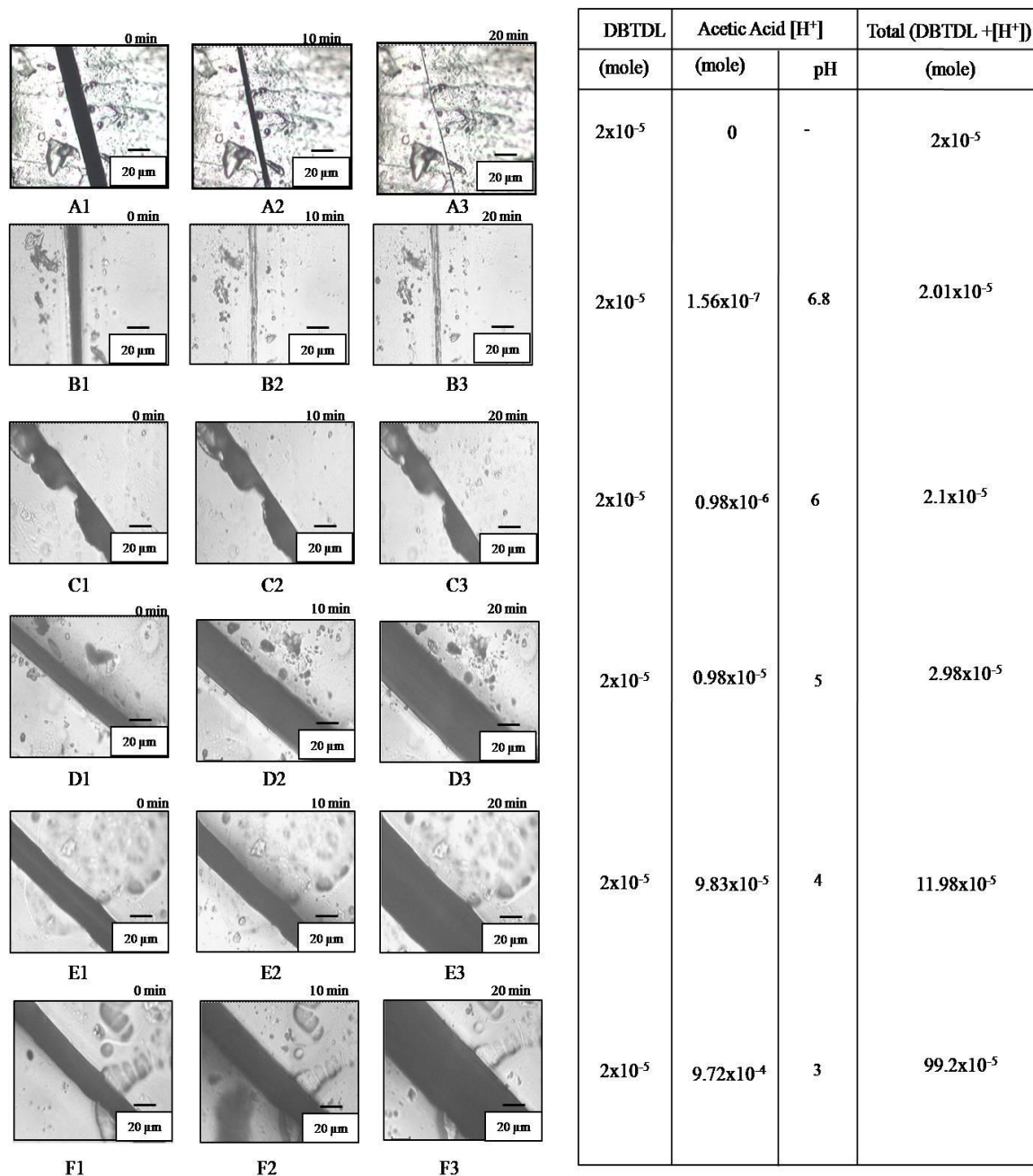


Figure 4.4. Optical images of OXE-CHI-PUR networks (HDI:PEG:OXE-CHI:DBTDL = 1.0:1.33:1.17x10⁻⁴:2x10⁻⁵) exposed to UV light without acidic environments (A1-A3), at pH=6.8 (B1-B3), 6 (C1-C3), 5 (D1-D3), 4 (E1-E3), 3 (F1-F3) and list of DBTDL, AA, and total proton concentration within the crack at various pH.

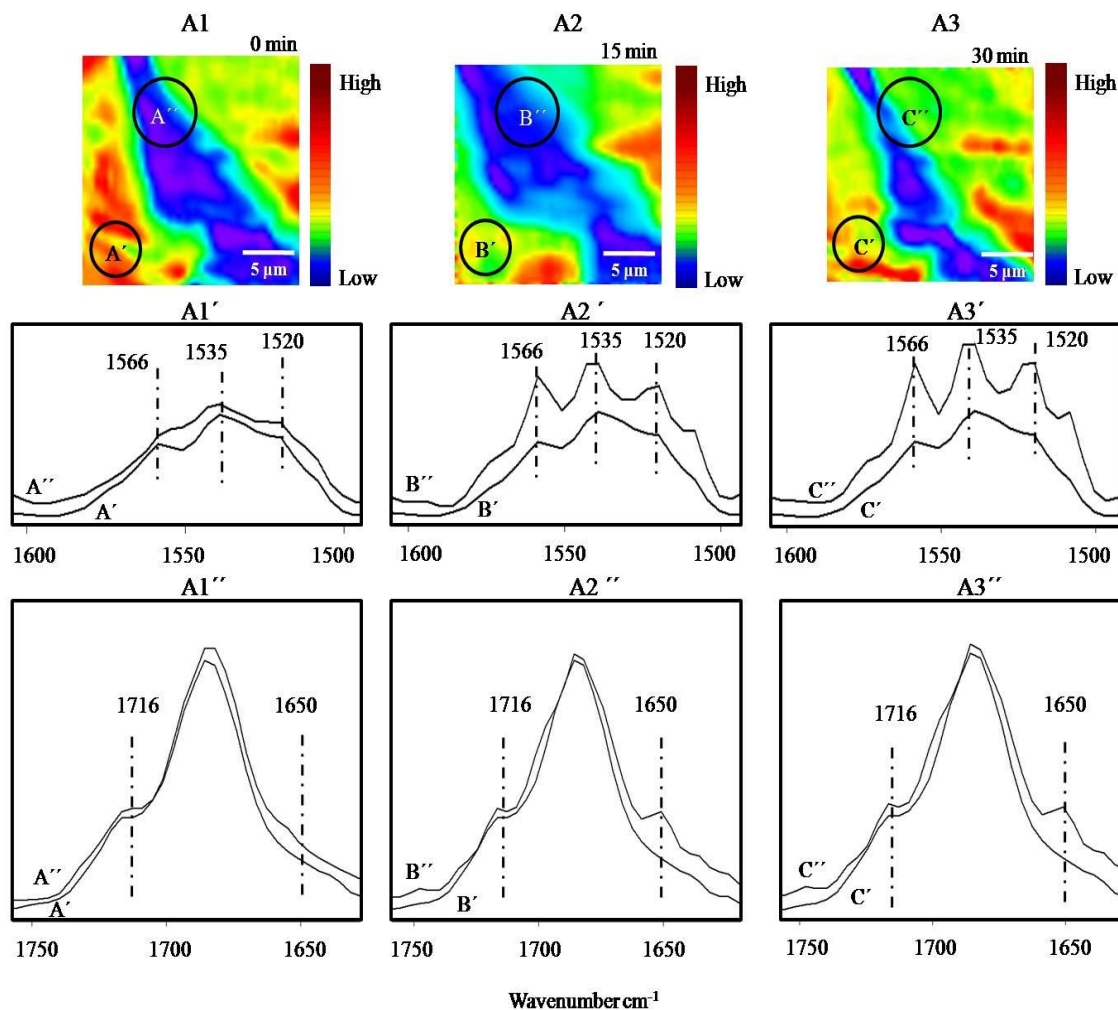


Figure 4.5. IRIRI images of OXE-CHI-PUR networks (HDI:PEG:OXE-CHI:DBTDL =1.0:1.33:1.17 $\times 10^{-4}$:2 $\times 10^{-5}$) containing 1:1 molar OXE-CHI at pH=3 recorded as a UV exposure time 0, 10, and 20 min, respectively. (A1-A3) images were obtained by tuning into the 1520 cm⁻¹ band; (A1'-A3', A1''-A3'') IR spectra recorded from mechanically damaged and undamaged areas.

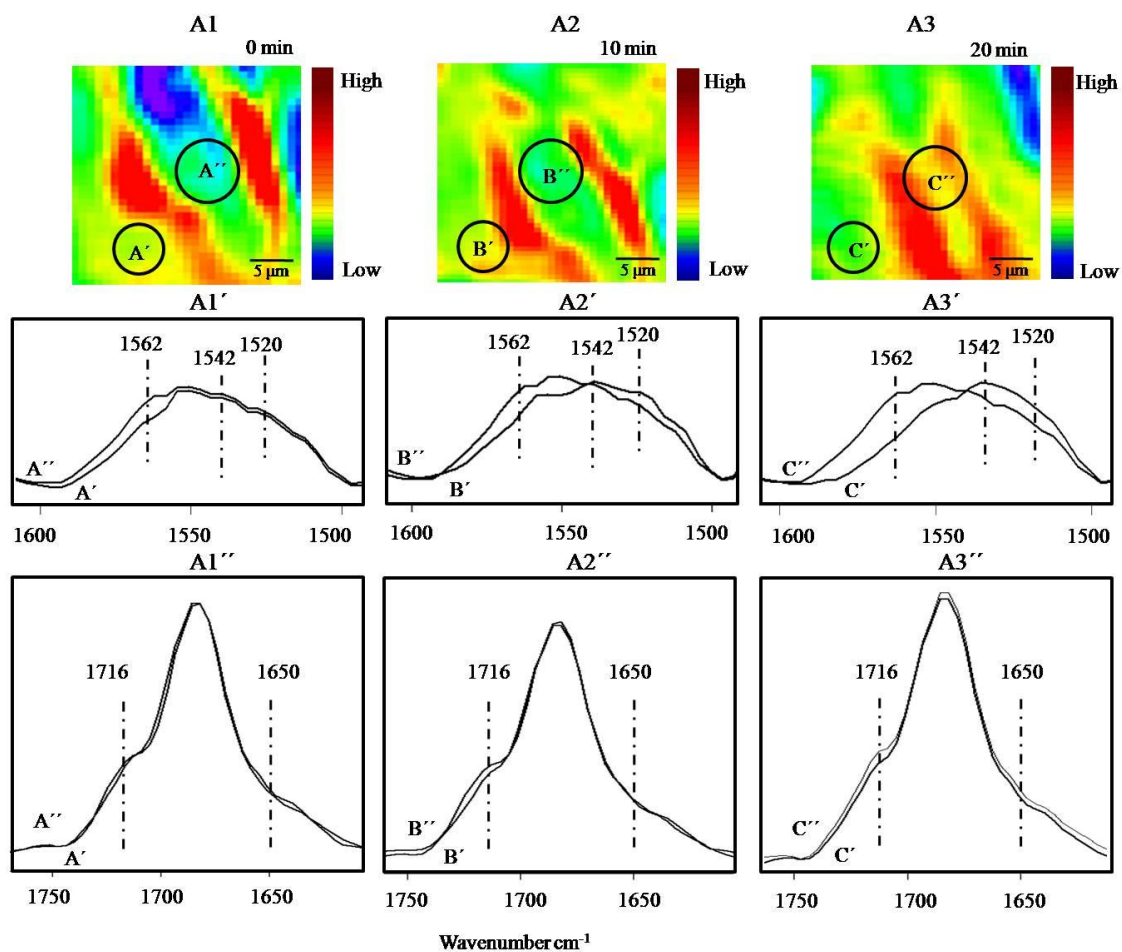
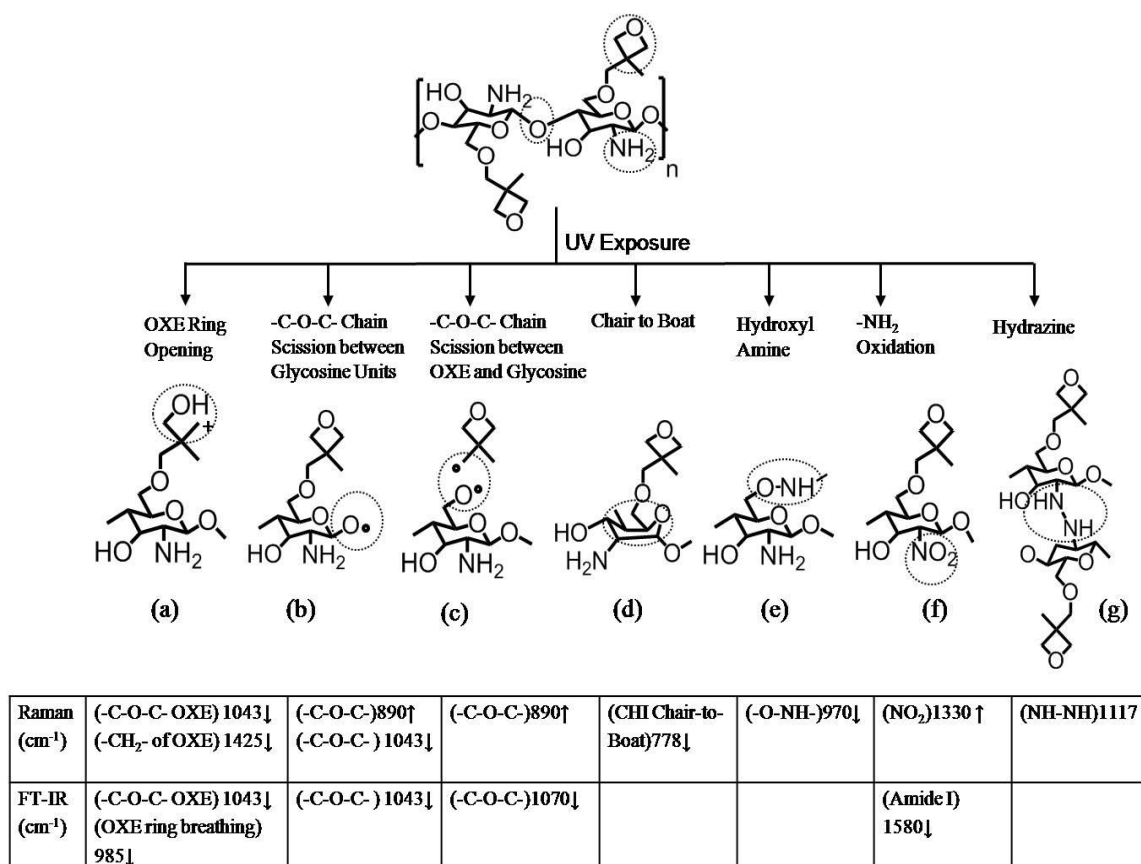


Figure 4.6. IRIRI images of OXE-CHI-PUR networks (HDI:PEG:OXE-CHI:DBTDL =1.0:1.33:1.17x10⁻⁴:2x10⁻⁵) containing 1:1 molar OXE-CHI at pH=6.8 recorded as a UV exposure time 0, 10, and 20 min, respectively. (A1-A3) images were obtained by tuning into the 1520 cm⁻¹ band; (A1'-A3', A1''-A3'') IR spectra recorded from mechanically damaged and undamaged areas.



↑↓ - arrows indicate intensity increase or decrease

Figure 4.7. Schematic diagram of reaction products and band assignments obtained from UV exposure of OXE-CHI. Spectroscopic data are presented in the supporting documents.

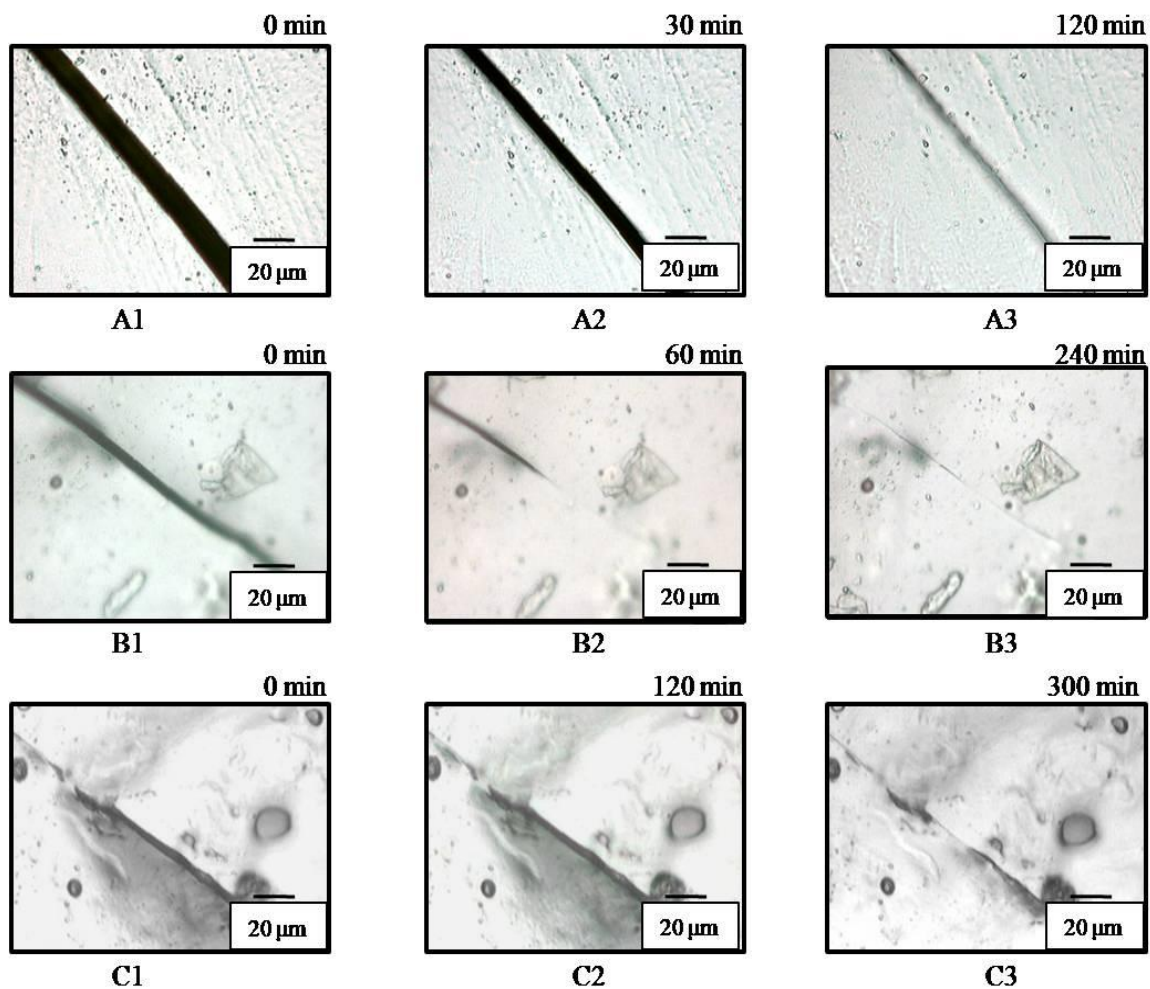


Figure 4.8. Optical images of OXE-CHI-PUR networks (HDI:PEG:OXE-CHI:DBTDL = 1.0:1.33:1.17 $\times 10^{-4}$:2 $\times 10^{-5}$) containing OXE-CHI of 1:1 (A1-A3), 1:4 (B1-B3), and 1:10 (C1-C3) molar ratios, respectively along with 1 % HALS in each network exposed to UV.

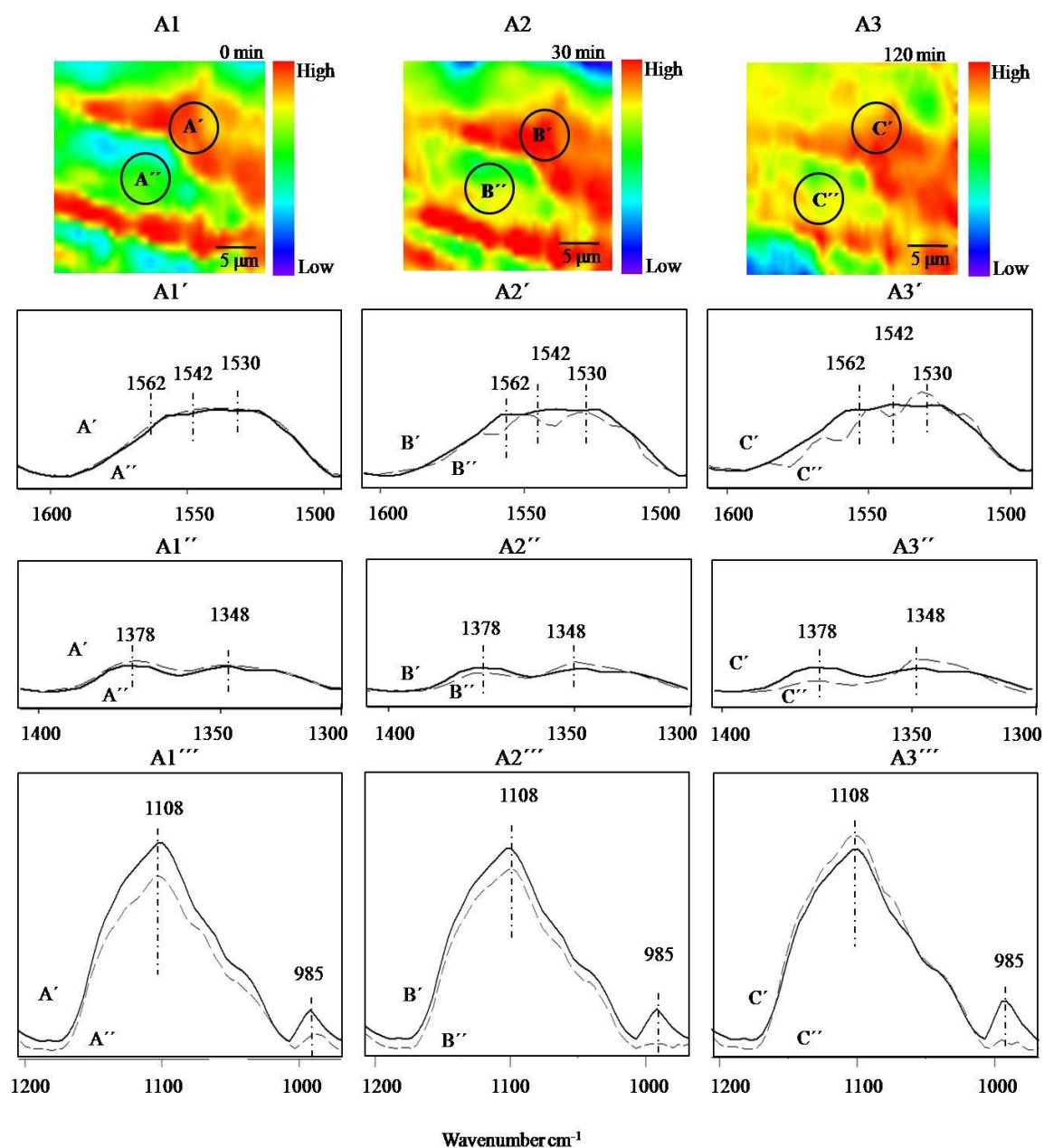


Figure 4.9. IRIRI images of OXE-CHI-PUR networks (HDI:PEG:OXE-CHI:DBTDL = 1.0:1.33:1.17 $\times 10^{-4}$:2 $\times 10^{-5}$) containing 1:1 molar OXE-CHI and 1% HALS recorded as a UV exposure time 0, 30, and 120 min, respectively. (A1-A3) images were obtained by tuning into the 1542 cm^{-1} band; (A1'-A3', A1''-A3'', A1'''-A3''') IR spectra recorded from mechanically damaged and undamaged areas.

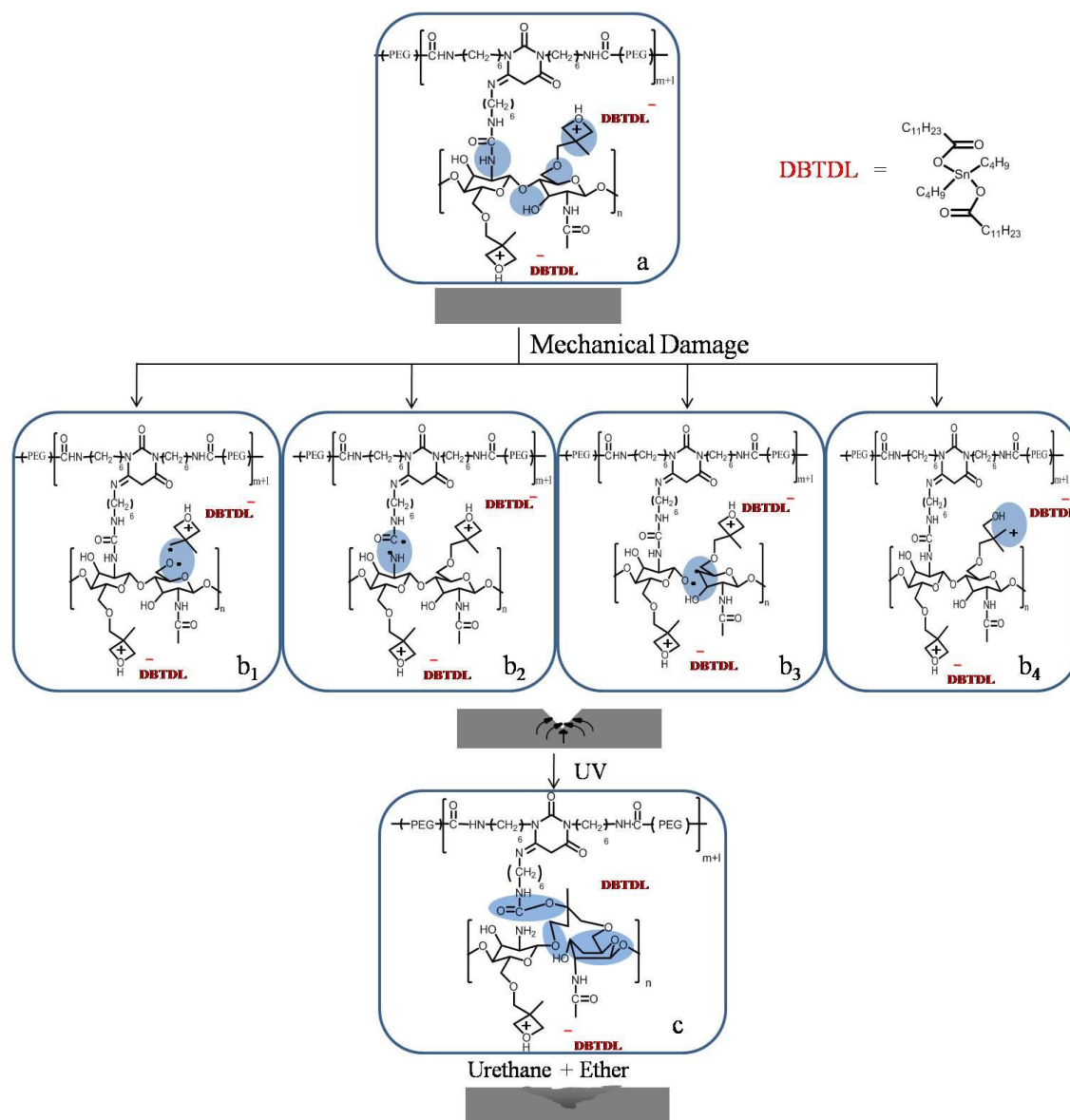


Figure 4.10. Proposed self-healing mechanism of OXE-CHI-PUR network under UV exposure.

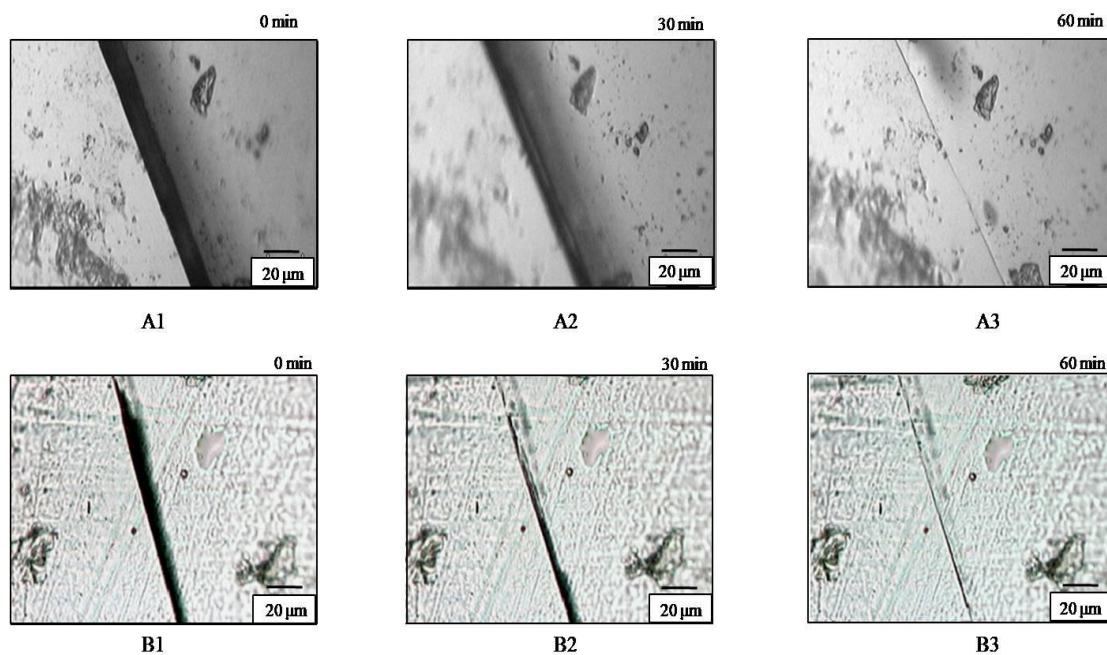


Figure 4.11. Repair of PUR network in the presence of external OXE-CHI in A) AA, and B) DMSO+DBTDL.

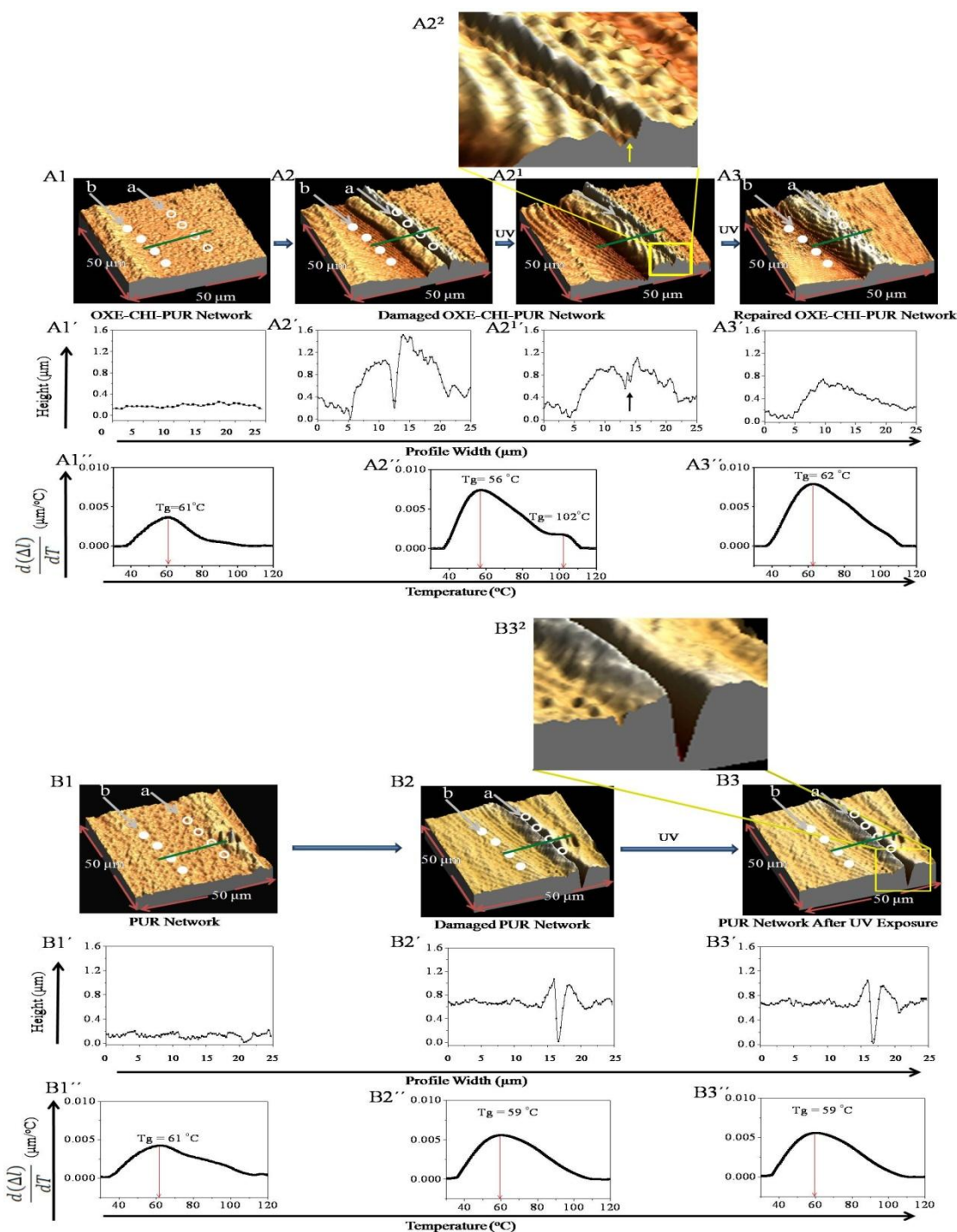


Figure 4.12. Atomic force microscopy (AFM) images of undamaged (A1), damaged (A2), UV-exposed (A2¹, A2²) and repaired (A3) OXE-CHI-PUR network (HDI:PEG:OXE-CHI:DBTDL = 1.0:1.33:1.17 × 10⁻⁴:2 × 10⁻⁵), and plot of height vs width profile of undamaged (A1'), damaged (A2'), UV exposed (A2¹') and repaired (A3') networks, and d(Δl)/dT vs temperature (A1''-A3'') for the same. AFM images of undamaged (B1), damaged (B2), and UV-exposed (B3, B3²) PUR network and plot of height vs width profile of undamaged (B1'), damaged (B2'), and UV-exposed (B3') networks, and d(Δl)/dT vs temperature (B1''-B3'') for the same.

References

1. Ghosh, B.; Urban, M. W. *Science*, **2009**, 323, 1458.
2. Rose, J. B. *J. Chem. Soc.* **1956**, 542.
3. Crivello, J. V. *Polymer*, **2005**, 46, 12109.
4. Pruckmayr, G.; Wu, T. K. *Macromolecules*, **1973**, 6, 33.
5. Crivello, J. V.; Faulk, B.; Zonca, M. R. *J. Polym. Sci. Polym. Chem. Part A*, **2004**, 42, 1630.
6. M.W. Urban, *Attenuated Total Reflectance Spectroscopy of Polymers; Theory and Applications* (American Chemical Society and Oxford University Press, Washington, DC, 1996)
7. Otts, D. B.; Zhang, P.; Urban, M. W. *Langmuir*, **2002**, 18, 6473.
8. Luo, S. –G.; Tan, H. –M.; Zhang, J. –G.; Wu, Y. –J.; Pei, D. –K.; Meng, X. –H. *J. Appl. Polym. Sc.* **1997**, 65, 1217.
9. Palaprat, G.; Ganachaud, F.; Mauzac, M.; Hemery, P. *Polymer*, **2005**, 46, 11213.
10. Kim, H.; Urban, M. W. *Langmuir* **2000**, 16, 5382.
11. Vuen, D. L.; Colthup, N. B.; Fateley, W. G.; Grasselli, J. G. *The Handbook of Infrared and Raman Characteristic Frequencies of Organic Molecules*, Academic Press, California, 1991.
12. Otts, D. B.; Pereira, K. J.; Jarret, W. L.; Urban, M. W. *Polymer*, **2006**, 46, 4776.
13. Pretsch E., B. P., Affolter C., *Structure Determination of Organic Compounds*. 3rd ed.; Springer: 2000.
14. Kubisa, P.; Penczek, S. *Prog. Polym. Sci.* **1999**, 24, 1409.
15. Boucekif, H.; Philbin, M. I.; Colclough, E.; Amass, A. J. *Macromolecules*, **2008**, 41, 1989.
16. Nakshio, M.; Kondo, M.; Tsuchita, H.; Yamada, M. *Makromol. Chem.*, **1962**, 52, 79.
17. Xu, J.; Zou, Y. F.; Pan, C. Y. *J. Macromol. Sci.- Pure Appl. Chem. A*, **2002**, 39, 431.
18. Skovstrup, S.; Hansen, S. G.; Skrydstrup, T.; Schiott, B. *Biomacromolecules*, **2010**, 11, 3196.

19. Chen, R. H.; Tsaih, M. L. *J. Appl. Polym. Sci.* **2000**, 75, 452.
20. Washington, R. P.; Steinbock, O. *J. Am. Chem. Soc.* **2001**, 123, 7933.
21. Pojman, J. A.; Ilyashenko, V. M.; Khan, A. M. *J. Chem. Soc., Faraday Trans.*, **1996**, 92, 2825.
22. Step, E. N.; Turro, N. J. *Macromolecules*, **1994**, 27, 2529.
23. Sung, L. P.; Comer, J.; Forster, A. M.; Hu, Haiqing, H.; Floryancic, B.; Brickweg, L.; Fernando, R. H. *Nanotechnology Applications in Coatings*, ACS Symposium Series, 2009.
24. Bonn, D.; Kellay, H.; Prochnow, M.; Djemiaa, K.B.; Meunier, J. *Science*, **1998**, 280, 265.
25. Fox, T. G.; Flory, P. J. *J. Appl. Phys.* **1950**, 21, 581.
26. Priestley, R. D.; Ellison, C.J.; Broadbelt, L.J.; Torkelson, J.M. *Science*, **2005**, 309, 456.
27. Chen, T. K.; Chui, J. Y.; Shieh, T. S. *Macromolecules*, **1997**, 30, 5068.
28. Fragiadakis, D.; Gamache, R.; Bogoslovov, R. B.; Roland, C. M. *Polymer*, **2010**, 51, 178.

CHAPTER V

THE INFLUENCE OF RING STRENGTH ON THE SELF-REPAIRING OF CHITOSAN-SUBSTITUTED POLYURETHANE NETWORKS

Introduction

Polyurethanes (PUR) are widely known for their heterogeneous nature and presence of different soft and hard blocks within the network along with urethane/urea rich domains allow easy control over fine tuning of their chemical and physical properties. Along the same line, recent studies showed that various biomaterials like unmodified/ modified chitosan, alginate, and cellulose can be easily incorporated within PUR network via chemical or physical processes by maintaining proper stoichiometric ratios of different components. In a typical UV-induced self-repairable oxetane-substituted chitosan polyurethane (OXE-CHI-PUR) network reported recently,¹ self-repairing kinetics can be controlled by utilizing different stoichiometric ratios of the chemical entities within the network. The chemical nature of the self-repairing reactions mainly consist of cationic ring opening as well as free radical polyurea-to polyurethane (PUA-to-PUR) conversion reactions. While the increased OXE content within the network decreases the duration of repair process and mild acidic environments (pH=6.8) are sufficient for ring opening, dormant oxonium ions remain unaffected until they are activated by mechanical damage followed by UV exposure. It is well established that the ring opening kinetics depend on the ring strain, 4-member OXE, $E=107$ kJ/mole; 5-member OXO, $E=23$ kJ/mole,² incorporation of OXO ring within PUR network instead of OXE ring is of particular interest. The fundamental questions to be addressed are as follows: (a) can OXO ring incorporated into CHI macromonomer facilitate self-repair

process in polyurethanes and (b) what is the role of OXO ring in mechanisms of OXO-CHI-PUR repair. In order to address the effect of ring strain on the kinetics of the self-repairing process as well as the chemical nature of the processes involved in these studies focus on the synthesis of OXO-CHI macromonomer with variable stoichiometric molar ratios (OXO-CHI=1:1, 1:4, 1:10) and followed by their incorporation within PUR network in order to design a controlled self-repairing networks. An ultimate goal of these studies is to correlate mechanistic aspects of chemical reactions involved in repair processes and correlate them with mechanical network rearrangement during UV exposure.

Experimental

Tri-functional homopolymer of hexamethylene diisocyanate (HDI) (Desmodur XP 2410) was obtained Bayer Material Science. Tetrahydro-furfuryl chloride (OXO-Cl) was purchased from TCI America. Chitosan (CHI) (degree of deacetylation 75-85%, $M_n \sim 5 \times 10^5$), methanol, polyethylene glycol ($M_w=300$), sodium hydroxide beads, acetone, dibutyltin dilaurate (DBTDL), dimethyl sulfoxide (DMSO), were purchased from Sigma Aldrich Co. Hindered amine light stabilizer (HALS) TINUVIN P was supplied by Ciba Chemicals. All chemicals were used as received except PEG which was heated upto 80 °C for 2 h in vacuum under N_2 atmosphere to remove any trace of moisture in it. CHI (2 g) was added into a 1(N) NaOH solution (150 g) in a three-neck flask and stirred for 24 h at -5 °C, followed by refrigeration at -18 °C for 48 h. Such solution was thawed and mixed with pre-cooled isopropyl alcohol and stirred for 1 h. Pre-cooled OXO-Cl was added to the mixture, the temperature was raised to 80 °C and the solution was stirred for

12 h. The product was filtered and washed several times with methanol until it became neutral, followed by drying it at 60 °C for 12 h.

In order to synthesize OXO-CHI-PUR networks (Figure C.1), OXO-CHI product was dispersed in DMSO by sonicating it at 25 °C for 12 h, followed by continuous stirring at 80 °C for 48 h. Next, tri-functional HDI was mixed in a 50ml three-neck reaction flask at 25 °C under N₂ atmosphere with dispersed OXO-CHI, PEG and DBTDL using overhead agitation at 500 rpm for 10 min. Using this procedure, polyurethane networks with the relative molar equivalent ratios of NCO, PEG and OXO-CHI were varied from 1:1.5:0 to 1:1.33:1.17x 10⁻⁴, while maintaining 38% (w/w) solids. FT-IR (Figure C.2) and ¹³C NMR (Figure C.3) were utilized to confirm covalent attachment of OXO ring in the backbone of CHI.

Three different molar ratios of OXO-CHI (1:1, 1:4, and 1:10) were introduced within the PUR networks to prepare model systems. Similarly, OXO-CHI-PUR networks containing 1 % w/w HALS were synthesized by dissolving HALS (TINUVIN P) within DMSO, followed by the addition of OXO-CHI macromonomer and HDI. Again, following the same route, a series of OXO-CHI-PUR networks were synthesized containing 2x10⁻⁵, 4x10⁻⁵, 1x10⁻⁴, 1x10⁻³ 1x10⁻² molar DBTDL.

Following the mixing process, such mixture was applied to obtain approx. 250 µm (±4 µm) thick films on a PTFE substrate at room temperature under 15 % relative humidity (RH) for 12 h in a vacuum oven followed by 80 °C for 48 h. A razor blade was utilized to mechanically damage the films to obtain a desired width and depth of the

damage. UV exposures of the films were conducted using a 120 W UV lamp of 302 nm wavelength of light.

For the purpose of these studies, acetic acid solutions at pH=3, 4, 5, 6, and 6.8 were prepared. OXO-CHI-PUR networks were mechanically damaged and each pH solution was injected into the crack using a 5 mL syringe followed by UV exposure.

Microscopic micro attenuated total reflectance Fourier transform infrared (μ ATR FT-IR) spectrum were obtained using a Bio-Rad FTS-6000 FTIR single-beam spectrometer setting at 4 cm^{-1} resolution. A 2 mm Ge crystal, with a 45° face angle maintaining constant contact pressure between crystal and the film specimens was used. All IR spectra were corrected for spectral distortions and optical effects using Urban-Huang algorithm.³ OXO-CHI powder was analyzed by diffuse reflectance Fourier transfer infrared (DRIFT). In a typical experiment 100 scans were collected. Each spectrum of film represents 100 co-added scans ratioed to 100 reference scans collected using an empty attenuated total reflectance (ATR) cell, whereas for DRIFT the number is 500.

FT-Raman spectra were measured using an IFS 55/FRA 106 FT-IR/Raman spectrometer (Bruker Instruments, Inc.). As an excitation source, a diode pumped Nd:YAG laser was used to provide a maximum power of 500 mW at the sampling area. WIRE 2.0 software (Bruker Instruments, Inc.), and GRAM were used to analyze spectra.

Internal reflection infrared (IRIR) images were obtained using a Bio-Rad FTS 7000 Stingray system equipped with internal reflection IR imaging (IRIRI) providing 1 micron spatial resolution. This system consists of a Bio-Rad FTS 7000 spectrometer, a

Varian 600 UMA microscope, an Image IR focal plane array (FPA) image detector, and IRIRI. The IR images were collected using the following spectral acquisition parameters: under sampling ratio 2, rapid-scan speed 5 Hz, number of images per step 64, and spectral resolution 4 cm^{-1} . In a typical experiment, spectral data set acquisition time was 1 min and image processing was performed using ENVI software (The Environment for Visualizing Images, Research Systems, Inc.) version 3.5.

Solid-state ^{13}C NMR measurements were performed on a Varian ^{UNIT}YINNOVA 400 spectrometer using a standard Chemagnetics 7.5 mm PENCIL-style probe. Samples were loaded into zirconia rotor sleeves, sealed with Teflon caps, and spun at a rate of 4.5 kHz. The standard cross-polarization magic angle spinning (CP/MAS) technique was used with a high-power proton decoupling implemented during data acquisition. The acquisition parameters were as follows: ^1H 90° pulse widths was $4.0\text{ }\mu\text{s}$, the cross-polarization contact time was $1\text{ }\mu\text{s}$, the dead time delay of 3 s between scans was utilized.

Localized thermo-mechanical analysis was conducted using a microthermal analyzer model (μTA) 2990 (TA Instruments) equipped with a $5\text{ }\mu\text{m}$ Wollaston thermal tip calibrated with biphenyl (melting point= 69°C), anisic acid (melting point= 183°C), and polyethylene terephthalate (melting point= 245°C). In a typical experiment, the displacement of the thermo-couple tip was monitored as the tip temperature was raised from 30 to 120°C at a heating rate of 10°C/s with an accuracy of $(\pm)1^\circ\text{C}$. The tip displacements $d(\Delta l/T)$ at a given temperature (T) illustrate the thermal network expansion changes as a function of temperature and were obtained by taking the first derivative of the displacement values (Δl vs T), and were normalized with respect to their initial values.

Results and Discussion

Figure 5.1, A1-A3, B1-B3, and C1-C3, illustrates optical images of OXO-CHI-PUR self-repair as a function of UV exposure time for 1:1, 1:4 and 1:10 OXO-CHI stoichiometries, respectively. As seen, the repair process of OXO-CHI-PUR is slowed down as the OXO-CHI molar ratios decreases from 1:1 to 1:4 (Figure 5.1, A1-A3, and B1-B3, respectively) and further decrease of OXO-CHI molar ratios to 1:10 does not result in self-repair. Compare to a 4-membered OXE ring in OXE-CHI-PUR networks,¹ the time required to repair damaged OXO-CHI-PUR networks are considerably higher. For reference, Figure 5.1, D1-D3 shows optical images of OXO-CHI-PUR network containing 1×10^{-4} molar DBTDL which does not exhibit self-repairing under UV exposure.

To assess response of OXO-CHI-PUR networks at microscopic scale, micro-thermal analysis was carried out. Figure 5.2 illustrates AFM images of the undamaged (A1), damaged (A2), UV-exposed ($A2^1$, $A2^2$) and repaired (A3) OXO-CHI-PUR network. The closed (a) and open (b) circles in Figure 5.2, A1-A3 show the data collection points of thermo-mechanical response, where closed circles (line a) represent undamaged areas, and open circles (line b) represent mechanical damage and UV induced repair areas. Surface topography changes of the network during repair process are illustrated in Figure 5.2, A1', A2', $A2^{1'}$ and A3', and show the heights of the surface plotted as a function of the displacement perpendicular to the damaged area (marked by a solid green line in Figure 5.2, A1, A2, $A2^1$, A3). As shown in Figure 5.2, A1', the undamaged surface of the network exhibits uniform heights over the surface, but mechanical damage of the network leads to the formation of damaged area along with

side banks (Figure 5.2, A2, and A2'). However, upon UV exposure, the heights of the side banks decrease (Figure 5.2, A2^{1'}), and shows upward growth inside the scratch from the bottom, as shown in the Figure 5.2, A2². These observations are in agreement with the support our previous studies in which thermo-mechanical response of self-repairing OXE-CHI-PUR networks, also showed mass flow towards the damaged area, and at the same, time frontal growth from the bottom of the scratch (Figure 5.2, A3').

Previous studies have also shown that micro-thermal analysis can be utilized to measure thermal expansion changes $d(\Delta l)$ inside the scratch by measuring of normalized $d(\Delta l)/dT$ as a function of temperature (T).⁴ As seen, Figure 5.2, A1'', A2'', and A3'' represents normalized $d(\Delta l)/dT$ values for undamaged, damaged, and self-repair areas plotted as a function of temperature, respectively. The maximum values of $d(\Delta l)/dT$ correspond to the T_g of the undamaged network is detected at 50 °C before damage, but . lower T_g inside the scratch at 47 °C (Figure 5.2, A2'') is observed, which increases to 51 °C in the repaired area (Figure 5.2, A3'') under UV exposure. Similarly, thermal expansion of the OXO-CHI-PUR networks (OXO-CHI= 1:4, and 1:10 molar ratios) within the damaged area were monitored as a function of temperature. As shown in the Supporting Documents (Figure C.4), the T_g values in the damaged area of OXO-CHI-PUR networks containing OXO-CHI of 1:4, and 1:10 molar ratios decrease to 47 and 46 °C, respectively, but upon UV exposure increase to 50 °C.

The next question is what molecular processes are responsible for self-repairing of OXO-CHI-PUR networks. Since IRIR imaging allows us to tune into a specific IR bands associated with a given species, the next step in this investigation is to determine distribution of OXO-CHI entities within the networks and following molecular events

responsible for self-healing. Images A1, A2, and A3 in Figure 5.3 represent distribution of these species in the undamaged (A') and damaged (A'') areas as a function of time, whereas spectral changes recorded from these areas in the $1650\text{-}1450\text{ cm}^{-1}$, $1450\text{-}1250\text{ cm}^{-1}$, and $1250\text{-}950\text{ cm}^{-1}$ are shown in Figures 5.3, A1'-A1''', A2'-A2''', and A3'-A3'''. These spectra represent band intensity changes of species participating in the repair process.

We tuned into the 1545 cm^{-1} band due to N-H bending of PUR, and Figure 5.3, A1-A3, represents three images recorded after UV exposure of OXO-CHI-PUR networks (OXO-CHI=1:1) for 0, 30, and 60 min, respectively. The damaged area (A'') shows lower concentration levels of the N-H, whereas the area A' away from the damage exhibits higher concentrations of these species. The corresponding spectra shown in Figure 5.3, A1' obtained from the areas A' and A'' confirms that the band intensities of the following vibrations change: decrease of 1562 , 1326 , and 1105 cm^{-1} bands of -NH-CO-NH- stretching vibrations of urea linkage, $\text{-CH}_2\text{-}$ deformation modes of OXO, and -C-O-C- stretching vibrations of OXO-CHI, respectively.^{1,5-7} The images recorded from the networks exposed to UV radiation for 30 and 60 min are shown in Figure 5.3, A2 and A3, respectively. Figure 5.3, A2'-A2''' and A3'-A3''' illustrate that as the scratch is exposed to UV, the urea linkage represented by the band at 1562 cm^{-1} shifts to 1545 cm^{-1} corresponding to urethane linkage, whereas the ring opening of OXO results in the decrease of the band intensities at 1326 cm^{-1} . The increase of the band intensities at 1105 , and 1046 cm^{-1} in the damaged area A'' in A1 and A2 indicate formation of -C-O-C- bonds of linear aliphatic ether. Similar analysis shown in Figure 5.4 was performed by tuning into the 1545 cm^{-1} band for OXO-CHI-PUR networks containing 1:4 molar

OXO-CHI. As shown in Figure 5.4, A1'-A1''', A2'-A2''', and A3'-A3''', intensities of the 1562, 1326 cm^{-1} bands decreases whereas the 1545, 1105, and 1046 cm^{-1} bands increase upon UV exposure. OXO-CHI-PUR network containing 1:10 molar OXO-CHI does not self-repair upon UV exposure for 120 min and the corresponding IRIR images are shown in Figure 5.5. As shown in Figure 5.5, A1'-A1''', mechanical damage of the network resulting decrease in 1562, 1105 cm^{-1} band intensities. Upon UV exposure, 1326 cm^{-1} band corresponding to $-\text{CH}_2-$ deformation modes of OXO decreases along with smaller increase in 1105 cm^{-1} band corresponding to $-\text{C}-\text{O}-\text{C}-$ linkages, but band intensities at 1562 and 1545 cm^{-1} corresponding to PUA and PUR linkages, respectively do not change. These observations indicate that OXO ring in 1:10 OXO-CHI is not sufficient to convert PUA-to-PUR and a new $-\text{C}-\text{O}-\text{C}-$ crosslink formation, therefore unable to self-repair the network. Compared to OXE-CHI-PUR networks, OXO-CHI-PUR networks show slower self-repairing kinetics and require higher OXO stoichiometry within the network to repair the damaged network.

At this point it is also important to realize the role of DBTDL in the self-repair process. For that reason, we incorporated 2×10^{-5} , 4×10^{-5} , 1×10^{-4} , 1×10^{-3} and 1×10^{-2} moles of DBTDL into OXO-CHI-PUR (OXO-CHI=1:1) which were mechanically damaged and exposed to UV to facilitate self-repair process. As shown in Figure 5.6, A1-A3, when DBTDL concentration is below 4×10^{-5} mole OXO-CHI-PUR network (Figure 5.1, A1-A3) exhibits self-repair behavior, whereas above 1×10^{-4} level inhibits this process (Figure 5.1, D1-D3). Again, we utilized IRIR imaging to identify spectroscopic changes inside the scratch of OXO-CHI-PUR network as a function of DBTDL concentration by tuning to the 1562 cm^{-1} band due to $-\text{NH}-\text{CO}-\text{NH}-$ stretching vibrations of PUA. Figure 5.6-A

illustrates a spatial distribution of the 1562 cm^{-1} band for OXO-CHI-PUR containing 2×10^{-5} (a), 4×10^{-5} (b), 1×10^{-4} (c), 1×10^{-3} (d), and 1×10^{-2} (e) moles of DBTDL, and Traces a-e of Figure 5.6-B are the FT-IR spectra collected from circled areas in the images a-e of Figure 5.6-A of OXO-CHI-PUR. Figure 5.6-B shows that when the DBTDL concentration increases, the band at 1046 and 1030 cm^{-1} due to linear -C-O-C- linkages of linear aliphatic ether, and out-of-plane 1° -OH increases which indicate OXO ring opening. On the other hand, a new band appears at 1085 cm^{-1} corresponding to cyclic equatorial 2° -OH when the concentration of DBTDL is more than 1×10^{-4} mole. These results combined with the results of macroscopic data shown in Figure 5.1, A1-A3, indicate that OXO-CHI-PUR network self-repair process occurs when DBTDL concentration is below 1×10^{-3} mole and previous studies have shown that in OXE-CHI-PUR networks, DBTDL catalyses HDI and PEG crosslinking reactions and follow cationic route, and an excess of DBTDL to OXE ring ratio result in protonation, generating oxonium ions.¹ This study also indicates that in the presence of excess DBTDL within the OXO-CHI-PUR network OXO rings open up, suggesting that cationic route is favorable for OXO ring opening.

To further examine the effect of protic environments on OXO ring opening as well as self-repairing process we conducted a series of experiments in which acidic acid (AA) solution was introduced into mechanically generated scratch of OXO-CHI-PUR (HDI:PEG:OXO-CHI=1.0:1.33:1.17 $\times 10^{-4}$) network. Figure 5.7, A1-A3, B1-B3, C1-C3, and D1-D3, shows optical images of mechanically damaged OXO-CHI-PUR films in which scratches were filled with AA solutions at pH=6 (A1-A3), 5 (B1-B3), 4 (C1-C3), and 3 (D1-D3). As seen, when AA is not added, self-repair occurs (Figure 5.1, A1-A3),

and the addition of AA of pH=6, still shows repair (Figure 5.7, A1-A3). However, when the pH decreases to 5, the repair process is stopped, as indicated by unchanging width of the scratch (Figure 5.7, B1-B3). Furthermore, as shown in Figure 5.7, C1-C3 and D1-D3 when the pH values of the added AA were further decreased to 4, and 3, the scratch expanded. .

In order to understand the molecular processes and the role of protic environments responsible for expansion (pH=3-5) and self-healing (pH=6) of OXO-CHI-PUR network we conducted IRIRI experiments and tuned into the 1520 cm^{-1} band of the C=O stretching vibrations of carbamic acid⁸ and monitored its intensity change as a function of UV exposure. As shown in Figure 5.8, Images A1, A2, and A3 illustrate the distribution of OXO-CHI species in the areas labeled A'/A'', (un-damaged/damaged area) for pH=3, and spectroscopic changes are shown in Figure 5.8, A1'-A3', A1''- A3'' in the 1500-1600, and 1600-1750 cm^{-1} regions. As seen, at pH=3 when the scratch is exposed to UV for 30 min, intensities of 1566, 1535, and 1520 cm^{-1} bands corresponding to $\text{-NH}_2^+\text{CO}_2^-$ increase and intensity of 1650 cm^{-1} band corresponding to -NH_2^+ vibrations also increase indicating protonation of PUA under acidic conditions.^{6,8} This process continues as the OXO-CHI-PUR network is further exposed to UV for 60 min (Figure 5.8, A1''-A3''). As reported earlier, PUA linkages of the OXO-CHI-PUR network are converted to carbamic acid in acidic environments, resulting in the expansion of the scratch due to the loss of CO_2 .

On the other hand, when AA of pH=6 was added to the same scratch, the 1520 cm^{-1} band corresponding to carbamic acid is not detected as illustrated in Figure 5.9, A1'-A3'. However, the 1545 cm^{-1} band corresponding to -NH-CO-O- stretching

vibration of PUR increases, signifying PUA-to-PUR conversion. The same observations were detected in Figure 5.3, A1'-A3' for OXO-CHI-PUR networks in absence of AA. On the other hand, unchanged 1650 cm^{-1} band intensity indicates no protonation of PUR or PUA linkages. These studies indicate that due to the lower ring strain of OXO compare to OXE, it requires higher acidic environment (pH=6) for ring opening during self-repairing of the network.

To further determine whether free radical processes parallel OXO ring opening in OXO-CHI-PUR networks we introduced 1% w/w hindered amine light stabilizers⁹ (HALS) within the network. Optical images in Figure 5.10, A1-A3, B1-B3, and C1-C3, show a progression of OXO-CHI-PUR network repair upon UV exposure containing 1:1, 1:4, and 1:10 OXO-CHI molar ratios and 1% w/w HALS, respectively. As seen, incorporation of HALS increases the time required for the repair process from 60, and 90 min (Figure 5.1, A1-A3, and B1-B3) for OXO-CHI-PUR containing OXO-CHI of 1:1, 1:4 molar ratios, respectively, to 300, and 360 min (Figure 5.10, A1-A3, B1-B3). Although, OXO-CHI-PUR containing OXO-CHI of 1:10 molar ratios does not exhibit self-repairing in presence of 1% w/w HALS within this time frame. In order to investigate the molecular process responsible for slower kinetics, IRIR imaging was employed and Figure 5.11, A1, A2, and A3, illustrates IR images of OXO-CHI-PUR (OXO-CHI=1:1) recorded after UV exposure for 0, 120 and 300 min, respectively and 11, A1'-A3', and A1''-A3'' illustrate the corresponding spectra recorded from undamaged (A') and damaged (A'') areas. As shown in Figure 5.11, A1'-A1'', band intensities at 1105 , and 1562 cm^{-1} due to -C-O-C- and -NH-CO-NH- stretching vibrations decrease and upon exposure to UV for 120 min, intensities of the 1562 cm^{-1}

band decreases significantly, whereas the intensity of the 1542, 1105, and 1046 cm^{-1} bands increase (Figure 5.11, A2', and A2''). These observations illustrate that HALS interference in PUA-to-PUR conversion reaction by slowing down the kinetics of repair process, therefore signifying free radical nature of this reaction, which continues upon further exposure to UV for 300 min (Figure 5.11, A3',A3''). IRIR imaging experiments conducted on OXO-CHI-PUR networks containing 1:4 OXO-CHI molar ratios and 1 % w/w HALS are shown in Figure 5.12. As seen in Figure 5.12, A1'-A2'', mechanical damage resulting in the decrease of the band intensities at 1562, 1105 cm^{-1} corresponding to $-\text{NH}-\text{CO}-\text{NH}-$ and $-\text{C}-\text{O}-\text{C}-$ stretching vibrations of PUA and OXO-CHI/CHI-CHI, respectively. Upon UV exposure for 240 min, the intensity of 1562 cm^{-1} band decreases, whereas the intensities of the 1545 and 1046 cm^{-1} bands increase. Further exposure to UV for 360 min result in the increase of the 1545, 1105, and 1046 cm^{-1} bands, indicating slower self-repairing kinetics of the network as free radicals required for PUA-to-PUR conversion are scavenged by HALS.

In order to examine the sensitivity of OXO rings to UV exposure, we conducted a series of model experiments in which we spectroscopically monitored chemical changes of OXO-CHI macromonomers of following molar ratios: 1:1, 1:4, and 1:10, before and after UV exposure. Raman and FT-IR spectra recorded before and after each exposure are shown in Figures C.5-C.7 and C.8-C.10, whereas the intensity changes of the vibrational bands sensitive to UV exposure are listed in Table C.1, and C.2 of Supporting Documents, respectively. Figure C.11 summarizes the reactions resulting from UV exposure and the reactions relevant for OXO-CHI-PUR repair process are OXO ring

opening, chain scission of the –C-O-C- segments of OXO- CHI and CHI-CHI and chair-to-boat conformational changes of pyranose units of CHI.

Combining the spectroscopic results of model experiments along with the DBTDL, AA and HALS effects on self-repairing kinetics of OXO-CHI-PUR networks Figure 5.13 illustrates the self-repairing mechanism of OXO-CHI-PUR networks. As seen in Figure 5.13-a, the linkages that undergo bond cleavages during mechanical damage of OXO-CHI-PUR networks are 1) –NHCONH- of PUA linkage, 2) –C-O-C- between CHI-CHI and CHI-OXE, and 3) –C-O-C- of OXO ring. Similar to the previous studies of OXE-CHI-PUR network, the spectroscopic analysis of the self-repairing processes indicate that reactive free radicals (b1, b2, and b3). Previous studies reported that OXO rings generally open up cationically but under UV irradiation they may follow radical-cation intermediate. Although Raman, FT-IR and IRIRI measurement techniques allow us to identify cleavage and bonding of specific groups; the question of cation or free radical formation remains open.¹⁰⁻¹⁴ In summary, these studies shown that chair-to-boat conformational changes resulting in close packing and/or network shrinkage upon UV exposure (Figure C. 11) of the glycosine units of CHI along with free radically cleavage of –NHCONH- (PUA) and –C-O-C- bonds (b1-b3) parallel DBTDL catalyzed OXO ring opening reactions resulting in self-repairing of the network. These remodeling processes resulting in reformed urethane and ether linkages (c).

Conclusion

These studies reveal that the presence of OXO rings within CHI-PUR networks show self-repairing, but the kinetics of repair is slower compared to OXE-CHI-PUR

networks, indicating that ring strain plays a major role in determining the time scale of the repair process. Mechanical damage decreases the T_g of the network due to the generation of smaller fragments within the scratch, and upon UV exposure crosslinking reactions during the repair process results in an increase of the T_g inside the scratch. These studies also show that the presence of HALS retards the repair process whereas higher OXO content as well as mild acidic conditions accelerate the process. In summary, these studies elucidates that free radical PUA-to-PUR conversion along with OXO ring opening and chair-to-boat conformational changes of glycosine units on the backbone of CHI responsible for self-repair process.

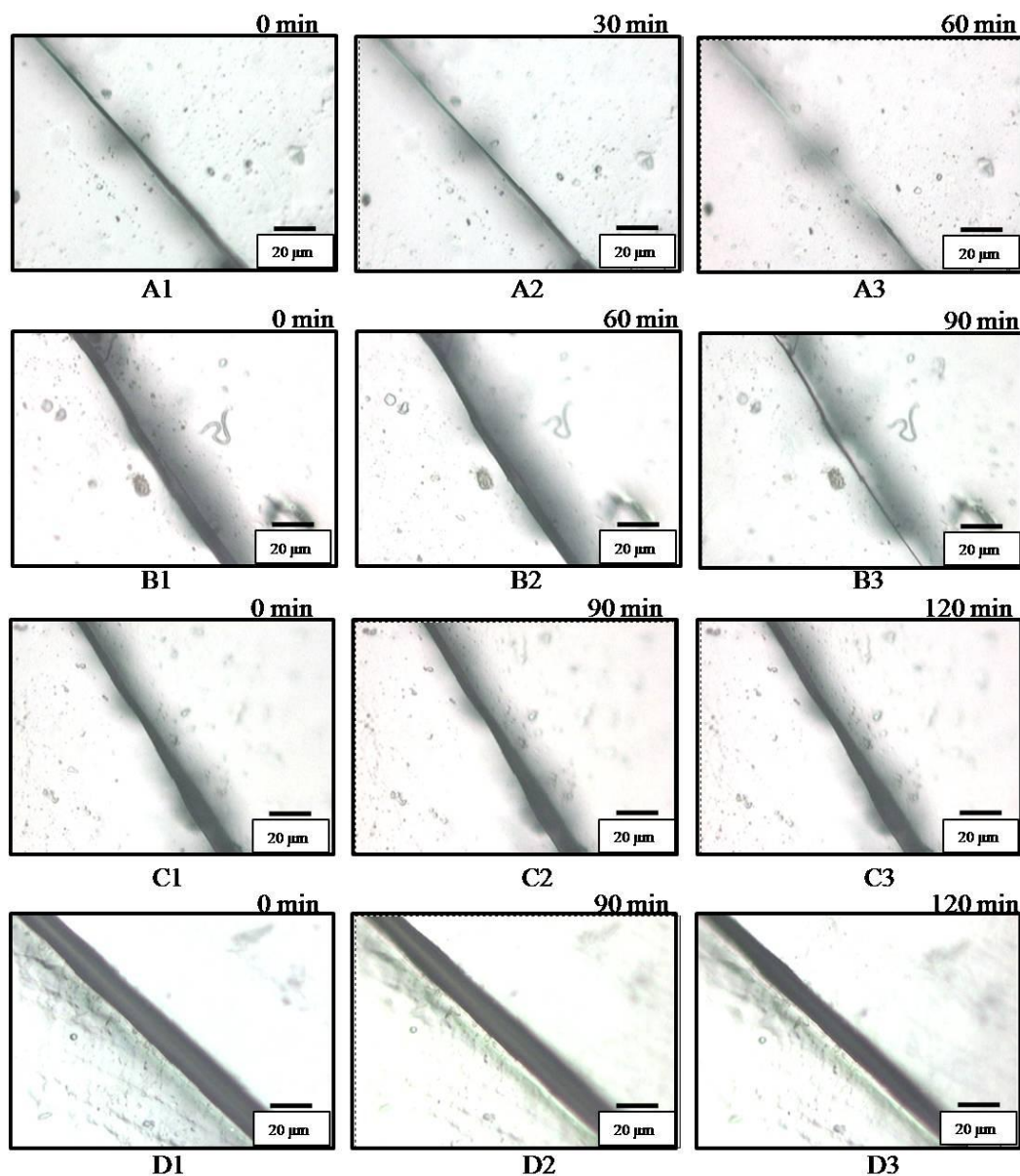


Figure 5.1. Optical images represent OXO-CHI-PUR networks (HDI:PEG:OXO-CHI:DBTDL=1.0:1.33:1.17 $\times 10^{-4}$:2 $\times 10^{-5}$) containing 1:1 (A1-A3), 1:4 (B1-B2), and 1:10 (C1-C3) molar OXO-CHI recorded as a function of UV exposure time. Optical images represent OXO-CHI-PUR networks (HDI:PEG:OXO-CHI:DBTDL=1.0:1.33:1.17 $\times 10^{-4}$:1 $\times 10^{-4}$) containing 1:1 molar OXO-CHI recorded as a function of UV exposure time.

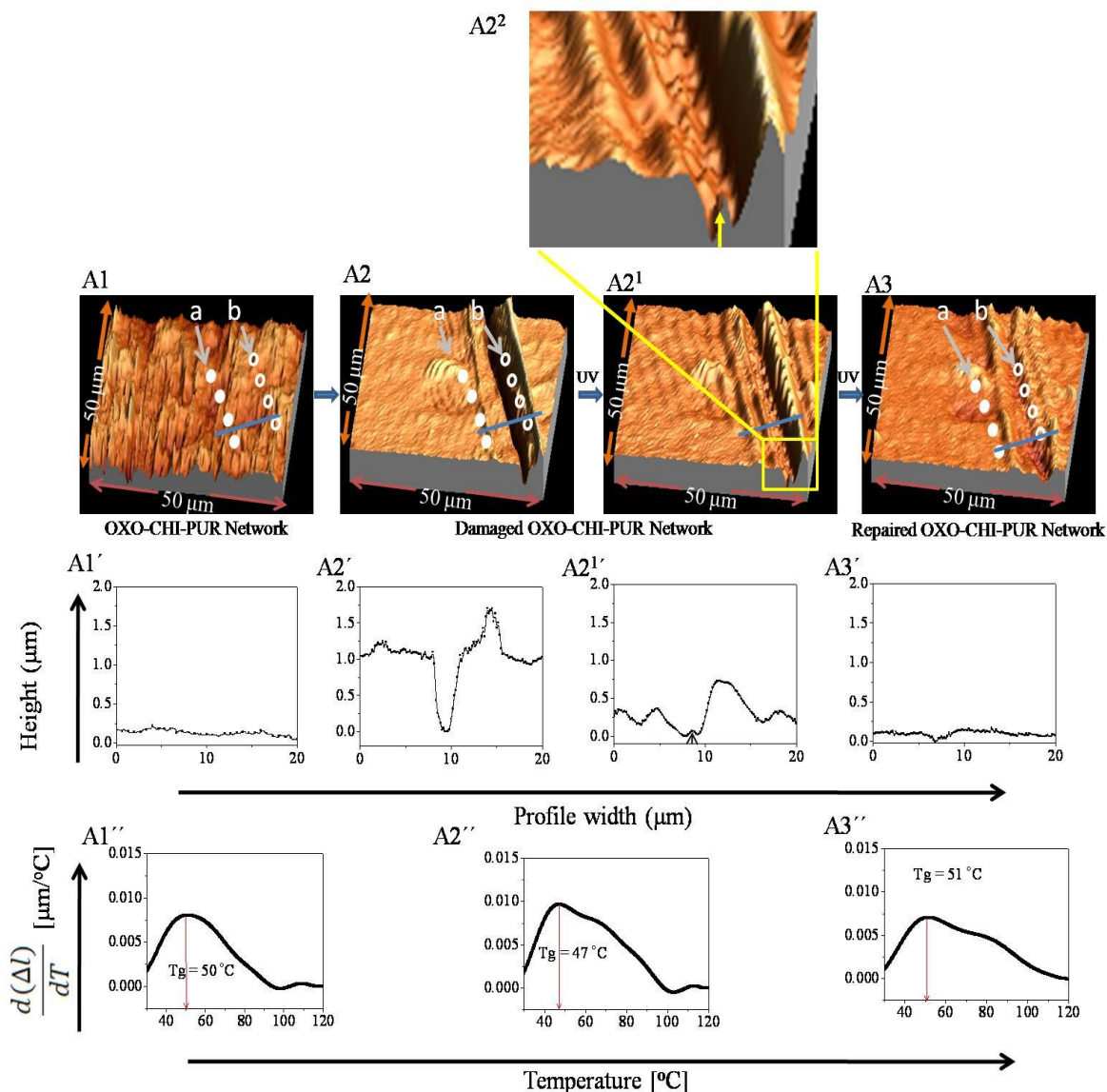


Figure 5.2. Atomic force microscopy (AFM) images of undamaged (A1), damaged and UV exposed (A2), and repaired (A3) OXO-CHI-PUR network (HDI:PEG:OXO-CHI:DBTDL = 1.0:1.33:1.17 $\times 10^{-4}$:2 $\times 10^{-5}$) containing OXO-CHI of 1:1 molar ratios, and plot of height vs width profile of undamaged (A1'), damaged and UV exposed (A2'), and repaired (A3') networks, and $d(\Delta I)/dT$ vs temperature (A1''-A3'') for the same.

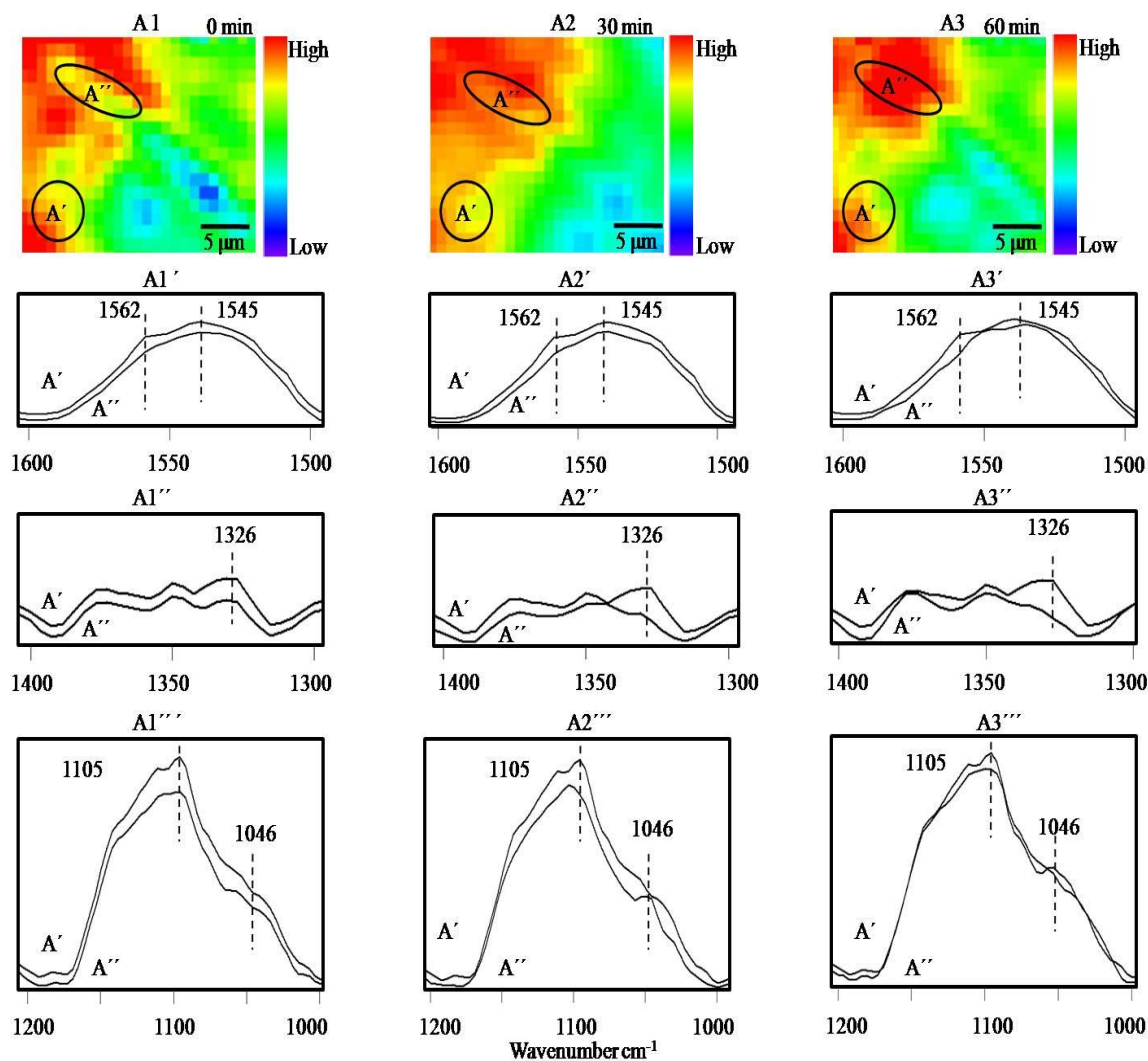


Figure 5.3. IRIRI images of OXO-CHI-PUR networks (HDI:PEG:OXO-CHI:DBTDL = 1.0:1.33:1.17 $\times 10^{-4}$:2 $\times 10^{-5}$) containing 1:1 molar OXO-CHI recorded as a UV exposure time 0, 30, and 60 min, respectively. (A1-A3) images were obtained by tuning into the 1545 cm^{-1} band; (A1'-A3', A1''-A3'', A1'''-A3''') IR spectra recorded from mechanically damaged and undamaged areas.

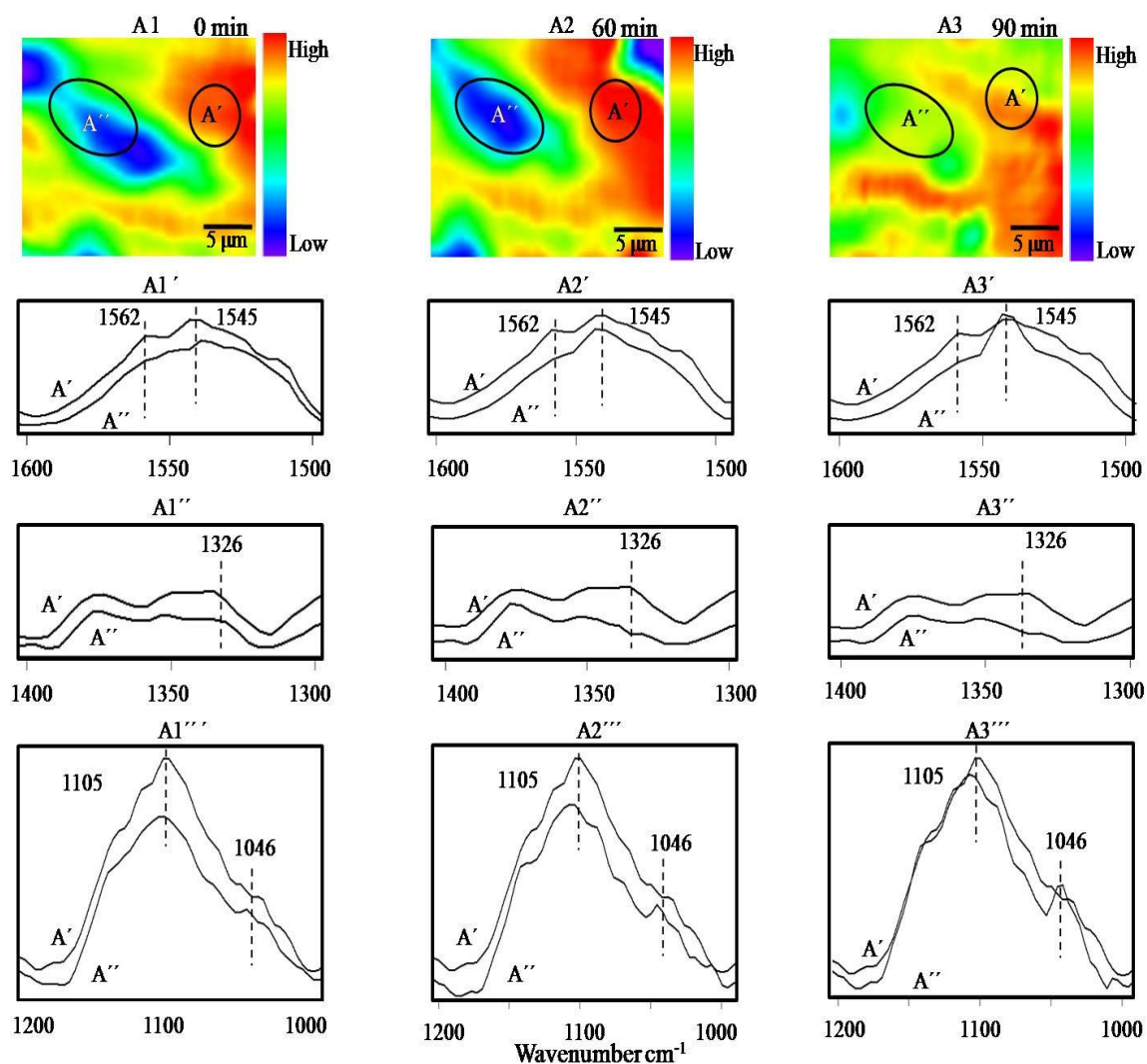


Figure 5.4. IRIRI images of OXO-CHI-PUR networks (HDI:PEG:OXO-CHI:DBTDL = 1.0:1.33:1.17 $\times 10^{-4}$:2 $\times 10^{-5}$) containing 1:4 molar OXO-CHI recorded as a UV exposure time 0, 60, and 90 min, respectively. (A1-A3) images were obtained by tuning into the 1545 cm^{-1} band; (A1'-A3', A1''-A3'', A1'''-A3''') IR spectra recorded from mechanically damaged and undamaged areas.

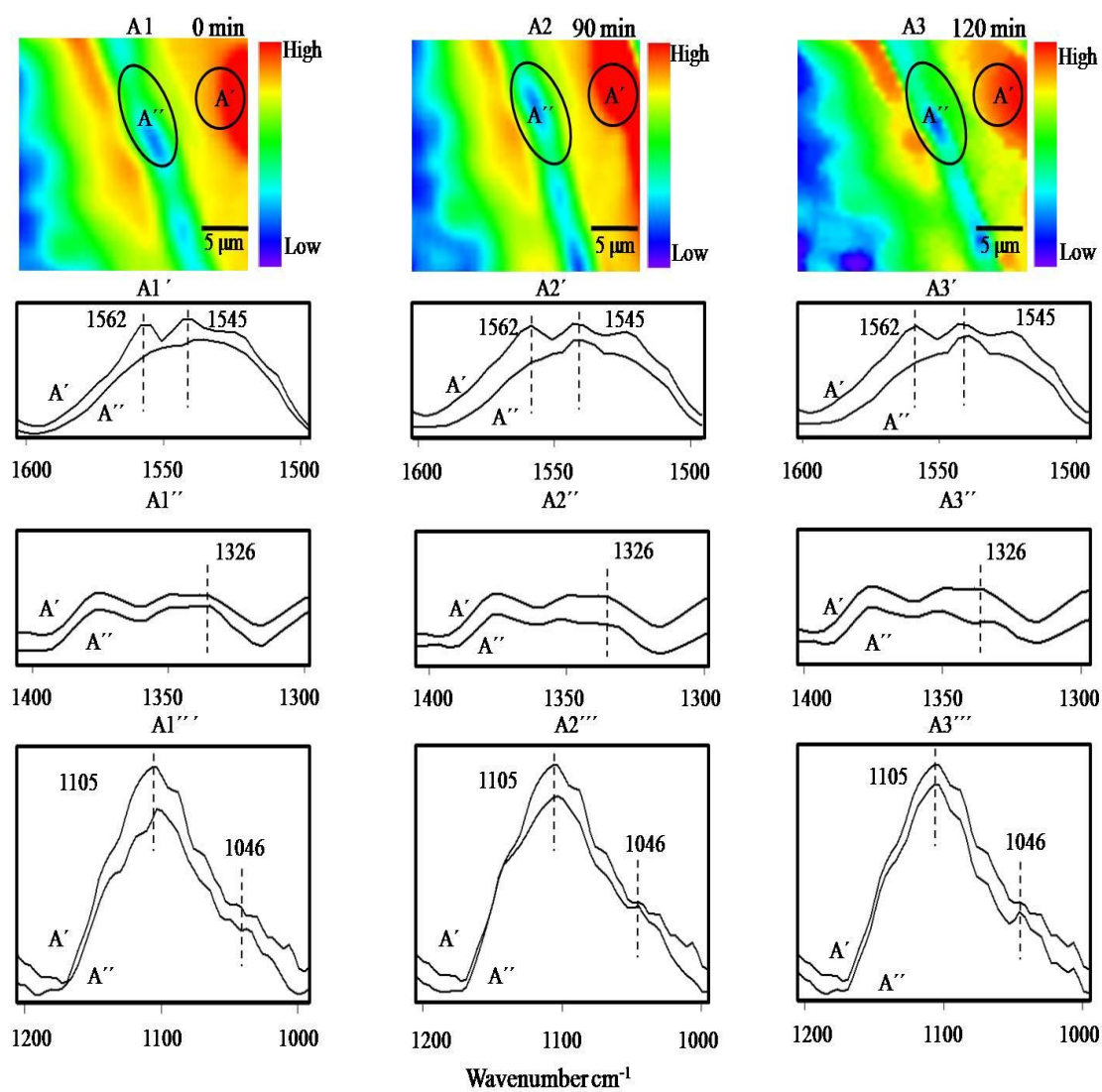


Figure 5.5. IRIRI images of OXO-CHI-PUR networks (HDI:PEG:OXO-CHI:DBTDL =1.0:1.33:1.17 $\times 10^{-4}$:2 $\times 10^{-5}$) containing 1:10 molar OXO-CHI recorded as a UV exposure time 0, 90, and 120 min, respectively. (A1-A3) images were obtained by tuning into the 1545 cm^{-1} band; (A1'-A3', A1''-A3'', A1'''-A3''') IR spectra recorded from mechanically damaged and undamaged areas.

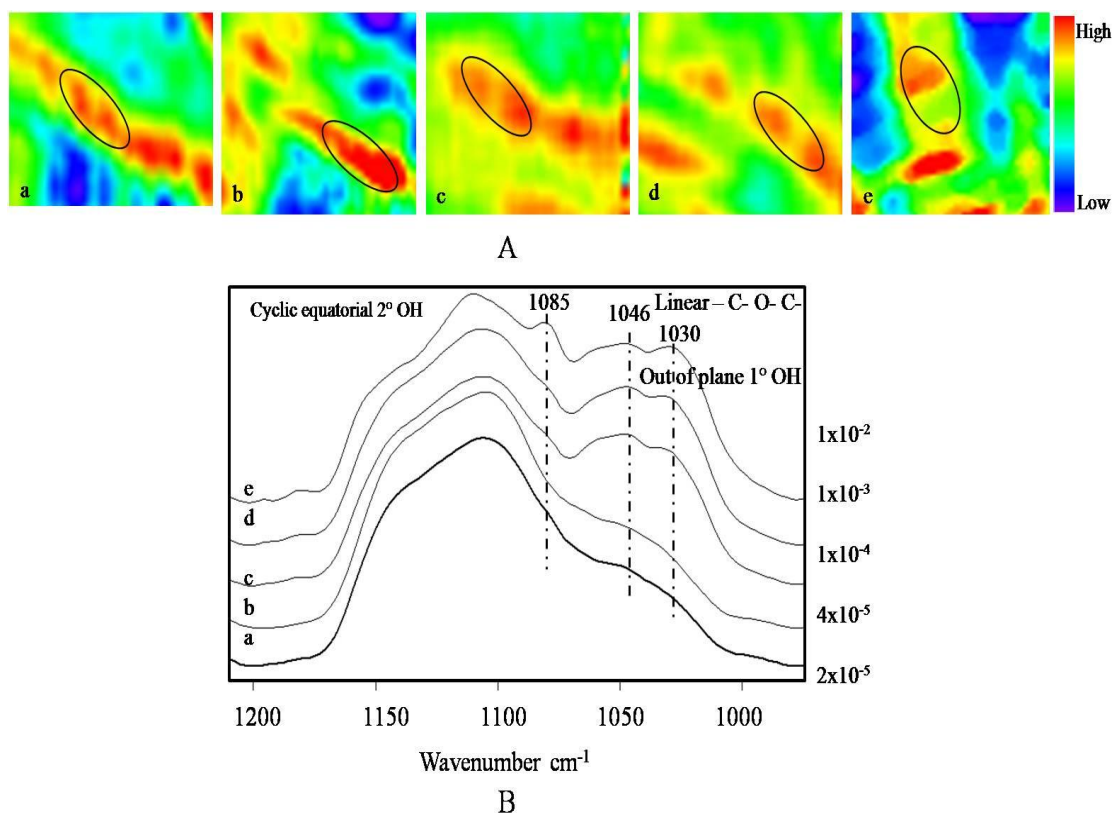


Figure 5. 6. IRIR images (A) and ATR-FTIR spectra (B) of OXO-CHI-PUR (HDI:PEG:OXO-CHI=1.0:1.33:1.17 $\times 10^{-4}$) networks containing a) 2 $\times 10^{-5}$, b) 4 $\times 10^{-5}$, c) 1 $\times 10^{-4}$, d) 1 $\times 10^{-3}$ and e) 1 $\times 10^{-2}$ mole DBTDL.

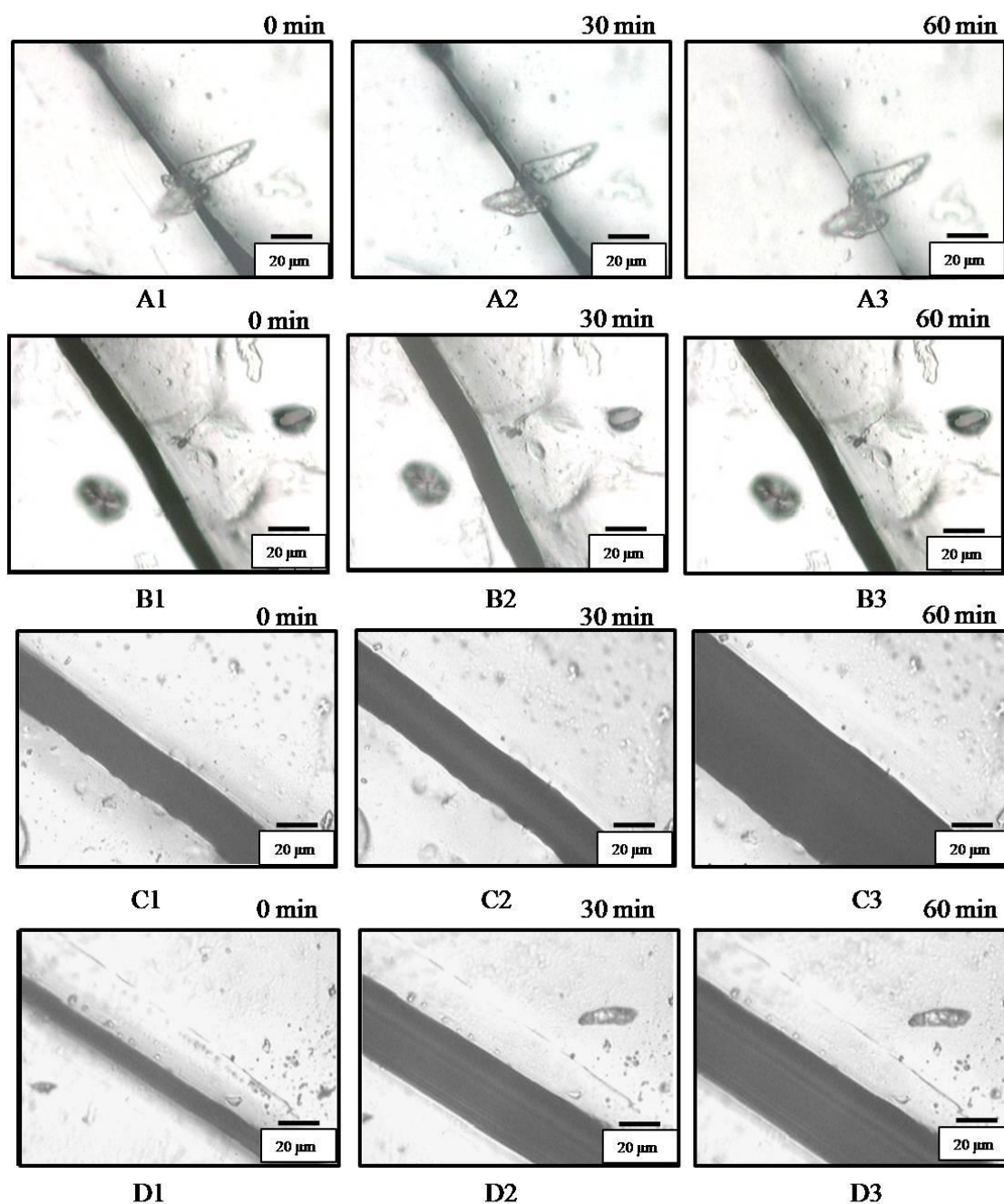


Figure 5.7. Optical images of OXO-CHI-PUR networks (HDI:PEG:OXO-CHI:DBTDL = 1.0:1.33:1.17 $\times 10^{-4}$:2 $\times 10^{-5}$) exposed to UV light at pH=3 (A1-A3), 4 (B1-B3), 5 (C1-C3), 6 (D1-D3).

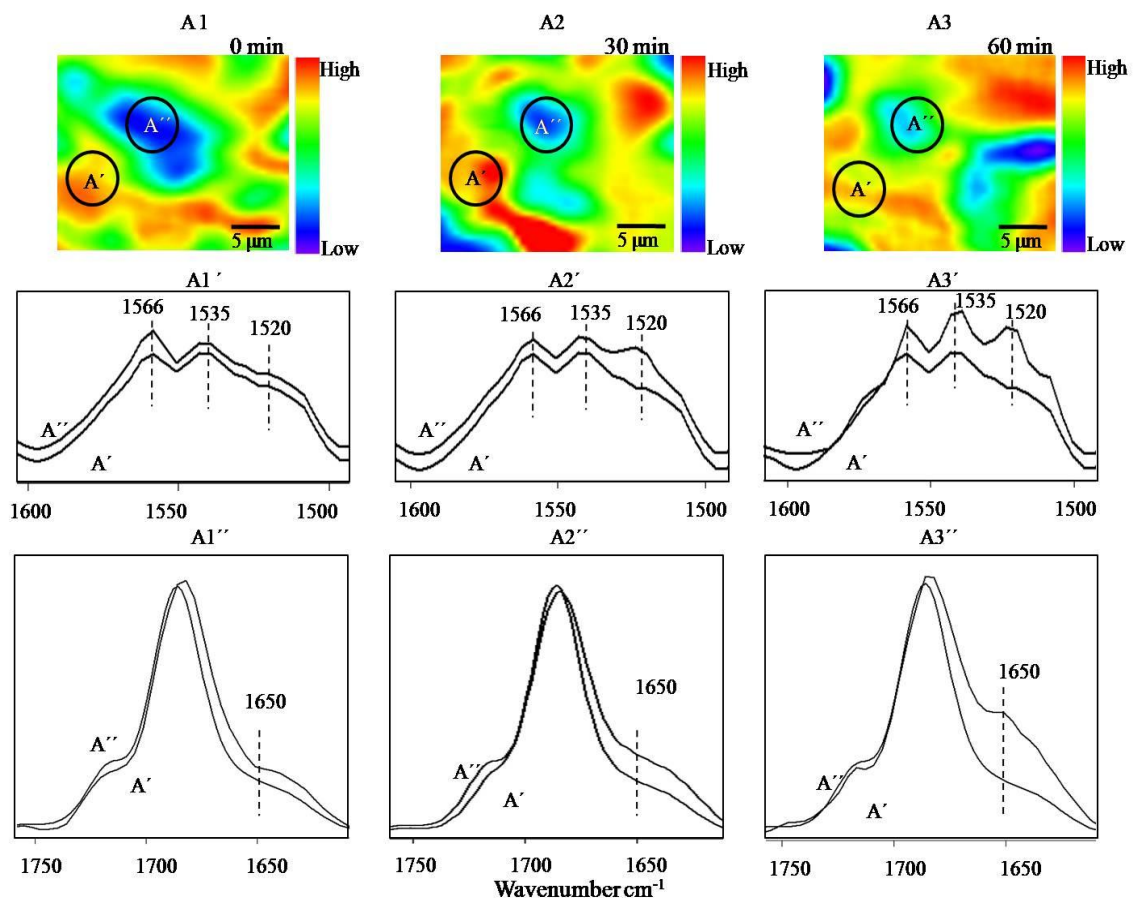


Figure 5.8. IRIRI images of OXO-CHI-PUR networks (HDI:PEG:OXO-CHI:DBTDL =1.0:1.33:1.17x10⁻⁴:2x10⁻⁵) containing 1:1 molar OXO-CHI at pH=3 recorded as a UV exposure time 0, 30, and 60 min, respectively. (A1-A3) images were obtained by tuning into the 1520 cm⁻¹ band; (A1'-A3', A1''-A3'') IR spectra recorded from mechanically damaged and undamaged areas.

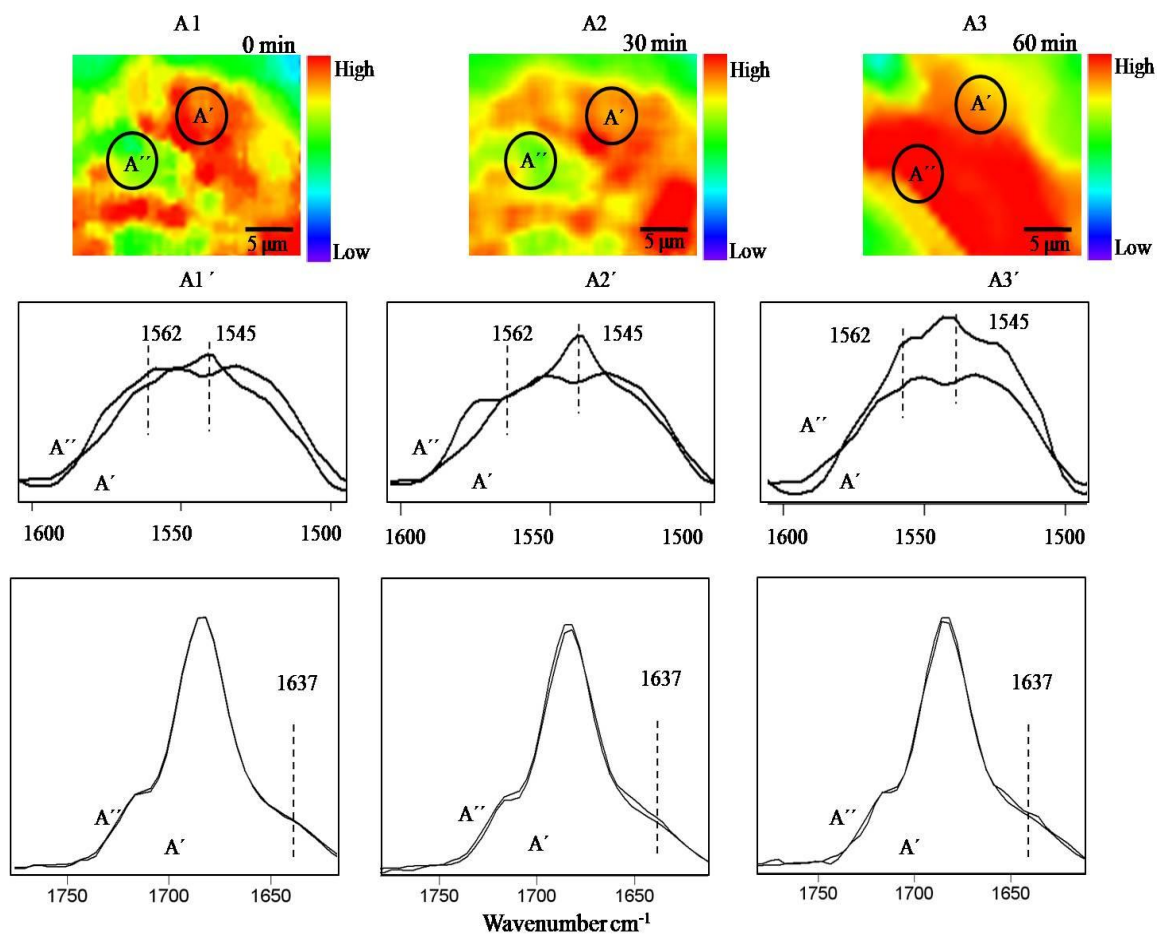


Figure 5.9. IRIRI images of OXO-CHI-PUR networks (HDI:PEG:OXO-CHI:DBTDL = 1.0:1.33:1.17 $\times 10^{-4}$:2 $\times 10^{-5}$) containing 1:1 molar OXO-CHI at pH=6 recorded as a UV exposure time 0, 30, and 60 min, respectively. (A1-A3) images were obtained by tuning into the 1520 cm^{-1} band; (A1'-A3', A1''-A3'') IR spectra recorded from mechanically damaged and undamaged areas.

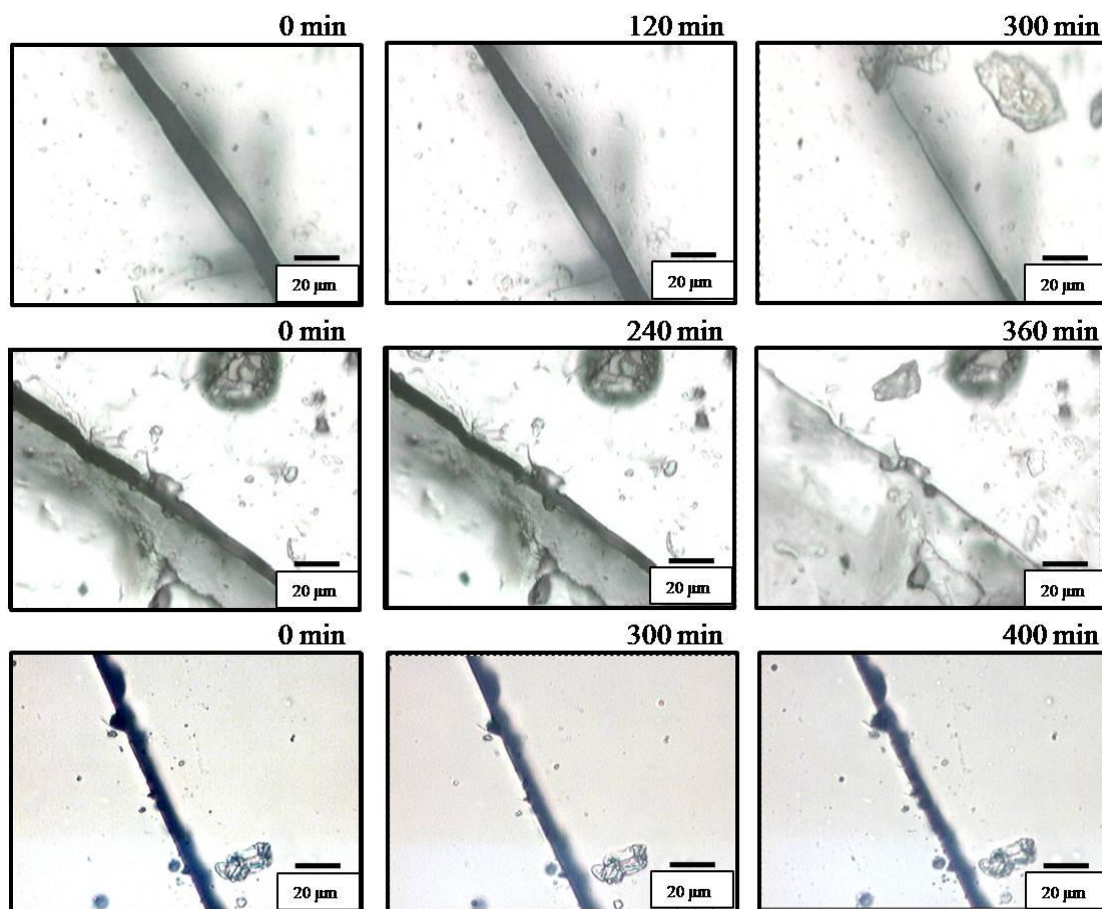


Figure 5.10. Optical images of OXO-CHI-PUR networks (HDI:PEG:OXO-CHI:DBTDL = 1.0:1.33:1.17 $\times 10^{-4}$:2 $\times 10^{-5}$) containing OXO-CHI of 1:1 (A1-A3), 1:4 (B1-B3), and 1:10 (C1-C3) molar ratios, respectively along with 1 % w/w HALS in each network exposed to UV.

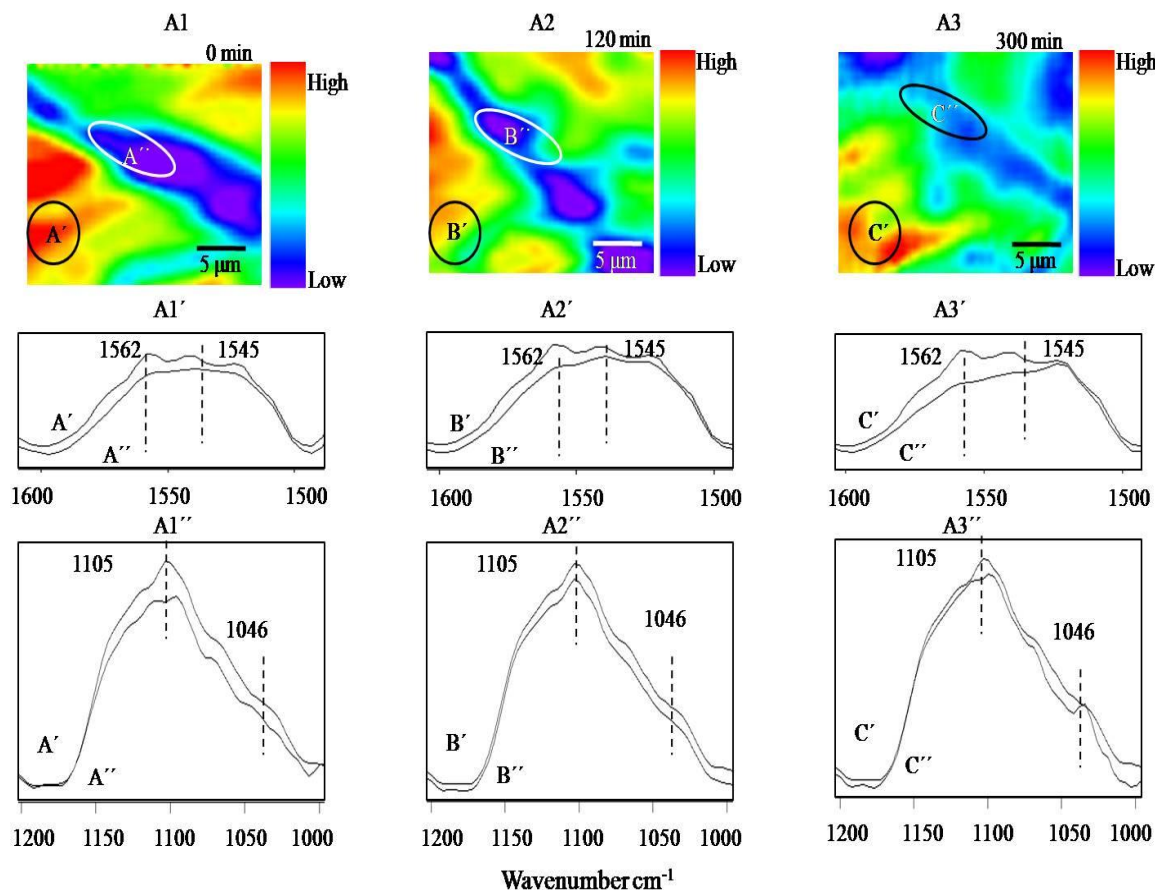


Figure 5.11. IRIRI images of OXO-CHI-PUR networks (HDI:PEG:OXO-CHI:DBTDL = 1.0:1.33:1.17x10⁻⁴:2x10⁻⁵) containing 1:1 molar OXO-CHI and 1 % w/w HALS recorded as a UV exposure time 0, 120, and 300 min, respectively. (A1-A3) images were obtained by tuning into the 1542 cm⁻¹ band; (A1'-A3', A1''-A3'', A1'''-A3''') IR spectra recorded from mechanically damaged and undamaged areas.

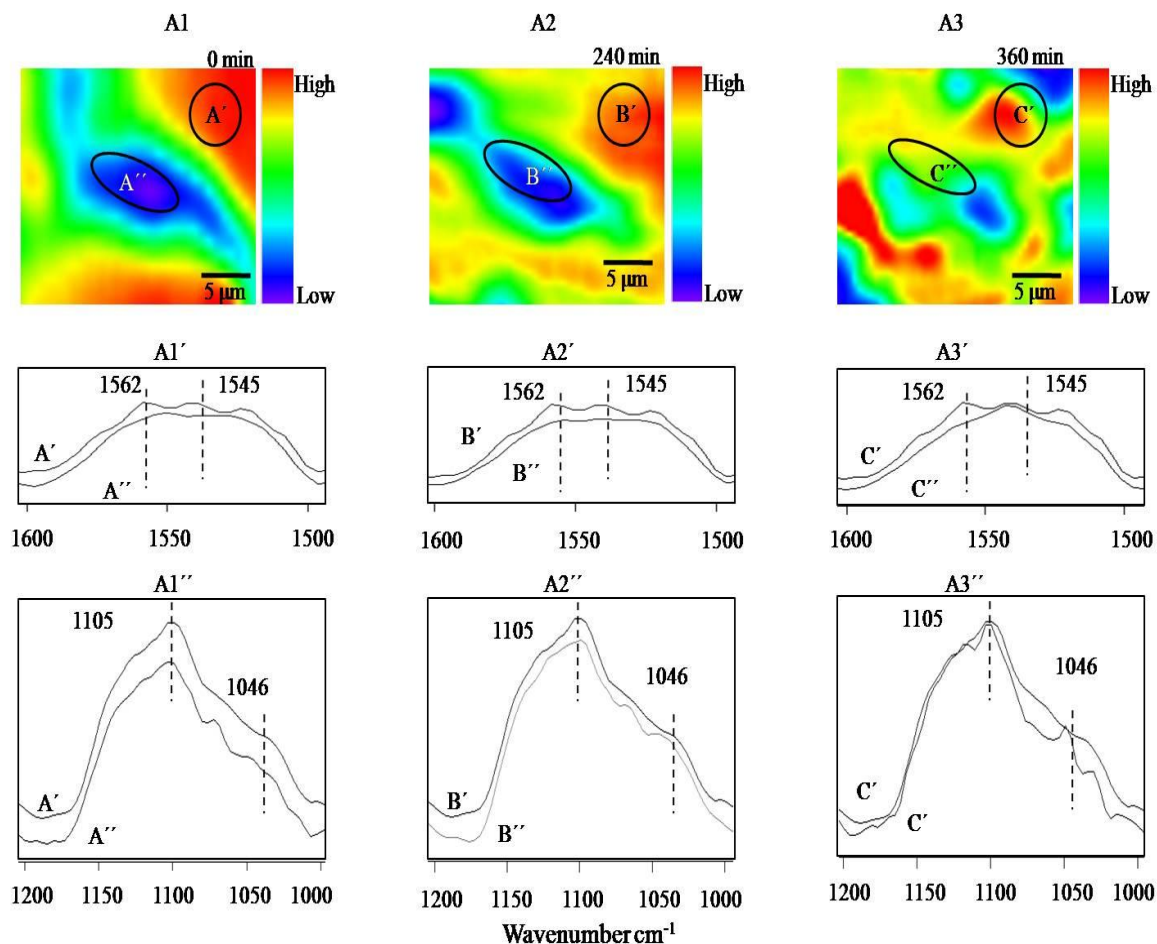


Figure 5.12. IRIRI images of OXO-CHI-PUR networks (HDI:PEG:OXO-CHI:DBTDL = 1.0:1.33:1.17x10⁻⁴:2x10⁻⁵) containing 1:4 molar OXO-CHI and 1 % w/w HALS recorded as a UV exposure time 0, 240, and 360 min, respectively. (A1-A3) images were obtained by tuning into the 1542 cm⁻¹ band; (A1'-A3', A1''-A3'', A1'''-A3''') IR spectra recorded from mechanically damaged and undamaged areas.

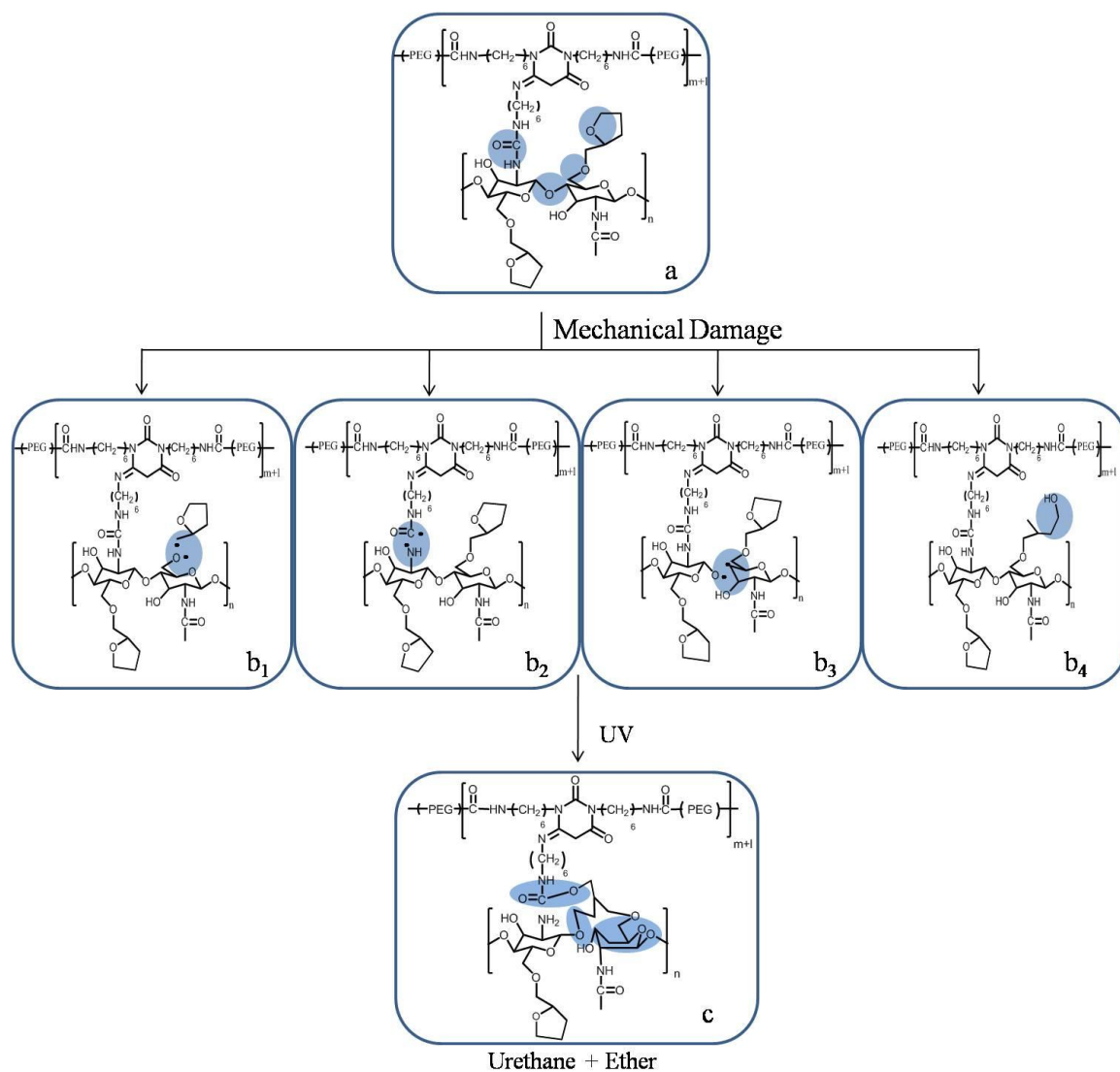


Figure 5.13. Proposed self-healing mechanism of OXO-CHI-PUR network under UV exposure.

References

1. Ghosh, B.; Urban, W. M. *Science* **2009**, 323, 1458.
2. Penczek, S.; Kubisa, P.; Matyjaszewski, K. *Adv. Polym. Sci.* **1980**, 37, 1.
3. Urban, M. W. *Attenuated Total Reflectance Spectroscopy of Polymers; Theory and Applications* (American Chemical Society and Oxford University Press, Washington, DC, 1996).
4. Priestley, R. D.; Ellison, C.J.; Broadbelt, L.J.; Torkelson, J.M. *Science*, **2005**, 309, 456.
5. Pretsch E., B. P., Affolter C., *Structure Determination of Organic Compounds*. 3rd ed.; Springer: 2000.
6. Lin-Vein, D.; Colthup., N.B.; Fateley, W. G.; Grasselli, J. G. , *The Handbook of Infrared and Raman Characteristics Frequencies of Organic Molecules*. Academic Press: San Diego, CA, , 1991.
7. Socrates, G., *Infrared and Raman Characteristic Group Frequencies: Tables and Charts*. 3rd ed. ed.; John Wiley and Sons Ltd: New York, 2001.
8. Otts, D. B.; Urban, M. W *Polymer*, **2005**, 46, 2699-2709.
9. Step, E. N.; Turro, N. J. *Macromolecules*, **1994**, 27, 2529.
10. Saegusa, T.; Matsumoto, S. *Macromolecules*, **1968**, 1, 442.
11. Ma, X. H.; Yamamoto, Y.; Hayashi, K. *Macromolecules*, **1987**, 20, 2703.
12. Janovsky, I.; Naumov, S.; Knolle, W.; Mehnert, R. *Radiat. Phys. Chem.* **2005**, 72, 125.
13. Pruckmayr, G.; Wu, T. K. *Macromolecules*, **1987**, 11, 662.
14. Saegusa, T.; Shiota, T.; Matsumoto, S.; Fujii, H. *Macromolecules*, **1972**, 5, 34.

CHAPTER VI

CONCLUDING REMARKS

Although Mother Nature has designed and developed mammals and plants in such way that damage due to natural or unnatural causes can be self-repaired under specific conditions, limited studies exist on remendable polymeric networks. For example, when skin is wounded, blood comes to the surface and clots to heal the damage area. Similarly in plants, damages of the leaf or bark resulting in outer flow of healing fluids like tanins, suberin etc. in order to repair the damaged area autonomously. This exciting phenomenon in biological systems opens up a new avenue for polymer scientists to mimic these processes in polymeric networks. Several attempts have been made to create self-repairable polymeric coatings in composite systems and Chapter I illustrates self-repairing polymeric composites or networks reported to date and various self-repairing networks were developed. However, all of them have limitations such as micro-encapsulation and microvascular techniques which result in brittle network formation or reversible cross-linking process that are limited by higher activation energy. These limitations have led us to the exploration of new avenues of self-healing and inspire us to investigate inexpensive commercially available biomaterials.

In view of these limitations Chapter II described modification of the second most commercially available carbohydrate, chitosan. The presence of two functional groups

(-NH₂ and -OH) as well as -C-O-C- linkages on the backbone of chitosan make these species pH and UV responsive. While maintaining the activity of -NH₂ functionalities in the backbone, we substituted primary -OH groups with highly strained

four-membered OXE rings to synthesize OXE-CHI macromonomer which will facilitate crosslinking reactions in the subsequent steps.

Polyurethanes, one of the most common polymeric coatings utilized in automobile, marine and other industries, were utilized in Chapter III for the design and synthesis of orchestrated OXE-CHI-PUR networks resulting from incorporation of OXE-CHI macromonomer that exhibit self-repairing characteristics upon UV exposure. Ring-strain and sensitivity to UV irradiation of CHI macromonomer and PUA linkages were utilized to self-repair the damaged network, and IRIRI technique gave us the chemical insight into the process.

While Chapter III elucidates self-repairing phenomenon of OXE-CHI-PUR networks under UV exposure, the effect of OXE and DBTDL catalyst within the networks as well as their exposure to different pH environments and the presence of HALS are spectroscopically determined in Chapter IV. Raman, ATR FT-IR and IRIRI experiments of several model OXE-CHI-PUR networks reveal that repair phenomenon of the damaged network is governed by cationic OXE ring opening along with free radical PUA-to-PUR conversion which parallels chair-to-boat conformational changes of glycosine units of the CHI backbone. Micro-thermal analysis of the damaged and repaired networks reveal that conservation of mass flow is maintained during the self-repair process while T_g decreases in the damaged area but increases upon repair due to new cross-link formation within the network.

In view of the influence of the 4-membered OXE ring in the self-repairing process of OXE-CHI-PUR networks, the influence of ring strain is further investigated by

incorporating 5-membered OXO ring within the PUR network. These studies described in Chapter V showed that lower ring strain and higher activation energies of OXO retard the self-repairing kinetics 2 to 3 fold and incorporation of HALS delays the process 5 to 6 fold suggesting substituted ring size on the CHI backbone plays a major role in self-repairing phenomenon.

APPENDIX A

SUPPORTING INFORMATION FOR CHAPTER III

Formation of OXE-CHI-PUR Networks

For reference purposes, Figure A.1 illustrates ^{13}C NMR spectrum of PUR with characteristic CH_2 and $\text{C}=\text{O}$ resonances. Upon incorporation of OXE-CHI in PUR characteristic resonances at 103 and 85 ppm due to the CHI ring and shift of the 13 ppm resonance due to methyl groups on the OXE ring signify the formation of OXE-CHI-PUR networks. This is illustrated in Figure A.2. Also, ATR-FT-IR spectra illustrated in Figure A.3 illustrates the disappearance of the $-\text{NH}_2$ bands at 1585 cm^{-1} of the product and detections of new bands at 1425 and 985 cm^{-1} due to $-\text{CH}_2$ scissoring and $-\text{C}-\text{O}-\text{C}-$ stretching vibration of OXE, respectively, thus further confirming the formation of OXE-CHI-PUR networks.

Self-Repairing Mechanism

Figure A.3 illustrates the spectra recorded before (Trace A) and after the UV exposure (Trace B) of the damaged area in a OXE-CHI-PUR network. The NH- bending vibrations due to polyurea, which is a part of the PUR network at 1562 cm^{-1} (Trace A), shift to 1542 cm^{-1} (Trace B). The latter corresponds to the NH-bending vibrations of the urethane functionality.³⁻⁵ These observations indicate a conversion of polyurea to polyurethane linkages. The decrease of the band intensity of the band due to tertiary methyl groups at 1376 cm^{-1} and a subsequent increase of the band of $-\text{CH}_2$ wagging at 1348 cm^{-1} along with the disappearance of $-\text{C}-\text{O}-\text{C}-$ stretching vibrations of OXE at 985 cm^{-1} results from the loss of OXE ring structure and the formation of linear alkyl groups

within the network. In contrast, the increase of the band intensities at 1135 and 1068 cm^{-1} due to the $-\text{C}-\text{O}-\text{C}-$ stretching vibrations and alkyl peroxide formation results from the scission of CHI linkages and OXE ring opening during UV exposure.^{1,2,6,7}

We used internal reflection IR imaging², which allows us to tune into specific IR bands associated with a given species, to determine the distribution of OXE-CHI entities within the networks, and follow molecular events responsible for repair. We tuned into the 1542 and 1348 cm^{-1} bands due to N-H bending of PUR and CH_2 wagging due to ether linkages of the OXE ring. Figure A.4, A, B, C represents three images recorded after UV exposure of OXE-CHI-PUR specimens for 0, 15, and 30 min, respectively. These images were collected from the damaged area shown in Figure A.4. A-C. As shown, Figure A.4, A, indicates heterogeneous distribution of the 1542 cm^{-1} band. The damaged area labeled A' shows lower concentration levels of N-H, whereas the area A'' away from the damage area exhibits higher concentration of these species. The corresponding spectra shown in A.4, A1 obtained from the areas A' and A'' confirms that the band intensities of the following vibrations change: decrease of 1562 cm^{-1} and 1378 cm^{-1} bands of urea linkages and $-\text{CH}_2-$ wagging of linear alkyl, respectively, increase of 1108 cm^{-1} band of $-\text{C}-\text{O}-\text{C}-$ stretching vibrations of linear aliphatic ethers and decrease of 985 cm^{-1} band due to $-\text{C}-\text{O}-\text{C}-$ stretch of the OXE ring.

The images recorded from the specimens exposed to UV radiation for 15 and 30 min are shown in Figure A.4, B and C, respectively. The distribution of chemical entities in areas B' and C' become homogenous, indicating surface repair. This is also reflected in spectroscopic changes illustrated in Figure A.4, B1-B3 and C1-C3. As the scratch is exposed to UV, the urea linkage represented by the band at 1562 cm^{-1} shifts to 1542 cm^{-1}

which is due to polyurea-polyurethane conversion, whereas the opening of the OXE ring results in the decrease of the band intensities at 1378 and 985 cm^{-1} . The increase of the band intensities at 1348, 1135, 1108, and 1038 cm^{-1} in the area B' and C' represent the –C-O-C- bond formation within the network that is responsible for self-repairing. Similar analysis shown in Figure A.5 was performed by tuning into the 1348 cm^{-1} band due to –CH₂- wagging and showed similar intensity changes of the 1562, 1542, 1135, 1108, 1038 and 985 cm^{-1} bands.

Based on the spectroscopic data analysis, the mechanism of remending of OXE-CHI-PUR networks is proposed (Figure A.6). The crosslinked network is represented by red thick lines, whereas dangling OXE entities are black thinner lines. As mechanical damage is created, such as shown in Figure A.6. B, the OXE ring opens up and a local cleavage occurs. Upon exposure to UV light, crosslinking reactions of OXE-CHI entities result in self-healing of the damage area. This is illustrated in Figure A.6. C.

Different molar ratios of OXE-CHI, HDI (NCO), and PEG (OH) utilized for synthesis of PUR, CHI-PUR, and OXE-CHI-PUR networks are listed in Table A.1.

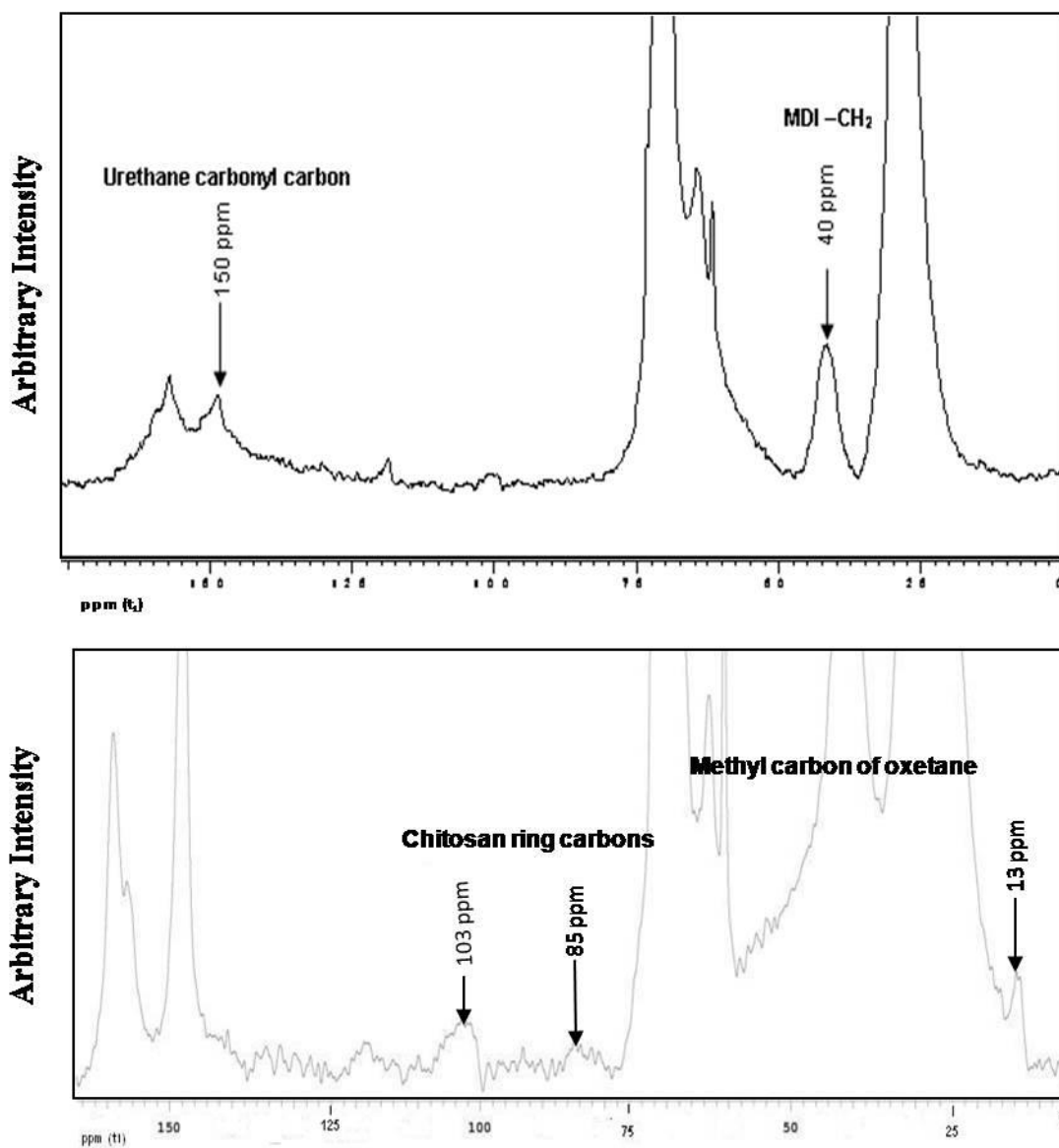


Figure A.1. Solid state ^{13}C NMR spectra of A) PUR and B) OXE-CHI-PUR networks.

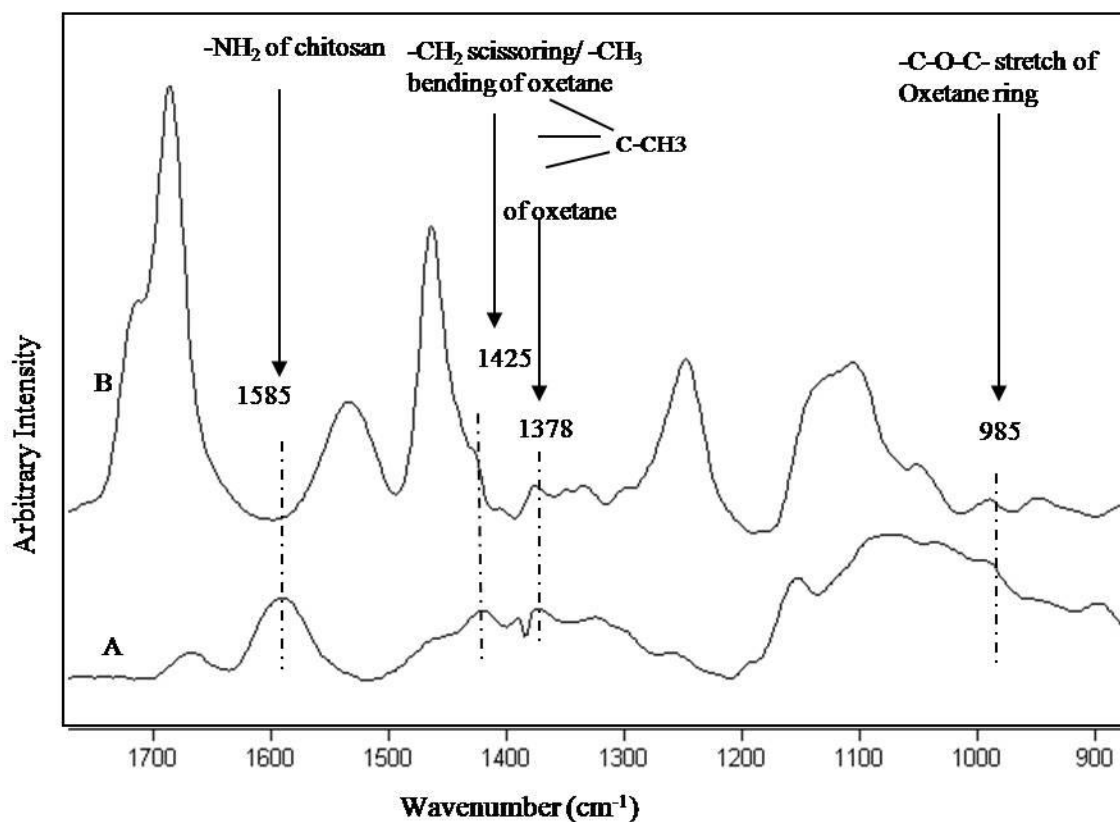


Figure A.2. ATR FT-IR spectra of (A) OXE-CHI products and (B) OXE-CHI-PUR networks.

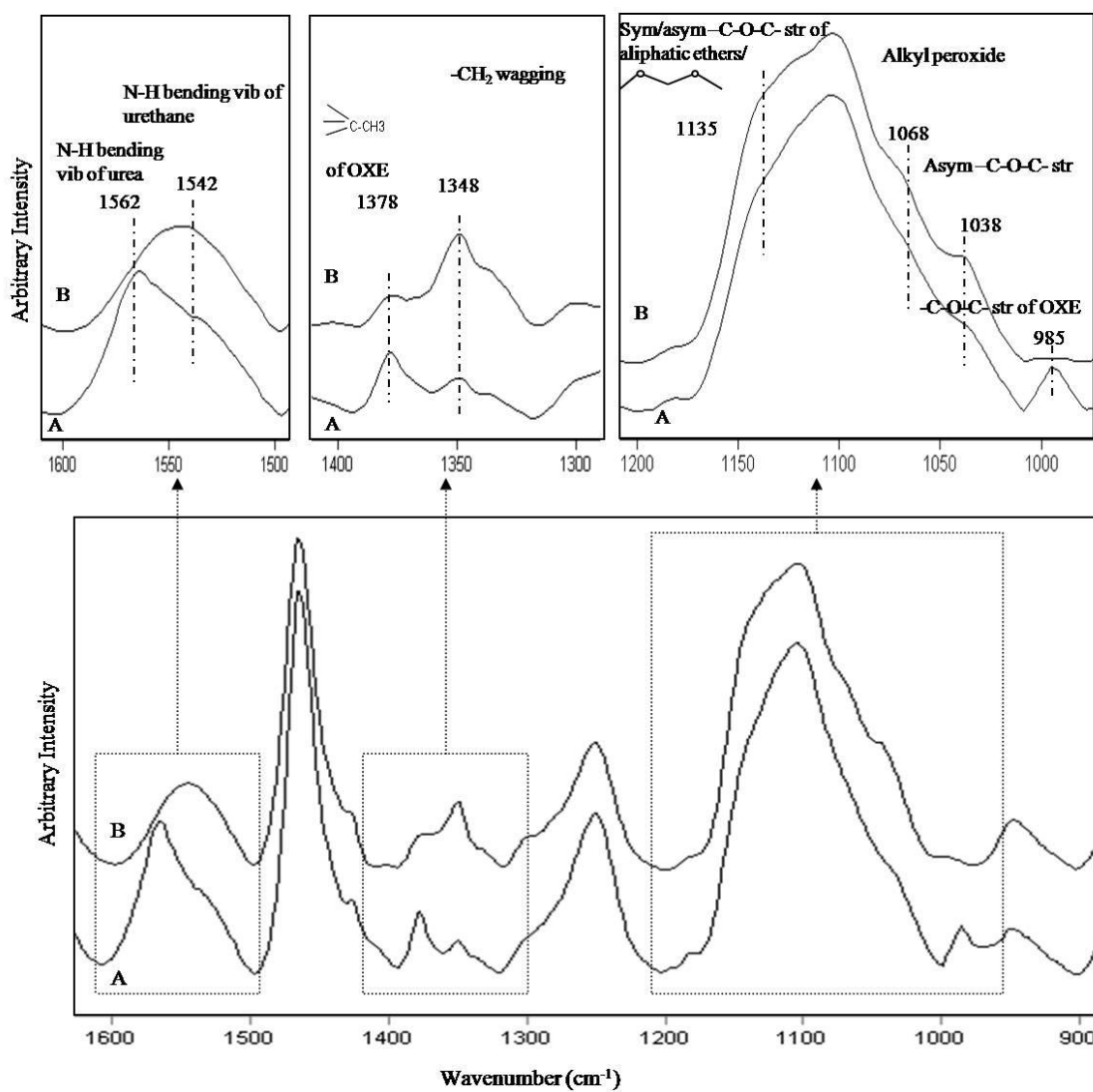


Figure A.3. ATR-FTIR spectra of OXE-CH-PUR networks recorded before (Trace A) and after (Trace B) UV exposure for 30min of specimen illustrated in Figure 3a.

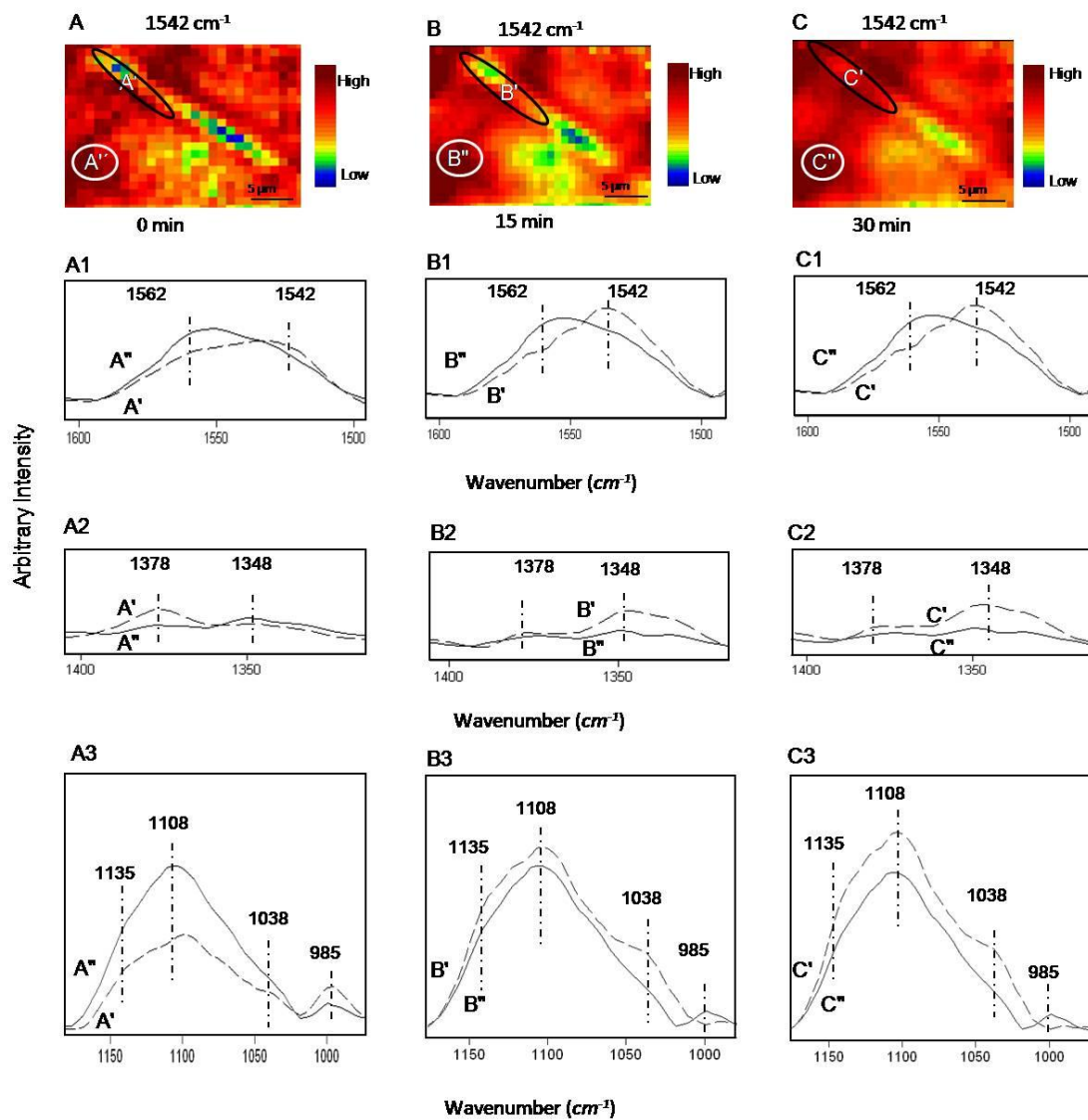


Figure A.4. Internal reflection IR images recorded from scratched and unscratched area of polyurethane network: (A-C) images obtained by tuning into 1542 cm^{-1} ; (A1-A3, B1-B3, C1-C3) IR spectra recorded from scratched and unscratched area of (A-C) images, respectively.

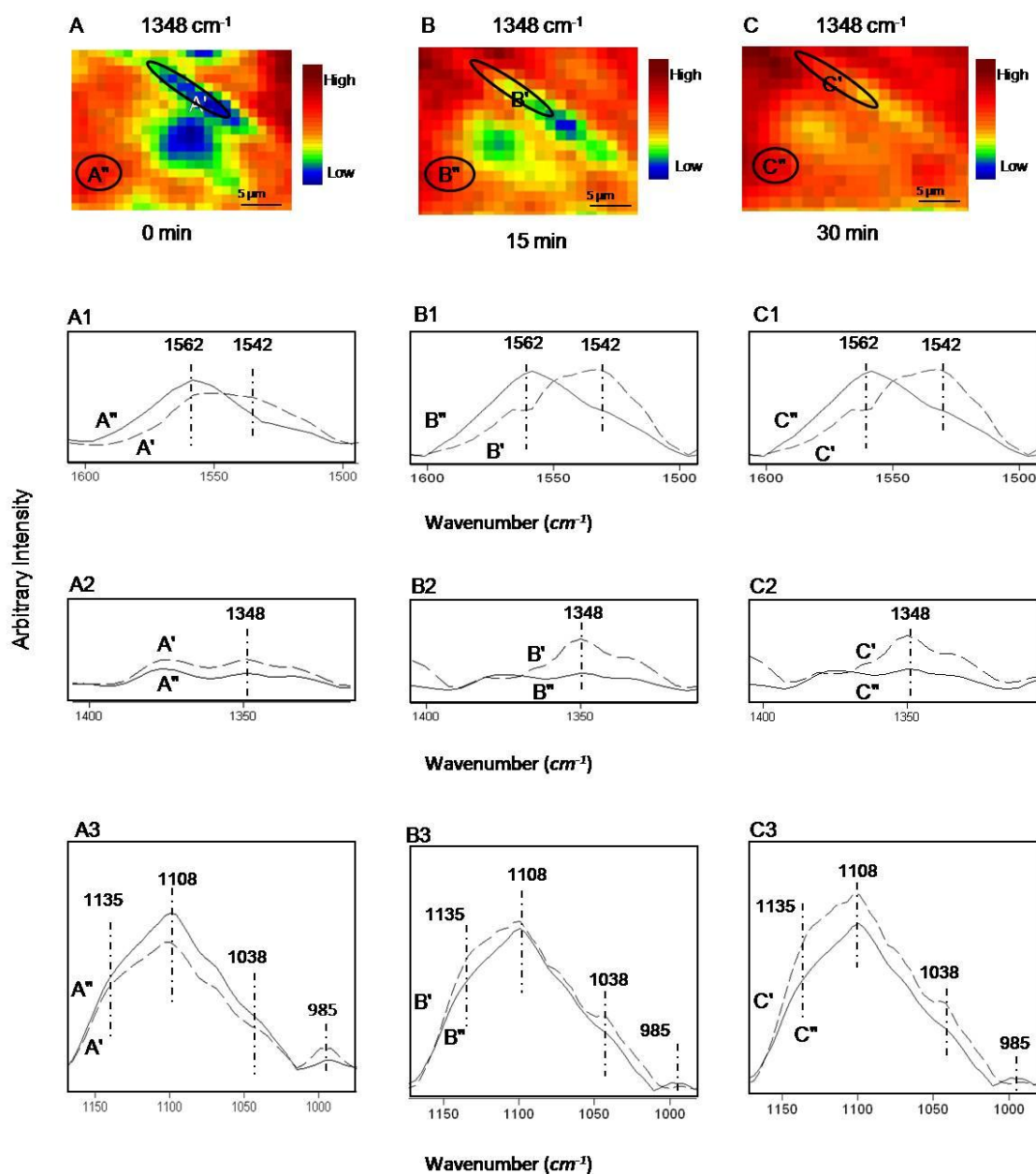


Figure A.5. Internal reflection IR images recorded from scratched and unscratched area of polyurethane network: (A-C) images obtained by tuning into 1350 cm^{-1} ; (A1-A3, B1-B3, C1-C3) IR spectra recorded from scratched and unscratched area of (A-C) images, respectively.

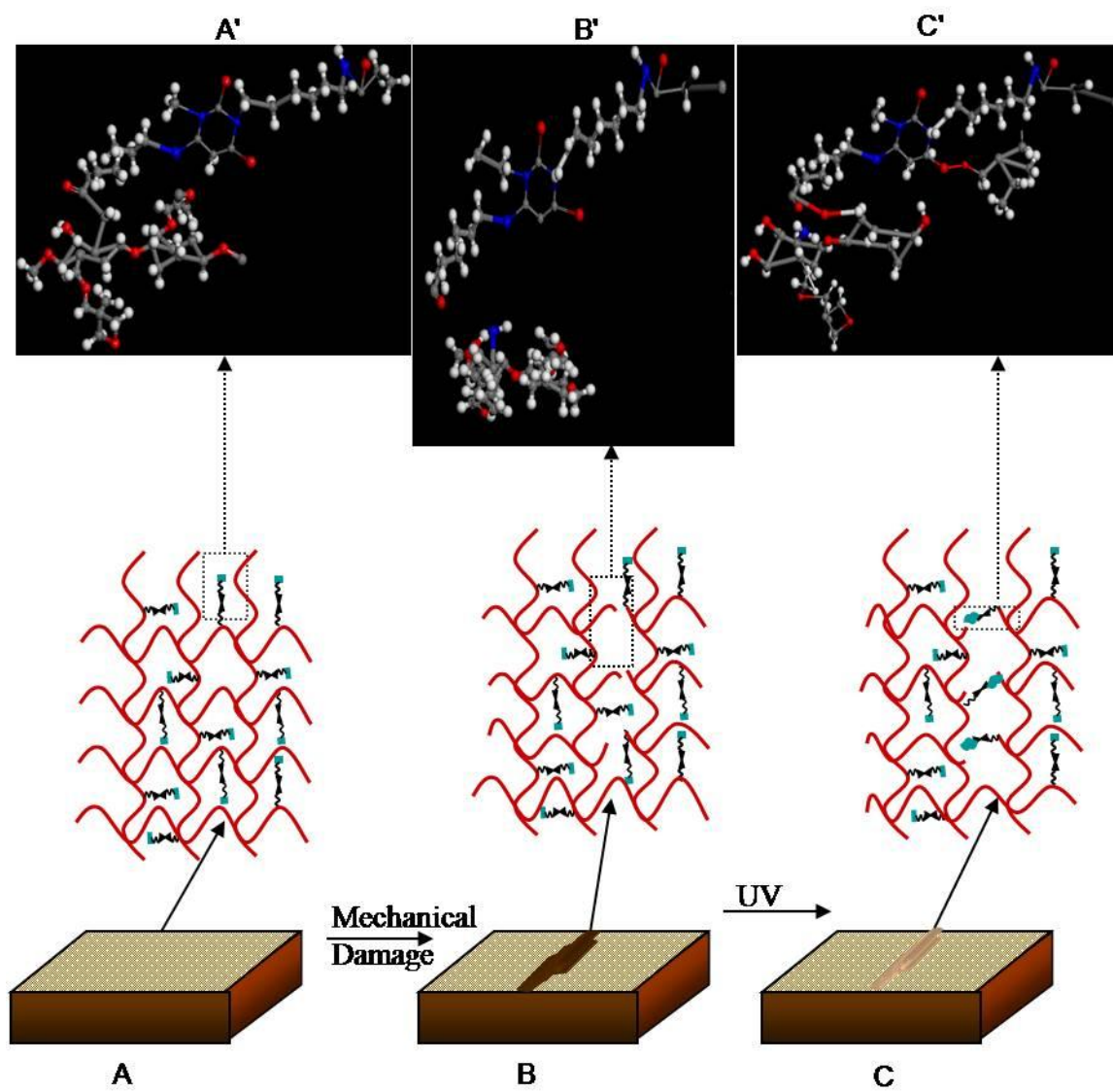


Figure A.6. Schematic diagram of self-repair of OXE-CHI-PUR networks.

Table A.1

Damage Width as a Function of UV Exposure Time for Different OXE-CHI-PUR

Compositions

Specimen	Composition	Exposure time (<i>min</i>)		
		0	15	30
		Damage Width (μm) ± 0.1		
A	(PUR) HDI:PEG:CHI = 1:1.5:0	10	10	10
B	(CHI-PUR) HDI:PEG:CHI = 1:1.4:0.57x10 ⁻⁴	20.5	20.5	20.5
C	(OXE-CHI-PUR) HDI:PEG:OXE-CHI = 1:1.4:0.57x10 ⁻⁴	2.26	1.08	0
D	(OXE-CHI-PUR) HDI:PEG:OXE-CHI = 1:1.33:1.17 x10 ⁻⁴	6	5.2	0

References

1. D. Lin-Vein, N.B. Colthup, W.G. Fateley, J.G. Grasselli, The Handbook of Infrared and Raman Characteristics Frequencies of Organic Molecules (Academic Press, San Diego, CA, 1991)
2. G. Socrates, Infrared and Raman Characteristic Group Frequencies: Tables and Charts, 3rd ed.; (John Wiley and Sons Ltd., New York, 2001)
3. D.B. Otts, M.W. Urban, Polymer **46**, 2699 (2005).
4. W.H. Nosal, D.W. Thompson, L. Yan, S. Sarkar, A. Subramanian, J. A. Woollam, Colloids Surf., B **43**, 131 (2005).
5. K. Heung, M. W. Urban, Langmuir **16**, 5382 (2000).
6. A. Pawlak, M. Mucha, Thermochim. Acta **396**, 153 (2003).
7. E. Pretsch, P. Buhlmann, C. Affolter, Structure Determination of Organic Compounds, 3rd ed; (Springer, Germany, 2000).

APPENDIX B

SUPPORTING INFORMATION FOR CHAPTER IV

Model OXE-CHI Macromonomer Experiments

Figure B.1, Traces A, B, and C, illustrate ATR FT-IR spectra of OXE-CHI (1:1) macromonomer, DBTDL catalyzed OXE-CHI macromonomer containing 1×10^{-5} and 2×10^{-5} molar DBTDL, respectively. All specimens were sonicated in DMSO for 60 min. Analysis of the spectra indicates that the primary features are the diminishing intensities of the -C-O-C- stretching vibrations of OXE at 1043 , and 985 cm^{-1} resulting from cationic OXE ring opening. Other OXE related vibrations include $\text{-CH}_2\text{-}$ scissoring and -C_4 bending vibrations at 1425 and 1378 cm^{-1} , respectively, which are only slightly affected. Also, higher concentration levels of DBTDL do not affect intensities of the -C-O-C- stretching vibrations (1070 cm^{-1}) of CHI-CHI and CHI-OXE entities, indicating the stability of the linear -C-O-C- segments between glycosine units (CHI-CHI) and OXE-CHI macromonomer under the same conditions.¹⁻³ These changes are also pointed out in Figure A.B.1 by arrow directions which depict the response of relevant bands to various conditions.

To determine UV sensitivity of OXE-CHI macromonomer, a series of model experiments were conducted in which OXE-CHI molar ratio was varied from 1:1, 1:2, 1:4, 1:6 to 1:10. Figures B.2-B.6, Traces A, B, and C show Raman spectra collected as a function of UV exposure for 0, 60 and 7 days, respectively, for 1:1, 1:2, 1:4, 1:6, and 1:10 OXE-CHI molar ratios. Comparison of Traces A and B in Figure B.2 shows the increase of the 1117 cm^{-1} band due to hydrazine formation upon UV exposure. On the other hand,

OXE ring opening associated with glycosine units of OXE-CHI result in the increase of the bands at 970 and 890 cm^{-1} which are due to $-\text{C}-\text{C}-\text{C}-\text{OH}$ and $-\text{C}-\text{O}-\text{C}-$ entities, respectively. Also, the decrease of the bands at 1425 and 1043 cm^{-1} due to $-\text{CH}_2-$ scission and $-\text{C}-\text{O}-\text{C}-$ linkages of OXE and glycosine units are also observed.¹⁻³ Furthermore, the band at 778 cm^{-1} decreases which signifies conformational chair-to-boat conversion of glycosine units along the CHI-backbone. These changes are further amplified in Trace C of Figure B.2, manifesting the fact that the free radical reactions continue several days after UV exposure. The same result, although smaller magnitude of band intensities were observed for 1:2, 1:4, 1:6, and 1:10 OXE-CHI ratios and are shown in Figures B.3-B.6. Table B.1 lists all spectroscopic changes resulting from UV exposure. As listed in Table B.1 for 1:1 and 1:2 molar ratios OXE-CHI macromonomers, the band intensities at 1117 and 970 cm^{-1} , respectively, due to hydrazine and 1° $-\text{OH}$ bands increase upon UV radiation. This is attributed to higher auxochromic effect of $-\text{C}-\text{O}-\text{C}-$ compared to $-\text{OH}$ groups. On the other hand, for 1:4, 1:6, and 1:10 molar ratios, the 1117 cm^{-1} band decreases at the expense of conversion of $-\text{NH}_2$ to $-\text{NO}_2$ (1330 cm^{-1}) as well as the decrease of the 970 cm^{-1} band as a result of 1° $-\text{OH}$ conversion to hydroxyl amine functionalities due to weaker auxochromic effect of $-\text{NH}_2$ groups.⁴ These changes are also pointed out in Figures B.2-B.6 by arrow directions which depict response of the relevant bands.

Figures B.7-B.11 illustrate FT-IR spectra of OXE-CHI macromonomer for 1:1, 1:2, 1:4, 1:6, and 1:10 stoichiometries exposed to the same conditions. Comparison of Traces A and B in Figure B.7 shows that the bands corresponding to $-\text{C}-\text{O}-\text{C}-$ stretching of OXE as well as ether linkages between glycosine units, $-\text{C}_4$, and $-\text{CH}_2-$ scissoring of

OXE ring at 985, 1043, 1070, 1378, 1425 cm^{-1} , respectively, decrease upon UV exposure.¹⁻³ Again, the 1580 cm^{-1} band corresponding to amide I decreases when OXE-CHI is exposed to UV radiation. OXE-CHI with 1:2, 1:4, 1:6, and 1:10 show the same results, with the exception of the band intensity decrease for lower OXE content in OXE-CHI macromonomer. These changes are also pointed out in Figures B.7-B.11 by arrow directions which depict response of relevant bonds. Table B.2 lists all IR bands sensitive to UV exposure.

OXE-CHI-PUR Networks

Figure B.12, A1-A3 illustrate IRIR images of OXE-CHI-PUR (OXE-CHI=1:4) containing 1% w/w HALS recorded after UV exposure for 0, 60, and 240 min, respectively. IR spectra recorded from areas A'/A'', B'/B'', and C'/C'' are shown in Figure B.12, A1'-A3', A1''-A3'', and A1'''-A3''' in 1600-1500, 1400-1300, and 1200-1000 cm^{-1} regions, respectively. As shown in Figure B.12, A1'-A1''', lower intensities of 1562 and 985 cm^{-1} bands in Trace A'' which indicates the cleavage of -NH-C(=O)-NH- bond and OXE ring opening. When such network was exposed to UV for 60 min, as shown in Figure B.12, A2'-A2'', the 985 cm^{-1} band disappears along with the significant decrease of the 1378 cm^{-1} band due to bending -C₄ vibrations of OXE. At the same time, the intensity of -NH-CO-NH- stretching vibrations of PUA at 1562 cm^{-1} remains unaffected in the damaged area B''. Further UV exposure for 240 min results in the decrease of the 1562 and 1378 cm^{-1} bands and the increase of the 1542 and 1108 cm^{-1} due to -NH-CO-O- stretching vibrations of PUR and linear -C-O-C- stretching vibrations. Similarly, Figure B.13, A1'-A1''', A2''-A2''', and A3'-A3''', illustrate IRIR images of OXE-CHI-PUR network containing 1 % w/w HALS for the 1:10 OXE-CHI molar ratio.

After 120 min of UV exposure, 1562, 1378, and 1108 cm^{-1} bands decrease, whereas the 985 cm^{-1} band is not detected. These observations signify that PUA-to-PUR conversion reactions are interrupted and become slower in the presence of HALS and continue upon further UV exposure for 300 min. The intensity of the 985 cm^{-1} band in the undamaged area (C') decreases after 240 min and 300 min of UV exposure of OXE-CHI-PUR networks containing 1:4 and 1:10 molar ratios of OXE-CHI (Figure B.12-C' and B.13-C'), respectively.

Figure B.14, A1-A3, illustrates thermal expansion changes of undamaged (A1), damaged (A2) and repaired (A3) areas of OXE-CHI-PUR network (HDI:PEG:OXE-CHI=1.0:1.33:1.17 $\times 10^{-4}$) as a function of temperature. As shown in Figure B.14, A1, the slope recorded from the undamaged area increases from 0.013 to 0.019 upon mechanical damage (Figure B.14-A2) due to chain cleavage resulting in the formation of shorter segments or oligomers. Under UV exposure, the damaged area is self-repaired and the slope increases to 0.015 (Figure B.14-A3), indicating regeneration of crosslink density resulting from self-repair process. Similarly, Figure B.14, B1-B3, shows the thermal expansion data for unmodified PUR network. As seen, the slope of the undamaged area (0.013) increases to 0.017 during network damage but does not change upon UV exposure (Figure B.14, B1-B3).

Figure B.15 illustrates the DSC thermogram of OXE-CHI-PUR network (HDI:PEG:OXE-CHI=1.0:1.33:1.17 $\times 10^{-4}$). As seen, one endothermic transition is detected at 62.9 °C.

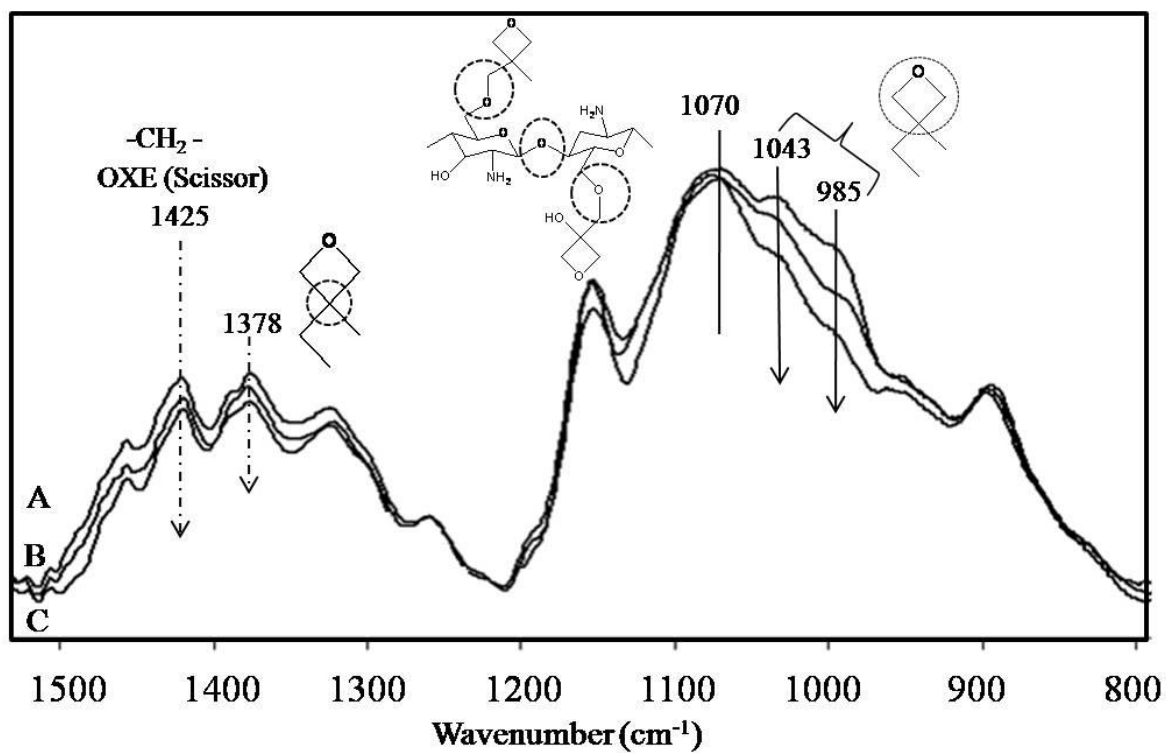


Figure B.1. ATR FT-IR spectra of OXE-CHI (1:1) macromonomer in absence of DBTDL(A), in presence of 1×10^{-5} (B), and 2×10^{-5} moles DBTDL in DMSO after 60 min; arrow directions point out increasing (\uparrow) and decreasing (\downarrow) intensities of relevant bands.

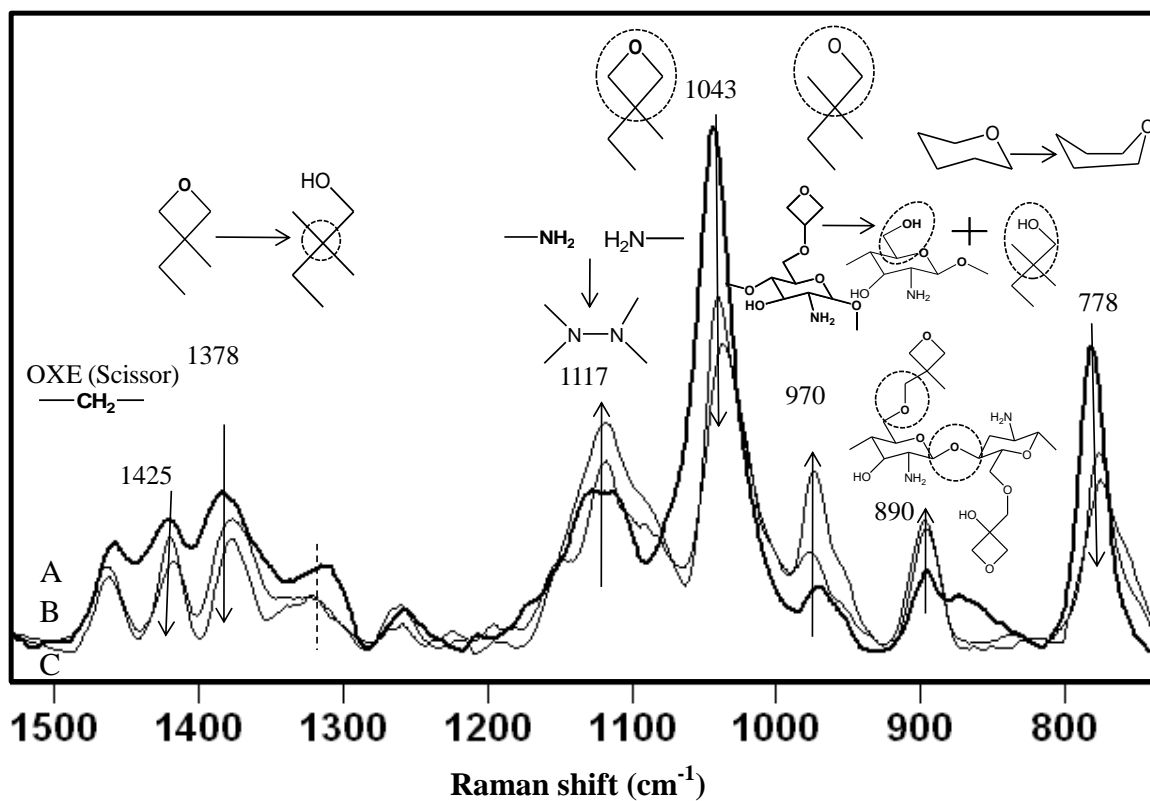


Figure B.2. Raman spectra of OXE-CHI (1:1), before (A), after 60 min of UV exposure (B), and 7 days later (C) of UV exposure; arrow directions point out increasing (\uparrow) and decreasing (\downarrow) intensities of relevant bands.

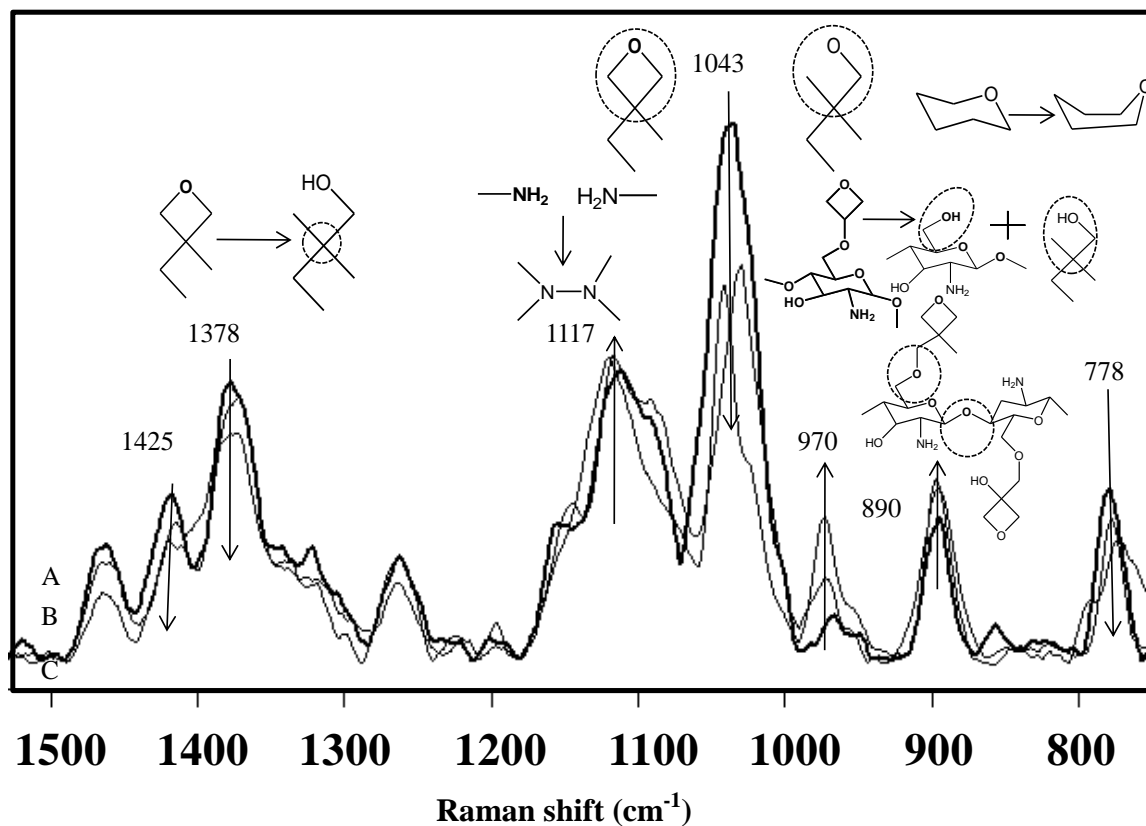


Figure B.3. Raman spectra of OXE-CHI (1:2), before (A), after 60 min of UV exposure (B), and 7 days later (C) of UV exposure; arrow directions point out increasing (↑) and decreasing (↓) intensities of relevant bands.

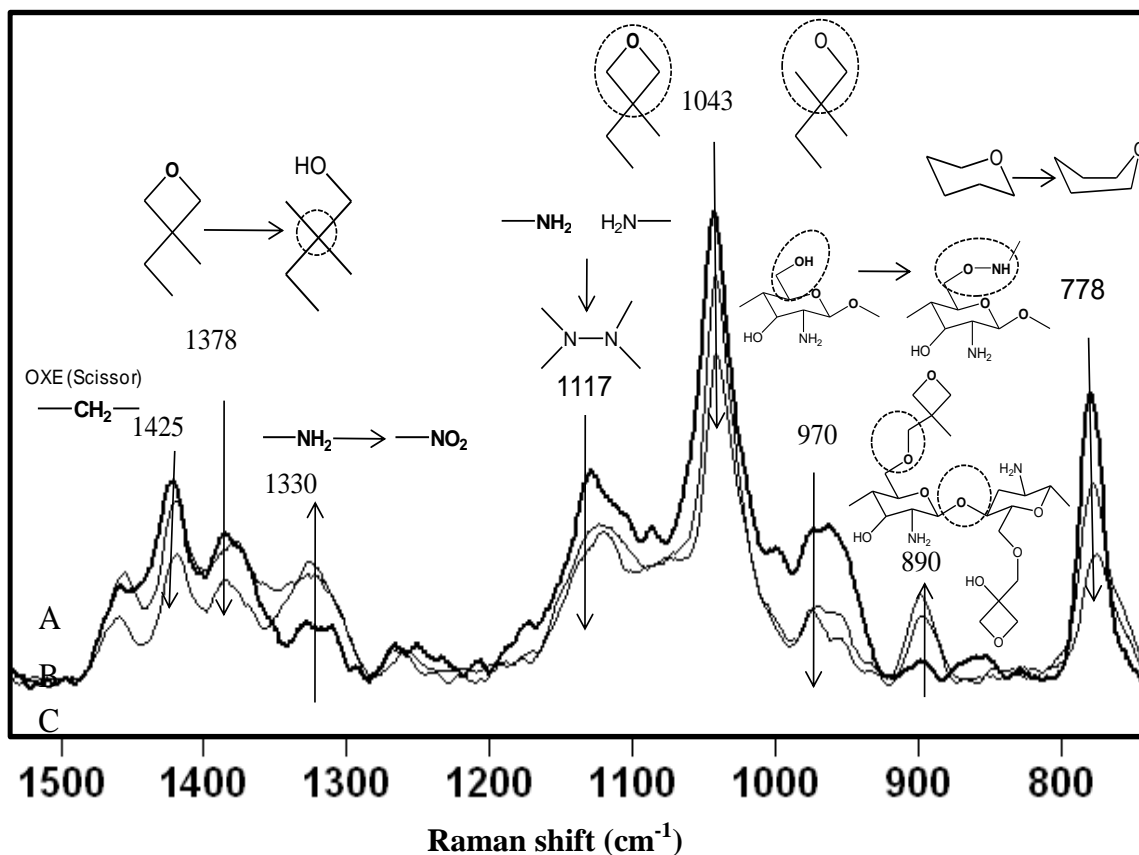


Figure B.4. Raman spectra of OXE-CHI (1:4), before (A), after 60 min of UV exposure (B), and 7 days later (C) of UV exposure; arrow directions point out increasing (\uparrow) and decreasing (\downarrow) intensities of relevant bands.

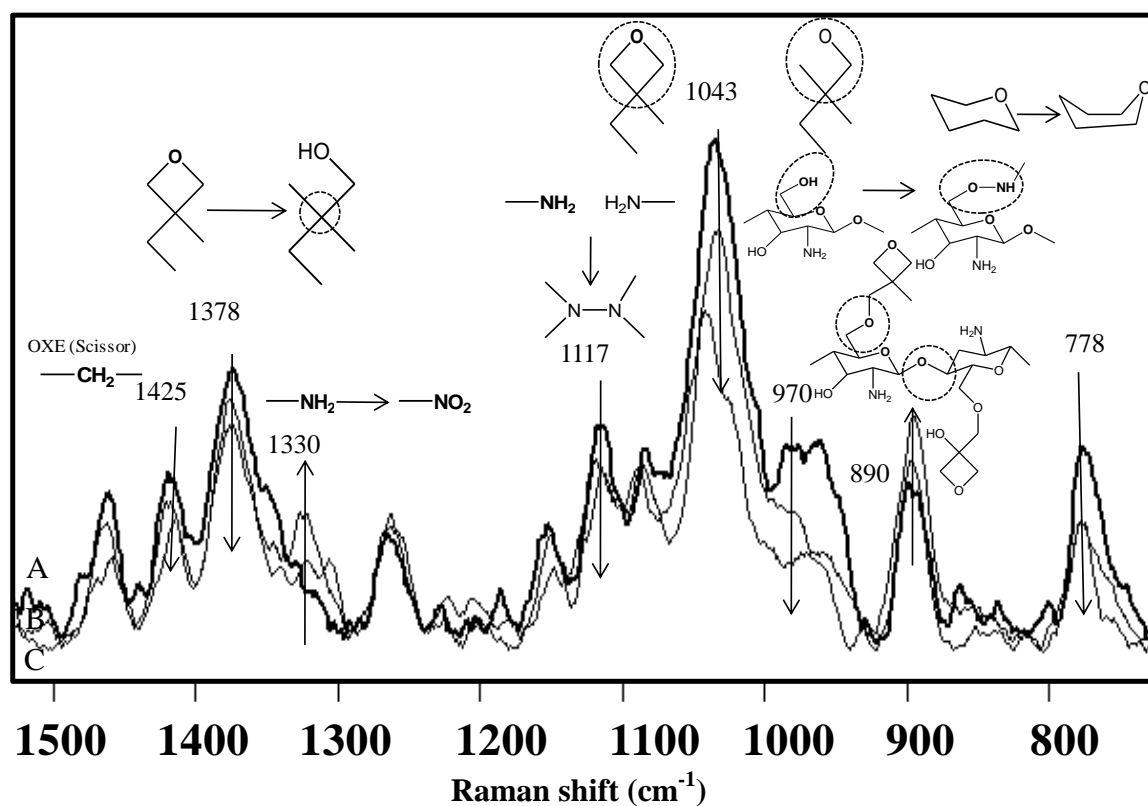


Figure B.5. Raman spectra of OXE-CHI (1:6), before (A), after 60 min of UV exposure (B), and 7 days later (C) of UV exposure; arrow directions point out increasing (\uparrow) and decreasing (\downarrow) intensities of relevant bands.

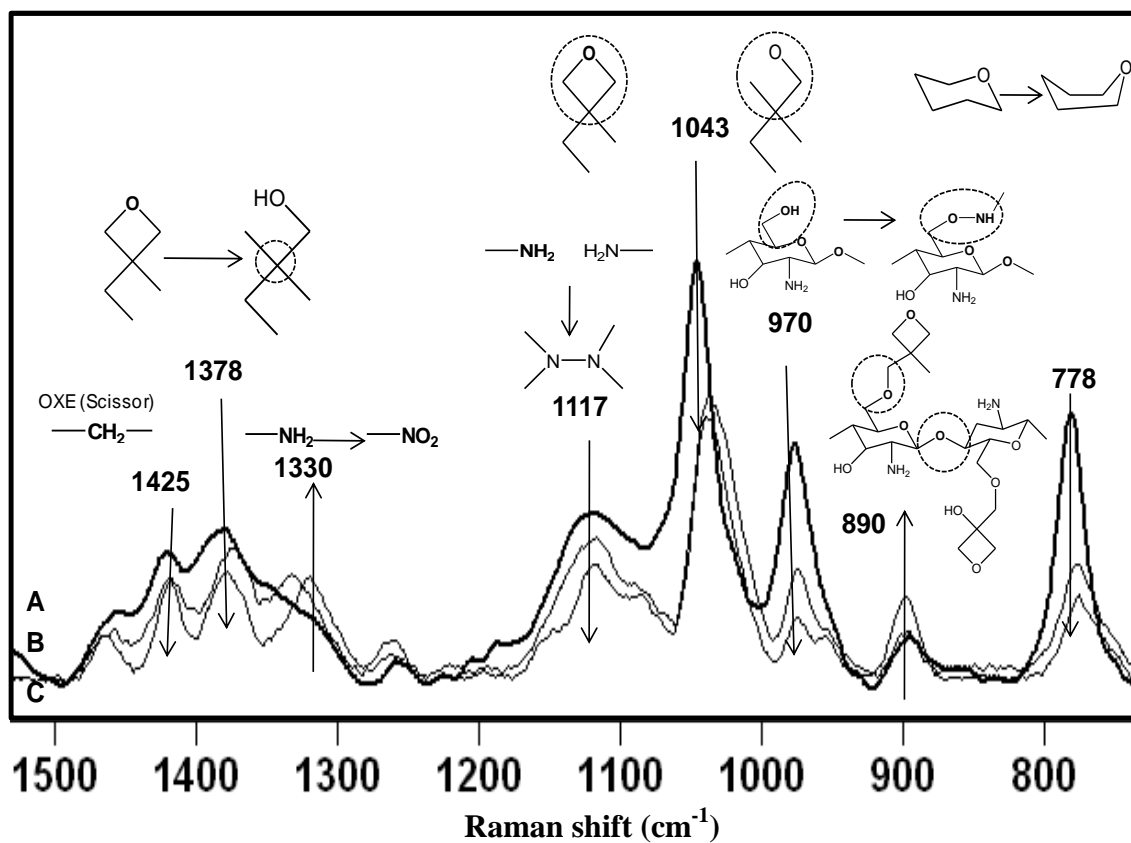


Figure B.6. Raman spectra of OXE-CHI (1:10), before (A), after 60 min of UV exposure (B), and 7 days later (C) of UV exposure; arrow directions point out increasing (↑) and decreasing (↓) intensities of relevant bands.

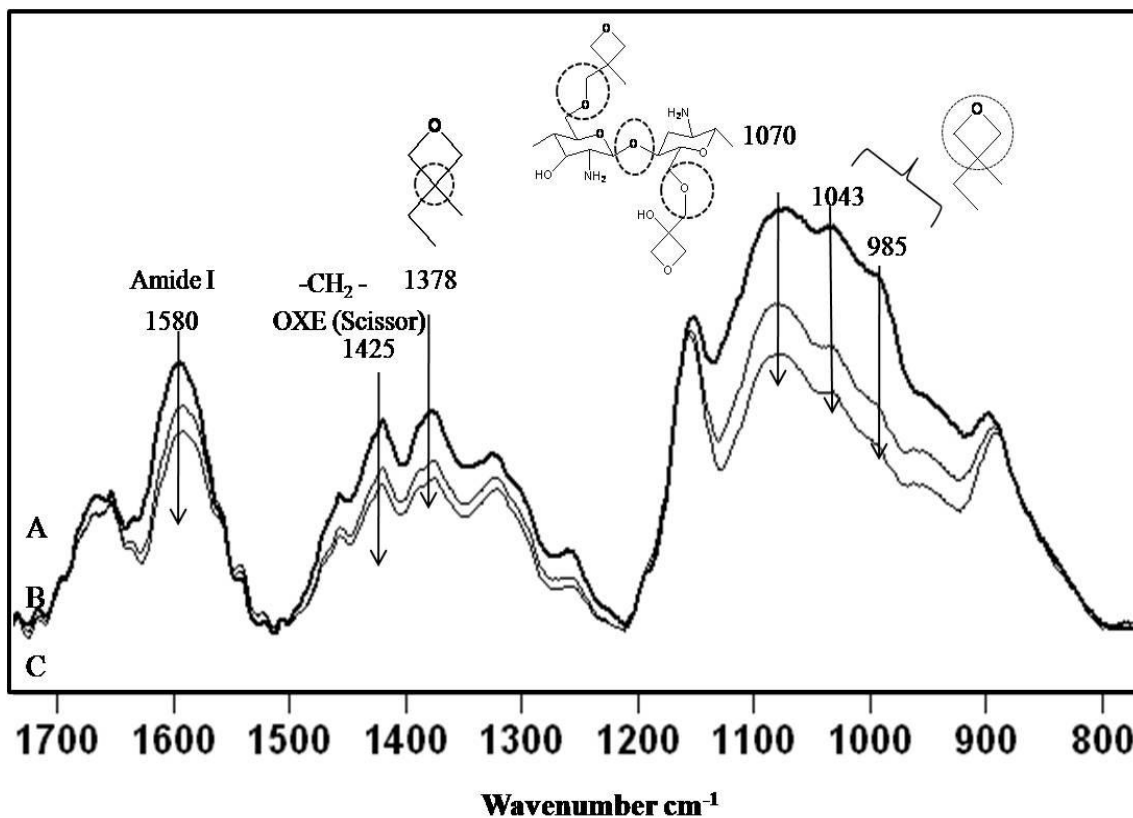


Figure B.7. ATR FT-IR spectra of OXE-CHI (1:1), before (A), after 60 min of UV exposure (B), and 7 days later (C) of UV exposure; arrow directions point out increasing (↑) and decreasing (↓) intensities of relevant bands.

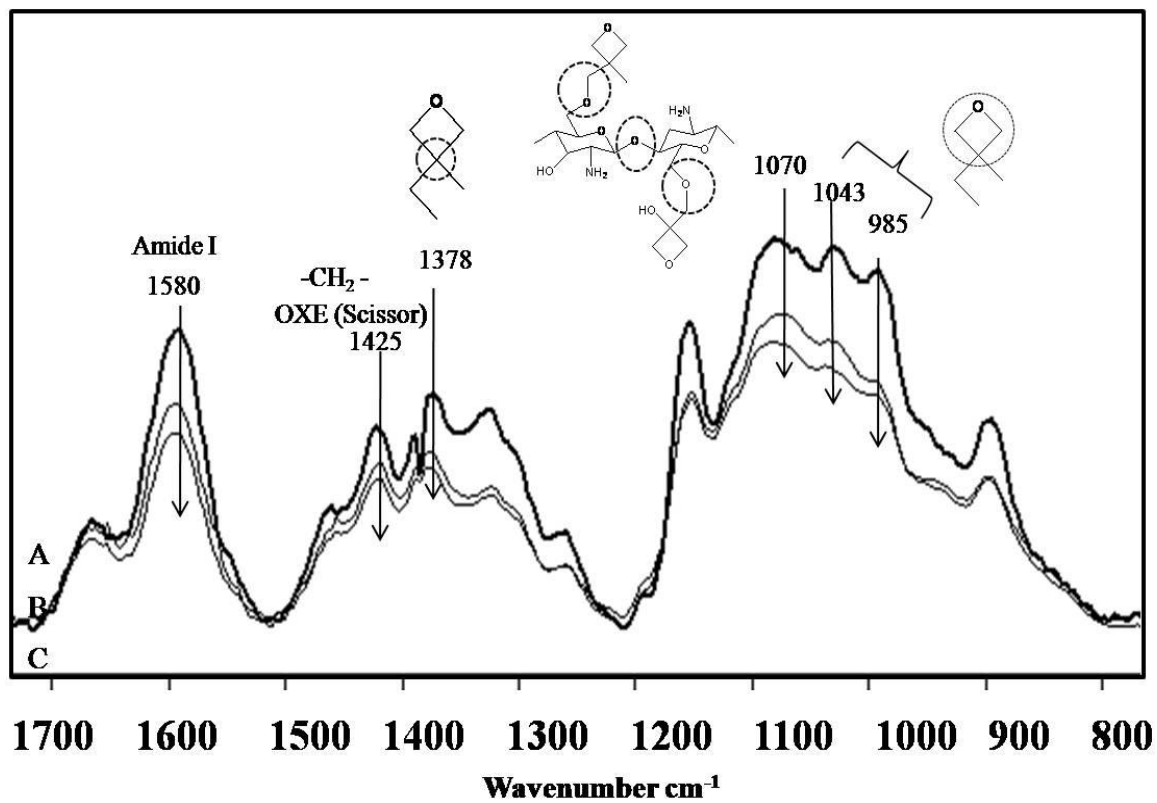


Figure B.8. ATR FT-IR spectra of OXE-CHI (1:2), before (A), after 60 min of UV exposure (B), and 7 days later (C) of UV exposure; arrow directions point out increasing (↑) and decreasing (↓) intensities of relevant bands.

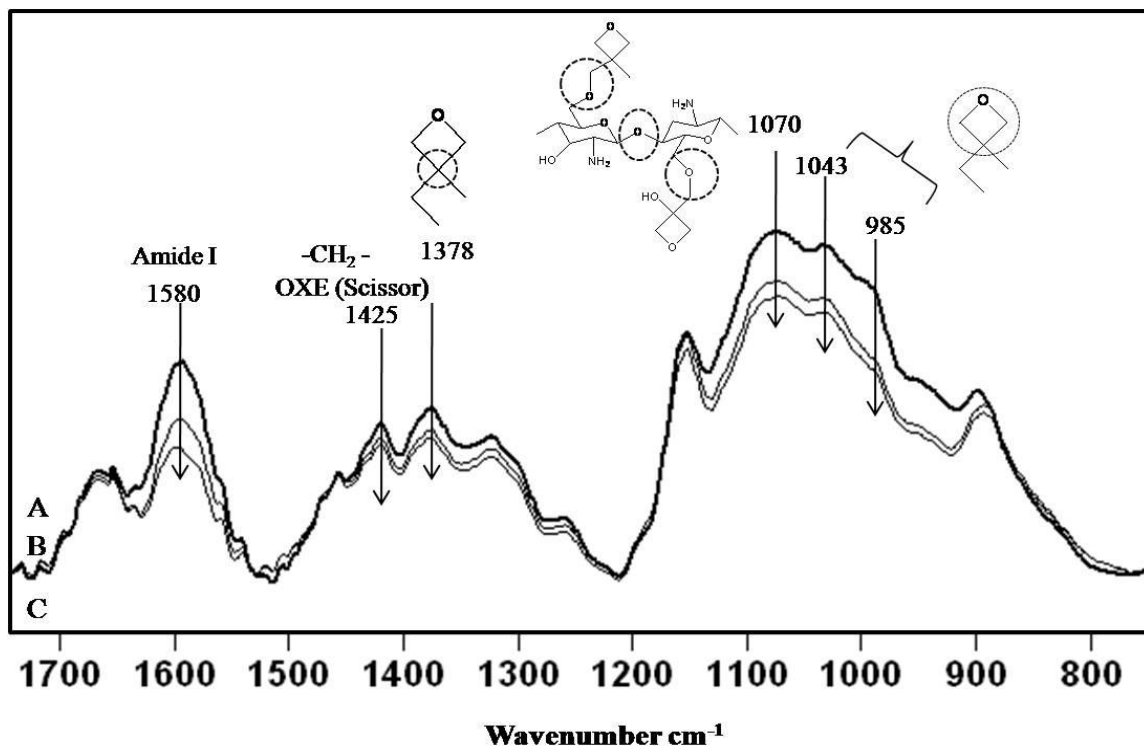


Figure B. 9. ATR FT-IR spectra of OXE-CHI (1:4), before (A), after 60 min of UV exposure (B), and 7 days later (C) of UV exposure; arrow directions point out increasing (↑) and decreasing (↓) intensities of relevant bands.

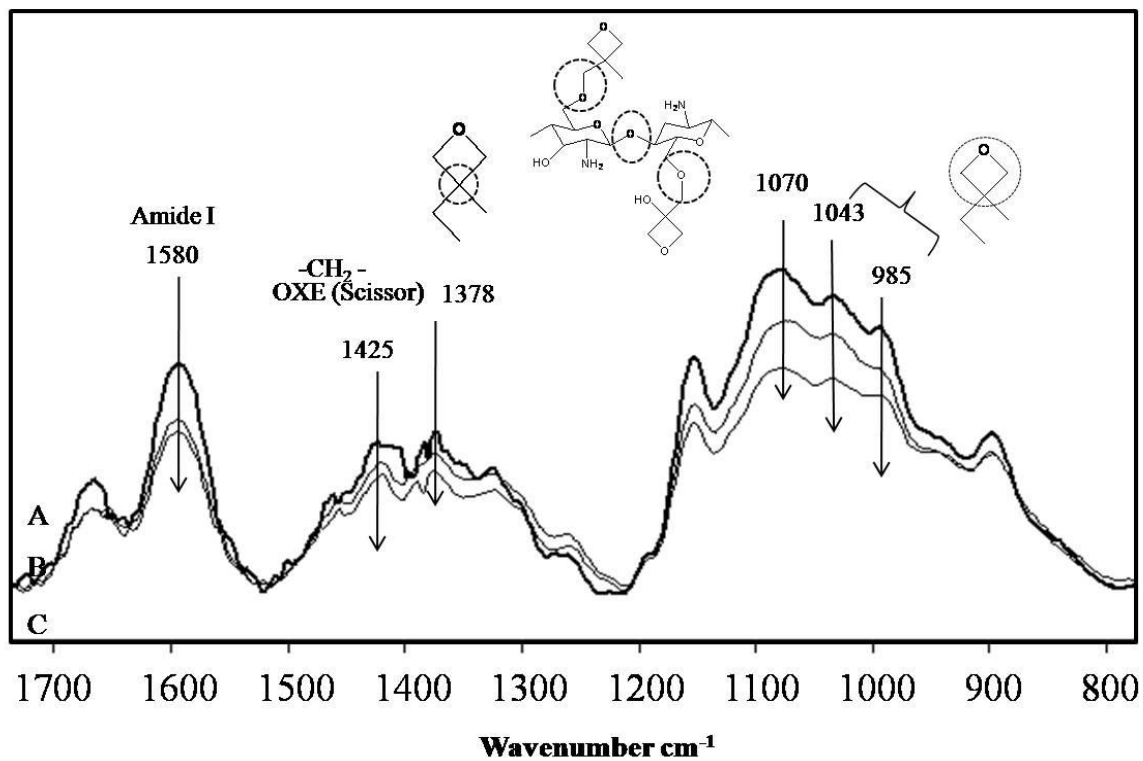


Figure B.10. ATR FT-IR spectra of OXE-CHI (1:6), before (A), after 60 min of UV exposure (B), and 7 days later (C) of UV exposure; arrow directions point out increasing (↑) and decreasing (↓) intensities of relevant bands.

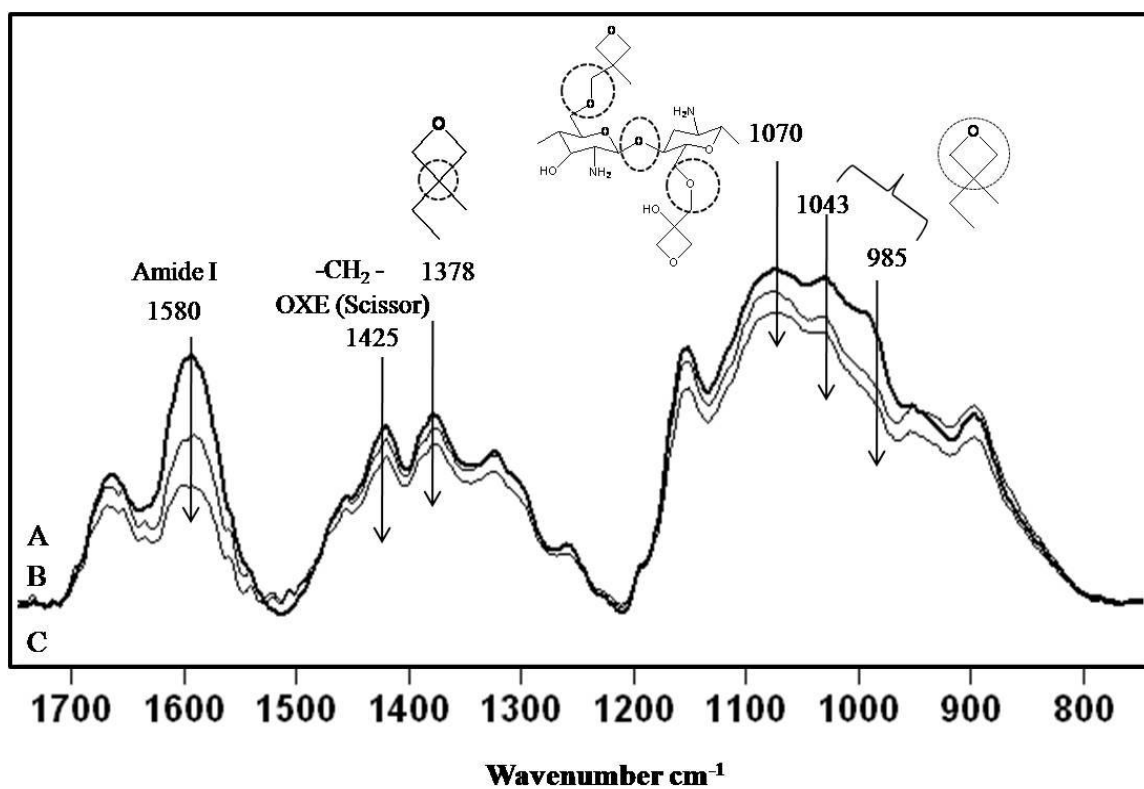


Figure B.11. ATR FT-IR spectra of OXE-CHI (1:10), before (A), after 60 min of UV exposure (B), and 7 days later (C) of UV exposure; arrow directions point out increasing (↑) and decreasing (↓) intensities of relevant bands.

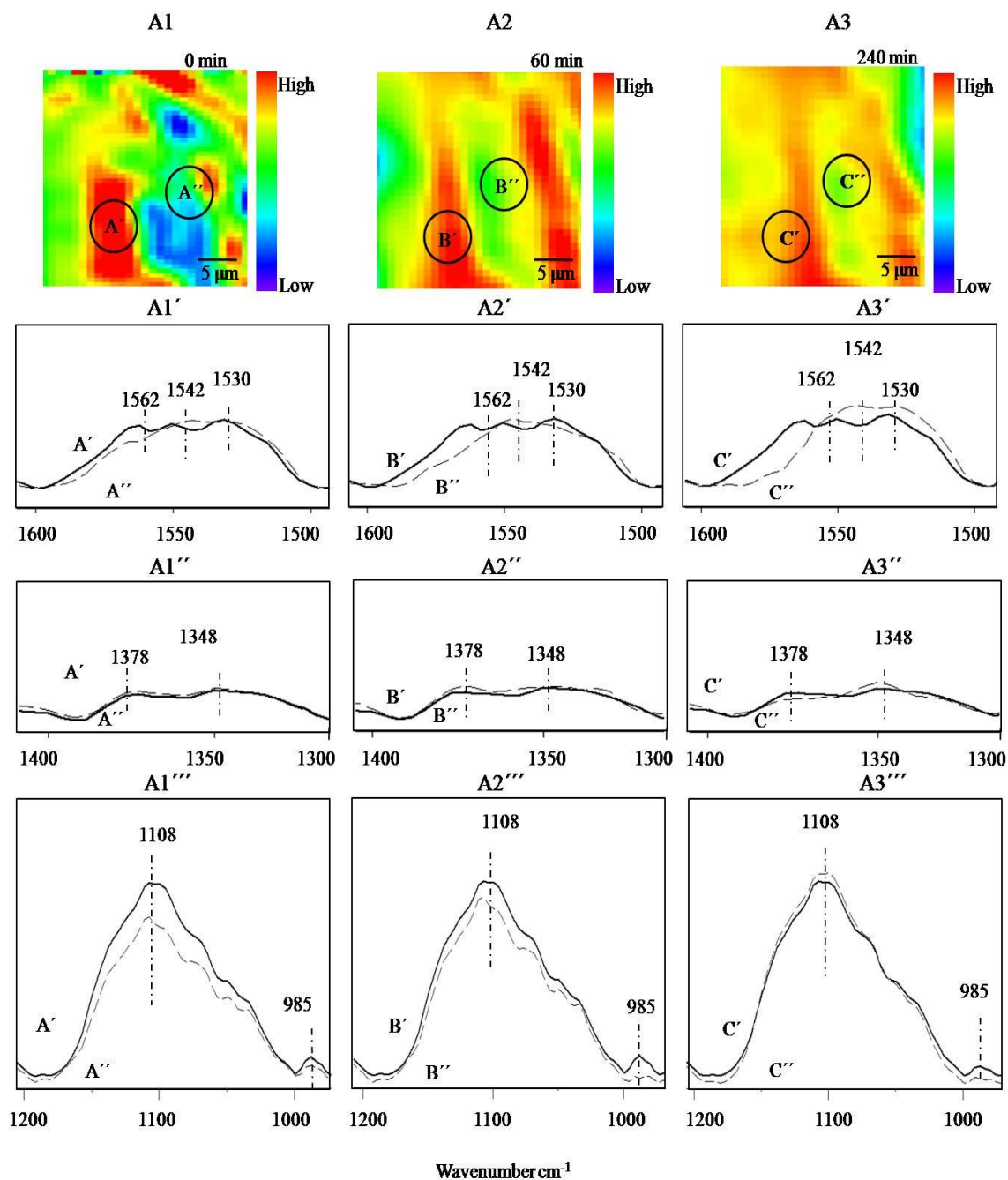


Figure B.12. IRIRI images of OXE-CHI-PUR networks (HDI:PEG:OXE-CHI:DBTDL =1.0:1.33:1.17 $\times 10^{-4}$:2 $\times 10^{-5}$) containing 1:4 molar OXE-CHI as well as 1% HALS recorded as a UV exposure time 0, 30, and 120 min, respectively. (A1-A3) images were obtained by tuning into the 1542 cm^{-1} band; (A1'-A3', A1''-A3'', A1'''-A3''') IR spectra recorded from mechanically damaged and undamaged areas.

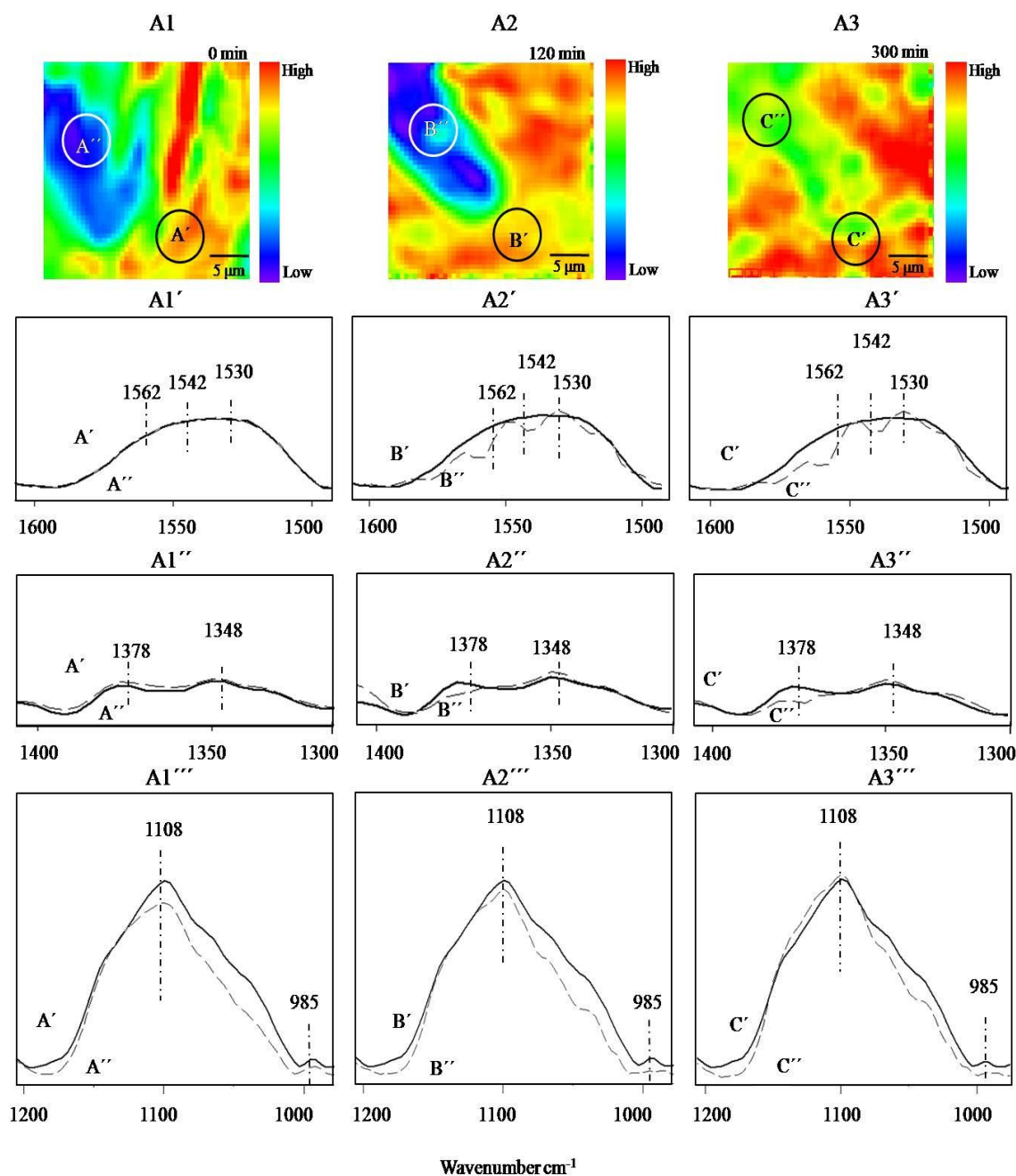


Figure B.13. IRIRI images of OXE-CHI-PUR networks (HDI:PEG:OXE-CHI:DBTDL =1.0:1.33:1.17x10⁻⁴:2x10⁻⁵) containing 1:10 molar OXE-CHI as well as 1% HALS recorded as a UV exposure time 0, 30, and 120 min, respectively. (A1-A3) images were obtained by tuning into the 1542 cm⁻¹ band; (A1'-A3', A1''-A3'', A1'''-A3''') IR spectra recorded from mechanically damaged and undamaged areas.

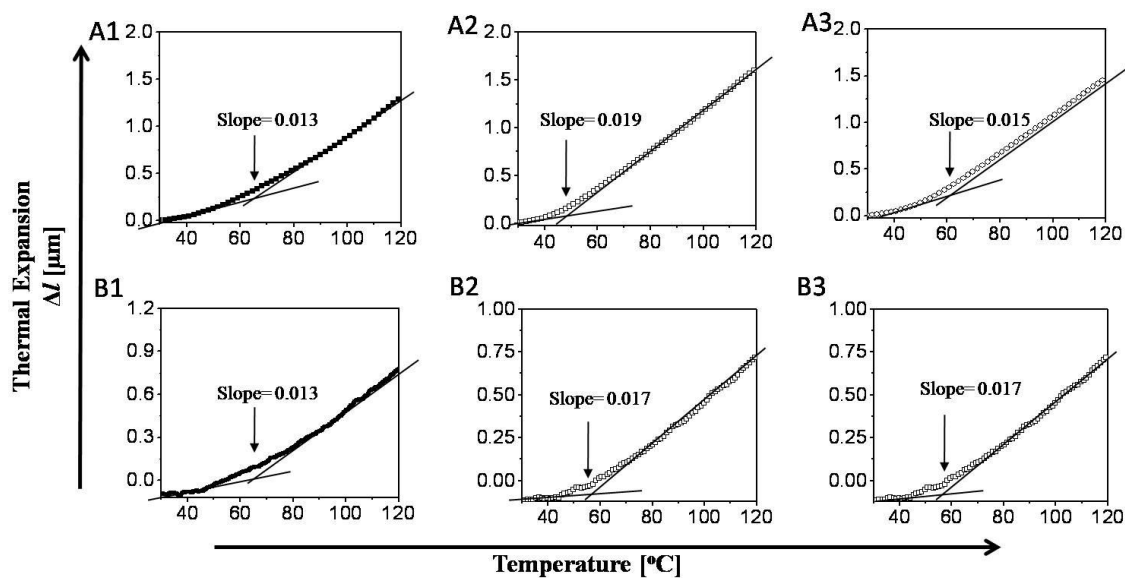


Figure B.14. Thermal expansion (Δl) plotted as a function of temperature of undamaged (A1), damaged (A2), and repaired (A3) OXE-CHI-PUR network (HDI:PEG:OXE-CHI=1.0:1.33:1.17 $\times 10^{-4}$). Thermal expansion (Δl) vs temperature of undamaged (A1), damaged (A2), and repaired (A3) PUR network.

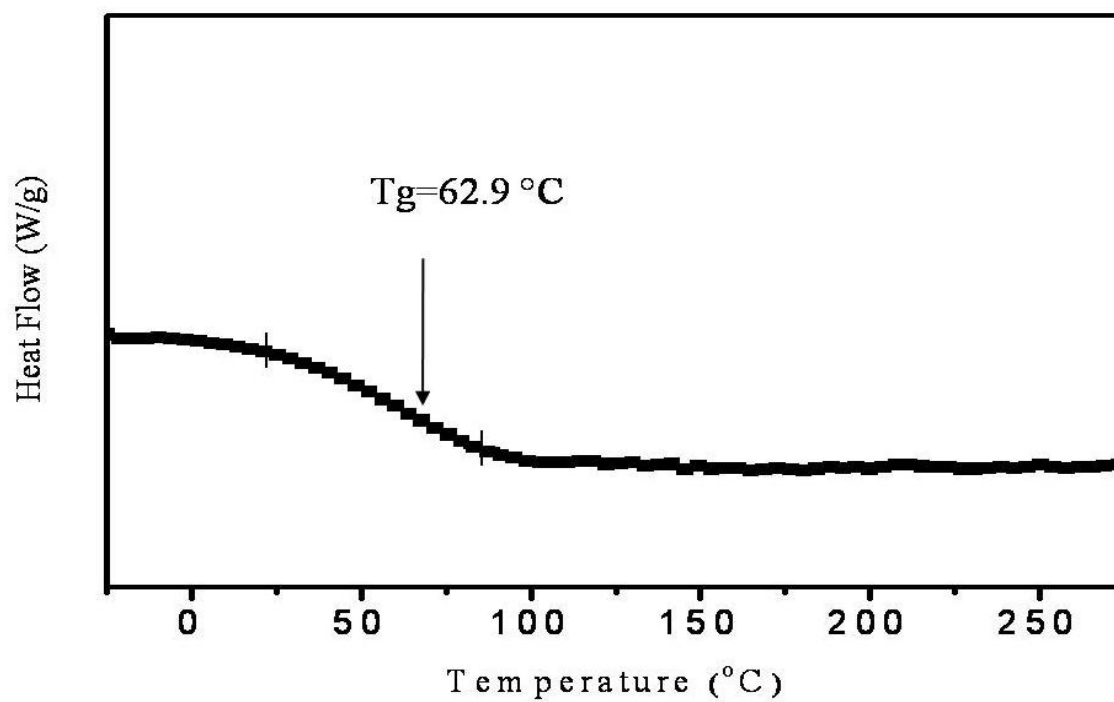


Figure B.15. DSC thermogram of OXE-CHI-PUR network (HDI:PEG:OXE-CHI=1.0:1.33:1.17x10⁻⁴).

Table B.1

Vibrational Bands Observed in Raman Measurements for 1:1, 1:2, 1:4, 1:6, and 1:10

OXE-CHI Molar Ratios. Arrows $\uparrow\downarrow$ Indicate Band Increase or Decrease for a Given

OXE-CHI Ratio

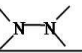
Raman OXE-CHI	1425 cm ⁻¹ -CH ₂ - scissor of OXE	1378 cm ⁻¹ -C ₄ of OXE	1330cm ⁻¹ -NO ₂	1117cm ⁻¹ 	1043 cm ⁻¹ -CH ₂ -O- stretch vib of OXE and linear alkyl ether	970 cm ⁻¹ 1° -OH	890 cm ⁻¹ -C-O-C-	778 cm ⁻¹ Chair-to-boat
1:1	↓	↓	-	↑	↓	↑	↑	↓
1:2	↓	↓	-	↑	↓	↑	↑	↓
1:4	↓	↓	↑	↓	↓	↓	↑	↓
1:6	↓	↓	↑	↓	↓	↓	↑	↓
1:10	↓	↓	↑	↓	↓	↓	↑	↓

Table B.2

Vibrational Bands Observed in IR Measurements 1:1, 1:2, 1:4, 1:6, and 1:10 OXE-CHI

Molar Ratios Arrows $\uparrow\downarrow$ Indicate Band Increase or Decrease for a Given OXE-CHI

Ratio

IR OXE-CHI	1580 cm ⁻¹ Amide I	1425 cm ⁻¹ -CH ₂ - scissor of OXE	1378 cm ⁻¹ -C ₄ of OXE	1070 cm ⁻¹ -C-O-C- stretch of CHI and OXE	1043 cm ⁻¹ -C-O-C- stretch of CHI	985 cm ⁻¹ -C-O-C- stretch of OXE
1:1	↓	↓	↓	↓	↓	↓
1:2	↓	↓	↓	↓	↓	↓
1:4	↓	↓	↓	↓	↓	↓
1:6	↓	↓	↓	↓	↓	↓
1:10	↓	↓	↓	↓	↓	↓

References

1. Ghosh, B.; Urban, M. W. *Science*, **2009**, 323, 1458.
2. Vuen, D. L.; Colthup, N. B.; Fateley, W. G.; Grasselli, J. G. *The Handbook of Infrared and Raman Characteristic Frequencies of Organic Molecules*, Academic Press, California, 1991.
3. Pretsch E., B. P., Affolter C., *Structure Determination of Organic Compounds*. 3rd ed.; Springer: 2000.
4. Krauffmann, H. *Ber.* **1906**, 39, 1959.

APPENDIX C

SUPPORTING INFORMATION FOR CHAPTER V

Synthesis of OXO-CHI Macromonomer

Figure C.1 illustrates a two-step reaction sequence leading to the OXO-CHI-PUR network synthesis. In the first step, CHI was dispersed in 50 % w/w NaOH solution at -5 °C for 24 h followed by -18 °C for 48 h. The reaction mixture was thawed to room temperature and reacted with tetrahydro-furfuryl chloride (OXO-Cl) to substitute the primary -OH groups of CHI in C₆ position with OXO ring as well as conversion of acetamide (-NHCOCH₃) functionalities to -NH₂ groups. OXO-CHI was isolated from the reaction mixture by precipitation and washed with methanol to neutralize it. In the next step, OXO-CHI was dispersed in DMSO and reacted with trifunctional HDI monomer and polyethylene glycol (PEG) in presence of DBTDL catalyst, resulting formation of OXO-CHI-PUR networks.

In order to determine the attachment of 5-membered OXO ring at the backbone of CHI macromonomer ATR FT-IR and ¹³C NMR analysis were conducted. As shown in Figure C.2, Traces A and B represent FT-IR spectra of CHI and OXO-CHI respectively. As seen, the intensity of 1665 cm⁻¹ corresponding to -C=O stretching vibrations of acetamide groups of CHI decreases, at the same time the intensity of 1580 cm⁻¹ corresponding to amide I increases in Trace B compared to Trace A. These observations suggest the conversion of acetamide groups into amide groups under experimental condition. On the other hand, new bands appear at 1326, and 1080 cm⁻¹ corresponding to

–CH₂– deformation vibration and –C–O–C– stretching vibration of OXO suggesting OXO ring attachment at the backbone of CHI.

Again, to confirm the incorporation of OXO ring within CHI backbone Figure C.3, Traces A and B represent ¹³C NMR spectra of CHI and OXO-CHI, respectively. In Trace A characteristics resonances due to carbonyl carbon (a) of acetamide group in glycosine units and carbon (b) attributed to the methyl of -NHCOCH₃ group at 175 and 22.5 ppm are detected, respectively. These resonances are not detected in Trace B due to the conversion of acetamide into primary amine groups and give rise to new resonances at 33 and 24 ppm which correspond to carbon atoms (a) and (b) of OXO ring, respectively.

Micro-Thermal Analysis

Figure C.4, A1-A3, B1-B3, illustrates normalized $d(\Delta l)/dT$ values for undamaged, damaged, and self-repair areas plotted as a function of temperature, for OXO-CHI-PUR networks containing OXO-CHI of 1:4, and 1:10 molar ratios, respectively. As seen in Figure C.4-A1, the rate of $d(\Delta l)/dT$ changes with T, and the maximum value is detected at 48 °C, which corresponds to the T_g values. However, in the damaged area the $d(\Delta l)/dT$ maximum is lowered to 46 °C, and the width of the $d(\Delta l)/dT$ values also increase, indicating the lower T_g values inside the scratch. Upon exposure to UV, the $d(\Delta l)/dT$ maximum shifts to 50 °C. Similarly, for OXO-CHI-PUR networks containing 1:10 molar ratios OXO-CHI, the $d(\Delta l)/dT$ maximum at 47 °C decreases to 45 °C upon mechanical damage, but remain unchanged when exposed to UV.

Model OXO-CHI Macromonomer Experiments

To determine UV sensitivity of OXO-CHI macromonomer, a series of model experiments were conducted in which OXO-CHI molar ratio was varied from 1:1, 1:4, and 1:10. Figures C.5-C.7, Traces A, B, and C show ATR FT-IR spectra collected as a function of UV exposure for 0, 60 min and 7 days, respectively, for 1:1, 1:4, and 1:10 OXO-CHI molar ratios. Comparison of Traces A and B in Figure A.C.5 shows that the bands corresponding to amide I as well as $\text{-CH}_2\text{-}$ deformation and -C-O-C- stretching vibrations of OXO ring at 1585, 1326, and 1080 cm^{-1} , respectively, decrease upon UV exposure. OXO-CHI with 1:4, and 1:10 molar ratios show the same results, but decrease in band intensity is lower compared to OXO-CHI containing 1:1 OXO-CHI molar ratios. These changes are also pointed out in Figures C.5-C.7 by arrow directions which depict response of relevant bands. Table C.1 lists all IR bands sensitive to UV exposure.

Figures C.8-C.10, Traces A, B, and C illustrate Raman spectra of OXO-CHI macromonomer for 1:1, 1:4, and 1:10 stoichiometries exposed to the same conditions. Comparison of Traces A and B in Figure C.8 shows the increase of the 1336 cm^{-1} band and decrease of 1117 cm^{-1} due oxidation of -NH_2 to -NO_2 and loss of hydrazine, respectively, upon UV exposure. On the other hand, the intensity of 1080, and 900 cm^{-1} bands due to asymmetric and symmetric -C-O-C- stretching vibrations of OXO also decrease. Again, the bands at 1042, and 972 cm^{-1} corresponding to -C-O-C- stretching vibrations of linear aliphatic ether and 1°-OH , respectively increase. These observations suggest OXO ring opening upon UV exposure. Furthermore, the band at 778 cm^{-1} increases which signifies conformational chair-to-boat conversion of glycosine units along the CHI-backbone. As shown in Trace C, further UV exposure of OXO-CHI

macromonomer resulting amplification of these changes which indicate the continuation of free radical reactions. Figures C.9-A.C.10, illustrating Raman spectra of OXO-CHI macromonomer containing 1:4, and 1:10 molar ratios, respectively, showed the same result, although smaller magnitude of band intensities were observed. These changes are also pointed out in Figures C.8-C.10 by arrow directions which depict response of relevant bands. Table C.2 lists all spectroscopic changes of Raman bands resulting from UV exposure.

These ATR FT-IR and Raman analysis of the intensity changes of the vibrational bands sensitive to UV exposure allowed us to identify reactions resulting from UV exposure which are summarized in Figure C.11: (a) OXO ring opening, reflected by the decrease of the -C-O-C- vibrations at 1080 , and 900 cm^{-1} , $\text{-CH}_2\text{-}$ deformation mode of OXO-ring at 1326 cm^{-1} ; (b) chain scission of the -C-O-C- segments shown by the increase of the linear -C-O-C- stretching vibrations at 1042 ; (c) the chair-to-boat conformational changes of pyranose units of CHI reflected by the increase of the 778 cm^{-1} band; (d) NH_2 oxidation, leading to the formation of NO_2 shown by the decrease of amide I band at 1580 cm^{-1} band as well as increase of 1336 cm^{-1} band corresponding to -NO_2 and (e) the formation of hydrazine manifested by the appearance of the band at 1117 cm^{-1} .

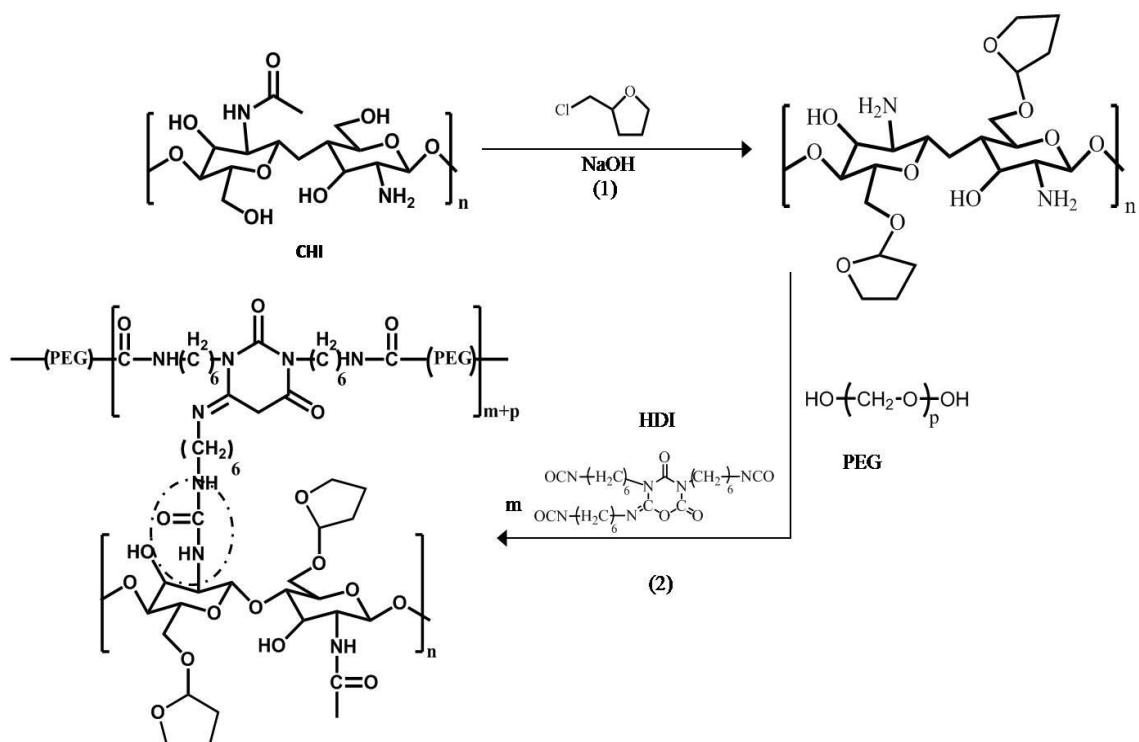


Figure C.1. Synthetic steps involved in the formation of OXO-CHI-PUR networks; 1) Reactions of OXO with CHI leading to the formation of OXO-CHI macromonomer; 2) Reactions of OXO-CHI with HDI and PEG leading to formations of OXO-CHI-PUR network.

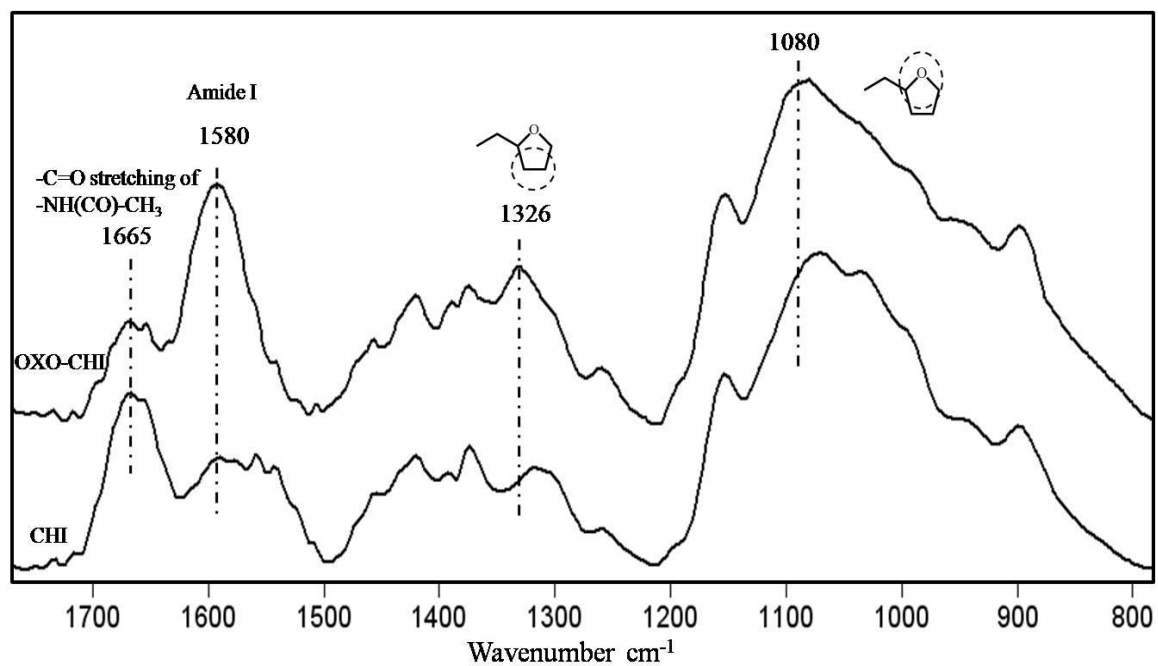


Figure C.2. ATR FT-IR spectra of CHI and OXO-CHI macromonomer.

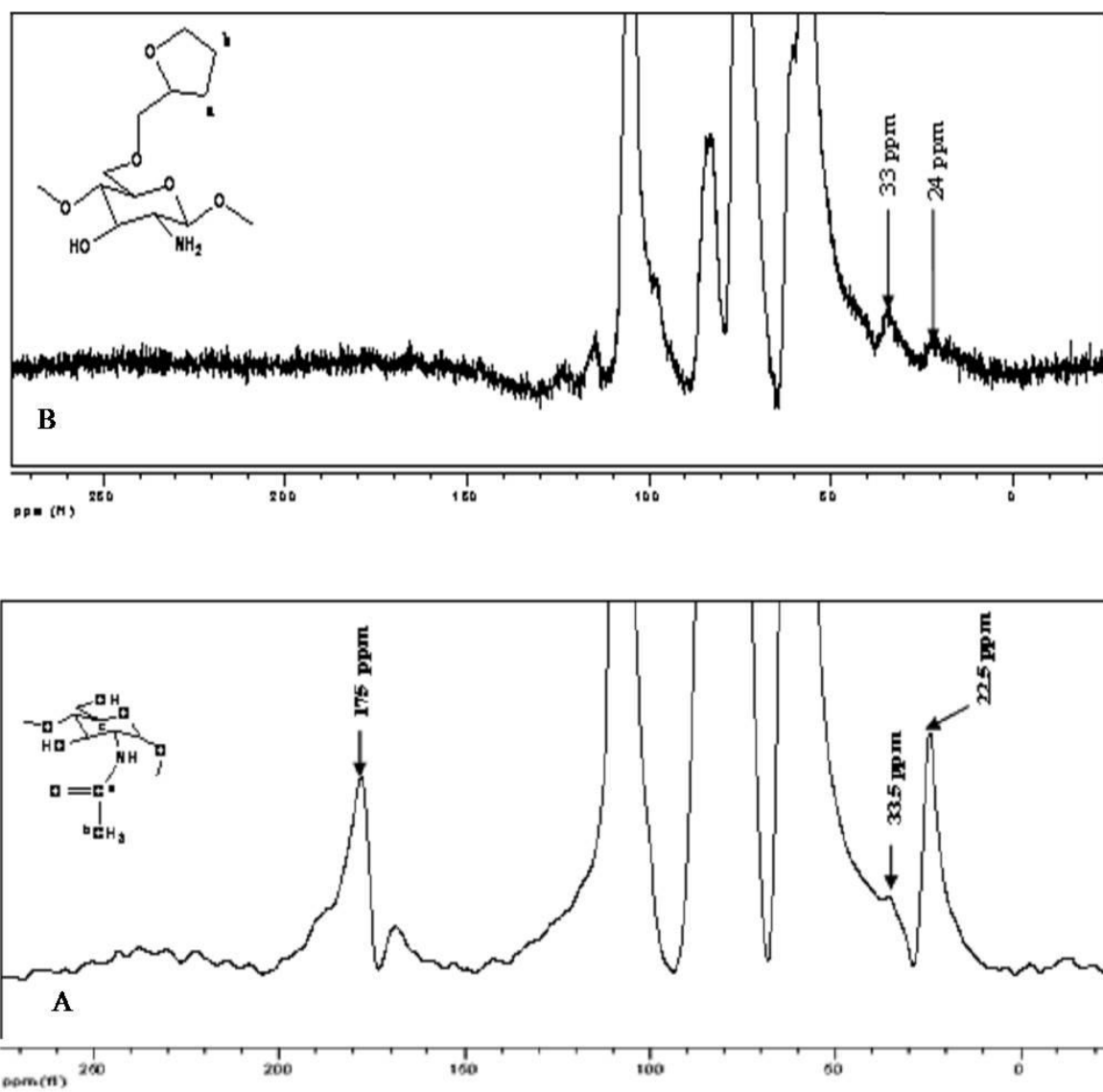


Figure C.3. ^{13}C NMR spectra of (A) CHI, and (B) OXO-CHI macromonomer.

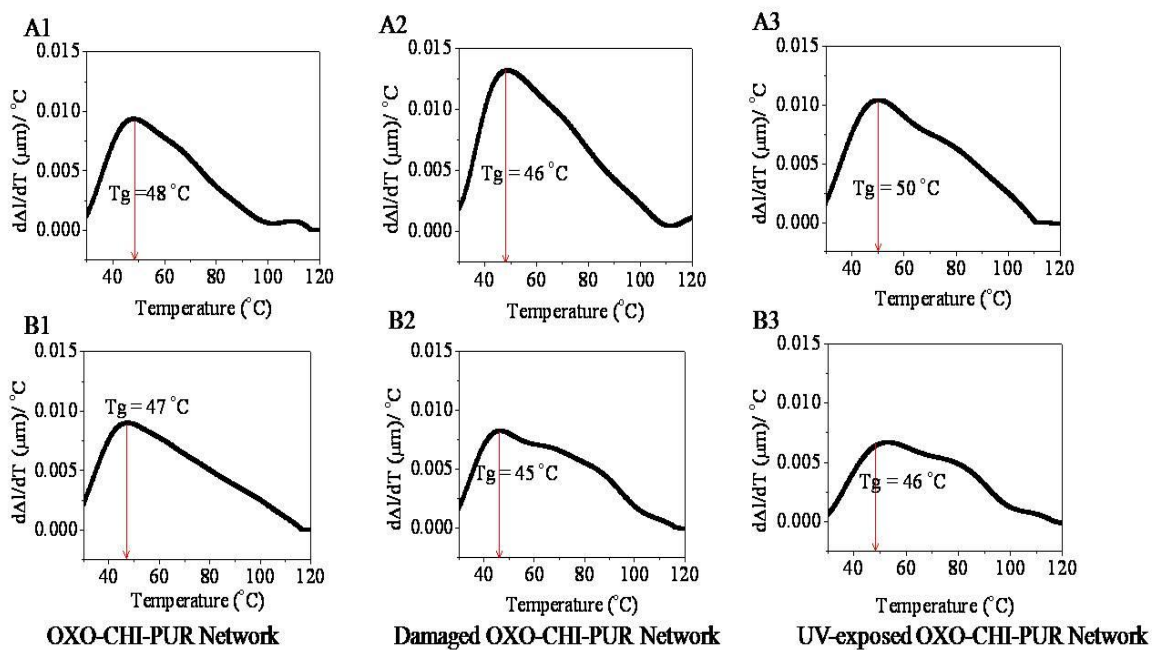


Figure C.4. Plot of $d(\Delta l)/dT$ vs temperature of OXO-CHI-PUR network (HDI:PEG:OXO-CHI:DBTDL = 1.0:1.33:1.17 $\times 10^{-4}$:2 $\times 10^{-5}$) containing OXO-CHI of 1:4 (A1-A3), and 1:10 (B1-B3) molar ratios, respectively.

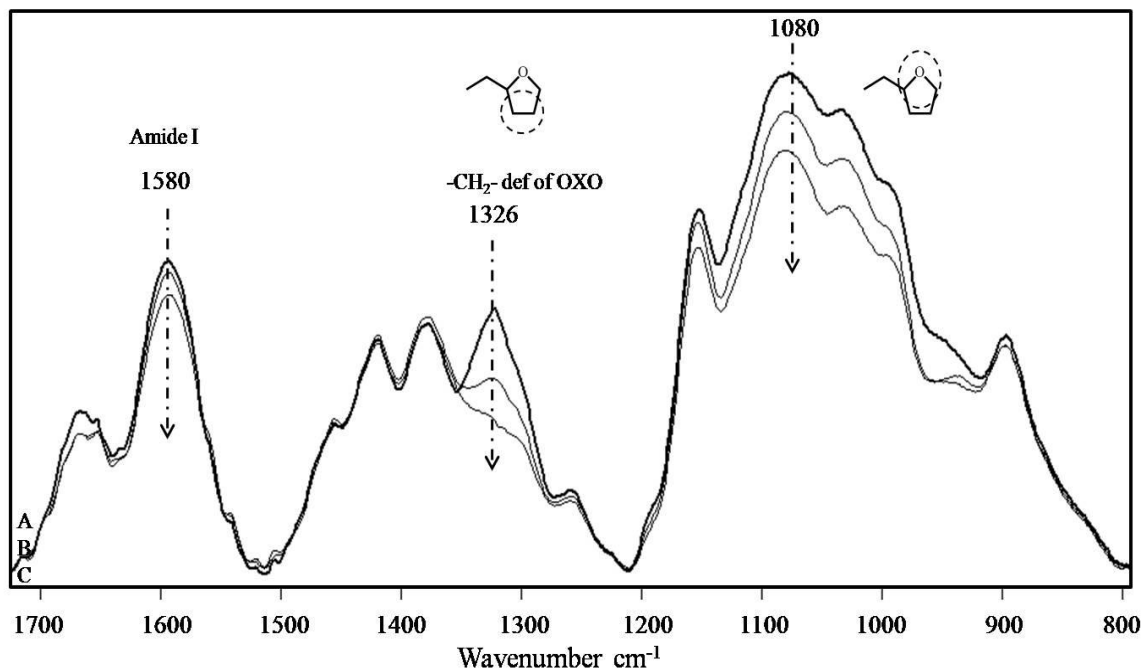


Figure C.5. ATR FT-IR spectra of OXO-CHI (1:1), before (A), after 60 min of UV exposure (B), and 7 days later (C) of UV exposure; arrow directions point out increasing (↑) and decreasing (↓) intensities of relevant bands.

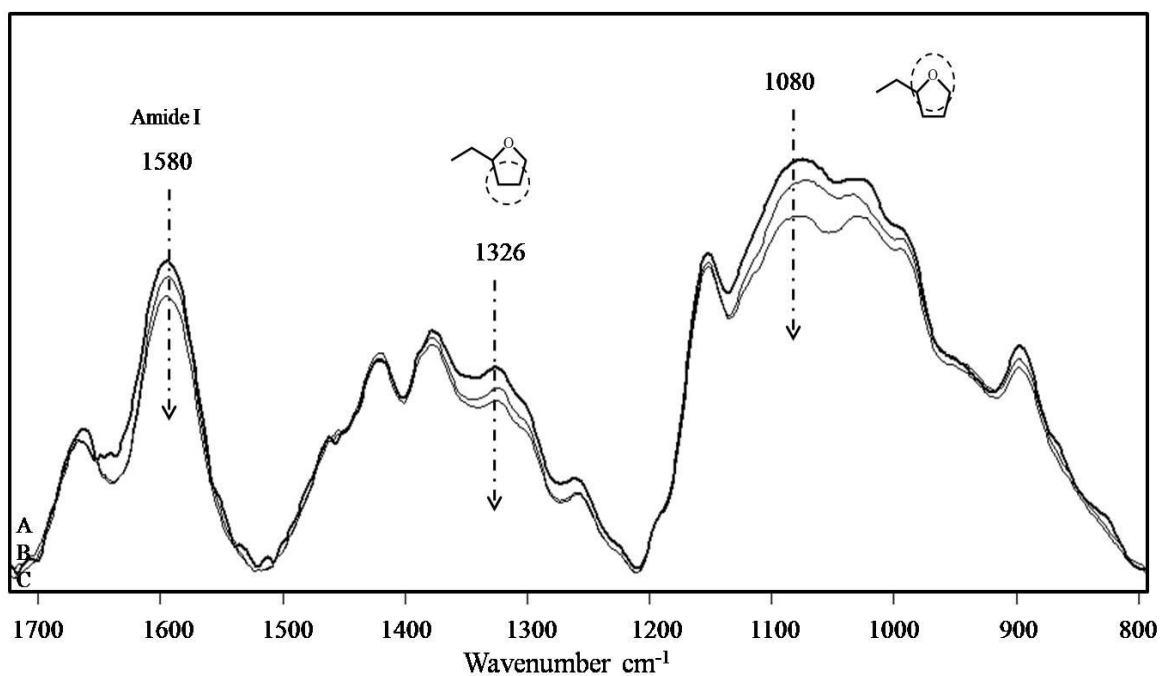


Figure C.6. ATR FT-IR spectra of OXO-CHI (1:4), before (A), after 60 min of UV exposure (B), and 7 days later (C) of UV exposure; arrow directions point out increasing (↑) and decreasing (↓) intensities of relevant bands.

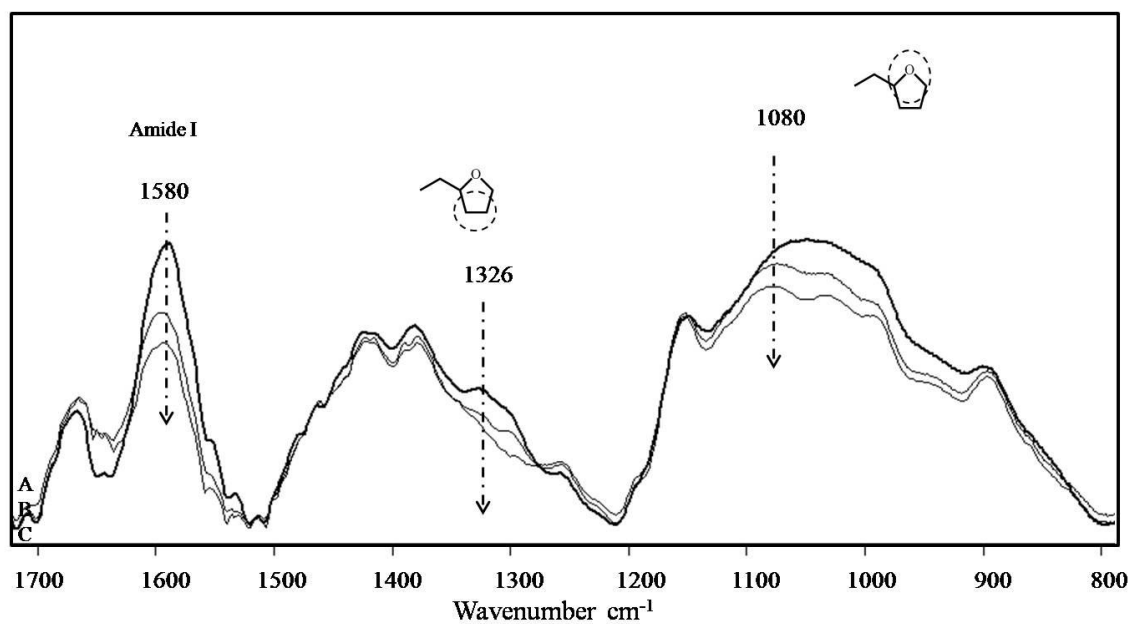


Figure C.7. ATR FT-IR spectra of OXO-CHI (1:10), before (A), after 60 min of UV exposure (B), and 7 days later (C) of UV exposure; arrow directions point out increasing (↑) and decreasing (↓) intensities of relevant bands.

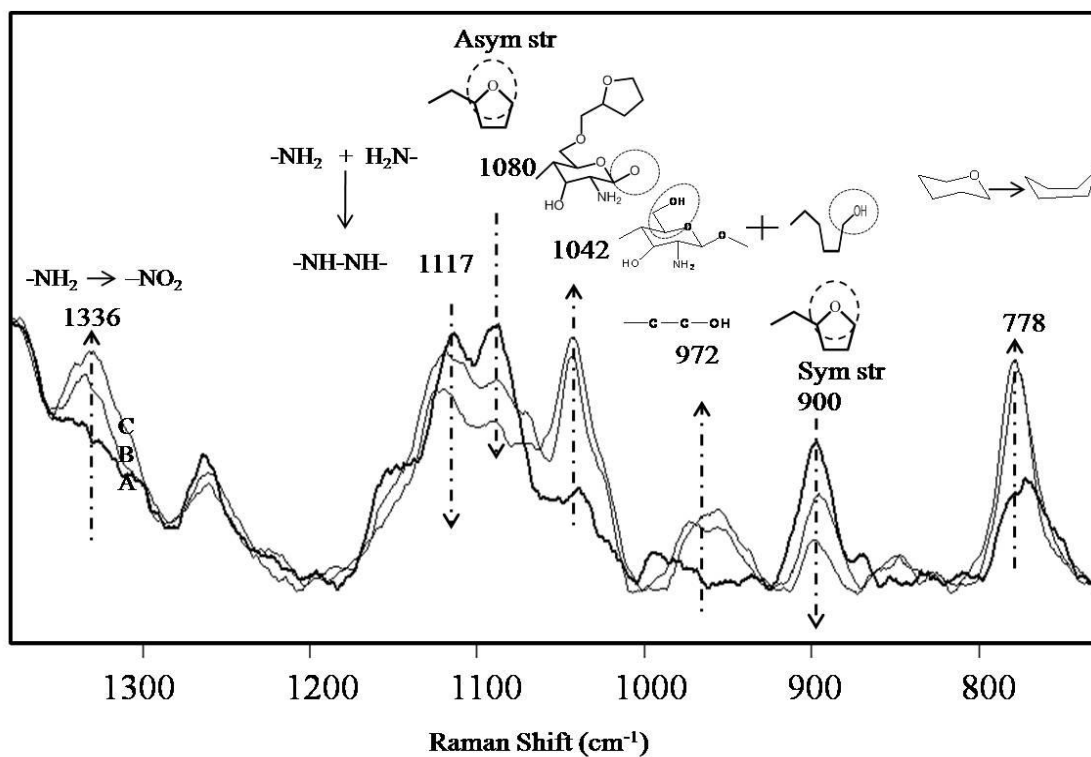


Figure C.8. Raman spectra of OXO-CHI (1:1), before (A), after 60 min of UV exposure (B), and 7 days later (C) of UV exposure; arrow directions point out increasing (\uparrow) and decreasing (\downarrow) intensities of relevant bands.

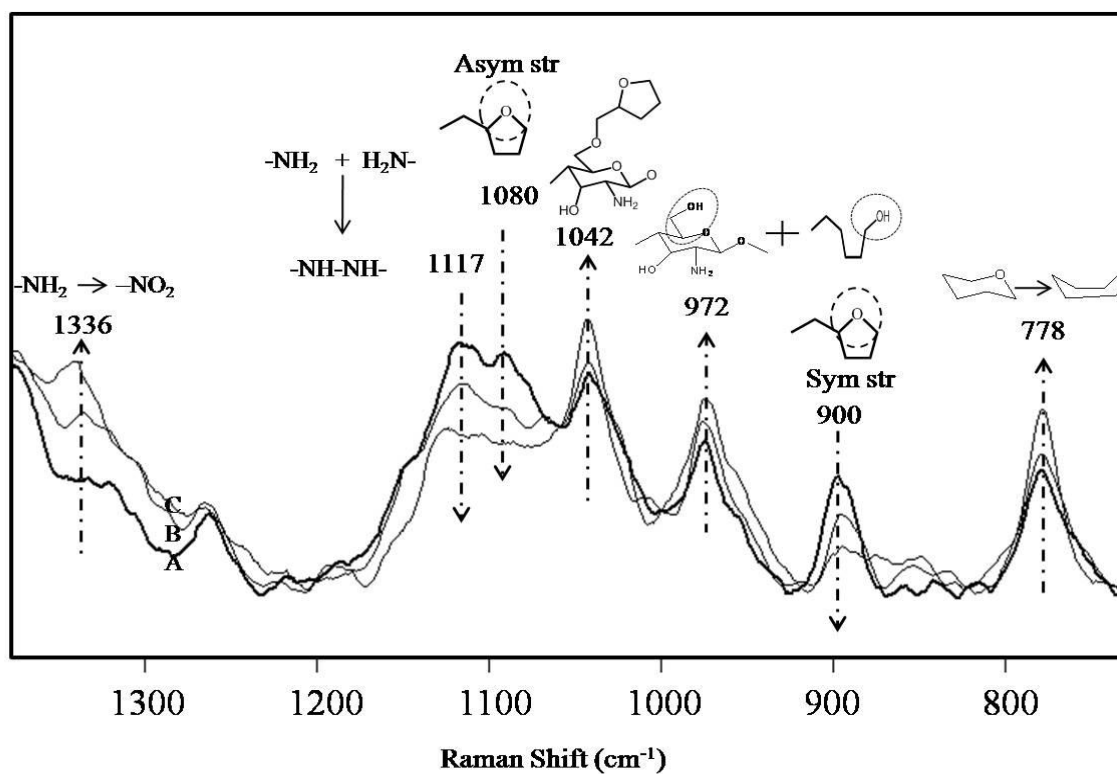


Figure C.9. Raman spectra of OXO-CHI (1:4), before (A), after 60 min of UV exposure (B), and 7 days later (C) of UV exposure; arrow directions point out increasing (\uparrow) and decreasing (\downarrow) intensities of relevant bands.

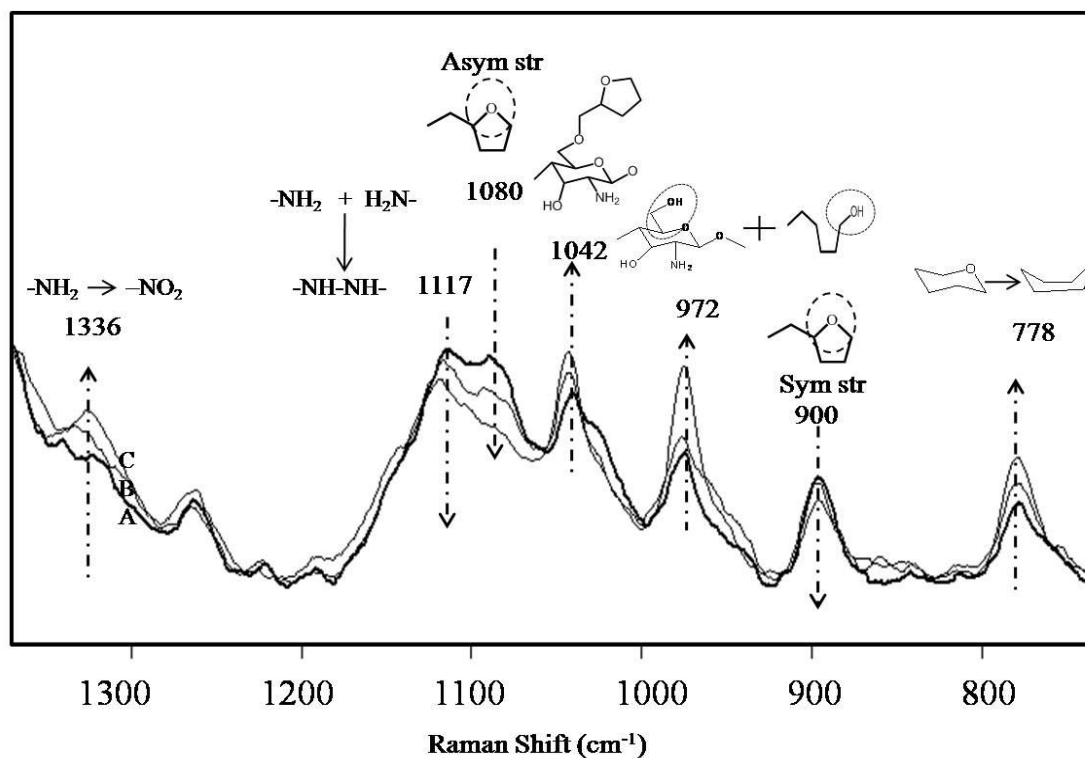


Figure C.10. Raman spectra of OXO-CHI (1:4), before (A), after 60 min of UV exposure (B), and 7 days later (C) of UV exposure; arrow directions point out increasing (↑) and decreasing (↓) intensities of relevant bands.

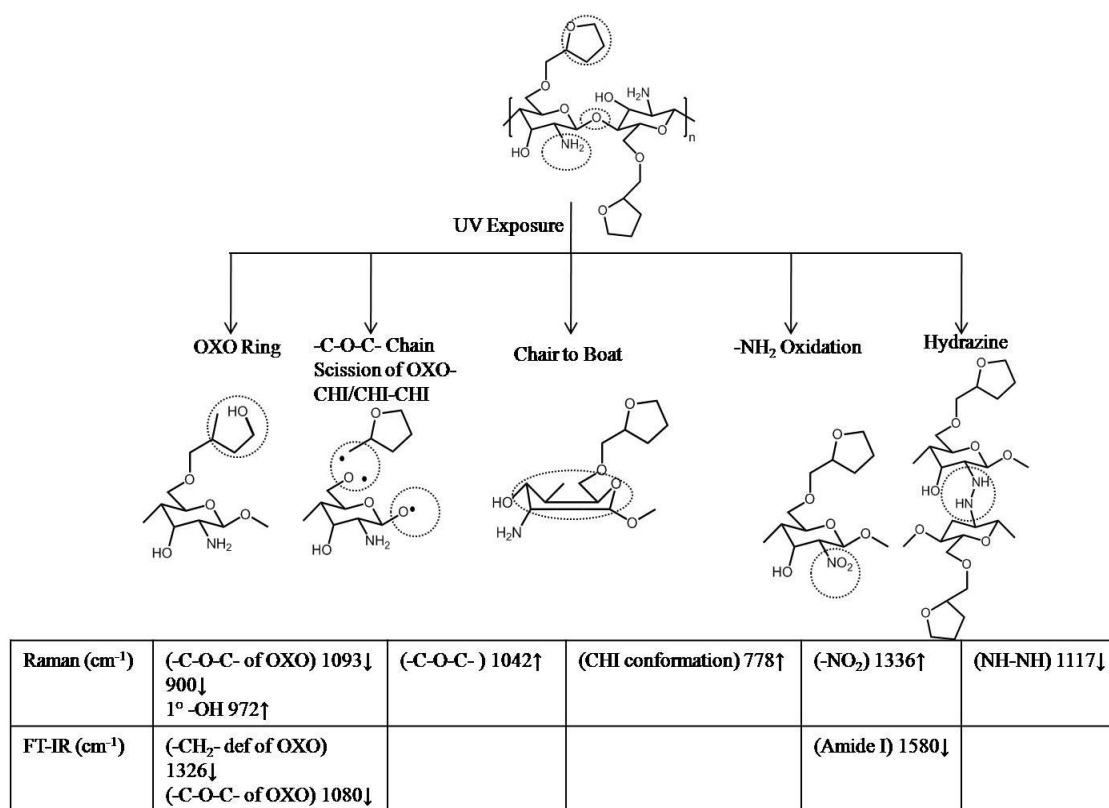


Figure C.11. Schematic diagram of reaction products and band assignments obtained from UV exposure of OXO-CHI.

Table C.1

Vibrational Bands Observed in IR Measurements 1:1, 1:4, and 1:10 OXO-CHI Molar

Ratios Arrows $\uparrow\downarrow$ Indicate Band Increase or Decrease for a Given OXO-CHI Ratio


IR OXO-CHI	1580 cm ⁻¹ Amide I	1326 cm ⁻¹ -CH ₂ - def of OXO	1080 cm ⁻¹ -C-O-C- stretch of OXO
1:1	↓	↓	↓
1:4	↓	↓	↓
1:10	↓	↓	↓

Table C.2

Vibrational Bands Observed in Raman Measurements 1:1, 1:4, and 1:10 OXO-CHI

Molar Ratios Arrows $\uparrow\downarrow$ Indicate Band Increase or Decrease for a Given OXO-CHI

Ratio

Raman OXO-CHI	1336 cm ⁻¹ -NO ₂	1117 cm ⁻¹ 	1080 cm ⁻¹ Asym-C-O-C- stretch of OXO	1042 cm ⁻¹ -C-O-C- of CHI-CHI	972 cm ⁻¹ 1° -OH	900 cm ⁻¹ Sym-C-O-C- stretch of OXO	778 cm ⁻¹ Chair-to-boat
1:1	↑	↓	↓	↑	↑	↓	↑
1:4	↑	↓	↓	↑	↑	↓	↑
1:10	↑	↓	↓	↑	↑	↓	↑